THE UNIVERSITY OF CHICAGO

RATIONAL DESIGN OF SILICON STRUCTURES FOR MULTI-SCALE BIOINTERFACES

A DISSERTATION SUBMITTED TO

THE FACULTY OF THE DIVISION OF THE PHYSICAL SCIENCES

IN CANDIDACY FOR THE DEGREE OF

DOCTOR OF PHILOSOPHY

DEPARTMENT OF CHEMISTRY

BY

YUANWEN JIANG

CHICAGO, ILLINOIS

MARCH 2018

Abstract

Silicon-based materials and devices represent a unique platform for interrogating fundamental biophysical processes. Recent advances in device designs and fabrications have enabled a wide variety of new silicon-based electronic and optoelectronic systems, which display multi-functional modalities that could be exploited for interfacing with various biological organizations. Besides the top-down fabrication which involves conventional lithographical processes, the bottom-up synthesis represents an alternative yet equally important method for the construction of silicon structures. In particular, the geometry and composition of the final construct can be tuned precisely during the materials growth, promising novel functions or applications beyond those offered by traditional platforms. In this thesis, I will report the design of a spectrum of silicon structures for the enhanced mechanical, electrical, and thermal biointerfaces, with targets spanning multiple length scales from nanoscopic organelles, microscopic single cells up to macroscopic tissues or organs. I will also focus on the study of fundamental aspects during the bottom-up synthesis to elucidate the underlying physicochemical processes that shape the silicon structures and properties.

First, I will introduce a biocompatible and degradable mesostructured form of amorphous silicon with multiscale structural and chemical heterogeneities. I will also show that the heterogeneous silicon mesostructures can be used to design a lipid-bilayer-supported bioelectric interface that is remotely controlled and temporally transient, and that permits non-genetic and subcellular optical modulation of the electrophysiology dynamics in single dorsal root ganglia neurons.

Secondly, I will demonstrate a biology-guided rational design principle for establishing intra-, inter- and extracellular silicon-based interfaces, where silicon and biological targets have matched properties. I will then demonstrate the utility of these interfaces by showing light-controlled non-genetic modulations of intracellular calcium dynamics, cytoskeleton-based transport and structures, cellular excitability, neural transmitter release from brain slices, and brain activities *in vivo*.

Then, I will demonstrate an atomic-gold enabled three-dimensional (3-D) lithography for silicon mesostructures, by showing one example where iterated deposition-diffusion-incorporation of gold over silicon nanowires can produce mesostructured silicon spicules. In addition, I will show the anisotropic spicule has a strong interfacial interaction with the extracellular matrix, suggesting enhanced mechanical biointegrations.

Finally, I will demonstrate that a liquid gold-silicon alloy established in classical vapor-liquid-solid growth can deposit ordered and three-dimensional rings of isolated gold atoms over silicon nanowire sidewalls. I will show that the single atomic gold-catalyzed chemical etching of silicon can lead to massive and ordered 3-D grooves on Si surfaces, which can serve as self-labelled and *ex situ* markers to resolve several complex silicon growths.

Acknowledgements

First and foremost, I would like to take this opportunity to express my sincere gratitude to my advisor, Professor Bozhi Tian, who has been offering tremendous support and insightful guidance over my entire journey in his research group. Professor Tian is an incredible person both as an extremely supportive mentor and as a close friend of mine. Since the first day when I joined the group, I was continuously inspired by his exceptional enthusiasm and persistence in research, extraordinary positive attitude towards setbacks, and scientific rigor in every detail, which really shaped my way of pursuing the essence of science. I was truly appreciative and honored by the numerous time and effort that Professor Tian has invested for the improvement of my scientific capability and career development, which was my invaluable privilege. All of our fruitful and encouraging discussions will be cherished and valued in the rest of my life.

I was also fortunate to have my thesis dissertation committee members, Professor Francisco Bezanilla and Professor Gregory S. Engel, who provided invaluable advices and constant encouragements me during previous collaborations and course studies. Their constructive and comments and suggstions for the improvement of this thesis were also truly appreciated.

My gratitude further extends to my colleagues in the Tian group, who helped me overcome all the hurdles and shared the enjoyable moments. I would like to thank Prof. Zhiqiang Luo, Dr. Raymond Wong, and Dr. Yin Fang, without whom all the works in this thesis would not have been possible. I would also like to acknowledge Prof. Yucai Wang, Dr. Yin Fang, Dr. Xiang Gao, Dr. Jaeseok Yi for all the stimulating discussions that helped to broadly expand my vision of science. My acknowledgements also go to my collaborators at UChicago, Northwestern and Argonne, especially Dr. João Luis Carvalho-de-Souza, Dr. Xiaojian Li, Dr. Bing Liu, Dr. Jiping Yue, for

their tremendous help on all the animal experiments, Dr. Mathew Cherukara and Dr. Subramanian Sankaranarayanan, for their great effort on the molecular dynamics simulation. I also enjoyed my interactions and conversations with other fellow lab members including not limited to Dr. John Zimmerman, Ms. Ramya Parameswaran, Mr. Vishnu Nair, Dr. Menahem Rotenberg, Ms. Youjin Lee, Mr. Hector Acaron Ledesma, Ms. Kelliann Koehler, and Mr. Andrew Phillips. Additionally, I would like to thank all the shared facility staff members and scientists, especially Dr. Justin Jureller, Ms. Yimei Chen at UChicago, Dr. Dieter Isheim at Northwestern, Dr. Fengyuan Shi, Dr. Alan Nicholls at UIC, Dr. Il Woong Jung, Dr. Xiaobing Zuo at Argonne, who provided enormous help for all the technical supports. In particular, I am indebted to Dr. Qiti Guo at MRSEC who enlightened me in many aspects not limited to science.

Finally, I would like to thank my friends and family who are always my strongest support out of the lab. Their continuous, unconditional love and care are the biggest motivation that drove me towards my Ph.D. degree. Thanks to my parent who always supported me on each endeavor throughout my life. I am also grateful to have my beloved girlfriend, Kefan Sun, who went through my entire journey in the graduate school with unparalleled love and understanding.

Table of Contents

Chapter 6

List of Figures

List of Tables

Chapter 1

Introduction

1.1 Historic overview of bioelectricity

Bioelectricity, that biological systems can generate and respond to electrical signals, is a fundamental process that is involved in many vital biological functions across all kinds of species. The initial discovery of the bioelectricity is widely credited to an Italian physicist Luigi Galvani. In the late 18th century, Galvani performed several epic works on frogs, which clearly demonstrated the electrical aspect of physiological activities[1,2]. In these experiments, electrical discharges from various sources, including lightning rods and static electricity generators were found to activate nerve conductions and cause muscle twitching. Galvani also noticed that the cut end of a frog sciatic nerve could stimulate contractions when it touched the muscles of the opposite leg.

Since the discovery of bioelectricity, scientists have numerous tools to investigate the nature of the bioelectric activities. What Galvani initially observed is now known due to the excitation and propagation of action potentials of neurons and muscle cells, whose features were systematically modeled by British biophysicists Alan Hodgkin and Andrew Huxley in their seminal paper published in 1952[3]. Both Hodgkin and Huxley were later awarded the Nobel Prize in Physiology or Medicine in 1963.

1.2 Resting potential of plasma membranes

The concept of an action potential can be better understood with the basic picture of a membrane potential. To take neurons as the example, at the resting state, there is an uneven

distribution of ions between the cytosol and the extracellular fluid, which gives rise to an electrical potential difference across the cell membrane, called the resting membrane potential (V_m). For V_m, the reference point is conventionally assigned to the extracellular space and therefore the membrane potential is defined as $V_m=V_{in}-V_{out}$. For a typical neuron, the membrane potential usually falls into the range between -50 mV and -70 mV. To quantitatively calculate the resting membrane potential V_m, one apparent factor is the ion concentration gradients across the cell membrane. In neurons and their surrounding fluid, the most abundant permeable ions are sodium (Na^+), potassium (K^+), chloride (Cl^-). In most neurons, K^+ is at a higher concentration in the cytosol than in the extracellular fluid. In contrast, Na^+ and Cl^- are usually rich outside the cell.

Ion	Intracellular concentration (mM)	Extracellular concentration (mM)
Potassium (K^+)	100	5
Sodium (Na^+)	15	150
Chloride (Cl^-)	13	150

Table 1-1. Approximate ion concentrations on either side of a mammalian neuronal membrane. Reproduced from Ref. 4.

Importantly, besides the ion concentration gradients, another important parameter namely, the membrane permeability of ions, also contribute significantly to the resting potential of a neuron. To fully appreciate the contribution of both factors, one can start with a simple case where only one ion (*e.g.,* K^+ ions) is allowed to move across the cell membrane. In the resting state, K^+ ions are present at a high concentration inside the cell and if the cell membrane is exclusively permeable to them, K^+ ions will tend to diffuse from the inside to the outside of the cell driven by the chemical gradient, through the so-called leak K^+ ion channels, which are open even in resting neurons. With

the K^+ diffusions, the outside of the membrane will gradually accumulate more positive charges due to the excessive K^+ ions while the inside is more negative. The charge separation due to the diffusion of K^+ will build up an electrical potential with the outside being more positive. As a result, K^+ ions will experience a new force driven by the electrical field that is pointing from the outside to the inside of the cell membrane, limiting further diffusion of K^+ ions. An equilibrium will be established eventually with the electrical driving force balancing the chemical driving force. This electrical potential is then called the potassium equilibrium potential, E_K. The equilibrium potential for any ion X can be calculated from the Nernst equation that

$$E_X = \frac{RT}{zF} \ln \frac{[X]_{out}}{[X]_{in}} \ , \qquad (1\text{-}1)$$

where R is the ideal gas constant, T is the absolute temperature, z is the valence of the ion, F is the Faraday constant, and $[X]_{out}$ and $[X]_{in}$ are the concentrations of the ion outside and inside of the cell. Taken the intra- and extracellular concentrations of K^+ ions from **Table 1-1**, one can calculate the potassium equilibrium potential E_K as -80 mV. However, electrophysiological recordings show that the resting membrane potential of a neuron is always higher than the value of -80 mV since there was only one ion being considered in the Nernst equation. In reality, all physiologically relevant ions need to be accounted for the resting potential and their relative contributions can be weighted by the ion permeabilities. David Goldman, Alan Hodgkin and Bernard Katz proposed the GHK equation[5,6] to better describe the membrane potential V_m as

$$V_m = \frac{RT}{F} \ln \frac{P_{K^+}[K^+]_{out} + P_{Na^+}[Na^+]_{out} + P_{Cl^-}[Cl^-]_{in}}{P_{K^+}[K^+]_{in} + P_{Na^+}[Na^+]_{in} + P_{Cl^-}[Cl^-]_{out}}, \qquad (1\text{-}2)$$

where P_{K^+}, P_{Na^+}, and P_{Cl^-} represent the permeability of K^+, Na^+, and Cl^- ions, respectively. For a neuron under its resting condition, the permeability ratios follow $P_{K^+} : P_{Na^+} : P_{Cl^-} = 1.0 : 0.04 : 0.45$.

Using the concentration values in **Table 1-1**, one can calculate the resting membrane potential as -61 mV. From the equation, it states that the higher the concentration of an ionic species and the greater its permeability, the larger its contribution in determining the membrane potential. In the extreme case when the permeability of one ion is extremely high, the GHK equation reduces to the Nernst equation for that ion.

Additionally, due to the potential difference across the cell membrane, the membrane is said to be polarized. If the membrane potential becomes more positive than it is at the resting potential, the membrane is said to be depolarized. Correspondingly, hyperpolarization refers to the case that the membrane potential becomes more negative than the resting potential.

For a cell to maintain its steady resting potential, passive diffusion itself is not sufficient for the task. As stated in the previous section, the real membrane potential is not the same as the equilibrium potential of any ion, which means that ions have the tendency to flow through the leak channels even at the resting state of a cell. For example, the membrane potential V_m = -61 mV is less negative than E_K = -80 mV, but less positive than E_{Na} = 62 mV. Thus, there will be a steady leak of K^+ out of the cell and of Na^+ into the cell. If no other mechanisms exist, the concentration gradients of K^+ and Na^+ will eventually run down. To maintain the ion concentration gradients, nature has evolved another mechanism named the Na^+-K^+ ATPase or Na^+-K^+ pump, which uses energy to move K^+ and Na^+ ions against their electrochemical gradients. The Na^+-K^+ ATPase is a large membrane-spanning protein with intracellular binding sites for Na^+ and ATP and extracellular binding sites for K^+. In one cycle of its operation, the pump uses the energy from the hydrolysis of one ATP molecule to extrude three Na^+ ions out of the cell and pump two K^+ ions into the cell. Because 3 Na^+ are exported for 2 K^+ brought into the cell, the pump itself is electrogenic by making the cytosol slightly more negative than it would otherwise be. The pump's

big contribution to the membrane potential, however, is indirect: It maintains steady Na^+ and K^+ gradients, which give rise to the membrane potential as both ions move down their respective concentration gradients through ion channels. Additionally, the pump also plays a crucial role in maintaining the osmotic balance of the cell. Due to the presence of non-permeable macromolecular anions such as proteins in the cytosol, the Donnan effect will cause a higher concentration of inorganic ions and correspondingly higher osmolarity inside the cell and cell will otherwise burst by the water flux. With the Na^+-K^+ pump actively extruding Na^+, the cytosol can always have a lower total concentration of inorganic ions than the extracellular fluid, thereby compensating for the excess intracellular organic anions.

1.3 Action potentials in excitable cells

With the basic understanding of the resting membrane potential, the action potential can be regarded as rapid changes of the membrane potential on the time scale of several milliseconds. Typically, a neuron first needs to be stimulated by external signals such as electrical and chemical cues such that the membrane is depolarized. Only if the depolarized membrane passes a threshold will the action potential be fired, known as the all-or-none principle. After the threshold, the membrane potential undergoes a rapid depolarization to a positive value followed by a rapid repolarization until the potential is even lower than the resting potential. Another important feature of the action potential is that its shape remains the same even if the stimulus strength further increases. Although firing frequency increases with the stimulus strength, there is a limit to the rate at which a neuron can generate action potentials. The maximum firing frequency is about 1000 Hz; once an action potential is initiated, it is impossible to initiate another for about 1 msec. This period of time is called the absolute refractory period. In addition, it can be relatively difficult to initiate another action potential for several milliseconds after the end of the absolute refractory

period. During this relative refractory period, the amount of current required to depolarize the neuron to action potential threshold is elevated above normal. Based on these basic features, Hodgkin and Huxley performed several elegant experiments and proposed that the action potential generation was related to the dynamics voltage-gated sodium and potassium ion channels. All the key features of an action potential can now be recapitulated on the molecular scale. For example, the threshold to fire an action potential is the membrane potential at which enough voltage-gated sodium channels open so that the relative ionic permeability of the membrane favors sodium over potassium (Threshold). After passing the threshold, since the inside of the membrane still has a negative electrical potential, there is a large driving force on Na^+ ions. Therefore, Na+ ions rush into the cell through the open sodium channels, causing the membrane to rapidly depolarize (Rising phase). Because the relative permeability of the membrane greatly favors sodium, the membrane potential goes to a value close to $E_{Na} = 62$ mV, which is greater than 0 mV (Overshoot). The behavior of two types of ion channels contributes to the subsequent falling phase. First, the voltage-gated sodium channels inactivate. Second, the delayed voltage-gated potassium channels finally open. Since there is a great driving force on K^+ ions when the membrane is strongly depolarized. K^+ ions rush out of the cell through the open channels, causing the membrane potential to become negative again (Falling phase). The opened voltage-gated potassium channels add to the resting potassium membrane permeability. Because there is very little sodium permeability, the membrane potential goes toward E_K = -80 mV, causing a hyperpolarization relative to the resting membrane potential until the voltage gated potassium channels close again (Undershoot). The absolute refractory period is due to the inactivation of sodium channels when the membrane becomes strongly depolarized. They cannot be activated again, and another action

potential cannot be generated, until the membrane potential goes sufficiently negative to recover from the inactivation of the channels (Absolute refractory period).

Besides the action potential generation, the propagation of action potentials along the axons is equally important as it passes the information encoded in the action potential patterns to other cells within the neural network. Aided by voltage-sensitive ion channels, action potentials propagate across neuronal membranes and trigger the release of neurotransmitters from presynaptic terminals into the synaptic cleft. Neurotransmitters can then bind to and activate receptors on the postsynaptic neuronal membrane, which results in signal transductions across the entire neural network.

1.4 Recording devices to probe bioelectric activities

Notably, the development of the basic neuroscience theories is largely limited by the available tools due to the extremely small sizes of single cells and the fast dynamics of action potentials. For example, During the 1950s, Hodgkin and Huxley were not able to perform intracellular recording of membrane potentials from mammalian cells, which typically have soma sizes of several microns. Instead, the H-H model was derived from neurons of invertebrates which can be 100-1000 times larger than the vertebrate ones[7,8]. Driven by the need to perform intracellular recordings of mammalian neurons, scientists finally developed a technique called the patch clamp in the 1970s[9,10]. German biophysicists Bert Sakmann and Erwin Neher, who invented the technique, received the Nobel Prize in Physiology or Medicine in 1991 for this important development. With the patch clamp technique, one can directly measure ionic currents either passing through single ion channels or the entire cell membrane, which is now the gold standard in electrophysiology.

Comparing to single cells, tissues or organs are much more difficult to study due to the extreme complexity of the system. For example, within the human brain, about 100 billion of neurons from thousands of genetically and structurally defined subtypes communicate with each other through an average of 10,000 synapses per cell[11]. Therefore, the motivation to answer fundamental questions in neuroscience has consistently inspired the invention of new technologies to understand neural activities on a large scale. In the late 1950s, stainless-steel wires were first introduced to animal brains to measure activities of single cells[12]. In the 1980s and 1990s, silicon based multielectrode arrays such as Utah arrays[13], Michigan probes[14], stereotrodes[15], and tetrodes[16] were developed to investigate communications between groups of neurons. Further advances in semiconductor micro-fabrications driven by the Moore's law have also enabled the implementation of miniaturized device designs with multiplexed modalities. Despite these progresses, traditional devices usually suffer from poor biointegrations mostly due to the foreign body responses of the soft tissues induced by the rigid electrode materials[17]. The elastic mismatch between the neural tissue (kilo- to megapascals) and the implanted probes (1–100 GPa), causes repeated injury to the tissue each time when the brain is displaced relative to the device[18]. To improve the biocompatibility of the devices for effective long-term operations, several strategies have been recently adopted in consideration of the mechanical, electrical and chemical properties of the tissue and the device. For example, soft polymer-based coating and substrate materials were used for the fabrication of the electrodes[19]. Alternatively, stiff materials can be made flexible by creating mesh- or serpentine-based open networks with reduced material thicknesses[20-23]. Additionally, low-modulus conductive materials such as conducting polymers can be used directly as the electrode materials[24,25].

1.5 Modulation techniques to interrogate bioelectric activities

1.5.1 Electrical

So far, we have only focused on the fundamental studies of the neurological system, if one can utilize the knowledge gleaned from the neural recordings and manipulate the natural electrical activities, there could be significant benefit for clinical applications. As we discussed in the earlier sections, action potentials are elicited by the depolarization of the cell membrane, which lays the foundation to all of the electrical stimulation techniques[26]. Electrical stimulation is clinically approved to treat Parkinson disease[27], and is a candidate for alleviating symptoms of major depression[28]. For other excitable tissues (*e.g.*, heart), cardiac pacemakers are also commonly used in clinics to treat cardiac arrhythmias[29]. Platinum and platinum–iridium electrodes with low impedance (< 10 kΩ) are typically used for electrical stimulations[30]. For the similar reason as mentioned earlier for recording devices, bulk and rigid stimulation electrodes also suffer from the mechanical mismatches with the soft tissue that induce significant foreign body responses[17,18]. To improve the overall device biocompatibility, besides the previously mentioned strategies to reduce the device nominal rigidities[19-23], a new direction emerged recently, which was to realize the neuromodulation with remotely-controlled external stimuli, such as light pulses, ultrasound waves, and magnetic fields. In electrical stimulations, even with the advanced materials and layout designs, wires are still required to deliver electrical signals, which will cause further inflammatory responses in the targeted tissue. Additionally, the geometry of the implanted device is fixed by its original design and therefore cannot be adapted in real-time to the actual morphology of the system under investigation.

1.5.2 Ultrasound

On the other hand, remotely-controlled stimuli do not require additional electrical connections and can easily be positioned to arbitrary locations for high-resolution multi-site stimulations. Among all three potential wireless stimulation mechanisms, each of them have their unique features and limitations, which will be elaborated in details in the following section (**Fig. 1-1**).

Ultrasound waves can induce cavitation inside the nervous system and can trigger action potentials by activating either mechanosensitive ion channels[31,32] or temperature-gated channels[33,34]. At low intensities for short exposure times when tissue heating does not occur, the mechanisms underlying the stimulation effects of ultrasound on neuronal activity are thought to mostly stem from the mechanical pressure effects on cellular membranes and ion channels[35]. In addition, acoustic waves can penetrate the tissue to a depth of several centimeter without significant attenuation in a frequency-dependent manner. Therefore, transcranial focused ultrasound at a low frequency of 0.5 MHz and with a small peak-to-peak amplitude of 0.12 MPa was shown to modulate the activities of primary somatosensory cortex in humans[36]. Although ultrasound with lower frequencies offer deeper tissue penetration depth, the spatial resolution, which is proportional to wavelength, is greatly compromised with lateral and axial spatial resolution of only 4.9 mm and 18 mm, respectively[36].

1.5.3 Magnetic

Magnetic fields can access deep tissues with little attenuation owing to the low magnetic susceptibility of biological matter. For the magnetic stimulation, a high-current pulse is produced in a magnetic coil which can produce a magnetic field with lines of flux passing perpendicularly to the plane of the coil with up to ~ 2 T[37]. An electric field is induced perpendicularly to the

magnetic field can cause current to flow in loops parallel to the coil plane with the strongest current near the coil itself[38]. The current becomes weaker near the center of the coil with no current at the center point. The motor cortex that is immediately underneath the skull has been shown to be stimulated by transcranial magnetic stimulations[37,38]. Nevertheless, magnetic stimulation is largely limited by the coil geometry, *e.g.*, round coils are relatively powerful; figure-eight-shaped coils are more focal with maximal current at the intersection of the two round components, and the spatial resolution is as low as the centimeter scale[38].

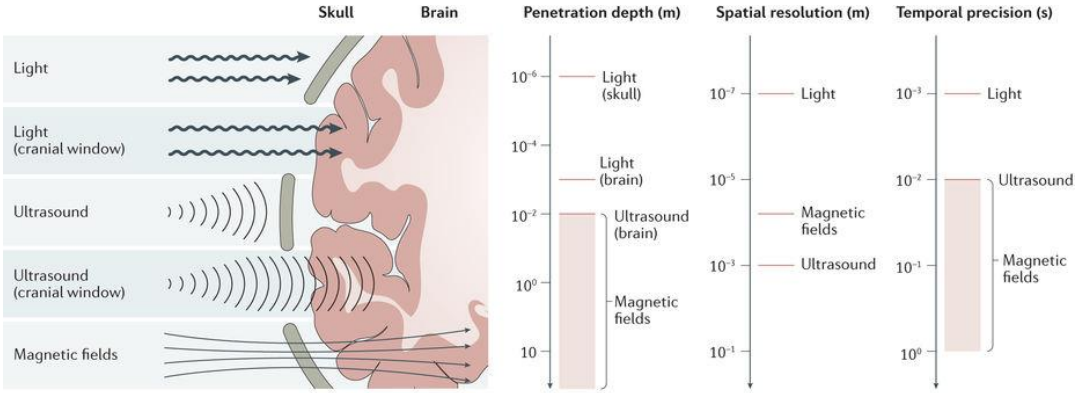

Figure 1-1. Tissue penetration by optical, ultrasonic and magnetic signals. Electromagnetic waves in the visible and (near-)infrared optical spectrum offer superior spatial and temporal resolution but limited penetration depth (~1–1.5 mm)[39]. Ultrasound can access deeper brain regions (>50 mm) with a spatial resolution that is inversely proportional to the wavelength, which, in turn, scales inversely with the penetration depth (in general for ultrasound, spatial resolution is >1 mm^3 and temporal precision is >10 ms)[36]. Alternating magnetic fields (AMFs) with low frequencies (<1 kHz) and high amplitudes (0.1–2 T) inductively couple to the upper 1–10 mm of tissue[37]. AMFs with amplitudes of ~1–100 mT and frequencies in the low radiofrequency range (0.1–1 MHz) travel through tissue unaffected. Temporal precision of neural activity is dependent on the chosen magnetic scheme. Reproduced from Ref. 18.

1.5.4 Optical

Comparing to acoustic and magnetic stimuli, optical signals offer superior spatial and temporal resolution but they are limited to penetration depths of < 1 mm owing to the significant

tissue absorbance and scattering. Light pulses, therefore, are ideal for precise stimulations of the brain cortex with subcellular resolution. The nervous system, however, does not normally respond to light stimulus except for the retina. Photosensitization of neurons is therefore necessary for the realization of optical modulation. Optogenetics is emerging as a powerful toolkit for neuroscientists that relies on the expression of light-sensitive microbial ion channels and pumps called opsins in mammalian neurons through genetic engineering methods[40,41]. Opsins are transmembrane proteins with the chromophore retinal, which changes its conformation upon light illumination and thus drives the ion transport to change the membrane potentials[42]. One example of the excitatory opsin is the channelrhodopsin 2 (ChR2)[43], which is a cation channel that mediates the membrane depolarization to initiate action potentials in response to light. Despite its widespread application in basic neuroscience studies, optogenetic interrogation of neural systems are mostly limited to small rodents where the genetic engineering techniques are relatively mature. It is currently technically challenging to achieve stable genetic manipulations on larger objects such as non-human primates or even human beings. The ethical issues related to the alteration of human genomes also need to be cleared before optogenetics could be applied in clinical trials. To circumvent these issues, an alternative strategy was proposed, that is to use materials-based photo-transducer for the sensitization of neurons in a non-genetic fashion.

1.6 Material candidates as photo-transducers

For a material that can serve as the photo-transducer, it needs to be a good light absorber and can also convert the light energy into another form, *i.e.*, thermal, electric, and mechanical energies which can directly impact the biological system.

1.6.1 Quantum dots

Several material systems have been developed in the past, including quantum dots, gold nanoparticles, and conducting polymers. HgTe quantum dot films have been shown to stimulate cultured neuronal cells upon light illumination[44]. In this case, the photo-generated excitons in quantum-confined nanoparticles produce electrons and holes. The injection of electrons from the film to the cell culture medium results in photocurrents, which was able to depolarize the adjacent cell membrane. However, this stimulation platform can only work in the film geometry, photostimulation of neurons with colloidal quantum dot suspension has not yet been reported. Moreover, the cytotoxicity of quantum dots, which typically involves heavy metal in their compositions, is constantly under debate[45].

1.6.2 Gold nanoparticles

Gold nanoparticles, on the other hand, exhibits strong photothermal efficacy due to the plasmonic heating effect when absorbing light its resonance wavelength[46,47]. Importantly, the photothermal effect can lead to both stimulation and inhibition of neural activities. It has been shown that the fast heating upon light illumination can transiently depolarize the cell membrane by increasing the membrane capacitance[48] while prolonged illumination will gradually hyperpolarize the cell with reduced membrane resistance[49]. Nevertheless, gold nanoparticles do not have the photovoltaic property as displayed in semiconductors.

1.6.3 Conducting polymers

Finally, conducting polymer is an emerging class of material that has been applied for non-genetic photostimulations. Poly(3-hexylthiophene) (P3HT) is a typical conducting polymer whose photophysical properties have been extensively studied[50]. In the presence of electron acceptors,

such as C_{61}-butyric acid methyl ester (PCBM) and an electrode, such as indium tin oxide (ITO), photovoltage is built up at the P3HT/ITO interface upon light illumination, which is coupled to the P3HT/electrolyte interface to induce depolarization of nearby cells[51-53]. Additionally, the photothermal effect of P3HT can also yields similar inhibitory effect on cells[54] like that from gold nanoparticles. Despite these promising progress, photo-responses from conducting polymers are usually complicated with relatively low energy-conversion efficiency. Furthermore, it is generally more difficult to tune the photovoltaic property and perform complicated device fabrications of conducting polymers comparing to inorganic semiconductors.

1.6.4 Silicon

1.6.4.1 Synthesis and fabrication of Si structures

In our research, we focus on the development of inorganic semiconductor materials, especially Si, for non-genetic optically-controlled neuromodulations. Si is the most well-studied semiconductor material, with a bandgap of ~ 1.1 eV for single crystalline Si. After decades of development from the semiconductor industry, manufacturing of Si structures can be readily achieved by a variety of approaches, which can be broadly categorized as bottom-up synthesis and top-down fabrications. The most commonly used approach for the bottom-up synthesis of Si is the chemical vapor deposition (CVD) technique. In a typical synthesis, a gaseous silicon precursor, *e.g.*, silane (SiH_4), is introduced to a vacuum chamber and it decomposes into Si and H_2 at a high temperature. The outcome of the synthesis can be either Si nanowires or Si films, depending on the detailed growth condition. For example, gold nanoparticles can serve as catalysts for the decomposition of silane by forming liquid alloy with Si (**Fig. 1-2**). Briefly, silane is absorbed by gold, decomposes at a lower temperature, and form liquid alloy droplets above the Si-Au eutectic temperature at ~ 363 ^{o}C. With further introduction of the Si content, Si will be supersaturated and

starts to precipitate in a directional manner resulting in the elongation of Si nanowires via the vapor-liquid-solid (VLS) mechanism[55-57]. Determined by the droplet size, the diameter of the Si nanowire can be tuned by various sizes of gold nanoparticles[58]. In the absence of catalysts, silane can still decompose at higher temperature and form films on the substrate via the vapor-solid (VS) mechanism[59,60]. During the synthesis, dopants can be introduced by flowing in additional gases such as diborane (B_2H_6) and phosphine (PH_3) to achieve both *p*-type and *n*-type Si[61,62]. Top-down fabrications, on the other hand, involve a series of lithographically-patterning and subsequent etching processes to shape the Si structures in a deterministic manner. With the recent advancement in device designs, Si membrane-based fabrications can now lead to flexible forms of devices, which are critical to interface with the soft and curvilinear biological tissues[20,21,63].

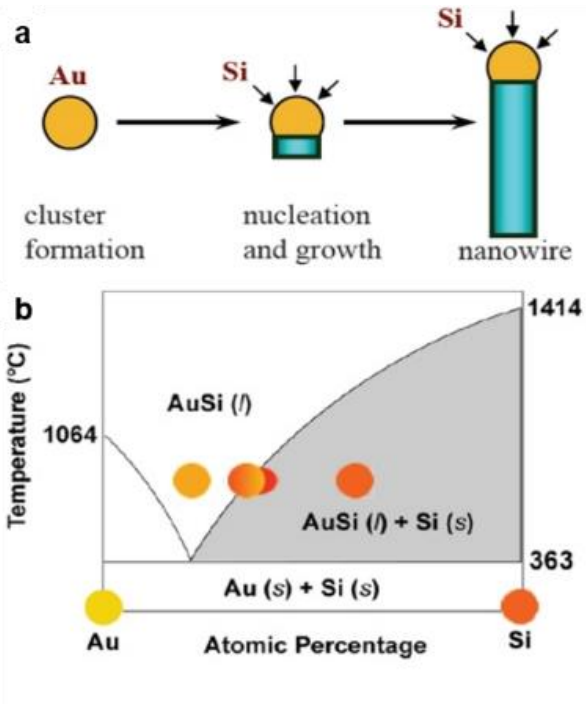

Figure 1-2. Schematics of the VLS growth of Si nanowires. a, A liquid alloy droplet AuSi is first formed above the eutectic temperature (363 °C) of Au and Si. The continued feeding of Si in the vapor phase into the liquid alloy causes oversaturation of the liquid alloy, resulting in nucleation and directional nanowire growth. **b**, A binary phase diagram for Au and Si illustrating the thermodynamics of the VLS growth. Reproduced from Ref. 64.

1.6.4.2 Existing Si-based bioelectronic devices

Due to the good biocompatibility and electrical properties of Si, there have been many recent reports of using Si-based electronic devices for probing electrical activities of biological systems from single cells[65-67] to an entire organ[20,63,68]. For example, kinked and dopant-modulated Si nanowire-based field-effect transistors (FET) have been used to record intracellular action potentials from single cardiomyocytes[65,67] (**Figs. 1-3a**, **1-3b**). Si nanomembranes can also be fabricated into multiplexed FET sensor arrays to map brain[20] and heart[63] activities in flexible configurations (**Figs. 1-3c**, **1-3d**). Although these electrically-addressable devices have proved their efficacy in probing bioelectric signal, free-standing and optically-controlled Si systems have yet been achieved.

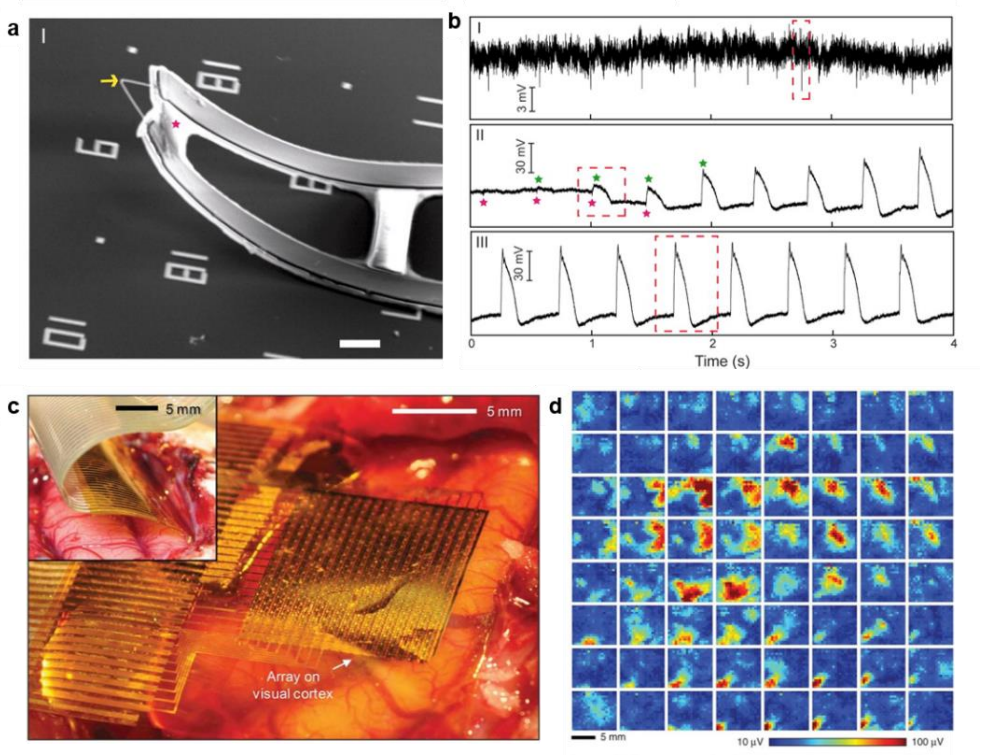

Figure 1-3. Si-based FETs for the recording of electrical signals from single cells to an entire organ. a, a SEM image of a device from a kinked and dopant modulated Si nanowire with two metal contacts. The stress release of the

Figure 1-3, continued. asymmetrical metal interconnects induced the 3D and free-standing configuration of the probe. The yellow arrow and pink star mark the nanoscale FET and SU-8, respectively. Scale bars, 5 μm. **b**, Electrical recording from beating cardiomyocytes: (**I**) extracellular recording, (**II**) transition from extracellular to intracellular recordings during cellular entrance, and (**III**) steady-state intracellular recording. Green and pink stars denote the peak positions of intracellular and extracellular signal components, respectively. Reproduced from Ref. 65. **c**, A flexible, high-density active electrode array was placed on the visual cortex of a feline model. Inset, the same electrode array was inserted into the interhemispheric fissure. **d**, 64-color maps, each showing the response (r.m.s. value of the zero-meaned signal in the response window) of the entire 360-channel electrode array. The color maps are arranged in the same physical layout as the stimuli were presented on the monitor, that is, the image map in the upper left-hand corner of the figure represents the neural response across the entire array to a flashing box presented in the upper left-hand corner of the monitor. The color scale is constant over all 64 image maps and is saturated at the 1st and 99th percentile to improve the visual display. Reproduced from Ref. 20.

1.6.4.3 Si for optically-controlled biointerfaces

Even though Si is an in-direct bandgap semiconductor, it still exhibits important optical properties, which can be useful to optically-controlled neuromodulations. Combining both the bottom-up and the top-down approaches, the photo-response of Si can be further tailored by the control of the doping level and crystallinity. Unlike conducting polymer, the photophysical properties of Si is well-understood. For example, bulk *p*-*n* junctions of single crystalline Si have very high photovoltaic performances, which are commonly used for commercial solar cells[69]. *p*-*i*-*n* junctions of amorphous Si has a much higher light absorptivity[70] comparing to single crystalline Si at the same thickness, which is beneficial to the manufacturing of thin film solar cells[71]. Other than the photovoltaic property, the photothermal property of Si can also be promoted with the amorphous structure. All of these properties could be potentially integrated together for the construction of free-standing and optically-controlled biointerfaces. Additionally, Si can be

degraded by extracellular fluids through an oxidation and dissolution pathway involving silicate[72] and the biodegradability can be further exploited to form transient biointerfaces[73].

1.7 Thesis overview

In this thesis, taking inspiration and guidance from biology, I will report the design of a spectrum of novel silicon (Si) structures for the enhanced mechanical, electrical, and thermal biointerfaces, spanning multiple length scales from nanoscopic organelles, microscopic single cells up to macroscopic tissues or organs. I will also focus on the study of fundamental aspects during the bottom-up synthesis to elucidate the underlying physicochemical processes that shape the Si structures and properties.

In Chapter 2, I will introduce a biocompatible and degradable mesostructured form of silicon with multiscale structural and chemical heterogeneities. The material is synthesized using mesoporous silica as a template through a chemical-vapor-deposition process. It has an amorphous atomic structure, an ordered nanowire-based framework, and random sub-micrometer voids, and shows an average Young's modulus that is 2-3 orders of magnitude smaller than that of single crystalline silicon. In addition, I will show that the heterogeneous silicon mesostructures can be used to design a lipid-bilayer-supported bioelectric interface that is remotely controlled and temporally transient, and that permits non-genetic and subcellular optical modulation of the electrophysiology dynamics in single dorsal root ganglia neurons.

In Chapter 3, I will demonstrate a biology-guided rational design principle for establishing intra-, inter- and extracellular Si-based interfaces, where Si and biological targets have matched properties. In particular, I will focus on the light-induced processes at these interfaces, and develop a set of matrices to quantify and differentiate the capacitive, Faradaic and thermal outputs from ~ 30 different Si materials in saline. Finally, I will demonstrate the utility of these interfaces by

showing light-controlled non-genetic modulations of intracellular calcium dynamics, cytoskeleton-based transport and structures, cellular excitability, neural transmitter release from brain slices, and brain activities *in vivo*.

In Chapter 4, I will explore the atomic-gold enabled three-dimensional (3-D) mesoscale lithography, by showing one example where iterated deposition-diffusion-incorporation of gold over silicon nanowires forms etchant-resistant patterns. I will also show that this process is facet selective and can produce mesostructured silicon spicules with skeleton-like morphology, three-dimensional tectonic motifs, and reduced symmetries. Atom-probe tomography, coupled with other quantitative measurements, indicates the existence and the role of individual gold atoms in forming 3-D lithographic resists. Finally, compared to other more uniform silicon structures, the anisotropic spicule requires greater force for detachment from collagen hydrogels, suggesting enhanced interfacial interactions at the mesoscale.

In Chapter 5, I will demonstrate that a liquid gold-silicon alloy established in classical vapor-liquid-solid growth can deposit ordered and three-dimensional rings of isolated gold atoms over silicon nanowire sidewalls. I will show that *ab initio* molecular dynamics simulation unveils a surprising single atomic gold-catalyzed chemical etching of silicon. Additionally, I will show the experimental verification of the catalytic process in silicon nanowires and yield dopant-dependent, massive and ordered 3D grooves with spacing down to ~ 5 nm. We can further use these grooves as self-labelled and *ex situ* markers and resolved several complex silicon growths, including the formation of nodes, kinks, scale-like interfaces, and curved backbones. Finally, the nanoscale topography on Si may be beneficial for potential interfaces with cytoskeleton for enhanced entanglements.

1.8 Bibliography

1 McCaig, C. D., Rajnicek, A. M., Song, B. & Zhao, M. Controlling cell behavior electrically: current views and future potential. *Physiological Reviews* **85**, 943-978, doi:10.1152/physrev.00020.2004 (2005).

2 Piccolino, M. Luigi Galvani and animal electricity: two centuries after the foundation of electrophysiology. *Trends in Neurosciences* **20**, 443-448, doi:10.1016/S0166-2236(97)01101-6 (1997).

3 Hodgkin, A. L. & Huxley, A. F. A quantitative description of membrane current and its application to conduction and excitation in nerve. *The Journal of Physiology* **117**, 500-544, doi:10.1113/jphysiol.1952.sp004764 (1952).

4 Bear, M. F., Connors, B. W. & Paradiso, M. A. *Neuroscience : exploring the brain*. (Lippincott Williams & Wilkins, 2007).

5 Goldman, D. E. Potential, Impedance, and Rectification in Membranes. *Journal of General Physiology* **27**, 37-60, doi:10.1085/jgp.27.1.37 (1943).

6 Hodgkin, A. L. & Katz, B. The effect of sodium ions on the electrical activity of giant axon of the squid. *The Journal of Physiology* **108**, 37-77, doi:10.1113/jphysiol.1949.sp004310 (1949).

7 Purves, D., Augustine, G. J., Fitzpatrick, D. & Katz, L. C. *Neuroscience*. (Sinauer Associates, 1997).

8 Young, J. Z. Fused neurons and synaptic contacts in the giant nerve fibres of cephalopods. *Philosophical Transactions of the Royal Society of London Series B-Biological Sciences* **229**, 465-U100, doi:DOI 10.1098/rstb.1939.0003 (1939).

9 Neher, E. & Sakmann, B. Single-channel currents recorded from membrane of denervated frog muscle fibres. *Nature* **260**, 799-802, doi:10.1038/260799a0 (1976).

10 Sakmann, B. & Neher, E. Patch clamp techniques for studying ionic channels in excitable membranes. *Annual Review of Physiology* **46**, 455-472, doi:10.1146/annurev.ph.46.030184.002323 (1984).

11 Kandel, E. R., Schwartz, J. H., Jessell, T. M., Siegelbaum, S. A. & Hudspeth, A. J. *Principles of neural science*. (McGraw-hill New York, 2000).

12 Strumwasser, F. Long-term recording from single neurons in brain of unrestrained mammals. *Science* **127**, 469-470, doi:10.1126/science.127.3296.469 (1958).

13 Campbell, P. K., Jones, K. E., Huber, R. J., Horch, K. W. & Normann, R. A. A silicon-based, three-dimensional neural interface: manufacturing processes for an intracortical electrode array. *IEEE Transactions on Biomedical Engineering* **38**, 758-768, doi:10.1109/10.83588 (1991).

14 Drake, K. L., Wise, K. D., Farraye, J., Anderson, D. J. & BeMent, S. L. Performance of planar multisite microprobes in recording extracellular single-unit intracortical activity. *IEEE Transactions on Biomedical Engineering* **35**, 719-732, doi:10.1109/10.7273 (1988).

15 McNaughton, B. L., O'Keefe, J. & Barnes, C. A. The stereotrode: A new technique for simultaneous isolation of several single units in the central nervous system from multiple unit records. *Journal of Neuroscience Methods* **8**, 391-397, doi:10.1016/0165-0270(83)90097-3 (1983).

16 Gray, C. M., Maldonado, P. E., Wilson, M. & McNaughton, B. Tetrodes markedly improve the reliability and yield of multiple single-unit isolation from multi-unit recordings in cat striate cortex. *Journal of Neuroscience Methods* **63**, 43-54, doi:10.1016/0165-0270(95)00085-2 (1995).

17 Polikov, V. S., Tresco, P. A. & Reichert, W. M. Response of brain tissue to chronically implanted neural electrodes. *Journal of Neuroscience Methods* **148**, 1-18, doi:10.1016/j.jneumeth.2005.08.015 (2005).

18 Chen, R., Canales, A. & Anikeeva, P. Neural recording and modulation technologies. *Nature Reviews Materials* **2**, doi:10.1038/natrevmats.2016.93 (2017).

19 Aregueta-Robles, U. A., Woolley, A. J., Poole-Warren, L. A., Lovell, N. H. & Green, R. A. Organic electrode coatings for next-generation neural interfaces. *Frontiers in Neuroengineering* **7**, 15, doi:10.3389/fneng.2014.00015 (2014).

20 Viventi, J., Kim, D. H., Vigeland, L., Frechette, E. S., Blanco, J. A., Kim, Y. S., Avrin, A. E., Tiruvadi, V. R., Hwang, S. W., Vanleer, A. C., Wulsin, D. F., Davis, K., Gelber, C. E., Palmer, L., Van der Spiegel, J., Wu, J., Xiao, J., Huang, Y., Contreras, D., Rogers, J. A. & Litt, B. Flexible, foldable, actively multiplexed, high-density electrode array for mapping brain activity in vivo. *Nature Neuroscience* **14**, 1599-1605, doi:10.1038/nn.2973 (2011).

21 Kim, D. H., Lu, N., Ma, R., Kim, Y. S., Kim, R. H., Wang, S., Wu, J., Won, S. M., Tao, H., Islam, A., Yu, K. J., Kim, T. I., Chowdhury, R., Ying, M., Xu, L., Li, M., Chung, H. J., Keum, H., McCormick, M., Liu, P., Zhang, Y. W., Omenetto, F. G., Huang, Y., Coleman, T. & Rogers, J. A. Epidermal electronics. *Science* **333**, 838-843, doi:10.1126/science.1206157 (2011).

22 Liu, J., Fu, T. M., Cheng, Z., Hong, G., Zhou, T., Jin, L., Duvvuri, M., Jiang, Z., Kruskal, P., Xie, C., Suo, Z., Fang, Y. & Lieber, C. M. Syringe-injectable electronics. *Nature Nanotechnology* **10**, 629-636, doi:10.1038/nnano.2015.115 (2015).

23 Fu, T. M., Hong, G., Zhou, T., Schuhmann, T. G., Viveros, R. D. & Lieber, C. M. Stable long-term chronic brain mapping at the single-neuron level. *Nature Methods* **13**, 875-882, doi:10.1038/nmeth.3969 (2016).

24 Khodagholy, D., Gelinas, J. N., Thesen, T., Doyle, W., Devinsky, O., Malliaras, G. G. & Buzsaki, G. NeuroGrid: recording action potentials from the surface of the brain. *Nature Neuroscience* **18**, 310-315, doi:10.1038/nn.3905 (2015).

25 Khodagholy, D., Doublet, T., Quilichini, P., Gurfinkel, M., Leleux, P., Ghestem, A., Ismailova, E., Herve, T., Sanaur, S., Bernard, C. & Malliaras, G. G. In vivo recordings of brain activity using organic transistors. *Nature Communications* **4**, 1575, doi:10.1038/ncomms2573 (2013).

26 Merrill, D. R., Bikson, M. & Jefferys, J. G. Electrical stimulation of excitable tissue: design of efficacious and safe protocols. *Journal of Neuroscience Methods* **141**, 171-198, doi:10.1016/j.jneumeth.2004.10.020 (2005).

27 Perlmutter, J. S. & Mink, J. W. Deep brain stimulation. *Annual Review of Neuroscience* **29**, 229-257, doi:10.1146/annurev.neuro.29.051605.112824 (2006).

28 Holtzheimer, P. E., 3rd & Mayberg, H. S. Deep brain stimulation for treatment-resistant depression. *American Journal of Psychiatry* **167**, 1437-1444, doi:10.1176/appi.ajp.2010.10010141 (2010).

29 Feiner, R. & Dvir, T. Tissue–electronics interfaces: from implantable devices to engineered tissues. *Nature Reviews Materials* **3**, 17076, doi:10.1038/natrevmats.2017.76 (2017).

30 Cogan, S. F. Neural stimulation and recording electrodes. *Annual Review of Biomedical Engineering* **10**, 275-309, doi:10.1146/annurev.bioeng.10.061807.160518 (2008).

31 Dalecki, D. Mechanical bioeffects of ultrasound. *Annual Review of Biomedical Engineering* **6**, 229-248, doi:10.1146/annurev.bioeng.6.040803.140126 (2004).

32 Krasovitski, B., Frenkel, V., Shoham, S. & Kimmel, E. Intramembrane cavitation as a unifying mechanism for ultrasound-induced bioeffects. *Proc Natl Acad Sci U S A* **108**, 3258-3263, doi:10.1073/pnas.1015771108 (2011).

33 O'Brien, W. D. Ultrasound–biophysics mechanisms. *Progress in Biophysics and Molecular biology* **93**, 212-255, doi:10.1016/j.pbiomolbio.2006.07.010 (2007).

34 Nyborg, W. L. Biological effects of ultrasound: Development of safety guidelines. Part II: General review. *Ultrasound in Medicine & Biology* **27**, 301-333, doi:10.1016/S0301-5629(00)00333-1 (2001).

35 Tufail, Y., Matyushov, A., Baldwin, N., Tauchmann, M. L., Georges, J., Yoshihiro, A., Tillery, S. I. & Tyler, W. J. Transcranial pulsed ultrasound stimulates intact brain circuits. *Neuron* **66**, 681-694, doi:10.1016/j.neuron.2010.05.008 (2010).

36 Legon, W., Sato, T. F., Opitz, A., Mueller, J., Barbour, A., Williams, A. & Tyler, W. J. Transcranial focused ultrasound modulates the activity of primary somatosensory cortex in humans. *Nature Neuroscience* **17**, 322-329, doi:10.1038/nn.3620 (2014).

37 Hallett, M. Transcranial magnetic stimulation: a primer. *Neuron* **55**, 187-199, doi:10.1016/j.neuron.2007.06.026 (2007).

38 Hallett, M. Transcranial magnetic stimulation and the human brain. *Nature* **406**, 147-150, doi:10.1038/35018000 (2000).

39 Yizhar, O., Fenno, Lief E., Davidson, Thomas J., Mogri, M. & Deisseroth, K. Optogenetics in Neural Systems. *Neuron* **71**, 9-34, doi:10.1016/j.neuron.2011.06.004 (2011).

40 Boyden, E. S., Zhang, F., Bamberg, E., Nagel, G. & Deisseroth, K. Millisecond-timescale, genetically targeted optical control of neural activity. *Nature Neuroscience* **8**, 1263-1268, doi:10.1038/nn1525 (2005).

41 Montgomery, K. L., Iyer, S. M., Christensen, A. J., Deisseroth, K. & Delp, S. L. Beyond the brain: Optogenetic control in the spinal cord and peripheral nervous system. *Science Translational Medicine* **8**, 337rv335, doi:10.1126/scitranslmed.aad7577 (2016).

42 Zhang, F., Vierock, J., Yizhar, O., Fenno, L. E., Tsunoda, S., Kianianmomeni, A., Prigge, M., Berndt, A., Cushman, J., Polle, J., Magnuson, J., Hegemann, P. & Deisseroth, K. The Microbial Opsin Family of Optogenetic Tools. *Cell* **147**, 1446-1457, doi:10.1016/j.cell.2011.12.004 (2011).

43 Nagel, G., Szellas, T., Huhn, W., Kateriya, S., Adeishvili, N., Berthold, P., Ollig, D., Hegemann, P. & Bamberg, E. Channelrhodopsin-2, a directly light-gated cation-selective membrane channel. *Proceedings of the National Academy of Sciences* **100**, 13940-13945, doi:10.1073/pnas.1936192100 (2003).

44 Pappas, T. C., Wickramanyake, W. M. S., Jan, E., Motamedi, M., Brodwick, M. & Kotov, N. A. Nanoscale Engineering of a Cellular Interface with Semiconductor Nanoparticle Films for Photoelectric Stimulation of Neurons. *Nano Letters* **7**, 513-519, doi:10.1021/nl062513v (2007).

45 Oh, E., Liu, R., Nel, A., Gemill, K. B., Bilal, M., Cohen, Y. & Medintz, I. L. Meta-analysis of cellular toxicity for cadmium-containing quantum dots. *Nature Nanotechnology* **11**, 479-486, doi:10.1038/nnano.2015.338 (2016).

46 Hu, M., Chen, J., Li, Z.-Y., Au, L., Hartland, G. V., Li, X., Marquez, M. & Xia, Y. Gold nanostructures: engineering their plasmonic properties for biomedical applications. *Chemical Society Reviews* **35**, 1084-1094, doi:10.1039/B517615H (2006).

47 Huang, X., Jain, P. K., El-Sayed, I. H. & El-Sayed, M. A. Plasmonic photothermal therapy (PPTT) using gold nanoparticles. *Lasers in Medical Science* **23**, 217, doi:10.1007/s10103-007-0470-x (2007).

48 Carvalho-de-Souza, João L., Treger, Jeremy S., Dang, B., Kent, Stephen B. H., Pepperberg, David R. & Bezanilla, F. Photosensitivity of Neurons Enabled by Cell-Targeted Gold Nanoparticles. *Neuron* **86**, 207-217, doi:10.1016/j.neuron.2015.02.033 (2015).

49 Yoo, S., Kim, R., Park, J.-H. & Nam, Y. Electro-optical Neural Platform Integrated with Nanoplasmonic Inhibition Interface. *ACS Nano* **10**, 4274-4281, doi:10.1021/acsnano.5b07747 (2016).

50 Sirringhaus, H., Brown, P. J., Friend, R. H., Nielsen, M. M., Bechgaard, K., Langeveld-Voss, B. M. W., Spiering, A. J. H., Janssen, R. A. J., Meijer, E. W., Herwig, P. & de Leeuw, D. M. Two-dimensional charge transport in self-organized, high-mobility conjugated polymers. *Nature* **401**, 685, doi:10.1038/44359 (1999).

51 Ghezzi, D., Antognazza, M. R., Maccarone, R., Bellani, S., Lanzarini, E., Martino, N., Mete, M., Pertile, G., Bisti, S., Lanzani, G. & Benfenati, F. A polymer optoelectronic interface restores light sensitivity in blind rat retinas. *Nature Photonics* **7**, 400-406, doi:10.1038/nphoton.2013.34 (2013).

52 Ghezzi, D., Antognazza, M. R., Dal Maschio, M., Lanzarini, E., Benfenati, F. & Lanzani, G. A hybrid bioorganic interface for neuronal photoactivation. *Nature Communications* **2**, 166, doi:10.1038/ncomms1164 (2011).

53 Maya-Vetencourt, J. F., Ghezzi, D., Antognazza, M. R., Colombo, E., Mete, M., Feyen, P., Desii, A., Buschiazzo, A., Di Paolo, M., Di Marco, S., Ticconi, F., Emionite, L., Shmal, D., Marini, C., Donelli, I., Freddi, G., Maccarone, R., Bisti, S., Sambuceti, G., Pertile, G., Lanzani, G. & Benfenati, F. A fully organic retinal prosthesis restores vision in a rat model of degenerative blindness. *Nature Materials* **16**, 681-689, doi:10.1038/nmat4874 (2017).

54 Martino, N., Feyen, P., Porro, M., Bossio, C., Zucchetti, E., Ghezzi, D., Benfenati, F., Lanzani, G. & Antognazza, M. R. Photothermal cellular stimulation in functional bio-polymer interfaces. *Scientific Reports* **5**, 8911, doi:10.1038/srep08911 (2015).

55 Wagner, R. S. & Ellis, W. C. Vapo-liquid-solid mechanism of single crystal growth. *Applied Physics Letters* **4**, 89-90, doi:10.1063/1.1753975 (1964).

56 Schmidt, V., Wittemann, J. V., Senz, S. & Gösele, U. Silicon nanowires: a review on aspects of their growth and their electrical properties. *Advanced Materials* **21**, 2681-2702, doi:10.1002/adma.200803754 (2009).

57 Schmidt, V., Wittemann, J. V. & Gösele, U. Growth, thermodynamics, and electrical properties of silicon nanowires. *Chemical Reviews* **110**, 361-388, doi:10.1021/cr900141g (2010).

58 Wu, Y., Cui, Y., Huynh, L., Barrelet, C. J., Bell, D. C. & Lieber, C. M. Controlled growth and structures of molecular-scale silicon nanowires. *Nano Letters* **4**, 433-436, doi:10.1021/nl035162i (2004).

59 Lauhon, L. J., Gudiksen, M. S., Wang, D. & Lieber, C. M. Epitaxial core–shell and core–multishell nanowire heterostructures. *Nature* **420**, 57, doi:10.1038/nature01141 (2002).

60 Tian, B., Zheng, X., Kempa, T. J., Fang, Y., Yu, N., Yu, G., Huang, J. & Lieber, C. M. Coaxial silicon nanowires as solar cells and nanoelectronic power sources. *Nature* **449**, 885-889, doi:10.1038/nature06181 (2007).

61 Gudiksen, M. S., Lauhon, L. J., Wang, J., Smith, D. C. & Lieber, C. M. Growth of nanowire superlattice structures for nanoscale photonics and electronics. *Nature* **415**, 617, doi:10.1038/415617a (2002).

62 Kempa, T. J., Tian, B., Kim, D. R., Hu, J., Zheng, X. & Lieber, C. M. Single and Tandem Axial p-i-n Nanowire Photovoltaic Devices. *Nano Letters* **8**, 3456-3460, doi:10.1021/nl8023438 (2008).

63 Fang, H., Yu, K. J., Gloschat, C., Yang, Z., Chiang, C. H., Zhao, J., Won, S. M., Xu, S., Trumpis, M., Zhong, Y., Song, E., Han, S. W., Xue, Y., Xu, D., Cauwenberghs, G., Kay, M., Huang, Y., Viventi, J., Efimov, I. R. & Rogers, J. A. Capacitively coupled arrays of multiplexed flexible silicon transistors for long-term cardiac electrophysiology. *Nature Biomedical Engineering* **1**, 0038, doi:10.1038/s41551-017-0038 (2017).

64 Wei, L. & Charles, M. L. Semiconductor nanowires. *Journal of Physics D: Applied Physics* **39**, R387 (2006).

65 Tian, B., Cohen-Karni, T., Qing, Q., Duan, X., Xie, P. & Lieber, C. M. Three-dimensional, flexible nanoscale field-effect transistors as localized bioprobes. *Science* **329**, 830-834, doi:10.1126/science.1192033 (2010).

66 Duan, X., Gao, R., Xie, P., Cohen-Karni, T., Qing, Q., Choe, H. S., Tian, B., Jiang, X. & Lieber, C. M. Intracellular recordings of action potentials by an extracellular nanoscale field-effect transistor. *Nature Nanotechnology* **7**, 174-179, doi:10.1038/nnano.2011.223 (2011).

67 Qing, Q., Jiang, Z., Xu, L., Gao, R., Mai, L. & Lieber, C. M. Free-standing kinked nanowire transistor probes for targeted intracellular recording in three dimensions. *Nature Nanotechnology* **9**, 142-147, doi:10.1038/nnano.2013.273 (2014).

68 Xie, C., Liu, J., Fu, T. M., Dai, X., Zhou, W. & Lieber, C. M. Three-dimensional macroporous nanoelectronic networks as minimally invasive brain probes. *Nature Materials* **14**, 1286-1292, doi:10.1038/nmat4427 (2015).

69 Lewis, N. S. Toward Cost-Effective Solar Energy Use. *Science* **315**, 798 (2007).

70 Zhu, J., Yu, Z., Burkhard, G. F., Hsu, C. M., Connor, S. T., Xu, Y., Wang, Q., McGehee, M., Fan, S. & Cui, Y. Optical absorption enhancement in amorphous silicon nanowire and nanocone arrays. *Nano Letters* **9**, 279-282, doi:10.1021/nl802886y (2009).

71 Carlson, D. E. & Wronski, C. R. Amorphous silicon solar cell. *Applied Physics Letters* **28**, 671-673, doi:10.1063/1.88617 (1976).

72 Hwang, S. W., Tao, H., Kim, D. H., Cheng, H., Song, J. K., Rill, E., Brenckle, M. A., Panilaitis, B., Won, S. M., Kim, Y. S., Song, Y. M., Yu, K. J., Ameen, A., Li, R., Su, Y., Yang, M., Kaplan, D. L., Zakin, M. R., Slepian, M. J., Huang, Y., Omenetto, F. G. & Rogers, J. A. A physically transient form of silicon electronics. *Science* **337**, 1640-1644, doi:10.1126/science.1226325 (2012).

73 Kang, S.-K., Murphy, R. K. J., Hwang, S.-W., Lee, S. M., Harburg, D. V., Krueger, N. A., Shin, J., Gamble, P., Cheng, H., Yu, S., Liu, Z., McCall, J. G., Stephen, M., Ying, H., Kim, J., Park, G., Webb, R. C., Lee, C. H., Chung, S., Wie, D. S., Gujar, A. D., Vemulapalli, B., Kim, A. H., Lee, K.-M., Cheng, J., Huang, Y., Lee, S. H., Braun, P. V., Ray, W. Z. & Rogers, J. A. Bioresorbable silicon electronic sensors for the brain. *Nature* **530**, 71, doi:10.1038/nature16492 (2016).

Chapter 2

Heterogeneous silicon mesostructures for lipid-supported bioelectric interfaces

2.1 Introduction

Silicon (Si) is a widely used material in biomedical research[1-11] because it is biocompatible and biodegradable, and it exhibits a spectrum of important electrical, optical, thermal and mechanical properties. For example, Si-based systems can sense electrical activities of the brain in flexible and adhesive configurations[12-14], deliver nucleic acids *in vivo* to induce angiogenesis[7], and perform intra- and intercellular force dynamics measurement[15]. So far, most of the applications of Si as biomaterials have been focused on or originated from single crystalline structures or substrates, which is primarily due to the need for high quality and controllable electrical or other properties. New Si-based forms that are unique in composition, structure, and property have the potential to yield nontraditional applications for Si-based biomaterials and open up unexpected new avenues for research and device manufacturing. In this chapter, I will introduce a biocompatible and degradable mesostructured form of silicon with multiscale structural and chemical heterogeneities. The material is synthesized using mesoporous silica as a template through a chemical-vapor-deposition process. It has an amorphous atomic structure, an ordered nanowire-based framework, and random sub-micrometer voids, and shows an average Young's modulus that is 2-3 orders of magnitude smaller than that of single crystalline silicon. In addition, I will show that the heterogeneous silicon mesostructures can be used to design a lipid-bilayer-

supported bioelectric interface that is remotely controlled and temporally transient, and that permits non-genetic and subcellular optical modulation of the electrophysiology dynamics in single dorsal root ganglia neurons. Finally, our findings suggest that the biomimetic expansion of silicon into heterogeneous and deformable forms can open up opportunities in extracellular biomaterial or bioelectric systems.

2.2 Results and Discussion

2.2.1 Structural heterogeneity

Natural biomaterials have remarkable diversity in structure and function and may guide the design[16] of new Si forms[17-22] for subcellular interfaces and biophysical modulation (**Fig. 2-1a**). Given this hypothesis, we first focused on the synthesis of three-dimensional (3D) Si-based biomaterials with an ordered and uni-directionally aligned fibril-based framework; we did so because this layout is fundamental to many natural biomaterials[16,23] (*e.g.*, bone[16]) and extracellular matrices (ECM)[24]. We employed a nano-casting approach[17,25-28] with ordered hexagonal mesoporous silica (SiO_2) SBA-15[29] as the template, in which silane (SiH_4) decomposition inside the channels and pores could provide the nanowire arrays with self-supporting micro-bridges[25,26]. While nano-casting synthesis of mesoporous solids is highly versatile and scalable, ordered and freestanding Si-based mesostructures with molecular-level principal feature sizes (*i.e.*, < 10 nm) are still challenging to achieve[17,18,27,30]. We designed a chemical vapor deposition (CVD) apparatus with a double-quartz-tubing system in which the SiO_2 template (SBA-15) was placed near the bottom of the inner tube (**Fig. 2-1**).

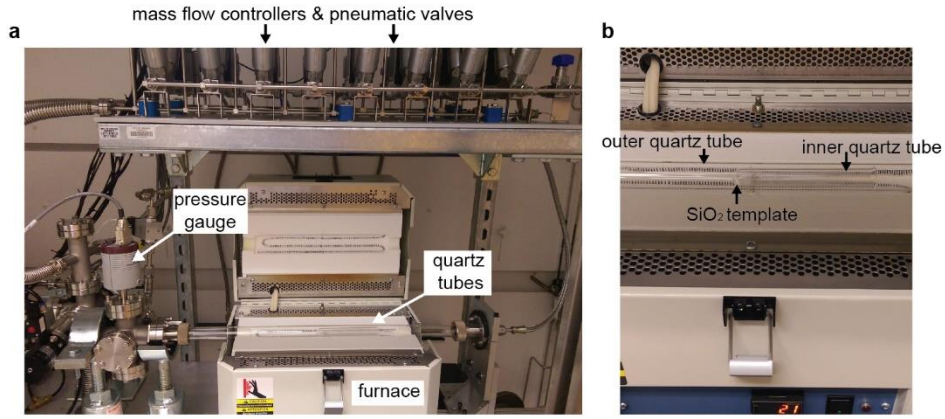

Figure 2-1. Home-built CVD system for bottom-up synthesis of mesostructured Si. **a**, Overview of the experimental setup. Silicon precursor SiH_4 and carrier gas H_2 were pre-mixed and introduced to the tube furnace with temperature, flow rate and pressure controlled throughout the synthesis. Mass flow controllers, pneumatic valves, a pressure gauge, a tube furnace, and quartz tubes are labeled. An inner quartz tube with SiO_2 template was placed at the center of an outer quartz tube, where Si would be subsequently deposited. **b**, Zoom-in view of the double-tubing system. White SiO_2 template was placed near the bottom of the inner tube.

We have identified an optimal growth temperature at 500 ^oC with a duration of 2 hours, when 200 mg of SBA-15 template was used. After CVD, subsequent wet chemical etching with hydrofluoric acid (HF) removed the SiO_2 and yielded a brownish powder (**Fig. 2-2a**). The scanning electron microscopy (SEM) image shows wheat-like aggregates with individual grain width of ~2 μm (**Fig. 2-2b**).

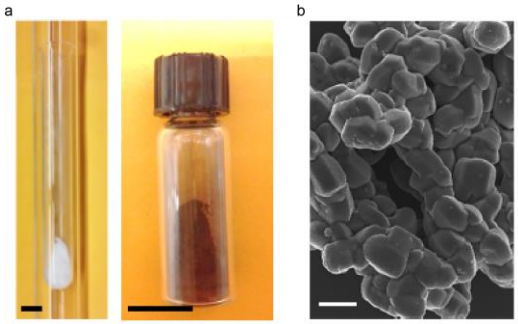

Figure 2-2. Physical appearance of the mesostructured Si. **a**, A double quartz-tubing system was used for nano-casting synthesis, with a mesoporous SiO_2 template placed near the bottom of the inner tube (left). After HF etching,

Figure 2-2, continued. the brownish product (right) can be yielded. Scale bars, 1 cm. **b**, SEM image of as-synthesized Si particles shows a morphology similar to that of SBA-15 template. Scale bar, 2 μm.

Nano-computed tomography (nano-CT) from transmission X-ray microscopy (TXM) measurement reveals that individual particle aggregate contains random micron- and sub-micron scale inter- or intra- (blue) granular voids (**Fig. 2-3**), reminiscent of the cavities in spongy bones. The voids have a total volume fraction of 0.7% (intra-)/50.0% (inter-) and width of ~ 0.2-2 μm, likely formed through the diffusion-limited incomplete filling of Si inside mesoporous SiO_2.

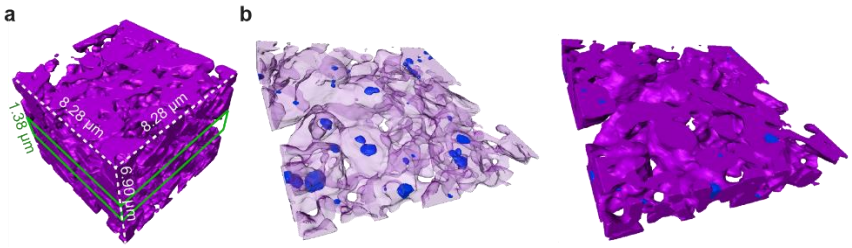

Figure 2-3. TXM 3D dataset of mesostructured silicon. a, A representative region of mesostructured Si showing the inter-granular voids. **b,** A thin slice of the dataset (green lines) highlights the presence of both intra- (left) and inter-granular voids (right). Representing silicon as a semi-transparent matrix allows clearer visualization of the voids (upper right). Magenta, silicon; blue, intra-granular voids; open regions in the whole volume or thin slice, inter-granular voids.

A small angle X-ray scattering (SAXS) profile (**Fig. 2-4a**) exhibits diffraction peaks indexed as (100), (110) and (200) of a two-dimensional hexagonal structure (space group, *p*6*mm*), as expected from the SBA-15 template[29]. The lattice constant *a* calculated from SAXS was 11.1 nm, which is consistent with that of the SiO_2 template (11.0 nm) and suggests a faithful replication. The Brunauer-Emmett-Teller (BET) specific surface area and total pore volume as measured by N_2 sorption were 462 m^2/g and 0.53 cm^3/g, respectively (**Fig. 2-4b**).

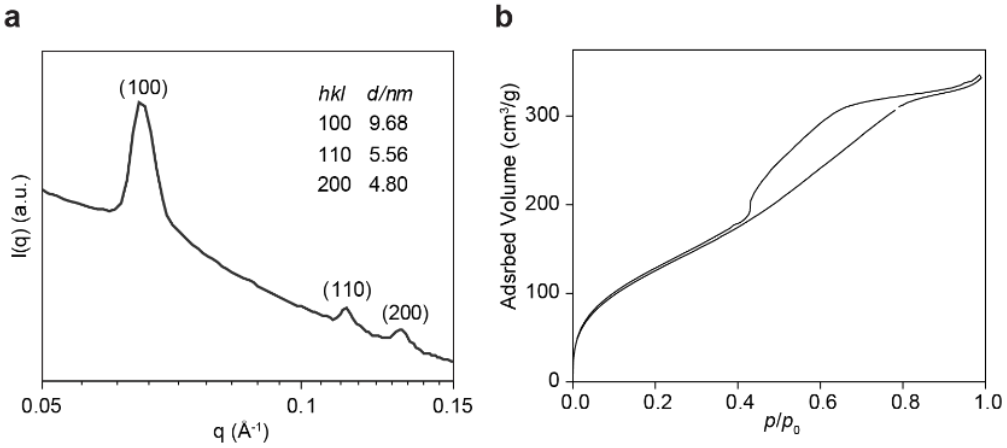

Figure 2-4. Mesostructured Si has an ordered porous structure. a, SAXS profile shows the mesoscale periodicity with a 2D hexagonal symmetry. **b,** Nitrogen adsorption/desorption isotherm shows a Type-IV characteristic.

The high-resolution SEM shows assemblies of aligned nanowires within individual grains (**Fig. 2-5a**), as expected from the channel structures in SBA-15 template. The end-view transmission electron microscopy (TEM) image and the fast Fourier transform (FFT) diffractogram (**Fig. 2-5b**) confirm the hexagonally ordered packing of nanowires. Selected area electron diffraction (SAED) shows diffuse rings and indicates that Si is amorphous, a useful property for improving light absorption[31] and reducing rigidity[32] in Si.

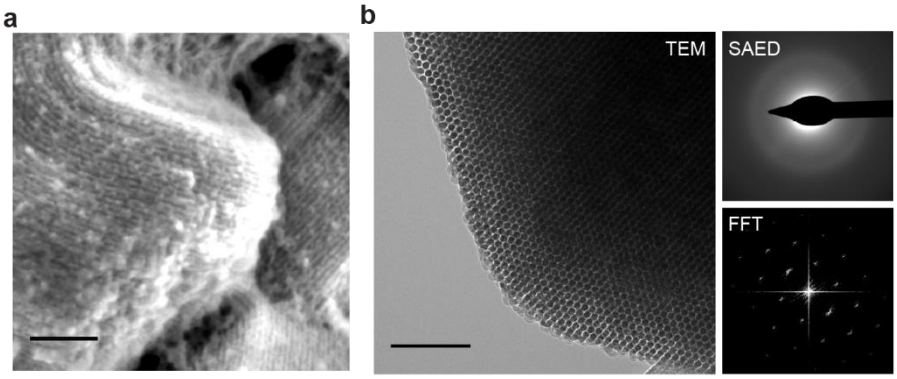

Figure 2-5. Mesostructured Si is consisting of aligned nanowire bundles packed in a hexagonal order. a, SEM image reveals periodic arrangement of Si nanowire assembly. Scale bar, 100 nm. **b,** TEM image (left) and its FFT

Figure 2-5, continued. diffractogram (lower right) indicate the hexagonal packing of Si nanowires (left panel). SAED pattern shows an amorphous atomic structure (upper right). Scale bar, 100 nm.

2.2.2 Chemical heterogeneity

The high-angle annular dark-field scanning transmission electron microscopy (HAADF STEM) image highlights individual nanowires (**Fig. 2-6a**), whose ordered packing suggests the existence of interconnecting micro-bridges[25,26]. Energy dispersive X-ray (EDX) mapping of one representative area shows an alternating distribution of oxygen (O) and Si (**Fig. 2-6b**). Because a long etching time (5-10 min in HF) was adopted to remove the SiO_2 template, and given the large pore volume (*i.e.*, 0.53 cm^3/g) exhibited by the material, the O signals came primarily from the oxidized portions in the Si open framework instead of from the SiO_2 template residuals.

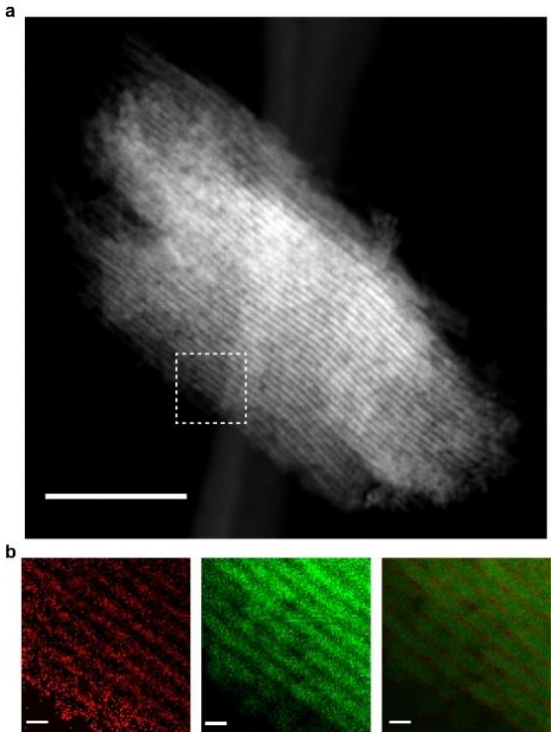

Figure 2-6. EDX mapping suggests heterogeneous oxygen distribution. a, HAADF STEM image of a free-standing Si mesostructure, showing ordered packing of individual nanowires. The structural integrity of the material suggests the existence of interconnecting micro-bridges which hold individual nanowires together. White dashed box marks

Figure 2-6, continued. the region for elemental mappings. **b,** EDX mapping of O (left, red), Si (middle, green) and the overlay of HAADF image and EDX maps (right) reveal alternating ordered spatial distribution of both elements. Scale bars, 200 nm (**a**) and 10 nm (**b**).

To quantitatively determine the heterogeneous O distribution, we used atom probe tomography (APT) to obtain elemental distributions in a Si framework with sub-nanometer scale spatial resolution. A reconstructed 3D dataset (**Fig. 2-7a**), collected from one Si particle with an intact SiO_2 template (*i.e.*, without dissolving SiO_2 by HF), displayed a hexagonal arrangement of nanowires with a lattice constant of 10.7 nm, consistent with the SAXS and TEM results. Additionally, individual micro-bridges can be readily visualized (**Fig. 2-7b**, yellow arrow), and the micro-bridge and its adjacent nanowires are quasi-orthogonal. Next, we studied the distribution of Si and O atoms with isoconcentration surface analysis. The results demonstrate that although the interconnecting micro-bridges are visible in the 60 at.% Si isoconcentration surface map (**Fig. 2-7b**, upper panel), most of them no longer appear in the 75 at.% one (**Fig. 2-7b**, lower panel), indicating that the overall Si (O) concentration is less (more) in the micro-bridges.

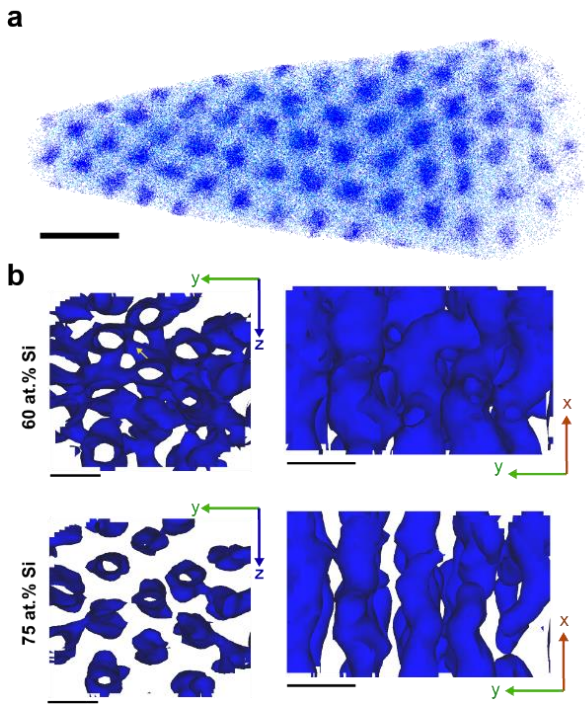

Figure 2-7. APT analysis of mesostructured Si. a, APT of one as-deposited sample (*i.e.*, without SiO_2 removal) exhibits hexagonal packing of Si nanowires in SiO_2 matrix. For clarity, only 5% of total Si (blue dots) and O (cyan dots) are displayed. Scale bar, 20 nm. **b**, 60 at.% (upper) and 75 at.% (lower) Si isoconcentration surfaces viewed from *x* (left) and *z* (right) directions. The presence of micro-bridges (yellow arrow) in 60 at.% surfaces (upper) and their absence in 75 at.% surfaces (lower) suggest that the overall Si concentration is less in micro-bridges than in Si nanowires. Scale bars, 10 nm.

Given the quasi-orthogonal arrangement between nanowires and micro-bridges, we were able to isolate two components in orthogonal thin slices (**Fig. 2-8a**). We further analyzed the proximity histogram concentration profile averaged over the selected region (**Fig. 2-8b**). Because the micro-bridges have smaller diameters than nanowires (*i.e.*, < 2 vs. ~7 nm), Si oxidation due to O incorporation from the SiO_2 template or air places the Si concentration generally below 75 at.% in micro-bridges (**Fig. 2-8b**, thick pink line). Moreover, this Si concentration difference can be quantified using a concentration distribution histogram derived from isoconcentration surface analysis within the two slices (**Fig. 2-8a**), which displays distinct distributions in each domain (<

75 at.% for micro-bridges, < 95 at.% for nanowires) (**Fig. 2-8c**). Finally, the Si concentration in the template (*i.e.*, SiO_2 regions that are away from the Si/SiO_2 interface) was ~43 at.% (**Fig. 2-8b**), higher than that in pure SiO_2 (*i.e.*, 33 at.%). This suggests that silane decomposition can also occur inside sub-nanometer cavities within the mesoporous SiO_2 walls, confirming a domain previously proposed as microporous 'corona'[33]. Taken together, the electron microscopy, EDX and APT demonstrate that the Si framework exhibits a chemical heterogeneity, where amorphous Si constitutes most of the nanowire-based component and the thinner micro-bridges have an overall higher O concentration and integrates the nanowires (**Fig. 2-8d**).

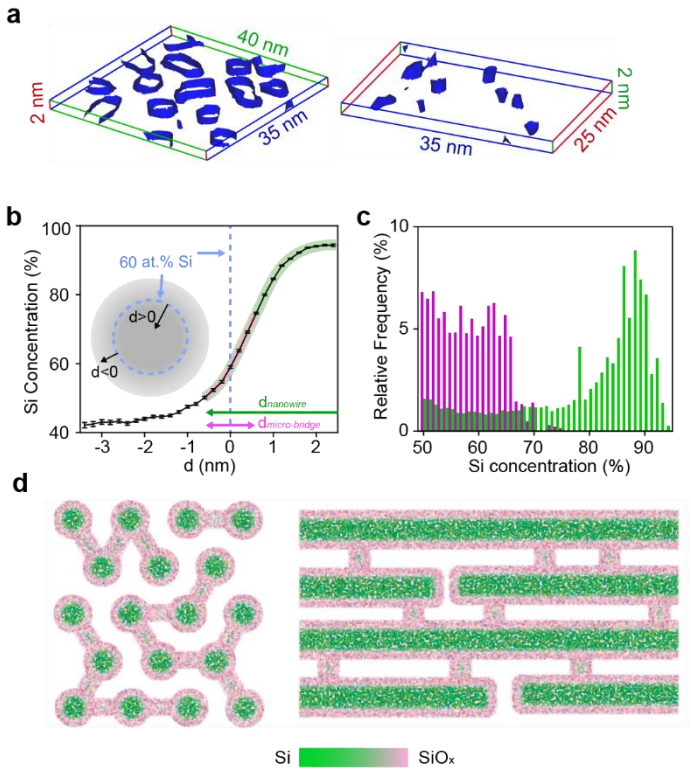

Figure 2-8. Mesostructured Si has size-dependent chemical heterogeneity. a, Representative slices showing Si nanowires (left) and micro-bridges (right) separately, rendered as 65 at.% Si isoconcentration surfaces. Lines and numbers denote dimensions along *x* (red), *y* (green) and *z* (blue) axes. **b**,**c**, Proximity histogram concentration profiles (**b**) and Si concentration distribution histograms (**c**) confirm the size-dependent Si concentration in Si nanowires (green) and micro-bridges (pink and magenta). '*d*' in **b** denotes the distance from the 60 at.% Si isoconcentration surfaces and

Figure 2-8, continued. a positive/negative value means that the point is inside/outside the enclosed isoconcentration surface. The curved pink and green thick lines estimate the decoupled Si distributions in micro-bridges and nanowires, respectively, given the different principal feature sizes in these two components (lines with arrows, magenta vs. green). **d**, End- (left) and side-view (right) schematics of mesostructured Si illustrate the graded Si/SiO_x (green/pink) interfaces and the observed chemical heterogeneity between nanowires and micro-bridges.

2.2.3 Deformable framework

We then explored the physical properties related to the observed structural and chemical heterogeneities. Given their critical role in establishing minimally invasive biointerfaces[3,34,35], we first studied the mechanical properties. In a dry state, the Si framework showed an average Young's modulus of 1.84 GPa (**Fig. 2-9a**), which is ca. 2 and 1 orders of magnitude smaller than that for bulk Si (~180 GPa) and electrochemically etched porous Si with similar porosity (~20 GPa)[1], respectively. This significant reduction in modulus is likely a combined result of multi-scale porosity, an amorphous framework, the molecular-level feature sizes of both nanowires and the micro-bridges, and the chemical heterogeneity as identified by APT.

After being immersed in a phosphate-buffered saline (PBS) solution for ~2 hours, the average Si Young's modulus decreased to 0.41 GPa (**Fig. 2-9a**), comparable to that of hydrated collagen fibers[36] and only 1 order of magnitude larger than that of phospholipid bilayers[37]. This reduction of modulus may come from framework degradation in saline, especially through the O-rich micro-bridges that maintain the framework integrity. However, *in-situ* and *ex-situ* SAXS (**Fig. 2-9b**) show that ordered mesostructures dominate in the remaining insoluble material for at least two days at room temperature in both PBS and collagen hydrogel. Cross-sectional TEM also shows long-range order in the interior of these saline treated samples, although partially-degraded nanowire segments can be observed (**Fig. 2-9c**). Raman and ultraviolet-visible (UV-vis) spectra indicate that the remaining Si materials displayed marginal changes in their atomic structures (*i.e.*,

the characteristic transverse optical Raman peak position and width, correlating with the spread in mean Si-Si-Si bond angle[38], remain at ~480 cm^{-1} and ~59 cm^{-1}) and optical properties (*e.g.*, the optical band gap) after being immersed in PBS for 1 day (**Figs. 2-9d**, **2-9e**). These results suggest that the interior of the Si mesostructures were preserved, and that the measured modulus reduction in saline is likely a result of degradation of particle surfaces.

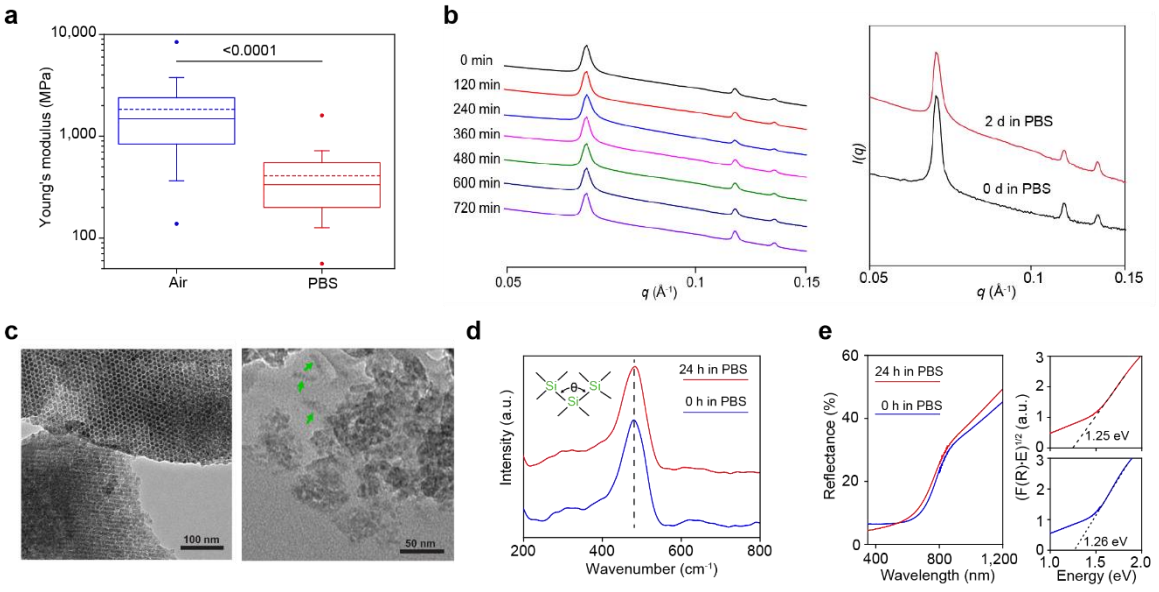

Figure. 2-9. Mesostructured Si has reduced rigidity on its surface. a, Box-and-whisker plot of Young's moduli of mesostructured Si measured in air (blue) and in a PBS solution (red). Half of the data points are within the boxes, 80% are within the whiskers. Solid and dashed lines represent the medians and means, respectively. The dots mark the maximum and minimum values. *n*=138 for measurement in air, *n*=94 in PBS. The number above the bar is the *p*-value of the Mann-Whitney test. **b**, Ordered Si mesostructure can still be resolved after immersion in PBS for two days. *In-situ* SAXS data (left) collected when mesostructured Si was placed in PBS over a time course of 12 h. *Ex-situ* SAXS data (right) taken from mesostructured Si after immersing in PBS for 0 d (black) and 2 d (red). No significant changes in peak position and width suggest the remaining Si material still has an ordered mesostructure network. **c**, Cross-sectional TEM image of two free-standing mesostructured Si particles (left). The sample was immersed in Tyrode's buffer overnight prior to the imaging preparation. The interior of the particles showed ordered nanowire packing, consistent with the results from SAXS, and suggests that there would be a mechanism to help preserve the particle's internal ordered structures in saline. A segregated region with degraded fragments is observed (right). The fragments

Figure 2-9, continued. still maintained nanowire morphology (green arrows) and, together with the fact that the particle interior was still ordered, suggests a surface degradation mechanism. **d**,**e**, Raman (**d**) and UV-vis (**e**) spectra of mesostructured Si submerged in PBS for 0 h (blue) and 24 h (red). The dashed line in **d** marks the position of Transverse Optical peak, whose position and width reflect the distribution of bond angle (θ). Extrapolation from Tauc plots (**e**, right) of the UV-vis spectra yield band gaps. Raman and UV-vis spectra were collected in PBS and air, respectively.

Overall, this degradation pathway is surface-initiated, instead of being bulk degraded (as usually expected for water-permeable nanoporous materials). We attribute this behavior to the possible blockage of molecular-level pores by the partially-degraded products (*i.e.* gel-like $Si_xO_y(OH)_z^{4x-2y-z}$) over particle surfaces (**Fig. 2-9**), which may delay the disruption of the internal ordered framework in saline --- as seen in both SAXS and TEM (**Fig. 2-9**). Finally, mesostructured Si can completely degrade[10,11] in saline over time and its behavior is dependent on multiple factors, such as initial Si/water ratio, solution exchange protocol, and temperature (**Fig. 2-10**).

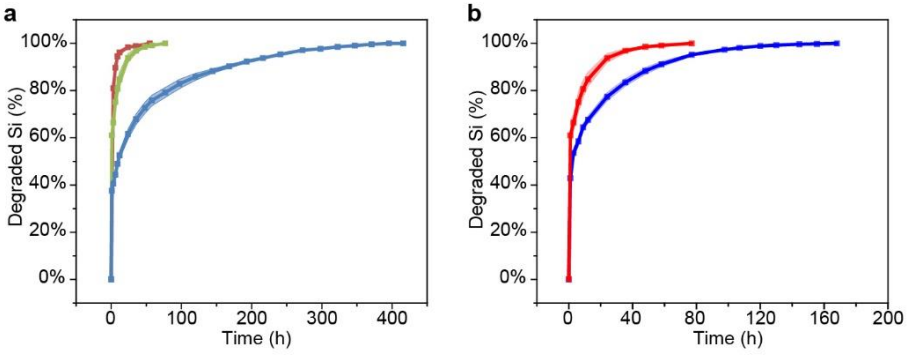

Figure 2-10. Mesostructured Si is degradable *in vitro.* a, Mesostructured Si degradation curves in 1 mL of 1× PBS at 37 °C over time. Half of the solutions were taken out for ICP-OES analysis at each time point and 500 µL of fresh 1× PBS were added back each time. Different amount of initial mass of Si added are color coded as 50 µg (red); 100 µg (olive); 300 µg (navy blue). In general, the solution exchange protocol, *i.e.*, the frequency of solution exchange and the volume of solution being exchanged each time, can affect the degradation rate. Additionally, larger Si/H_2O ratio yields slower degradation. Finally, the degradation rate drops significantly at the later stage in the tests of 300

Figure 2-10, continued. μg sample, although fresh solution was added at each exchange point (navy blue). This is likely due to the Si oxidation into gel-like $Si_xO_y(OH)_z^{4x-2y-z}$. **b**, Degradation curves under different temperatures. With the same amount of mesostructured Si added (100 μg), the sample degraded faster at higher temperature; red, 37 °C, blue, room temperature. For each group, *n*=5. The shaded areas denote the means ± 1 standard deviation.

Close inspection at the Si/HUVEC interfaces reveals a minimum of ~ 30 nm wide space between the ordered domains of Si particle and the plasma membrane (**Fig. 2-11a**), likely filled with degraded Si that is more deformable and natural ECM. Additionally, we observed little correlation between the nanowire orientation and the cell surfaces, as shown in samples prepared with both freeze-substitution (**Fig. 2-11a**) and chemical fixation (**Fig. 2-11b**) methods, suggesting that nanoscale surface topography from Si particle may not be critical for establishing stable biointerfaces.

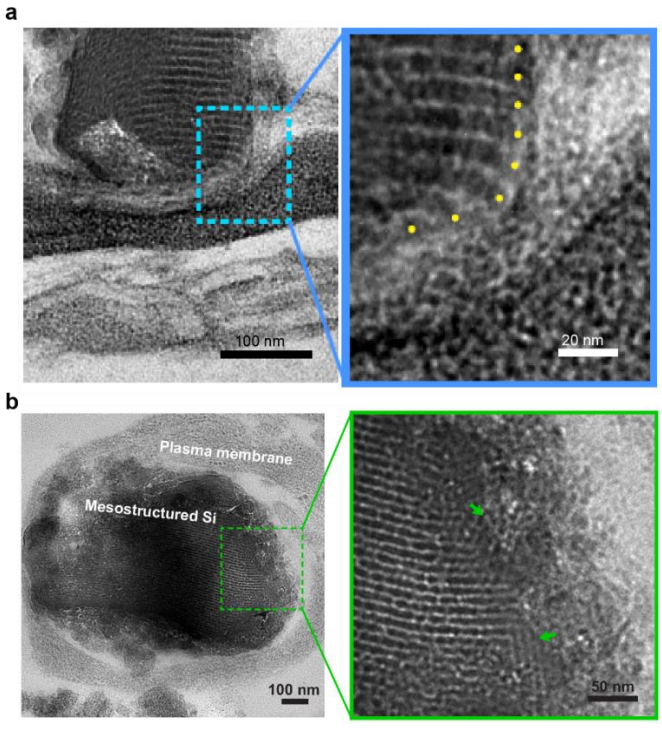

Figure 2-11. The surface of mesostructured Si is deformable. a, Cross-sectional TEM image of a representative mesostructured Si/HUVEC interface after freeze-substitution and resin embedding. Blue dashed box marks the region for a zoom-in view on the right. The nanowires ends are marked with yellow dots. **b**, A mesostructured Si particle

Figure 2-11, continued. enclosed within a plasma membrane bounded cavity. The green dashed box marks a surface region for the zoom-in view on the right. The green arrows mark the degraded and fractured nanowire domains.

2.2.4 Biocompatibility

To evaluate the biological benefit of using mesostructured Si, we developed a single cell calcium-imaging assay in which fluorescence dynamics were recorded upon pressing vertically on a HUVEC cell-supported Si particle (size: ~ 5 μm) with a glass micropipette (**Fig. 2-12a**). Compared to grinded single crystalline Si particles, mesostructured Si yields statistically smaller values in both amplitude ($\Delta F/F_0$) and slope ($(dF/dt)/F_0$) in the mechanically-induced calcium dynamics curves (**Fig. 2-12**). These single cell studies confirm that deformable materials are less invasive to cellular components[3]. Finally, mesostructured Si yielded negligible cytotoxicity in several mammalian cell cultures (**Fig. 2-13**). And when tested in rats subcutaneously, the inflammatory response that was caused by injection and the materials decreased substantially from 1-day to 3-week time points as mesostructured Si degraded (**Fig. 2-14**).

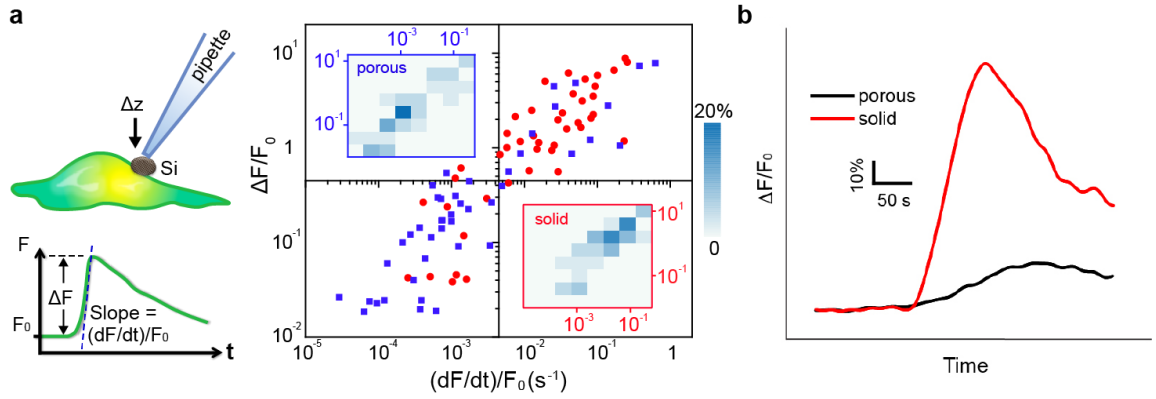

Figure 2-12. Mesostructured Si can establish minimal invasive biointerfaces. a, A schematic diagram (upper left) of the single-cell calcium imaging assay, with relative amplitude ($\Delta F/F_0$) and slope ($(dF/dt)/F_0$) defined (lower left). A scattered plot (right) for the amplitude and slope values of the calcium dynamics, recorded from porous/mesostructured/amorphous (blue) and solid/single crystalline (red) particles. Insets display 2D distribution histograms associated with porous (upper left) and solid (lower right) samples. $n = 44$ for each group. **b**, Representative

Figure 2-12, continued. Fura-2 AM fluorescence recording from HUVECs before and after being mechanically perturbed by porous Si mesostructures (black) and solid Si particles (red). The particle sizes are ~ 5 μm.

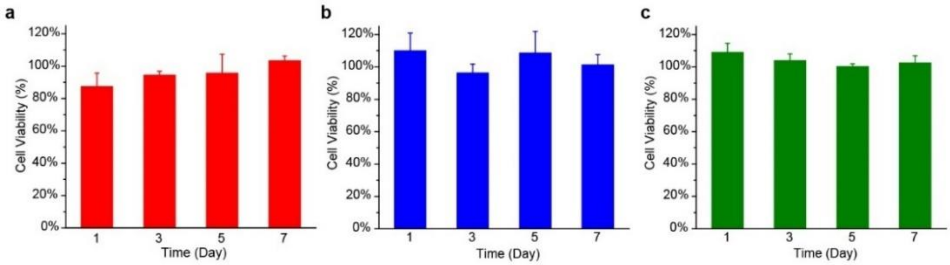

Figure 2-13. Mesostructured Si particles are biocompatible *in vitro*. MTT assays show minimal cytotoxicity when co-culturing mesostructured Si with different cell lines for up to 7 days (**a**, red, HUVEC; **b**, blue, C2C12; **c**, olive, HASMC, 0.1 mg/mL Si in all cell culture media). Data points are mean ± standard deviation, *n*=8 for each group.

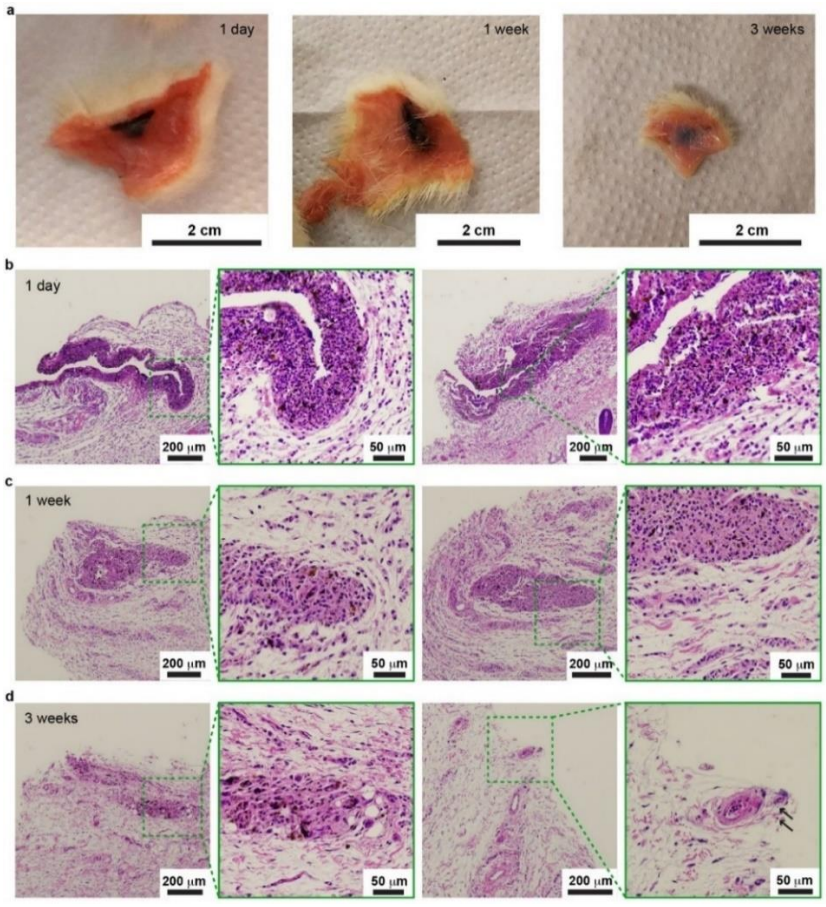

Figure 2-14. Mesostructured Si is biocompatible and biodegradable *in vivo*. a, Photographs showing degradation of Si in the subcutaneous regions of adult male CD® IGS rats. No appreciable nodules were formed within the 3-week

Figure 2-14, continued. period. **b-d**, Hematoxylin and eosin (H&E) staining of the injection sites after 1 day (**b**), 1 week (**c**) and 3 weeks (**d**) periods. Images from 1 day post-injection (**b**) show diffused immune cell distribution. The channel-like void was created by the injection needle. Samples from 1-week post-injection (**c**) have defined boundaries of inflammatory responses. The total amount and density of Si particles, shown as black dots in the zoom-in views, are in general less than those in the 1-day post-injection samples (**b**). Samples from 3-week post-injection (**d**) exhibit least amount of Si particles and smallest areas of inflammatory regions. The arrows in (**d**) highlight remaining Si particles. There was no significant injury to surrounding tissues (*e.g.*, muscle, blood vessels). There were no appreciable nodules developed during the test period. The animals did not show difficulty in moving, and no animal death occurred. For each group, n=4.

2.2.5 Bioelectric interfaces

Altogether, this biocompatible and degradable form of Si has intrinsic (*i.e.*, as grown,) and induced (*e.g.*, by water) chemical and structural heterogeneities, despite its origin from a single Si precursor (*i.e.*, SiH_4). Given that these heterogeneities are spatially organized and seamlessly integrated, a single particle may exhibit multiple functions (**Fig. 2-15**), a scenario similar to that in natural biominerals[16,39]. For example, we expect good photothermal efficacy from the interior of the Si mesostructures due to enhanced intrinsic light absorptivity in amorphous Si[31], and reduced thermal conductivity and capacity as previously demonstrated for porous Si[1].

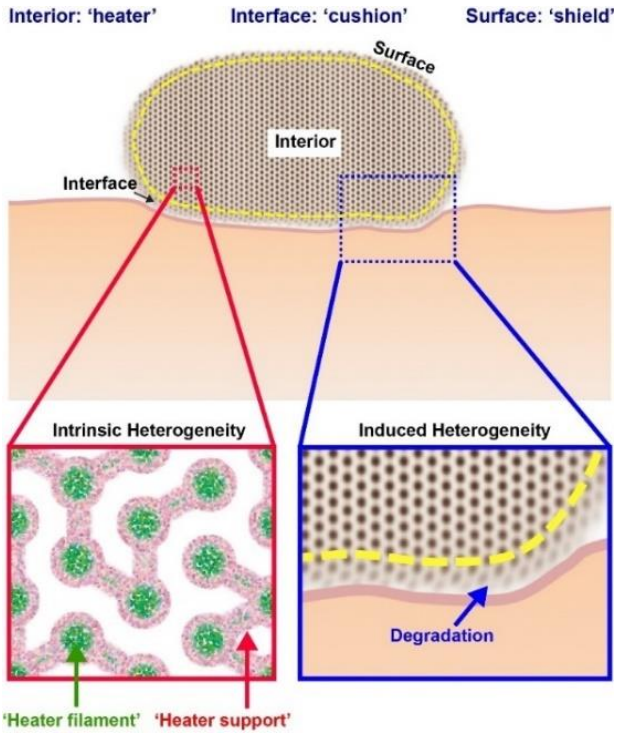

Figure 2-15. Intrinsic and induced chemical and structural heterogeneities enable multiple functions in mesostructured Si. Freshly prepared mesostructured Si has intrinsic size-dependent chemical heterogeneity, where nanowires are rich in Si and micro-bridges contain more O. The porous structures, the chemical heterogeneity, as well as the amorphous nature of Si, together promote a good photothermal effect. The material ***interior*** retains its structures and optical properties in buffer solution within days, which functions as a 'heater' upon light illumination. Within the 'heater', micro-bridges 'support' the Si-rich 'heater filaments', and the oxidized layers (SiO_x, pink) over both the micro-bridges and nanowires slow down the reaction of Si with H_2O. The ***surface*** of the particle is degraded and softer, which may 'shield' the interior by possibly blocking the nanoscale pores with the degraded species. This proposed shielding effect from the particle outer surface, as well as SiO_x-enabled passivation of Si, may lead to the observed structure preservation in the particle interior. The ***interface*** between mesostructured Si particle and plasma membrane shows local fragmentation. The Si/cell interface thus behaves as a less invasive 'cushion'. The degradation/fragmentation of Si surfaces by water and possibly extracellular forces represents induced heterogeneity.

Taking advantage of the fact that a rapid temperature variation can induce transient capacitive currents in phospholipid bilayers[40,41], we constructed a hybrid Si/phospholipid system as a remotely controlled bioelectric interface. A layer of grinded Si mesostructures (individual

particle size: ~ 1-2 μm) was supported over one side of a phospholipid bilayer, and its local junction with lipids was remotely actuated with 532 nm laser pulses (laser beam diameter: ~ 40 μm; **Fig. 2-16a**). We measured the temperature change near the mesostructured Si layer using a calibrated micropipette resistance method[40]; we simultaneously assessed the electrical capacitance dynamics with the impedance method[40] using a sinusoidal voltage (**Fig. 2-16a**). Next, we recorded membrane current dynamics under voltage-clamp mode. Experiments and finite element analysis simulation revealed a fast photothermal effect (**Fig. 2-16b**, upper panel; **Fig. 2-17**), and such a fast response is critical for capacitive current generation in lipid bilayer[40]. For example, one 11.2 μJ laser pulse causes a ~5.8 K increase of local temperature within 1.8 ms, followed by a decay to baseline with ~2.2 ms time constant (**Fig. 2-16b**, upper panel). With the same pulse, the estimated capacitance change accompanying the fast temperature rise peaks at ~0.6 % (**Fig. 2-16b**, lower panel). Because impedance correlates inversely to capacitance when there is no resistive component, a fast increase in bilayer capacitance due to laser pulses leads to a reduction of impedance, and correspondingly, a light-induced transient membrane current. Such a membrane current is capacitive and depolarizing (*i.e.,* current flow tends to reduce the polarization in the phospholipid bilayer); its amplitude is tunable with either the laser input energy or a voltage drop across the bilayer (**Fig. 2-16c**). Because both the membrane current output and the local temperature variation are transient, this Si/bilayer platform may be adapted for minimally invasive and dynamic biomaterials or devices.

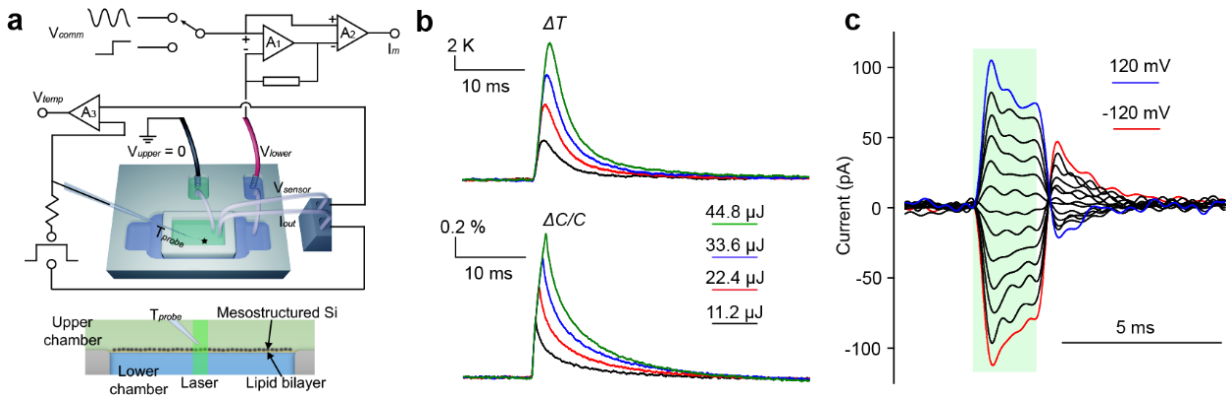

Figure 2-16. Mesostructure Si can be used for light actuated bioelectric interfaces. a, A planar and remotely controlled bioelectric interface made from densely packed Si mesostructures and an artificial lipid bilayer. Experimental setup (top) shows measurements of local solution temperature, bilayer electrical capacitance, and membrane current, upon localized laser illumination at the Si/lipid interface (top panel). The star marks a drilled hole at the bottom of top chamber, where lipid bilayer forms. Two independent circuits are shown. The first circuit uses A_1 and A_2 as a patch clamp that measures membrane currents (I_m) in response to a command voltage (V_{comm}) clamped at V_{lower}, connected to the solution pool below the bilayer. V_{comm} can be conventional voltage pulses or a sinusoidal voltage signal. V_{upper} connects the pool on top of the chamber to ground. The second circuit, using A_3, records a voltage drop (V_{temp}) between the pipette (T_{probe}) and V_{sensor}, in response to a current applied between the pipette and I_{out}. V_{temp} is proportional to the pipette resistance, which in turn is a function of the temperature (see details in the text). A zoom-in side view of the setup (bottom) shows Si/lipid interface. **b**, Averaged local solution temperature (top) and bilayer capacitance (bottom) dynamics upon laser pulses with different input energies (laser power, 22.4 mW; black, 0.5 ms; red, 1.0 ms; blue, 1.5 ms; olive, 2.0 ms). *n*=50. **c**, Capacitive currents in response to laser pulses (44.8µJ), recorded in voltage-clamp mode. Red and blue traces indicate the currents when the potentials were clamped at -120 mV and 120 mV, respectively. Black traces are recordings at intermediate potentials in increments of 20 mV. Green bar indicates when laser pulse was on. *n*=10.

2.2.6 Theoretical analysis of the photothermal effect

We simulated the laser-induced temperature dynamics in mesostructured silicon and buffer solution with *COMSOL Multiphysics* (*COMSOL Inc.*, USA). In the lipid bilayer experiment, we applied mesostructured silicon particles into the upper buffer solution and let them settle down to

form a quasi-continuous layer of silicon particles. We then illuminated a circular area (diameter ~40 μm) with 532 nm laser from the bottom of silicon film and probed the temperature profile using pipette resistance method from an adjacent point above the bilayer. For simulation, we adopted a three dimensional (3D) cylindrical geometry. Specifically, we simplified the mesostructured silicon particle layer as a thin slab of cylinder with a radius of 150 μm and a thickness of 15 μm (**Fig. 2-17a**). This layer was assumed to be packed compactly with mesostructured silicon particles with their internal channels/pores completely filled with water. On each side of the mesostructured silicon layer, we modeled the water phase as cylinders with a radius of 150 μm and a thickness of 200 μm.

The laser energy can be absorbed by mesostructured silicon and the surrounding medium is subsequently heated up due to the heat conduction from silicon to solution. The spatiotemporal profiles for temperature within both silicon and buffer solution are governed by a time-dependent heat transfer equation (in cylindrical coordinates):

$$\rho c_p \frac{\partial T}{\partial t} = \alpha(1-R)I_0 e^{-\alpha z} + \frac{1}{r}\frac{\partial}{\partial r}\left(\kappa r \frac{\partial T}{\partial r}\right) + \frac{1}{r^2}\frac{\partial}{\partial \phi}\left(\kappa \frac{\partial T}{\partial \phi}\right) + \frac{\partial}{\partial z}\left(\kappa \frac{\partial T}{\partial z}\right), \qquad (2\text{-}1)$$

where T is the absolute temperature (K), and ρ, c_p, κ, R and α are the density (kg/m^3), specific heat (J/kg·K), thermal conductivity (W/m·K), reflectance and absorption coefficient (m^{-1}) of mesostructured silicon ($0 \le z \le 15$) or water ($z < 0$ or $z > 15$). Since water is almost transparent at 532 nm, its α value is set to 0. I_0 is the light power density (W/m^2). The surface of mesostructured silicon framework is oxygen rich and therefore hydrophilic. We consider a case in which water can wet completely the inner surfaces of the silicon mesostructures. In this scenario, heat conduction from silicon to water is facilitated due to the large interfacial area. We used weighted arithmetic means to estimate corresponding physical properties of porous silicon, respectively.

$$\rho_{\mathrm{pSi}} = (1-\varphi)\rho_{\mathrm{Si}} + \varphi\rho_{\mathrm{water}}; \tag{2-2}$$

$$\rho_{\mathrm{pSi}} c_{p\mathrm{pSi}} = (1-\varphi)\rho_{\mathrm{Si}} c_{p\mathrm{Si}} + \varphi\rho_{\mathrm{water}} c_{p\mathrm{water}}; \tag{2-3}$$

$$\kappa_{\mathrm{pSi}} = (1-\varphi)\kappa_{\mathrm{Si}} + \varphi\kappa_{\mathrm{water}}, \tag{2-4}$$

where φ is the volumetric porosity, which is 55% in this specific case, as estimated from nitrogen adsorption/desorption result.

Physical properties of amorphous silicon were taken from textbooks or literature as: ρ_{Si}=2330 kg/m^3, $c_{p\mathrm{Si}}$=891 J/kg·K and κ_{Si}=1.61 W/m·K. The final input values were calculated as follows: ρ_{pSi}=1598.484 kg/m^3, $c_{p\mathrm{pSi}}$=2024.525 J/kg·K and κ_{pSi}=1.0545 W/m·K. Light absorption coefficient for mesostructured silicon is 203540 m^{-1} at 532 nm, which is estimated using the UV-vis reflectance (R=0.068) and transmittance (T=0.015) recorded at the same wavelength, $T = \left[(1-R)^2 \exp(-\alpha d)\right] / \left[1 - R^2 \exp(-2\alpha d)\right]$, where film thickness d is ~20 μm measured using a profilometer. The input laser power was 22.4 mW, with a spot diameter of 40 μm. We used 15 μm, a size comparable to the silicon film thickness, for the estimated distance between silicon top surface and micropipette tip where local temperatures were recorded. Initial and boundary conditions are defined as below, with the interfacial thermal resistance R_s of 10^{-8} K·m^2/W.

$$T(r, \phi, z, t = 0) = 300 \text{ K}, \tag{2-5}$$

$$T(r = 150 \text{ μm}, \phi, z, t) = 300 \text{ K}, \tag{2-6}$$

$$T(r, \phi, z = -200 \text{ μm}, t) = 300 \text{ K}; \tag{2-7}$$

$$T(r, \phi, z = 215 \text{ μm}, t) = 300 \text{ K}, \tag{2-8}$$

$$-\kappa_{\mathrm{pSi}} \left.\frac{\partial T}{\partial z}\right|_{(r,\phi,z=0\ \mu\mathrm{m})} = \frac{T_{\mathrm{pSi}}(r,\phi,z=0\ \mu\mathrm{m},t) - T_{\mathrm{water}}(r,\phi,z=0\ \mu\mathrm{m},t)}{R_s}; \qquad (2\text{-}9)$$

$$-\kappa_{\mathrm{pSi}} \left.\frac{\partial T}{\partial z}\right|_{(r,\phi,z=15\ \mu\mathrm{m})} = \frac{T_{\mathrm{pSi}}(r,\phi,z=15\ \mu\mathrm{m},t) - T_{\mathrm{water}}(r,\phi,z=15\ \mu\mathrm{m},t)}{R_s}. \qquad (2\text{-}10)$$

By computing the Heat Transfer in *COMSOL Multiphysics* (Solids Module), we simulated the spatiotemporal temperature profiles in both porous silicon and surrounding medium (**Fig. 2-17b**). The output results recapitulate the experimental results (**Fig. 2-16b**, upper).

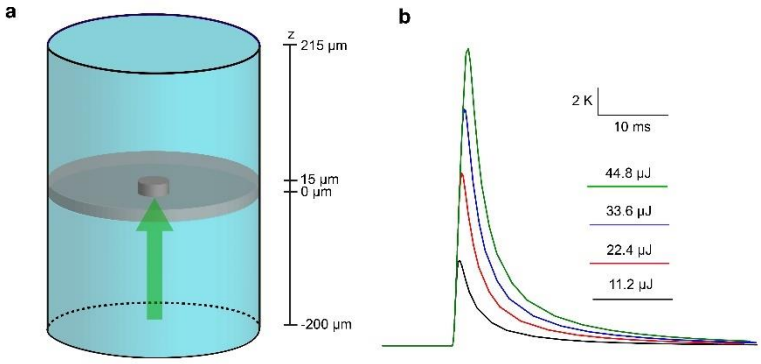

Figure 2-17. Photothermal simulation model. a, 3D geometry model used for photothermal simulation of mesostructured Si. Blue cylinders mark water layers on both sides of Si layer (diameter, 300 µm; height, 200 µm). Dark grey cylinder denotes mesostructured Si being illuminated by green laser (diameter, 40 µm; height, 15 µm; laser wavelength, 532 nm). Light grey ring is the rest of mesostructured Si that is not illuminated. The probe location is at (0, 0, 30 µm), where the temperature profile was simulated. **b**, Simulated temperature dynamics recapitulates the experimental data, supporting the controllability of the photothermal effect.

To investigate this possibility, we proposed a dynamic hybrid Si/cell system (**Fig. 2-18**) where individual mesostructured Si particles attached to dorsal root ganglia (DRG) neurons, with 532 nm laser pulses and intracellular electrical recordings as input and output, respectively. We prefer to use individual micron-scale and thermally stable Si mesostructures over ensembles of existing nanoparticles[41] in order to achieve efficient and point-like localized extracellular control,

as well as to avoid material internalization by neurons[42] or laser heating-induced particle change[43]. By varying the laser stimulation duration while fixing its wavelength and power (532 nm, 5.32 mW, beam diameter: ~ 10 μm), we identified an average of 5.32 μJ (**Fig. 2-19a**) threshold energy for reliably eliciting single action potentials (AP) in DRG neurons with a singly attached Si particle (particle size: ~ 2 μm). This energy level is ~30× less than those used for a recently reported precise neuromodulation with Au nanoparticles[41]. Given the experiments on phospholipid bilayers (**Fig. 2-16**) and the controls with mesoporous SiO_2 (**Fig. 2-20**), under current-clamp conditions, the fast and transient photothermal effect from the Si framework (**Fig. 2-18**) induces depolarization that opens sodium channels thus triggering APs. Since neurons process information *via* spike trains, we mimicked this process by delivering trains of 5.32 μJ laser pulses with different frequencies. We demonstrated reproducible and precise optical stimulation up to 15 Hz (**Fig. 2-18c**, upper left). At higher frequencies, AP generation becomes less efficient, although a deterministic sub-threshold depolarization remains evident (**Fig. 2-19b**). After reaching 20 Hz, *e.g.*, at 25 Hz (**Fig. 2-18c**, middle), the neural stimulation efficacy declined, response time (spike latency) and its standard deviations (trial-to-trial jitter and throughout train jitter) increased (**Fig. 2-19c**), all of which are most likely limited by the intrinsic ion channel kinetics (**Fig. 2-18a**) [40,44]. Interestingly, at 30 Hz input, the real-time electrical recording trace shows a quasi-alternating pattern of APs and sub-threshold depolarization (**Fig. 2-18c**, lower left). Accordingly, fast Fourier transform of the time-dependent trace shows a splitting distribution in the frequency domain (**Fig. 2-18c**, lower right), one at half-input frequency (for APs) and the other at the original input frequency (for sub-threshold depolarization). This emergent output behavior results from dynamic feedback[44] among Si-induced thermal and ionic effects, ion channel activities and membrane potentials (**Fig. 2-18a**). A return map analysis (**Figs. 2-18d**, **2-21**, A_n-A_{n+1}, A_n is the area of the n^{th} induced neuronal

signal)[44] shows frequency dependent 2-D patterns, being either focused (*e.g.*, 15 Hz) or partitioned/diffused (*e.g.*, 30 Hz), suggesting another mechanism for output recognition.

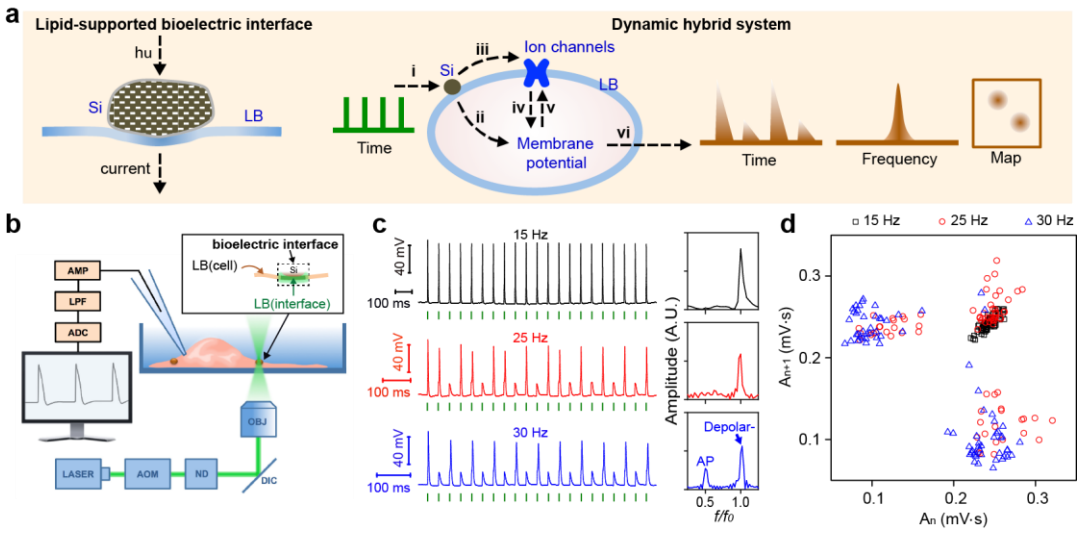

Figure 2-18. Remotely actuated and lipid-supported bioelectric interface as a dynamic hybrid system. a, Schematics of a light actuated bioelectric interface (left), where transient capacitive currents across lipid bilayer (LB) are generated due to the photothermal effect of mesostructured Si. A hybrid Si/cell system (right) uses pulsed optical signals as the input (**i**) and yields local transient heating. The fast transient heating generates capacitive currents through LB (**ii**) which, together with the currents passing through ion channels (**iv**), determine the membrane potential. The ion channel activities can be affected by the membrane potential (**v**) which is the result of either ionic currents and/or of the change in membrane capacitance by transient heating but also by direct heating (**iii**). All these processes integrate together as a single dynamic hybrid system, generating output (**vi**) that is recognizable in time and frequency domains and as 2D maps. **b**, Experimental setup used to elicit action potentials in DRG neurons by illuminating a single Si particle attached to a cell. Neurons were patch clamped in the current-clamp whole-cell mode. AOM, acousto-optic modulator; ND, neutral density filters; DIC, dichroic mirror; OBJ, microscope objective; AMP, amplifier; LPF, low-pass filter; ADC, analog-to-digital converter. Inset shows that a portion of the cell membrane functions as a built-in bioelectric interface. **c**, Representative intracellular potential recordings of a DRG neuron to trains of laser pulses (5.32 μJ) at different frequencies, with corresponding FFTs (right). f and f_0 are output and input frequencies, respectively. Green bars indicate when laser pulses were delivered. **d**, An area-based return map reveals

Figure 2-18, continued. an evolution of frequency-dependent 2-D patterns. Data points are analyzed from 20 spikes per trial, 4 trials per frequency.

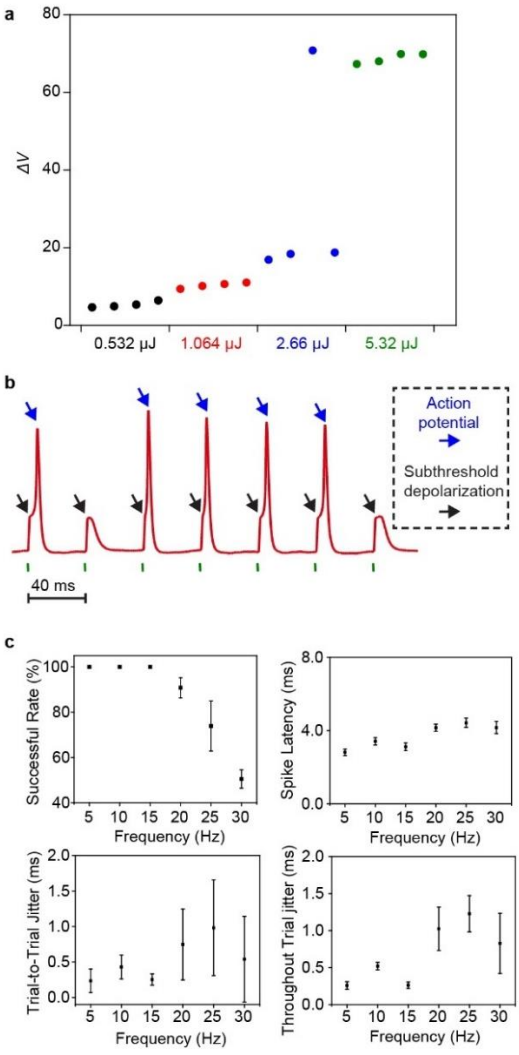

Figure 2-19. Mesostructured Si enables wireless control of the electrophysiology dynamics in DRG neurons. a, Peak voltage response (unit: mV) of a representative DRG neuron at different laser excitations indicates that laser pulses at 5.32 μJ can elicit reliable APs. Laser power was 5.32 mW with durations of 0.1 ms (black), 0.2 ms (red), 0.5 ms (blue), or 1.0 ms (olive). **b**, At high spike train frequency (*e.g.*, 25 Hz), action potential (blue arrows) generation becomes less efficient, although a deterministic subthreshold depolarization (black arrows) remains evident. Green bars indicate when laser pulses are delivered. **c**, Successful rate, spike latency, trial-to-trial jitter and throughout trial jitter were analyzed for different pulse train stimulations. At frequencies higher than 15 Hz, the stimulation efficacy

Figure 2-19, continued. decreased as indicated by the reduced successful rates, delayed spike latencies and elongated jitters. Data points are mean ± standard deviation, analyzed from 21 pulses per trial, 4 trials per frequency.

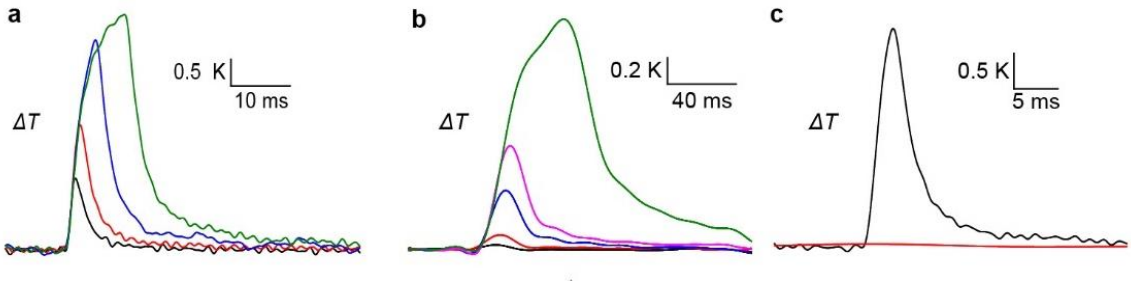

Figure 2-20. Control experiments suggest the role of Si. a and **b**, Local temperature increases following laser illumination on single particles of both mesostructured Si (**a**) and SiO_2 template (**b**). Color denotes different laser energies (black, 3.29 μJ (**a**), 10.92 μJ (**b**); red, 6.58 μJ (**a**), 110 μJ (**b**); blue, 16.45 μJ (**a**), 550 μJ (**b**); magenta, 1100 μJ (**b**); olive, 32.9 μJ (**a**), 5500 μJ (**b**), objective lens, 40×). **c**, Comparison of temperature dynamics between mesostructured Si and SiO_2 template when illuminating with similar laser energies (black, 9.87 μJ, Si; red, 10.92 μJ, SiO_2). Negligible temperature change could be observed for SiO_2.

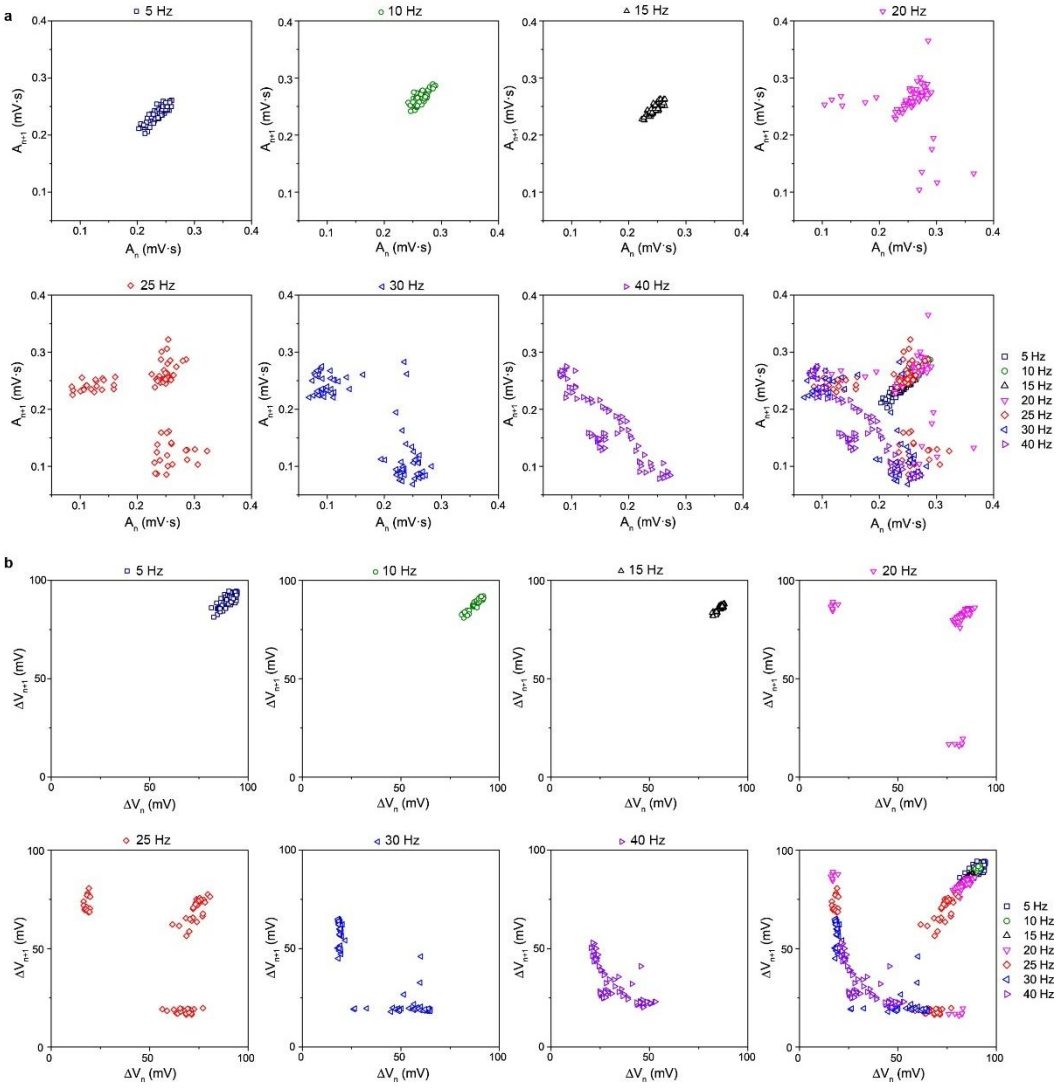

Figure 2-21. Return maps reveal the evolution of cellular output patterns. a, Area-based return maps calculated at each input frequencies and the overlay show a gradual transition from focused to partitioned/diffused patterns. Areas were obtained by integrating the voltage with respect to time, *t*, from *t* of peak voltage -10 ms to *t* of peak voltage +10 ms. **b**, Height-based return maps at each input frequency. Heights were calculated as the difference between the peak and the holding voltages. All return maps were analyzed from the 2nd to the 21st spike per trial, 4 trials per frequency.

2.2.7 Outlook

Future efforts include systematic control of the position and efficacy of Si/cell interfaces and demonstration of more complex dynamic behaviors in the hybrid system. These are feasible

given that individual mesostructured Si particles can be positioned in an arbitrary manner by a glass micropipette (**Fig. 2-22**), that Si particles can be patterned as a micro-pad array over centimeter-scale area by photolithography (**Fig. 2-23**), and that size- and shape-controlled preparation of Si particles is achievable (**Figs. 2-24**, **2-25**, and **2-26**). Additionally, tools such as light-emitting diode and calcium imaging can be explored for stimulation and recording of neural activities, which would be beneficial for *in vivo* studies.

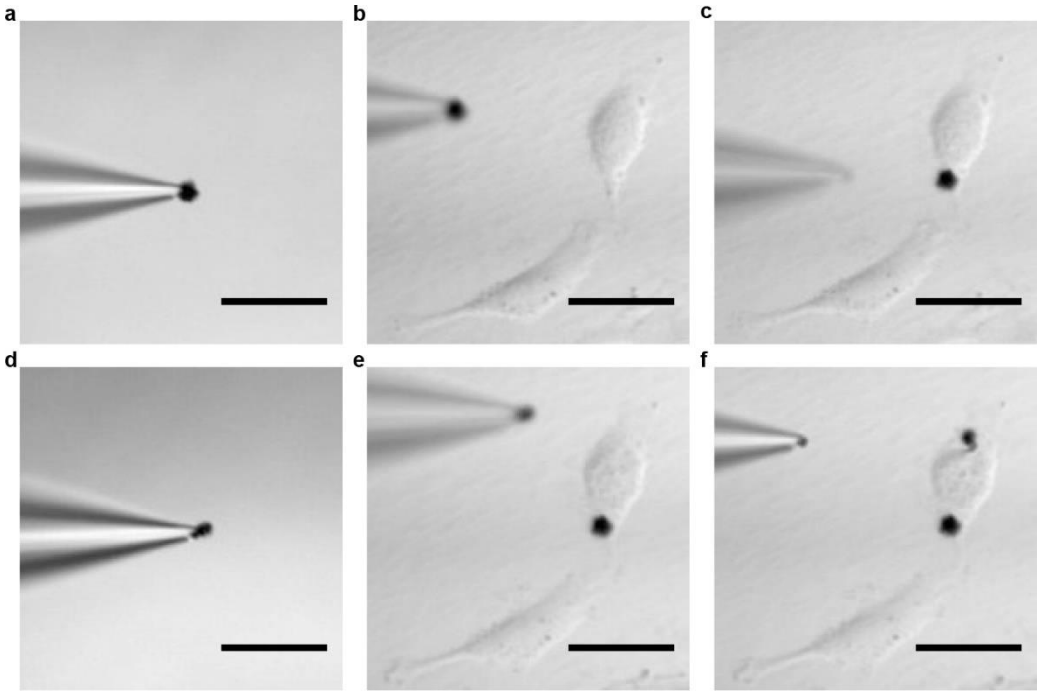

Figure 2-22. Glass micro-pipette can be used to manipulate individual mesostructured Si particles to form deterministic biointerfaces. HUVEC was used in this demonstration. Both particle position and number can be controlled in this way. Scale bars, 50 μm.

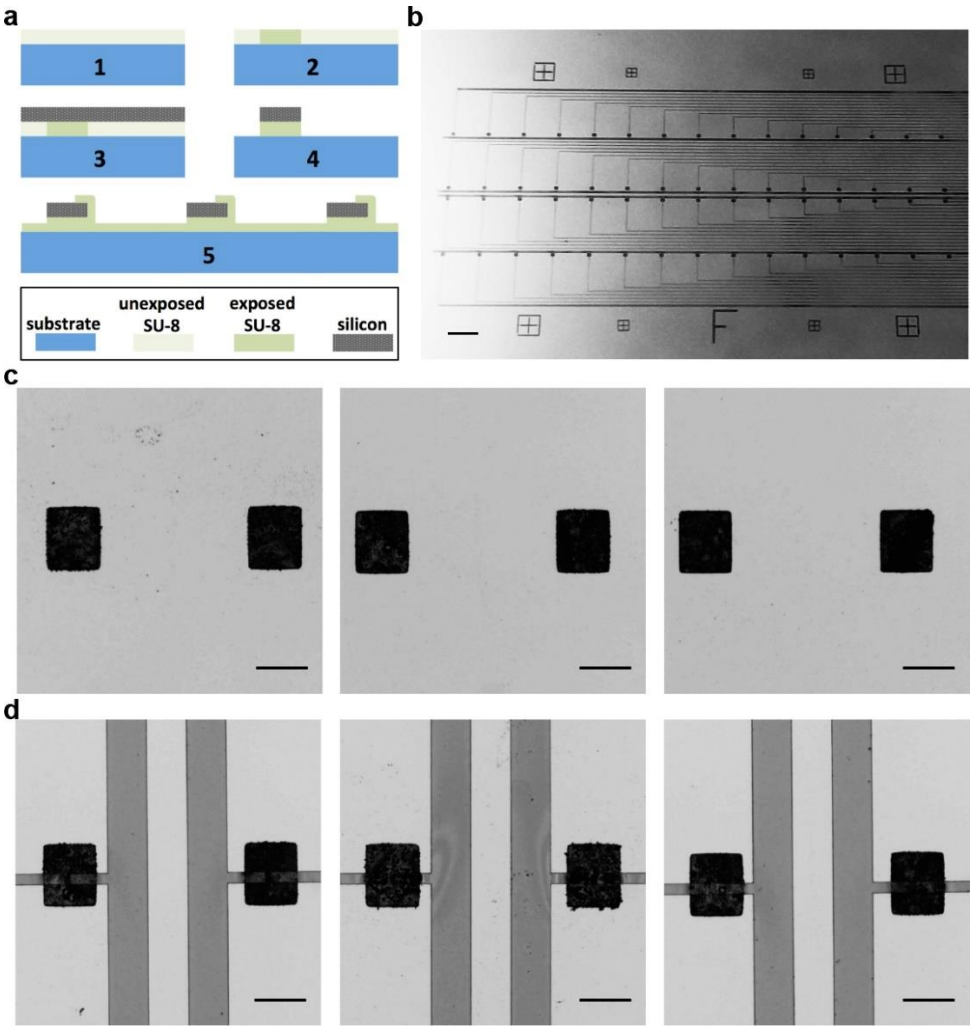

Figure 2-23. Mesostructured Si particles can be patterned over large areas. a, Fabrication schematics. **b**, A photograph of a patterned array where Si regions are black micro-pads with SU-8 interconnects. **c** and **d**, Optical micrographs showing the zoom-in views of the Si micro-pads before (**c**) and after (**d**) SU-8 interconnects were made, recorded from 3 different areas. Scale bars, 2 mm (**b**) and 200 μm (**c** and **d**).

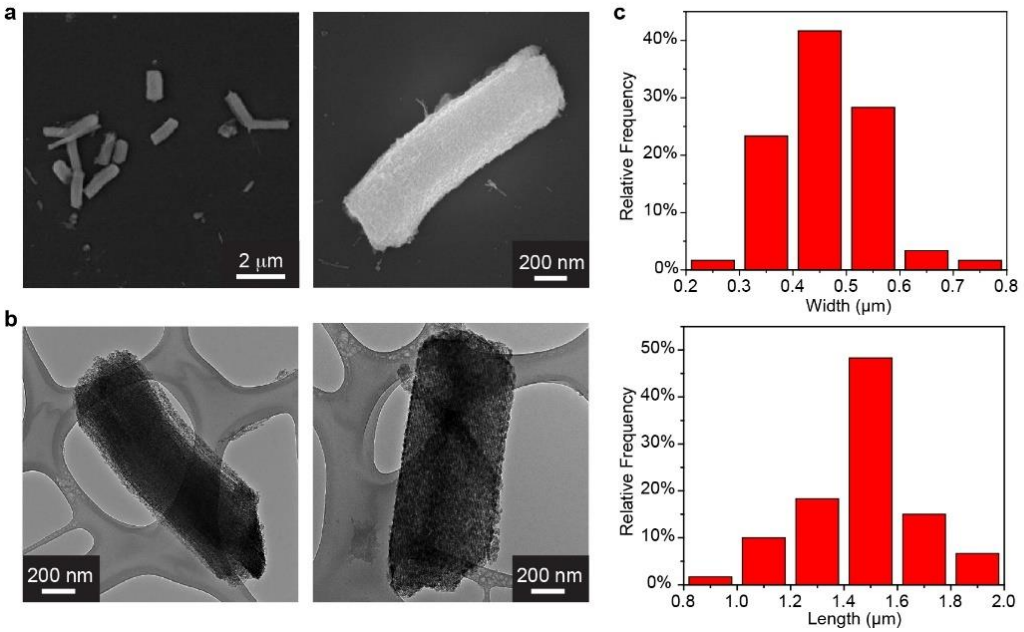

Figure 2-24. SEM (a) and TEM (b) images of rod-like mesostructured Si. The rod-like materials were synthesized through a static aging step. The width and length distributions (**c**) suggest decent shape uniformity.

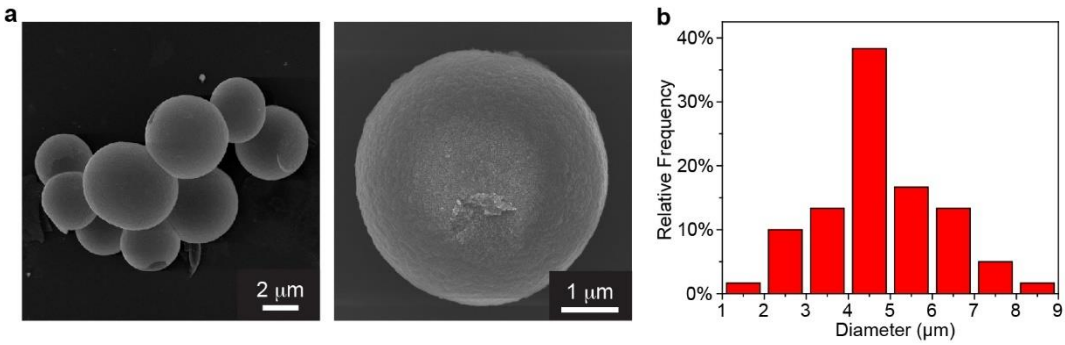

Figure 2-25. SEM images (a) and diameter distribution (b) of sphere-like mesostructured Si. The spheres were synthesized using cetyltrimethylammonium bromide (CTAB) as a co-surfactant and ethanol as a co-solvent.

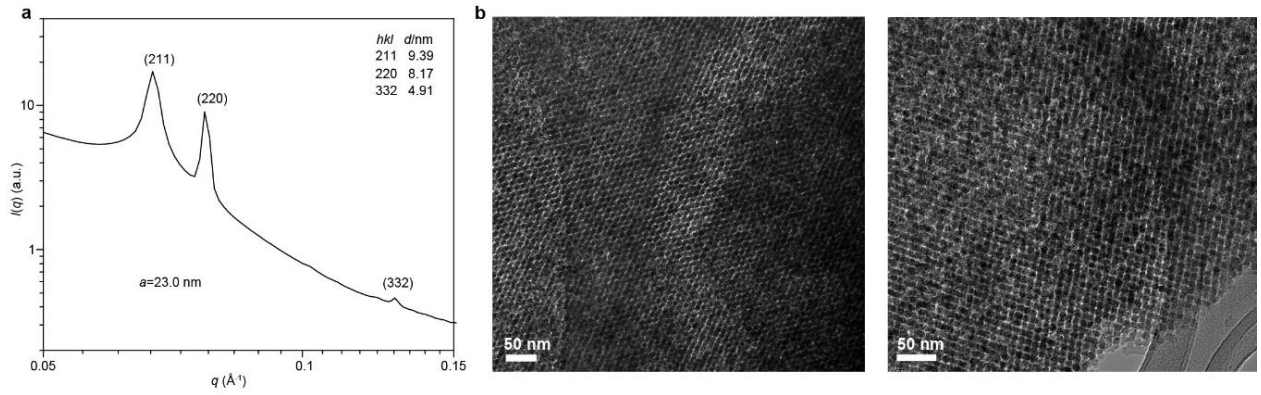

Figure 2-26. The synthesis of mesostructured Si is general. a, KIT-6 silica could be used as a template for mesostructured Si synthesis. SAXS profile of an as-casted Si shows a gyroidal lattice (space group, $Ia\bar{3}d$; lattice constant, 23.0 nm) with (211), (220), and (332) peaks, in accordance with the structure of KIT-6 template. **b**, Representative TEM images of the Si casted from KIT-6 template, showing ordered mesostructures.

Existing materials, such as particles of single crystalline silicon or carbon, may be configured into similar interfaces, although they do not currently exhibit the deformability or degradability desired for biomaterials. Hydrogels and polymers[45,46] are softer and may form mechanically compliant interfaces for similar studies, however appropriate chemical designs are needed for achieving both degradability and fast photothermal dynamics (*e.g.*, a few degrees of temperature increase within milliseconds). Regardless of exploring other materials, the current demonstrations of lipid bilayer-level integration of a bioelectric interface and the hybrid cellular system suggest that it may be possible to use amorphous Si, a much less exploited material in biomedical research, as a building block in establishing functional bio-interfaces[13,35,47-49] and as a new bio-orthogonal and dynamic component for future synthetic biology[50].

2.3 Experimental

Synthesis of mesostructured silicon (Si). Mesostructured Si materials were prepared by chemical vapor deposition (CVD) of Si inside mesoporous silica (SiO_2), followed by hydrofluoric acid (HF)

etching to remove the template. Four types of mesoporous silica templates were adopted for the synthesis of mesostructured Si, including wheat-like SBA-15, rod-like SBA-15, sphere-like SBA-15, and KIT-6. Mesostructured Si synthesized from wheat-like SBA-15 was used for all the characterizations and applications shown in the main figures.

Wheat-like mesoporous silica SBA-15 was synthesized according to a previous report[1]. Briefly, Pluronic P123 (Sigma-Aldrich, USA) was dissolved in a hydrochloric acid (HCl) (Sigma-Aldrich, USA) solution. Next, tetraethyl orthosilicate (TEOS) (Sigma-Aldrich, USA) was added and the mixture was stirred at 35 ^{o}C for 24 h. The chemical composition of the reaction mixture was 4 g P123: 0.04 mol TEOS: 0.24 mol HCl: 6.67 mol H_2O. The mixture was then aged hydrothermally at 100 ^{o}C. Finally, the powders were filtered, dried and calcined at 500 ^{o}C for 6 h.

Rod-like SBA-15 was synthesized following a previous report[2]. 4.0 g of P123 was first dissolved in a mixture of 30 g of deionized (DI) water and 120 g of 2 M hydrochloric acid (HCl) by stirring at 35 °C overnight. 8.5 g of TEOS was then added to the aqueous solution under vigorous stirring. The mixture was stirred for 5 min before being kept under static condition at 35 °C for 20 h. The product was aged at 100 °C for another 24 h. After filtering and washing with water, the final product was dried and calcined at 550 °C for 6 h.

Sphere-like SBA-15 template was made based on a previous report using cetyltrimethylammonium bromide (CTAB) as a co-surfactant and ethanol (EtOH) as a co-solvent[3]. In a typical synthesis, 3.0 g of P123 was dissolved in 60 mL of 1.5 M HCl while 0.6 g CTAB (Sigma-Aldrich, USA) was mixed with a separate 25 mL of water. After both surfactants have been dissolved, two solutions were mixed together and 20 mL of 100% EtOH (Thermo-Fisher Scientific, USA) was added to the mixture. 10 mL of TEOS was then added dropwise to the above mixture solution of surfactants under vigorous stirring (~500 rpm). After stirring at 35 °C for 45

min, the mixture was kept static under 75 °C for 10 h and aged at 100 °C for another 24 h. The product was filtered, washed, dried and calcined at 550 °C for 6 h.

The synthesis of KIT-6 template followed a previous report using *n*-butanol (BuOH) as a co-solvent[4]. 6 g of P123 was dissolved in 217 g of DI water and 11.8 g of concentrated HCl (37%). 6 g of BuOH (Sigma-Aldrich, USA) was added under stirring at 35 °C. After 1 h stirring, 12.9 g of TEOS was added at 35 °C to make the molar ratio as TEOS : P123 : HCl : H_2O : BuOH = 1 : 0.017 : 1.83 : 195 : 1.31. The mixture was left under stirring for 24 h at 35 °C, and subsequently heated for 24 h at 100 °C under static conditions. The solid product obtained after hydrothermal treatment was filtered and dried at 100 °C without washing. The template was removed by calcination at 550 °C for 6 h.

Next, the as-synthesized mesoporous SiO_2 powder was loaded close to the bottom of a small quartz tube (diameter: ~1.5 cm), which serves as the inner reactor. The inner tube containing SiO_2 template was then placed into the center of an outer quartz tube (diameter: ~2.5 cm) for CVD. Si was deposited at 500 ^oC and 40 Torr using silane (SiH_4) as the Si precursor and hydrogen (H_2) as the carrier gas. In a typical synthesis of mesostructured Si, we used 200 mg of SiO_2 template, with flow rates of H_2 and SiH_4 set at 60 and 2 standard cubic centimeters per minute (sccm), and a total CVD duration of 120 min. Subsequent HF (Sigma-Aldrich, USA, 48%) etching for 5-10 min was used to remove the template at room temperature. The etched samples were filtered, rinsed with DI water, isopropanol (IPA) and dried in air. The final product is in brownish powered form.

Electron microscopy. Mesostructured Si was sonicated in IPA, and then dispersed onto Si wafers (Nova Electronic Materials, USA, *p*-type, 0.001 Ω·cm) for scanning electron microscopy (SEM) (Carl Zeiss, Germany, Merlin FE-SEM) and over copper grids (Ted Pella Inc., USA, Lacey Formvar/Carbon, 200 mesh) for transmission electron microscopy (TEM) (FEI, USA, Tecnai F30).

The high-angle annular dark field (HAADF) scanning transmission electron microscope (STEM) images were recorded using an aberration corrected STEM (JEOL, Japan, JEM-ARM200CF). The electron-dispersive X-ray spectroscopy (EDX) maps were collected simultaneously with HAADF images using the same microscope equipped with an Oxford X-Max^N 100TLE windowless SDD X-ray detector (Oxford Instruments, UK). For *in-situ* heating TEM study, samples were dispersed on molybdenum grids (Structure Probe Inc., USA, Holey Carbon, 200 mesh) and imaged using a JEOL JEM-3010 (JEOL, Japan) with a double-tilt heating stage (Gatan Inc., USA, Model 652). The temperature ramping was set as 50 ^{o}C/min from ambient to 900 ^{o}C. Images were taken at room temperature, and at 10 min, 30 min, 60 min, 90 min and 120 min time points at 900 ^{o}C.

Nitrogen sorption measurements. Nitrogen sorption isotherms were collected on a Micromeritics ASAP 2020 (Micromeritics, USA) surface area and pore size analyzer at 77 K. Pore size distribution was calculated in the Micromeritics ASAP2020 software package (assuming slit pore geometry), using a non-linear density functional theory (NLDFT) model. All samples were degassed at 180 ^{o}C overnight prior to experiment. For all measurements, ultra high purity (UHP) grade helium (He) and nitrogen (N_2) were used.

Small angle X-ray scattering (SAXS). SAXS measurements were conducted at the 12ID-B station at the Advanced Photon Source (APS), Argonne National Laboratory (ANL). The wavelength of the X-ray beam was 0.8856 Å, and the beam size was 0.20(H) × 0.03(V) mm^2. The detector for SAXS measurements was the Pilatus 2M (DECTRIS Ltd., Switzerland). The exposure time was set to 1 s for all measurements and the sample-to-detector distance was about 2 m, which allows covering scattering momentum transfer, q, up to 1.0 Å^{-1}. The q value calibration was performed using silver behenate prior to measurements. The isotropic 2-D images were converted to 1-D scattering profiles using the Matlab software package developed at the beamline. For static

SAXS measurements, powder samples were sandwiched with kapton tapes and loaded onto the sample holder. For *in-situ* heating SAXS measurements, samples were first pelleted and loaded in a Linkam TS1500 heating stage (Linkam Scientific Instruments Ltd., UK). The sample chamber of the heating stage was sealed and purged with N_2 during the whole heating process. The temperature ramping rate was set as 60 ^oC/min and the first temperature set point was 800 ^oC. After reaching the set point, the temperature was fixed at 800 ^oC for 20 min, 900 ^oC for 20 min and 1000 ^oC for 20 min, respectively. SAXS data were collected every 38 s. For *in-situ* stability assays in aqueous systems, 1× phosphate buffered saline solution (PBS) or 0.60 mg/mL collagen hydrogel were added into individual quartz capillary tubes (O.D.,1.5 mm), respectively. Powders were subsequently added into the tubes and mixed with solution or gel to form suspensions at room temperature. Data were collected every 30 min in the first 6 h and every 2 h in the last 6 h.

Transmission X-ray microscopy (TXM). Absorption full-field nano-computed tomography (nano-CT) was performed on the new transmission X-ray microscope at sector 32-ID of APS in ANL. Mesostructured Si was first mounted onto a micromanipulator installed in a focused ion beam (FIB) system (FEI, USA, Nova 600 NanoLab). The micromanipulator was secured on a custom-built holder for data collection. Acquisition was conducted with a monochromatic beam tuned at 8 keV. The condenser and the objective lens used are diffracting optics developed in-house. X-rays are focused to the sample thanks to a beam-shaping condenser (BSC), *i.e.*, a mosaic of diffraction gratings organized in concentric rings. The round BSC can collect a large portion of the beam with its diameter of 1.6 mm. Gratings in each rings have spacing decreasing down to 60 nm at the optic periphery. A 180 μm large Fresnel zone plate with 60 nm outer most zone width was used as a microscope objective lens in order to magnify radiographs of the sample placed on a high accuracy air-bearing rotary stage. With a distance CCD-sample set to 3.4 m, a magnification

of ~47 was obtained. The X-ray detection system corresponds to an assembly comprising a scintillator (LuAG), a 5× microscope objective, a 45° mirror and a low noise fast CCD cooled at -40 °C. The voxel width obtained in this geometry was 27.6 nm and the field of view was about 70 × 60 μm^2 while the illumination coming from the BSC was a disk slightly larger than 70 µm. The true spatial resolution given by the zone plate is ~60 nm. 3D reconstructions were performed with the software Tomopy (http://www.aps.anl.gov/tomopy/), an open source Python based toolbox for the analysis of synchrotron tomographic data.

The 3D iso-intensity surfaces were constructed and visualized using Amira 5.5 (FEI Visualization Sciences Group). Segmentation of intra- and inter-granular voids was carried out based on intensity. Inter-granular voids were assigned to intensity value less than -0.00015. Intra-granular voids were determined manually by choosing low intensity regions within particles slice by slice using a magic wand tool.

Atom-probe tomography (APT). Mesostructured Si particles were transferred onto Si microposts using a micromanipulator installed in a focused ion beam (FIB) system (FEI, USA, Nova 600 NanoLab). Samples were then mounted and milled into needle-like microtip specimen for APT characterization. The APT was run in an ultraviolet (UV) laser-assisted local-electrode atom-probe (Cameca, USA, LEAP 400XSi). Surface atoms from a microtip were evaporated with an applied voltage of 1~6 kV and the assistance of a 30 pJ UV (wavelength λ=355 nm) laser pulsing at 250 kHz frequency. The mass-to-charge (m/z) ratios of individual evaporated ions and their corresponding (x, y, z) coordinates in space were recorded with a position sensitive detector. The samples were held at 30 K and 2×10^{-11} Torr during APT experiments. The 3D reconstructions and data analyses were performed using Cameca's Integrated Visualization and Analysis Software (IVAS) 3.4 code. Typical regions of both Si nanowires and micro-bridges were cropped from **Fig.**

2-7a using a region-of-interest (ROI) tool in IVAS. A series of Si isoconcentration surface from 50 at.% to higher concentrations were created for both regions, *i.e.*, nanowires and micro-bridges until no isoconcentration surface with higher atomic concentration could be created. The proximity histograms (**Fig. 2-8b**) was calculated using the 60% Si isoconcentration surface of the dataset in **Fig. 2-7a**, and included information of both Si nanowires and inter-connecting micro-bridges. For histogram shown in **Fig. 2-8c**, the number of Si atoms per Si concentration interval was calculated by subtracting the total number Si atoms enclosed within one isoconcentration surface from the precedent isoconcentration surface. For example, the number of Si atoms that is 50~51 at.% is the difference between the total Si atoms enclosed in 50% isoconcentration surface and that in 51% at.%. The Si concentration distribution was plotted by calculating the relative frequency of the number of Si atoms per Si atomic concentration.

Electrical measurements. Mesostructured Si particles were gently sonicated in IPA and dispersed onto Si substrates (Nova Electronic Materials, 600 nm oxide, *p*-type, 0.001 Ω·cm) with photo-lithographically patterned gold electrodes. Electrical contacts onto individual Si particles were made with an FIB system (FEI, USA, Nova 600 NanoLab) by depositing platinum (Pt) wires with a built-in gas-injection system (GIS). The electrical conductance measurements were evaluated using a dual-channel source-meter (Keithley 2636A) and a probe station (Rucker & Kolls, Model 680A). The particles were then removed from the interconnects by sonication and the conductance was subsequently measured as controls.

Atomic force microscopy (AFM) measurements. Force curves were collected using an Asylum MFP-3D AFM (Asylum Research, USA) with ACTA (AppNano, USA, nominal spring constant 40 N/m) probes in air and AC240 (Olympus, Japan, nominal spring constant 2 N/m) probes in liquid. Prior to measurements, the inverse optical lever sensitivity and cantilever spring constant

were calibrated following vendor's standard procedures. For all measurements, mesostructured Si particles were first transferred onto Si substrates (Nova Electronic Materials, USA, *p*-type, 0.001 Ω·cm). Prior to solution phase AFM experiments, samples were also soaked in 1× PBS solution at room temperature for ~2 h. Force curves were recorded by loading at a rate of 1μm/s up to an indentation depth of ~10 nm, followed by unloading at the same rate. For both measurements in air and in fluid, ten particles were chosen to take force curves by making indentations on random sites over the particle surfaces. The total number of data points is n=138 for the sample in air and n=94 for the sample in liquid. Asylum Research software was used for data collection and analysis. Oliver-Pharr method was used by fitting the range between 25% and 75% of maximum indentation of the retraction curve. The as-calculated value was reduced Young's modulus E_c, which was comprised of the indenter and sample's Young's modulus (E_i for indenter, E_s for sample) and Poisson ratio (ν_i for indenter, ν_s for sample) by $1/E_c=(1-\nu_i^2)/E_i+(1-\nu_s^2)/E_s$. The indenter's Poisson's ratio was 0.17 and its Young's modulus was 150 GPa, for both Si cantilevers. The sample's Poisson's ratio was chosen as 0.10 from literature[5]. Based on the equation, $1/E_c=(1-\nu_i^2)/E_i+(1-\nu_s^2)/E_s$, it is noted that even an appreciable deviation in the Poisson's ratio will not introduce significant error into the calculated sample modulus[5].

Ultraviolet-visible (UV-vis) spectroscopy. Prior to measurements, mesostructured Si powders were soaked in 1× PBS for 0 h, 2 h, 12 h and 24 h. After filtration and rinsing with DI water, samples were re-dispersed in IPA and drop casted over glass slides and air dried. The thickness of the Si films was ~20 μm, as determined by a profilometer (Bruker, USA, Dektak XT-S). Diffuse reflectance UV-Vis spectra were collected on a Cary 5000 UV-Vis-NIR spectrometer (Varian, USA) equipped with a diffuse reflectance accessory (DRA). The acquired diffuse reflectance

spectra were converted to Kubelka-Munk functions defined as $F(R) = (1-R)^2/2R$, where R is reflectance. Tauc plots were then plotted to calculate band gap energies.

Raman spectroscopy. Prior to measurements, mesostructured Si powders were soaked in 1× PBS for 0 h, 2 h, 12 h and 24 h. Raman spectra were recorded using a LabRAM HR evolution system (Horiba, Japan), with samples immersed in PBS solutions.

Cell/Si interface imaging.

A. High-pressure freezing and freeze-substitution. Human umbilical vein endothelial cells (HUVEC) were first seeded on a transwell with 96 permeable supports (Corning Inc., USA, polyester membrane, pore size, 1.0μm) and cultured in Medium 200 (Life Technologies, USA) until reaching confluency. Mesostructured Si particles (~0.01 mg) were added to the transwell, which settled down within 15 min. The polyester membrane was peeled off from the well and transferred to an aluminum planchet, with excess space filled with 1-hexadecene (Sigma-Aldrich, USA). Samples were frozen in a Baltec HPM 010 high-pressure freezer (Technotrade, USA) and then freeze-substituted in 0.25% glutaraldehyde (Electron Microscopy Sciences, USA) and 0.1% urinal acetate (Electron Microscopy Sciences, USA) dissolved in anhydrous acetone (Electron Microscopy Sciences, USA), using an automated freeze substitution machine (AFS2, Leica Microsystems, Germany). The temperature increased from -180 °C to -80 °C in 12 h and stayed at -80 °C for 72 h. The temperature was then ramped from -80 °C to -20 °C over 12 h. Samples were washed with anhydrous acetone three times at -20 °C, then transferred to 4 °C, held overnight, and warmed to room temperature. Samples were then infiltrated with increasing concentrations of epoxy resin in anhydrous acetone (low viscosity Spurr, Ted Pella Inc., USA, 20%, 25%, 33%, 50%, and 100%; v/v) and finally solidified at 60 °C for 24 h. Epoxy sections of ~100 nm were cut using a ultramicrotome (Ultracut E, Reichert-Jung, USA) collected on copper grids (Electron

Microscopy Sciences, USA, 200 mesh). Sections were stained with 2% (w/v) uranyl acetate and 0.5% (w/v) lead citrate (Electron Microscopy Sciences, USA). Samples were imaged using a Tecnai F30 TEM (FEI, USA).

B. Chemical fixation. HUVECs and mesostructured Si mixture were prepared in the same way for freeze substitution on transwell membranes. The samples were fixed with 2% glutaraldehyde and 4% paraformaldehyde (Electron Microscopy Sciences, USA) in 0.1 M sodium cacodylate buffers (Electron Microscopy Sciences, USA) overnight at 4 °C. The samples were then washed three times with sodium cacodylate buffers for 5 min each time. After replacing with 1% osmium tetroxide (Electron Microscopy Sciences, USA) in sodium cacodylate buffers and incubating for 60 min, the samples were washed twice with sodium cacodylate buffers for 5 min each time. Maleate buffers (Electron Microscopy Sciences, USA, pH 5.1) were then used to rinse the samples for 5 min. The samples were subsequently stained with 1% uranyl acetate in maleate buffers for 60 min. After the staining, the samples were washed three times with maleate buffers with 5 min each time. The following dehydration process involves a series of washing steps with increasing concentrations of acetone in maleate buffers (25% 2×5 min, 50% 2×5 min, 70% 2×5 min, 95% 2×5 min, 100% 3×15 min; v/v). The infiltration process was performed in the same way as that used in freeze-substitution method (epoxy in anhydrous acetone, 20%, 25%, 33%, 50%, and 100%; v/v). The final epoxy resins were solidified at 60 °C for 24 h. Epoxy sections were cut, stained and imaged in the same way as those used for freeze substitution.

***In vitro* Si degradation.** A series of samples with 50 μg, 100 μg and 300 μg mesostructured Si in 1 mL of 1× PBS solution were incubated at both room temperature and 37 °C. An aliquot of 0.5 mL solution was removed at different time points from each tube and diluted with 4.5 mL 2% HNO_3 and subjected to analysis by inductively coupled plasma optical emission spectroscopy (710

ICP-OES, Agilent Technologies, USA). 0.5 mL of fresh PBS solutions were added back each time to all tubes. For each group of samples, 5 independent tests were performed (*i.e.*, $n = 5$).

Calcium imaging. HUVECs were first cultured on petri dishes to reach a confluency of ~80% before experiments. Cells were stained with 1 μM Fura-2 AM (Life Technologies, USA) for 30 min and washed three times with a HEPES-buffered Tyrode's solution (119 mM NaCl, 5 mM KCl, 25 mM HEPES, 2 mM $CaCl_2$, 2 mM $MgCl_2$, 6 g/L glucose, pH 7.4). Solid silicon particles were prepared by mechanically grinding of a silicon wafer (Silicon Quest, USA, *p*-type, 1-10 Ω cm). Both mesostructured and solid Si particles were immersed in HEPES-buffered Tyrode's solutions overnight before applying to the stained cell cultures. About 0.01 mg of Si particles were delivered and allowed to settle down for about 5 min to form interfaces with cells. Glass pipettes with tip diameters of ~1.5 μm were pulled in a flaming/brown type micropipette puller (P-97, Sutter Instruments, USA). Micropipettes were filled with the same Tyrode's solution as the bath and controlled with a motorized micromanipulator (PatchStar, Scientifica, UK). In general, only particles sitting on cell bodies, with lateral sizes of ~5 μm, were chosen. Glass pipettes were approached vertically using the micromanipulator and the pipette resistances were monitored in real time. The contact point was determined by the time where a transient or steady increase in the pipette resistance was observed. After making contact with the particles, pipettes were lowered by another 1 μm and held still for 20 s before retraction. During the whole process, fluorescence images were collected using an upright microscope (BX61WI, Olympus, Japan) equipped with an EM-CCD camera (C9100-13, Hamamatsu Photonics, Japan). Images from excitation wavelengths at 340 nm and 380 nm were taken every 1 s. Ratiometric information was obtained from the images collected at 340 nm and 380 nm, and was used for quantitative analysis in MetaFluor software (Molecular Devices, USA). The amplitude and the slope of the ratio changes after mechanical

perturbation were defined in **Fig. 2-12a,** and statistically compared between porous/mesostructured/amorphous and solid/single crystalline Si samples. The amplitude was calculated as a ratio between the peak ratiometric difference and the baseline. The slope was determined by linear fitting of the range between 25% and 75% of the maximum from baseline.

Cytotoxicity assays. HUVEC (Life Technologies, USA), C2C12 cells (ATCC, USA) and human aortic smooth muscle cells (HASMC) (Life Technologies, USA) were seeded in 96-well plates and settled down for 1 d prior to applying mesostructured Si particles. The particles were added to make the final concentration as 0.1 mg/mL in each well. In the positive control groups, no particles were added. On days 1, 3, 5, 7 of the co-culture with Si particles, 3-(4,5-dimethylthiazol-2-yl)-2,5-diphenyltetrazolium bromide (MTT) (Life Technologies, USA) were added and the mixtures were incubated for 4 h at 37 ^{o}C. Dimethyl sulfoxide (DMSO) (Thermo Fisher Scientific, USA) was added to dissolve the as-formed formazan after all the solutions were removed. After 10 min incubation at 37 ^{o}C, the absorbance of the DMSO solution in each well was recorded with a multi-plate reader (Tecan Group Ltd., Switzerland, Infinite 200 PRO) at 570 nm. For each group, n=8.

***In vivo* Si biocompatibility and degradability.** The animal protocol used for this study was in accordance to the policies of the University of Chicago and were approved by the Institutional Animal Care and Use Committee (IACUC). Young adult male CD® IGS rats weighing 226~250 g were ordered from Charles River Laboratories (USA) and housed in pairs in a 6 AM–6 PM light dark cycle. Mesostructured Si and sodium carboxymethyl cellulose (CMC, MW ~250,000, Sigma-Aldrich, USA) were sterilized by UV irradiation for 24 h. Si particles were suspended in 1% CMC solution of 1× PBS and sonicated for 1 h before being loaded into 1 mL syringes under sterile conditions. CMC was added as a stabilizing agent to prevent the aggregation and sedimentation of mesostructured Si particles in saline, and it is biocompatible. Anesthesia was induced briefly, prior

to injection, with isoflurane in 100% oxygen. Each rat received one subcutaneous injection of 5 mg mesostructured Si in 0.5 mL of 1% CMC. 1 day, 7 days and 21 days after the injection, four rats were sacrificed at each time point for examination. Tissues retrieved from the necropsy were fixed in 10% neutral buffered formalin (Sigma-Aldrich, USA), embedded in paraffin, sectioned, and stained with hematoxylin and eosin for histological examination using standard techniques and then reviewed by a pathologist.

Artificial lipid bilayer experiments.

A. Experimental setup. An inverted microscope (Zeiss IM35, Germany) was used with a 10×/0.25 NA and a 40×/0.55NA lens to deliver focused laser pulses with spot sizes in diameter of ~40 μm and ~10 μm, respectively. The beam of the diode-pumped solid-state (DPSS) laser (UltraLaser, Canada) was modulated with an acousto-optic modulator (NEOS Technologies, USA), controlled by transistor-transistor logic (TTL) pulses, delivered individually or in trains of pulses at desired frequencies by a custom-made circuit board. Voltage- and current-clamp protocols were done by an Axopatch 200B amplifier (Molecular Devices, USA), controlled by a personal computer (PC) through a digital-to-analog converter (Innovative Integration SBC-6711-A4D4, USA) with an in-house program control. Analog data were low-pass filtered by an 8-pole Bessel filter (Frequency Devices 950L8L, Canada), converted into digital signal by the same board and acquired by a PC. Patch pipettes were pulled in a CO_2 laser micropipette puller (Sutter Instruments P-2000, USA) and polished in a custom-made microforge for a final resistance of 2-4 M□ when filled with adequate solution. For the temperature measuring experiments, the resistance of a positioned patch pipette was monitored and recorded by an OC-725A amplifier (Warner Instrument, USA). Experiments to measure capacitance change were carried out with a sinusoidal command voltage using a function generator (Krohn-Hite 1200A, USA).

B. Lipid bilayer formation. Asolectin lipids (25 mg/mL in chloroform, soybean polar lipid extract, Avanti Polar Lipids, USA) were smoothed in a test tube to form a thin film, and then dried inside a nitrogen desiccator for about an hour before use. The film was dissolved in *n*-decane (Thermo-Fisher Scientific, USA) in order to produce a lipid mix with final concentration 25 mg/mL. A custom-made upper chamber containing a 300 μm diameter hole for planar lipid bilayer formation was used and placed in a glass-bottomed lower chamber. Typically, 1 μL of the lipids in *n*-decane was deposited on the upper chamber hole and let dry for about 15 minutes. Afterwards both chambers were filled with bilayer bath solution (in mM: KCl 90, HEPES 10; pH 7.4). Each chamber was then connected to the patch amplifier headstage through Ag/AgCl hemicells *via* salt bridges made with 1% ultrapure agar (USB Corp., USA) melted in a solution containing 1M N-methyl-D-glucamine (NMG) (Sigma-Aldrich, USA) and 10 mM HEPES, pH 7.4. A lipid bilayer was painted with an air bubble held by a pipette tip. The formation of the lipid bilayer was monitored under voltage clamp by observing the current responses to a 1V/s voltage ramp. The recording electrode was connected to the lower chamber and the reference electrode was connected to the top chamber. Data was low-pass filtered at 50 kHz by the 8-pole Bessel filter and sampled at 200 kHz.

The material was grinded and sonicated to roughly spherical shape of ~ 1-2 μm in diameter. Approximately 0.01 mg of mesostructured Si particles were delivered into the upper bath solution and allowed to settle down for about 5 min. Most of the particles sank to the bottom of the upper chamber and made contact with the bilayer. The laser power was adjusted by a set of neutral density filters manually. The laser pulse frequency and duration were controlled by the in-house software and external custom-made hardware. For these experiments we used the 10× objective lens which produced a laser spot size approximately 40 μm in diameter.

C. Capacitance measurements. Briefly, the current responses of the bilayer were recorded when a 5-kHz sinusoidal carrier voltage signal was concurrently used as the voltage command, while Si-based film was illuminated by the laser pulses. When the sinusoidal signal passes through a *RC* circuit consisting of the lipid bilayer and series resistance, the in-phase current would be determined by the resistance, $V/I_{\text{in-phase}}=R$, while the 90^{o} out-of-phase current would be determined by the capacitive reactance $V/I_{\text{out-of-phase}}=X_c$. The total impedance can be calculated as $Z=\sqrt{R^2+X_c^2}$. Upon illumination, if the bilayer impedance was altered, the magnitude and the phase of the output current would change. Since the capacitive reactance (X_c) is inversely related to the capacitance (C) and the frequency (f), $X_c=\frac{1}{2\pi fC}$, an increase in bilayer capacitance due to a temperature rise would lower the impedance, resulting in an increase of output current. After low-pass filtered at 20 kHz and sampled at 100 kHz, the sinusoidal current output signals were rectified, and low-pass filtered at a cutoff frequency of 2 kHz. Therefore, the difference of the out-of-phase current outputs, with and without the laser stimulation, reflects the capacitance change in the bilayer.

D. Local temperature measurements. During the bilayer stimulation experiment, a pipette electrode (2~4 MΩ) filled with bilayer bath solution was placed adjacent to the stimulation site. As the solution inside the pipette was the same as in the bath, the effect of liquid junction potential is diminished, *i.e.*, no ionic gradient across the pipette tip. The resistance of this temperature-monitoring electrode was recorded. After the stimulation experiment, the temperature-monitoring electrode was placed carefully into a chamber with bilayer bath solution pre-heated to about 50 ^{o}C. A thermocouple was positioned close to the pipette tip. A calibration curve was constructed, based

on the pipette resistances in the range of 50 to 20 ^{o}C. Subsequently, the calibration curve was used to estimate the temperature change from the pipette resistances values recorded earlier.

E. Capacitive current recording. Capacitive currents were recorded in voltage-clamp mode. A laser pulse was delivered to the preparation 300 ms after the voltage was jumped from a holding potential of 0 mV to the desired voltage. The amplifier output was low-pass filtered at 50 kHz and sampled at 200 kHz.

Dorsal root ganglia (DRG) neurons experiments.

A. DRG culture. DRGs were extracted from decapitated P1-P3 Sprague-Dawley rats and were placed immediately in Dulbecco's modified eagle medium (DMEM) (Life Technologies, USA) on ice. The ganglia were transferred to a 0.25% solution of trypsin (Worthington, USA) in Earle's balanced salt solution (EBSS) (in mM: NaCl 132, KCl 5.3, HEPES 10, NaH_2PO_4 1, glucose 5.5; pH 7.4) and placed for 20 min in a 37 ^{o}C shaker. Afterwards, the cells were centrifuged and the supernatant was replaced with EBSS added with 10% fetal bovine serum (FBS) (ATCC, USA). After mechanically dispersing the cells with pipetting, they were centrifuged and the supernatant was replaced with DMEM containing 5% FBS. Next, cells were seeded into poly-L-lysine (PLL) (Sigma-Aldrich, USA) coated glass-bottom Petri dishes, and allowed 30 min for cell adhesion. Finally, the dishes were flooded with DMEM supplemented with 5% FBS, 100 U/ml penicillin (Sigma-Aldrich, USA), and 100 μg/ml streptomycin (Sigma-Aldrich, USA), and incubated at a 37 ^{o}C chamber with 5% CO_2 until used for experiments. The DRG neurons are ready for use in about 3 hours and can be used for experiment for about a week.

The animal protocol used in this step was in accordance to the policies of the University of Chicago and were approved by the Institutional Animal Care and Use Committee (IACUC).

B. Electrophysiology. Before the experiment, supplemented DMEM in the Petri dish with DRG neurons was rinsed three times with recording solution (in mM: NaCl 132, KCl 4, $MgCl_2$ 1.2, $CaCl_2$ 1.8, HEPES 10, glucose 5.5; pH 7.4). About 0.01 mg of mesostructured Si particles were delivered and settled for approximately 5 min. In general, we visually selected a DRG neuron with a single particle (size: ~ 2 μm) attached to the soma for patching. Desired neurons were patched with a ~2 MΩ pipette, filled with pipette solution (in mM: NaCl 10, KCl 150, $MgCl_2$ 4.5, EGTA 9, HEPES 10; pH 7.3). Voltage recordings were made in current clamp mode. Every three seconds, a 1 ms suprathreshold amplitude current injection was delivered to the neuron to assess its excitability and followed by a 1 ms laser pulse, 300 ms later. We used the 40× objective lens for these experiments, therefore a 10 μm diameter laser spot was delivered to the preparation. Then we determined the minimal power enough to elicit action potentials (APs) and applied it in trains of laser pulses at different frequencies. Spike responses elicited by either individual pulses or pulse trains were low-pass filtered at 5 kHz and sampled at 20 kHz.

C. Data analysis. Spike latency was calculated as the time between the onsets of the light pulses and the spike peaks. Jitter was calculated as the standard deviation (SD) of spike latencies, measured either across all the spikes throughout a spike train (throughout trial jitter), or for individual spike across different trials of trains (trial-to-trial jitter). Specifically, we collected 21 spikes at each frequency, and repeated 4 times. To calculate 'throughout trial jitter', we took SDs of latencies throughout 21 spikes in a single trace, followed by averaging them over 4 trials, To calculate 'trial-to-trial jitter', we took SDs of latencies for one specific spike (*e.g.*, the second spike in the train) in 4 independent trials, followed by averaging them throughout 21 spikes in a single trace. For all latency and jitter analyses, light pulses which failed to elicit a spike were ignored.

Fast Fourier transform was performed on representative traces for each frequency in OriginPro. Area-based return map, A_n-A_{n+1} (A_n is the area of the n^{th} induced neuronal signal)[6], was obtained by plotting the integrated area for each signal (range: peak-10 ms ~ peak+10 ms) using a MATLAB code. Height-based return map was obtained using the amplitude values of each signal in MATLAB. At each frequency, 4 traces were analyzed. For each trace, analysis was performed for spikes from the 2^{nd} to the 21^{st}.

Device fabrication. The device was fabricated on a Si substrate (*n*-type, 0.001~0.005 Ω·cm, Nova Electronic Materials, USA). The fabrication process consists of two steps of photolithography. The first step yields mesostructured Si-covered SU-8 micro-pads. The as-fabricated micro-pads were then connected by a second step of lithography. Briefly, one layer of SU-8 photoresist (SU-8 2002, MichroChem Corp., USA) was first spin-coated on the substrate, followed by baking at 65 °C for 2 min and 95 °C for 4 min, respectively. The SU-8 coated substrate was then photolithographically patterned and post-exposure baked at 65 °C for 2 min and 95 °C for 4 min. Mesostructured Si suspension in IPA was drop casted on the SU-8 layer and dried before developing in the SU-8 developer (MicroChem Corp., USA) for 4 min to reveal the micro-pad array. To connect the micro-pads, the as-formed isolated array was covered with another SU-8 layer. The second layer was baked at 65 °C for 2 min and 95 °C for 4 min. A mask aligner (EVG 620, EVGroup, Austria) was used to make the interconnections between micro-pads followed by post-exposure baking at 65 °C for 2 min and 95 °C for 4 min. The second layer was next developed using the SU-8 developer for 4 min. The final hard baking at 180 °C for 30 min is optional.

2.4 Bibliography

1 Leigh, C. *Handbook of porous silicon*. 1st edn, (Springer, 2014).

2 Sailor, M. J. *Porous silicon in practice: preparation, characterization, and applications*. (Wiley-VCH: Weinheim, Germany, 2012).

3 Kim, D.-H., Ghaffari, R., Lu, N. S. & Rogers, J. A. Flexible and stretchable electronics for biointegrated devices. *Annual Review of Biomedical Engineering* **14**, 113-128, doi:10.1146/annurev-bioeng-071811-150018 (2012).

4 Tian, B. Z. & Lieber, C. M. Synthetic nanoelectronic probes for biological cells and tissues. *Annual Review of Analytical Chemistry* **6**, 31-51, doi:10.1146/annurev-anchem-062012-092623 (2013).

5 Cogan, S. F. Neural stimulation and recording electrodes. *Annual Review of Biomedical Engineering* **10**, 275-309, doi:10.1146/annurev.bioeng.10.061807.160518 (2008).

6 Tasciotti, E., Liu, X. W., Bhavane, R., Plant, K., Leonard, A. D., Price, B. K., Cheng, M. M. C., Decuzzi, P., Tour, J. M., Robertson, F. & Ferrari, M. Mesoporous silicon particles as a multistage delivery system for imaging and therapeutic applications. *Nature Nanotechnology* **3**, 151-157, doi:10.1038/nnano.2008.34 (2008).

7 Chiappini, C., De Rosa, E., Martinez, J. O., Liu, X., Steele, J., Stevens, M. M. & Tasciotti, E. Biodegradable silicon nanoneedles delivering nucleic acids intracellularly induce localized in vivo neovascularization. *Nature Materials* **14**, 532-539, doi:10.1038/nmat4249 (2015).

8 Gu, L., Hall, D. J., Qin, Z. T., Anglin, E., Joo, J., Mooney, D. J., Howell, S. B. & Sailor, M. J. In vivo time-gated fluorescence imaging with biodegradable luminescent porous silicon nanoparticles. *Nature Communications* **4**, doi:10.1038/ncomms3326 (2013).

9 Kim, W., Ng, J. K., Kunitake, M. E., Conklin, B. R. & Yang, P. Interfacing silicon nanowires with mammalian cells. *Journal of the American Chemical Society* **129**, 7228-7229, doi:10.1021/ja071456k (2007).

10 Hwang, S.-W., Tao, H., Kim, D.-H., Cheng, H., Song, J.-K., Rill, E., Brenckle, M. A., Panilaitis, B., Won, S. M., Kim, Y.-S., Song, Y. M., Yu, K. J., Ameen, A., Li, R., Su, Y., Yang, M., Kaplan, D. L., Zakin, M. R., Slepian, M. J., Huang, Y., Omenetto, F. G. & Rogers, J. A. A Physically transient form of silicon electronics. *Science* **337**, 1640-1644, doi:10.1126/science.1226325 (2012).

11 Park, J.-H., Gu, L., von Maltzahn, G., Ruoslahti, E., Bhatia, S. N. & Sailor, M. J. Biodegradable luminescent porous silicon nanoparticles for in vivo applications. *Nature Materials* **8**, 331-336, doi:10.1038/nmat2398 (2009).

12 Kim, D.-H., Viventi, J., Amsden, J. J., Xiao, J., Vigeland, L., Kim, Y.-S., Blanco, J. A., Panilaitis, B., Frechette, E. S., Contreras, D., Kaplan, D. L., Omenetto, F. G., Huang, Y., Hwang, K.-C., Zakin, M. R., Litt, B. & Rogers, J. A. Dissolvable films of silk fibroin for ultrathin conformal bio-integrated electronics. *Nature Materials* **9**, 511-517, doi:10.1038/nmat2745 (2010).

13 Liu, J., Fu, T.-M., Cheng, Z., Hong, G., Zhou, T., Jin, L., Duvvuri, M., Jiang, Z., Kruskal, P., Xie, C., Suo, Z., Fang, Y. & Lieber, C. M. Syringe-injectable electronics. *Nature Nanotechnology* **10**, 629-636, doi:10.1038/nnano.2015.115 (2015).

14 Zhang, A. Q. & Lieber, C. M. Nano-bioelectronics. *Chemical Reviews* **116**, 215-257, doi:10.1021/acs.chemrev.5b00608 (2016).

15 Zimmerman, J. F., Murray, G. F., Wang, Y. C., Jumper, J. M., Austin, J. R., II & Tian, B. Z. Free-standing kinked silicon nanowires for probing inter- and intracellular force dynamics. *Nano Letters* **15**, 5492-5498, doi:10.1021/acs.nanolett.5b01963 (2015).

16 Wegst, U. G. K., Bai, H., Saiz, E., Tomsia, A. P. & Ritchie, R. O. Bioinspired structural materials. *Nature Materials* **14**, 23-36, doi:10.1038/nmat4089 (2015).

17 Chomski, E. & Ozin, G. A. Panoscopic silicon - A material for "all" length scales. *Advanced Materials* **12**, 1071-1078, doi:10.1002/1521-4095(200007)12:14<1071::aid-adma1071>3.0.co;2-j (2000).

18 Bao, Z. H., Weatherspoon, M. R., Shian, S., Cai, Y., Graham, P. D., Allan, S. M., Ahmad, G., Dickerson, M. B., Church, B. C., Kang, Z. T., Abernathy, H. W., Summers, C. J., Liu, M. L. & Sandhage, K. H. Chemical reduction of three-dimensional silica micro-assemblies into microporous silicon replicas. *Nature* **446**, 172-175, doi:10.1038/nature05570 (2007).

19 Dai, F., Zai, J. T., Yi, R., Gordin, M. L., Sohn, H., Chen, S. R. & Wang, D. H. Bottom-up synthesis of high surface area mesoporous crystalline silicon and evaluation of its hydrogen evolution performance. *Nature Communications* **5**, doi:10.1038/ncomms4605 (2014).

20 Hochbaum, A. I., Gargas, D., Hwang, Y. J. & Yang, P. Single crystalline mesoporous silicon nanowires. *Nano Letters* **9**, 3550-3554, doi:10.1021/nl9017594 (2009).

21 Qu, Y., Liao, L., Li, Y., Zhang, H., Huang, Y. & Duan, X. Electrically conductive and optically active porous silicon nanowires. *Nano Letters* **9**, 4539-4543, doi:10.1021/nl903030h (2009).

22 Li, X. & Bohn, P. W. Metal-assisted chemical etching in HF/H(2)O(2) produces porous silicon. *Applied Physics Letters* **77**, 2572-2574, doi:10.1063/1.1319191 (2000).

23 Gordon, L. M., Cohen, M. J., MacRenaris, K. W., Pasteris, J. D., Seda, T. & Joester, D. Amorphous intergranular phases control the properties of rodent tooth enamel. *Science* **347**, 746-750, doi:10.1126/science.1258950 (2015).

24 Ott, H. C., Matthiesen, T. S., Goh, S. K., Black, L. D., Kren, S. M., Netoff, T. I. & Taylor, D. A. Perfusion-decellularized matrix: using nature's platform to engineer a bioartificial heart. *Nature Medicine* **14**, 213-221, doi:10.1038/nm1684 (2008).

25 Gu, D. & Schuth, F. Synthesis of non-siliceous mesoporous oxides. *Chemical Society Reviews* **43**, 313-344, doi:10.1039/c3cs60155b (2014).

26 Wan, Y., Yang, H. F. & Zhao, D. Y. "Host-guest" chemistry in the synthesis of ordered nonsiliceous mesoporous materials. *Accounts of Chemical Research* **39**, 423-432, doi:10.1021/ar050091a (2006).

27 Arora, H., Du, P., Tan, K. W., Hyun, J. K., Grazul, J., Xin, H. L., Muller, D. A., Thompson, M. O. & Wiesner, U. Block copolymer self-assembly-directed single-crystal homo- and heteroepitaxial nanostructures. *Science* **330**, 214-219, doi:10.1126/science.1193369 (2010).

28 Joo, S. H., Choi, S. J., Oh, I., Kwak, J., Liu, Z., Terasaki, O. & Ryoo, R. Ordered nanoporous arrays of carbon supporting high dispersions of platinum nanoparticles. *Nature* **412**, 169-172, doi:10.1038/35084046 (2001).

29 Zhao, D. Y., Feng, J. L., Huo, Q. S., Melosh, N., Fredrickson, G. H., Chmelka, B. F. & Stucky, G. D. Triblock copolymer syntheses of mesoporous silica with periodic 50 to 300 angstrom pores. *Science* **279**, 548-552, doi:10.1126/science.279.5350.548 (1998).

30 Richman, E. K., Kang, C. B., Brezesinski, T. & Tolbert, S. H. Ordered mesoporous silicon through magnesium reduction of polymer templated silica thin films. *Nano Letters* **8**, 3075-3079, doi:10.1021/nl801759x (2008).

31 Tanaka, K., Maruyama, E., Shimada, T. & Okamoto, H. *Amorphous silicon*. 1st edn, (Wiley, 1999).

32 Freund, L. B. & Suresh, S. *Thin film materials: stress, defect formation and surface evolution*. 1st edn, (Cambridge University Press, 2009).

33 Imperor-Clerc, M., Davidson, P. & Davidson, A. Existence of a microporous corona around the mesopores of silica-based SBA-15 materials templated by triblock copolymers. *Journal of the American Chemical Society* **122**, 11925-11933, doi:10.1021/ja002245h (2000).

34 Minev, I. R., Musienko, P., Hirsch, A., Barraud, Q., Wenger, N., Moraud, E. M., Gandar, J., Capogrosso, M., Milekovic, T., Asboth, L., Torres, R. F., Vachicouras, N., Liu, Q., Pavlova, N., Duis, S., Larmagnac, A., Voeroes, J., Micera, S., Suo, Z., Courtine, G. & Lacour, S. P. Electronic dura mater for long-term multimodal neural interfaces. *Science* **347**, 159-163, doi:10.1126/science.1260318 (2015).

35 Lanzani, G. Materials for bioelectronics: Organic electronics meets biology. *Nature Materials* **13**, 775-776, doi:10.1038/nmat4021 (2014).

36 Gautieri, A., Vesentini, S., Redaelli, A. & Buehler, M. J. Hierarchical structure and nanomechanics of collagen microfibrils from the atomistic scale up. *Nano Letters* **11**, 757-766, doi:10.1021/nl103943u (2011).

37 Picas, L., Rico, F. & Scheuring, S. Direct measurement of the mechanical properties of lipid phases in supported bilayers. *Biophysical Journal* **102**, L1-L3, doi:10.1016/j.bpj.2011.11.4001 (2012).

38 Han, D. X., Lorentzen, J. D., Weinberg-Wolf, J., McNeil, L. E. & Wang, Q. Raman study of thin films of amorphous-to-microcrystalline silicon prepared by hot-wire chemical vapor deposition. *Journal of Applied Physics* **94**, 2930-2936, doi:10.1063/1.1598298 (2003).

39 Li, L., Connors, M. J., Kolle, M., England, G. T., Speiser, D. I., Xiao, X. H., Aizenberg, J. & Ortiz, C. Multifunctionality of chiton biomineralized armor with an integrated visual system. *Science* **350**, 952-956, doi:10.1126/science.aad1246 (2015).

40 Shapiro, M. G., Homma, K., Villarreal, S., Richter, C. P. & Bezanilla, F. Infrared light excites cells by changing their electrical capacitance. *Nature Communications* **3**, doi:10.1038/ncomms1742 (2012).

41 Carvalho-de-Souza, J. L., Treger, J. S., Dang, B., Kent, S. B. H., Pepperberg, D. R. & Bezanilla, F. Photosensitivity of neurons enabled by cell-targeted gold nanoparticles. *Neuron* **86**, 207-217, doi:10.1016/j.neuron.2015.02.033 (2015).

42 Sanders, A. W., Jeerage, K. M., Schwartz, C. L., Curtin, A. E. & Chiaramonti, A. N. Gold nanoparticle quantitation by whole cell tomography. *ACS Nano* **9**, 11792-11799, doi:10.1021/acsnano.5b03815 (2015).

43 Liu, Y., Ai, K., Liu, J., Deng, M., He, Y. & Lu, L. Dopamine-melanin colloidal nanospheres: An efficient near-infrared photothermal therapeutic agent for in vivo cancer therapy. *Advanced Materials* **25**, 1353-1359, doi:10.1002/adma.201204683 (2013).

44 Kaplan, D. T., Clay, J. R., Manning, T., Glass, L., Guevara, M. R. & Shrier, A. Subthreshold dynamics in periodically stimulated squid giant axons. *Physical Review Letters* **76**, 4074-4077, doi:10.1103/PhysRevLett.76.4074 (1996).

45 Liu, Y., Ai, K. & Lu, L. Polydopamine and its derivative materials: Synthesis and promising applications in energy, environmental, and biomedical fields. *Chemical Reviews* **114**, 5057-5115, doi:10.1021/cr400407a (2014).

46 Pan, L., Yu, G., Zhai, D., Lee, H. R., Zhao, W., Liu, N., Wang, H., Tee, B. C. K., Shi, Y., Cui, Y. & Bao, Z. Hierarchical nanostructured conducting polymer hydrogel with high electrochemical activity. *Proceedings of the National Academy of Sciences of the United States of America* **109**, 9287-9292, doi:10.1073/pnas.1202636109 (2012).

47 Ghezzi, D., Antognazza, M. R., Dal Maschio, M., Lanzarini, E., Benfenati, F. & Lanzani, G. A hybrid bioorganic interface for neuronal photoactivation. *Nature Communications* **2**, doi:10.1038/ncomms1164 (2011).

48 Tee, B. C. K., Chortos, A., Berndt, A., Nguyen, A. K., Tom, A., McGuire, A., Lin, Z. C., Tien, K., Bae, W.-G., Wang, H., Mei, P., Chou, H.-H., Cui, B., Deisseroth, K., Ng, T. N. & Bao, Z. A skin-inspired organic digital mechanoreceptor. *Science* **350**, 313-316, doi:10.1126/science.aaa9306 (2015).

49 Tian, B. Z, Liu, J., Dvir, T., Jin, L., Tsui, J. H., Qing, Q., Suo, Z., Langer, R., Kohane, D. S. & Lieber, C. M. Macroporous nanowire nanoelectronic scaffolds for synthetic tissues. *Nature Materials* **11**, 986-994, doi:10.1038/nmat3404 (2012).

50 Karzbrun, E., Tayar, A. M., Noireaux, V. & Bar-Ziv, R. H. Programmable on-chip DNA compartments as artificial cells. *Science* **345**, 829-832, doi:10.1126/science.1255550 (2014).

Chapter 3

Rational design of silicon structures for multiscale and optically-controlled biointerfaces

3.1 Introduction

Silicon (Si)-based materials have a wide range of utilities in biophysical and biomedical research. Fundamental discoveries of new forms and properties in materials can lead to new designs of biophysical tools and biomedical devices[1-15]. For example, dopant modulated and kinked silicon (Si) nanowires allow for intracellular electrical recording from cardiomyocytes with a field effect transistor configuration[2]. Bendable integrated circuits, based on Si nanoscale membranes and their seamless interface with thermal oxide, open the way for long-lived bioelectronic implants for the heart[6]. Although the electrically registered device components have yielded impressive results, remotely-controlled and freestanding systems are rarely employed in biointerface studies[16-23]. This is largely due to our limited understanding of the physicochemical processes at the freestanding Si surfaces under physiological conditions. In particular, a quantitative understanding of the light-induced electrical, electrochemical, and thermal pathways across multiple length scales, if achieved, would likely promote future biointerface innovations. In this chapter, I will demonstrate a biology-guided rational design principle for establishing intra-, inter- and extracellular Si-based interfaces, where Si and biological targets have matched properties. In particular, I will focus on the light-induced processes at these interfaces, and develop a set of matrices to quantify and differentiate the capacitive, Faradaic and thermal outputs from ~ 30 different Si materials in saline. Finally, I will demonstrate the utility of these interfaces by

showing light-controlled non-genetic modulations of intracellular calcium dynamics, cytoskeleton-based transport and structures, cellular excitability, neural transmitter release from brain slices, and brain activities *in vivo*.

3.2 Results and Discussion

3.2.1 The principle of biology-guided biointerface design

Si displays many size- and doping-dependent physicochemical processes. To efficiently leverage these processes in the context of biointerfaces, the Si-based materials or devices should be in tight contact (**Fig. 3-1a**, **Selection I**) with their biological counterparts. Such tight interfaces can be established by van der Waals forces at the organ level, by dynamic cellular focal adhesion at the single cell and tissue level, and by protein-associated tethering and active motions at the organelle level. To promote these forces, we focus our Si materials on flexible and distributed mesh (at the organ level)[1], membrane with rough surfaces (at the cell and tissue level)[24] and nanowire (at the organelle level) geometries[25], where at least one dimension of the material properties can be tuned to promote tight interfaces (**Fig. 3-1b**). After the material/device structures are determined, we are next in a position to examine the effects of other orthogonal controls (*e.g.*, size, doping, surface chemistry) to produce the desirable physicochemical processes (**Fig. 3-1a**, **Selection II**) at the biointerfaces. These two-step selections, guided by the need to form tight junctions (**Selection I**) and efficient signal transduction (**Selection II**) with the biological targets, would narrow the material options to those that are better suited for the targeted biophysical or biomedical questions.

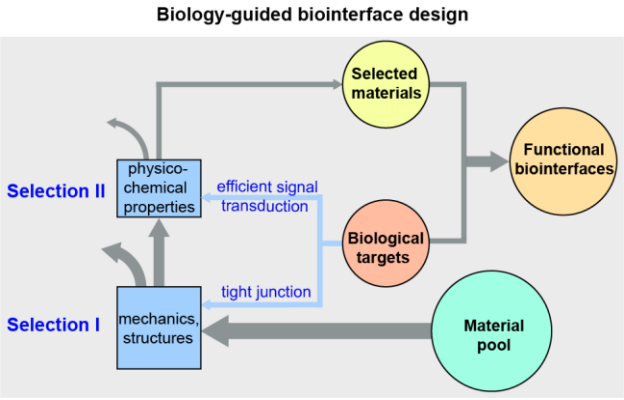

Figure 3-1. The principle of biology-guided biointerface design. A schematic diagram illustrating the principle of biology-guided biointerface design. The intended biological targets place selection criteria for material structure (**I**) and function (**II**), so that the selected materials would display a better chance to establish functional biointerfaces.

3.2.2 Selection I for material structures

For example, to create a conformal interface with a mouse brain cortex, we explored a flexible device made of a distributed mesh of Si membrane (~ 2.3 μm in thickness) and a porous polydimethylsiloxane (PDMS) substrate (**Figs. 3-2, 3-3**). The holey structures in both Si and PDMS can mitigate the stress accumulated across a large device area (**Fig. 3-4**), and enhance the device mechanical compliance.

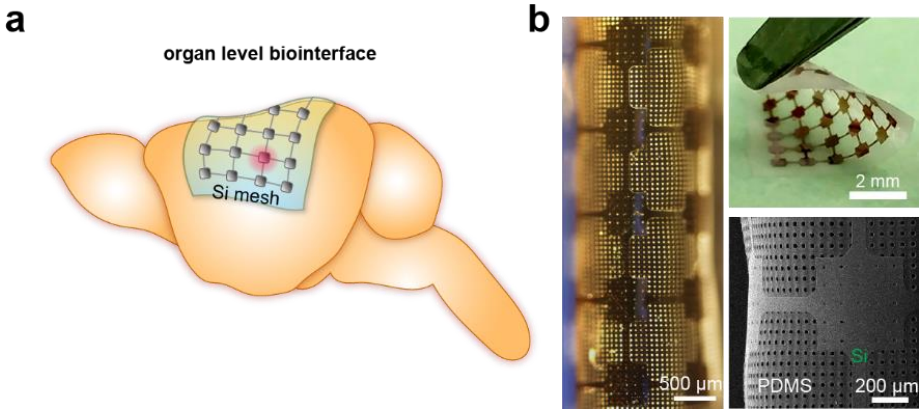

Figure 3-2. A distributed Si mesh for organ-level biointerface. a, Distributed Si meshes are chosen after **Selection I** to form tight interfaces with organs. **b,** A flexible device composed of a stack of a distributed Si mesh and a holey

Figure 3-2, continued. PDMS membrane. The flexibility is demonstrated by optical (left) and scanning electron (lower right) micrographs and a photograph (upper right) taken from the same device under rolling or bending.

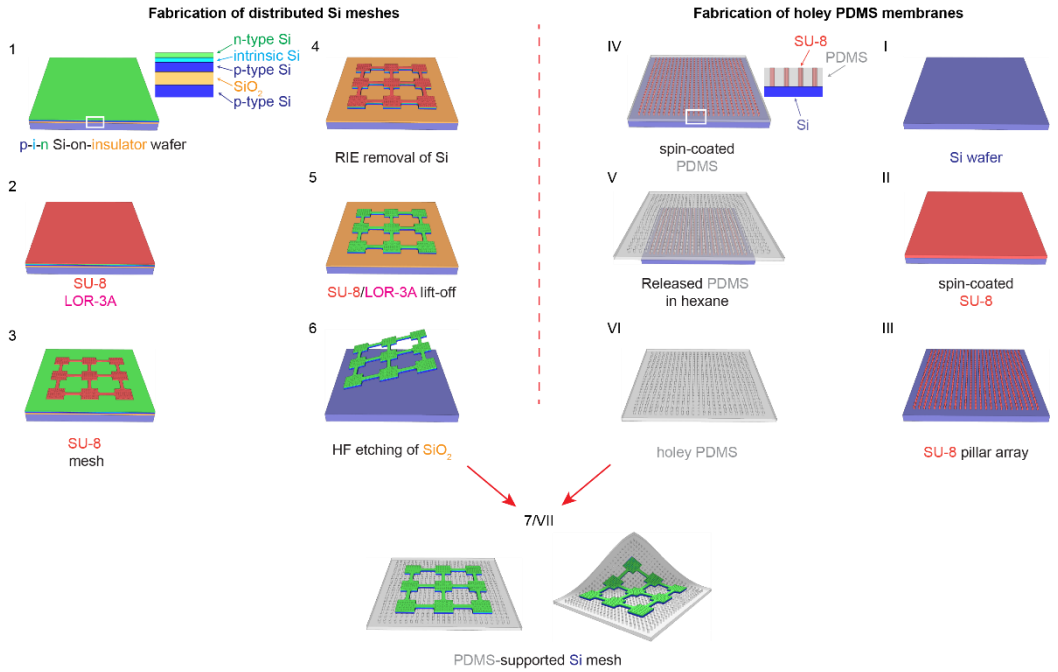

Figure 3-3. Schematic diagrams illustrating the fabrication procedures of the flexible device made of PDMS and Si. (1-6) Fabrication of the distributed Si mesh by a combination of photolithography, reactive ion etching, and wet etching processes. (I-VI) Fabrication of the holey PDMS membrane with the soft lithography technique. (7/VII) Transfer of the Si mesh onto the PDMS membrane for the final device.

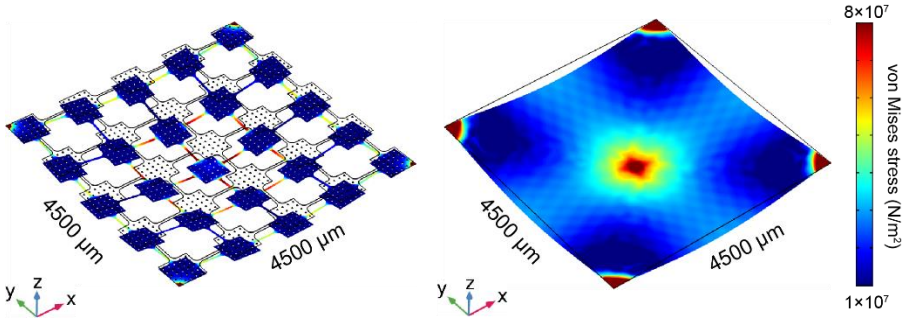

Figure 3-4. A distributed Si mesh mitigate stress over a large area. Finite element analysis of the *von Mises* stress distributions in a distributed Si mesh (left) and a solid Si membrane (right) upon indentation. The Si mesh with the holey structure shows a more uniform stress distribution across individual Si pads, suggesting a potentially more consistent optical stimulation performance in different locations. For the solid Si membrane, a large stress variation

Figure 3-4, continued. was observed, suggesting performance heterogeneity. Additionally, the relaxed stress in the distributed mesh suggests a better mechanical stability during the device assembly and operation.

With this Si membrane alone, we can examine uniformly doped and dopant modulated configurations to identify the effect of doping. In particular, a *p*-type/intrinsic/*n*-type (*p*-*i*-*n*) Si heterojunction was synthesized by chemical vapor deposition (CVD) of intrinsic and *n*-type Si layers (~ 140 and ~ 190 nm in thickness, respectively) over a *p*-type Si semiconductor-on-insulator (SOI) substrate (*p*-type Si thickness, ~ 2 μm) (**Fig. 3-5**). Cross-sectional (scanning) transmission electron microscope (TEM) images taken at the interface between the SOI wafer and the as-deposited layers indicate a columnar shell structure with a sharp and oxide-free interface (< 1 nm junction width) (**Fig. 3-5b**, upper right). While the *p*-type substrate is single crystalline, the *i*-/*n*-layers are nanocrystalline (**Fig. 3-5b**, lower right; **Fig. 3-6**), which is reminiscent of the Si nanostructures used for thin film solar cells. The surface of the nanocrystalline layer is rough, which would promote cellular focal adhesions[24]. Beyond doping control, we also prepared metal (*i.e.*, gold, silver, and platinum) nanoparticle or nanomesh-covered Si heterojunctions by electroless deposition in order to expand the repertoire of Si-based biointerfaces (**Fig. 3-7**).

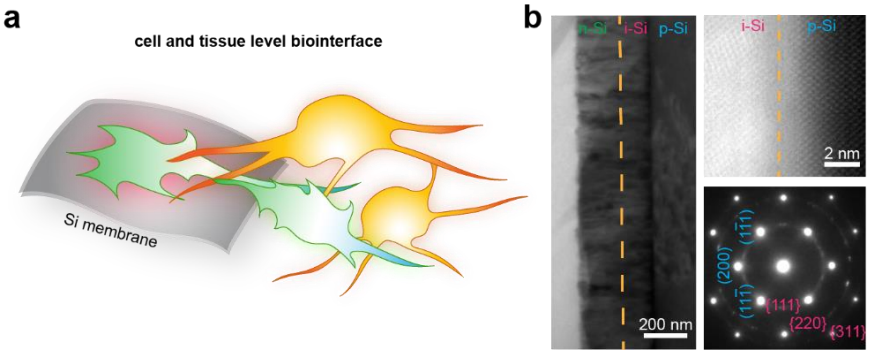

Figure 3-5. A multilayered Si membrane for cell- and tissue-level biointerface. a, Multilayered Si membranes are chosen after **Selection I** to form tight interfaces with cells and tissues. **b,** A multilayered *p*-*i*-*n* Si heterojunction made by a CVD synthesis of intrinsic (magenta) and *n*-type (green) Si layers onto a *p*-type (cyan) Si SOI substrate. A cross-sectional TEM image (left) shows the columnar structures of the intrinsic and *n*-type layers. A low-angle annular dark

Figure 3-5, continued. field scanning TEM (LAADF STEM) image (upper right) and a SAED (zone axis B = [011], lower right) pattern taken at the *p*-type (cyan)/intrinsic (magenta) interface both highlight the single crystalline *p*-type layer (isolated spots (blue) from SAED, periodic atomic columns from STEM) and the nanocrystalline intrinsic layer (concentric rings (magenta) from SAED, small crystal domains from STEM). A sharp and oxide free interface is evident from the STEM image with a junction width of < 1 nm. Orange dashed lines mark the intrinsic/*n*-type (left) and the *p*-type/intrinsic (upper right) interfaces.

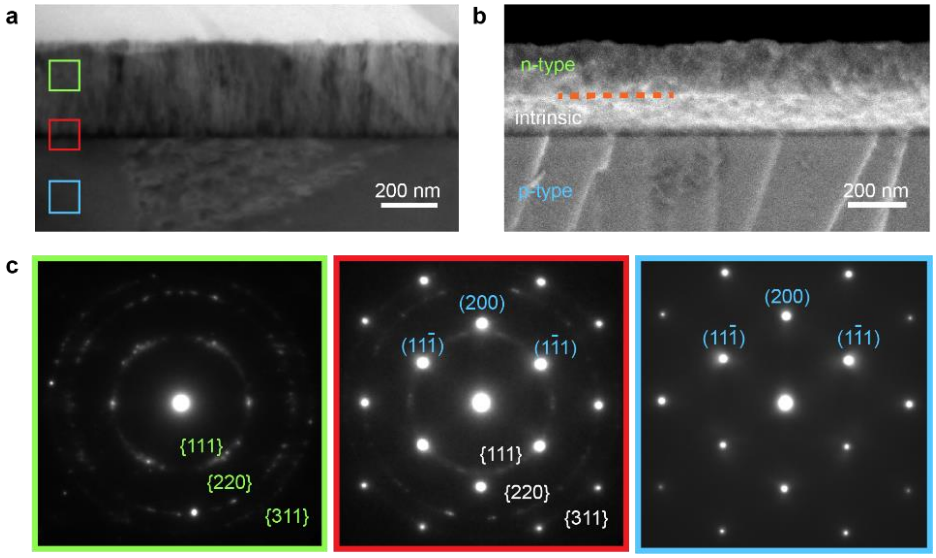

Figure 3-6. Cross-sectional views of the *p-i-n* Si heterojunction. a, A TEM image showing the columnar structure of the intrinsic and *n*-type layers grown on the *p*-type substrate. Colored boxes (green, *n*-type Si; red, *p*-type/intrinsic interface; blue, *p*-type Si) denote the regions for SAED in **c**. **b,** A SEM image showing the thicknesses of both the intrinsic (white) and *n*-type layers (green). The sample was prepared by the etching of a *p-i-n* heterojunction in a 20% (w/v) potassium hydroxide (KOH) aqueous solution at 60 ^{o}C for 10 s. The orange dashed line highlights the intrinsic/*n*-type interface. **c,** SAED patterns taken from the [011] zone axis showing the transition of crystallinity from the [100]-oriented single crystalline *p*-type substrate (isolated spots with blue labels) to the nanocrystalline intrinsic (concentric rings with white labels) and *n*-type (concentric rings with green labels) layers with grain boundaries roughly aligned with the [100] direction.

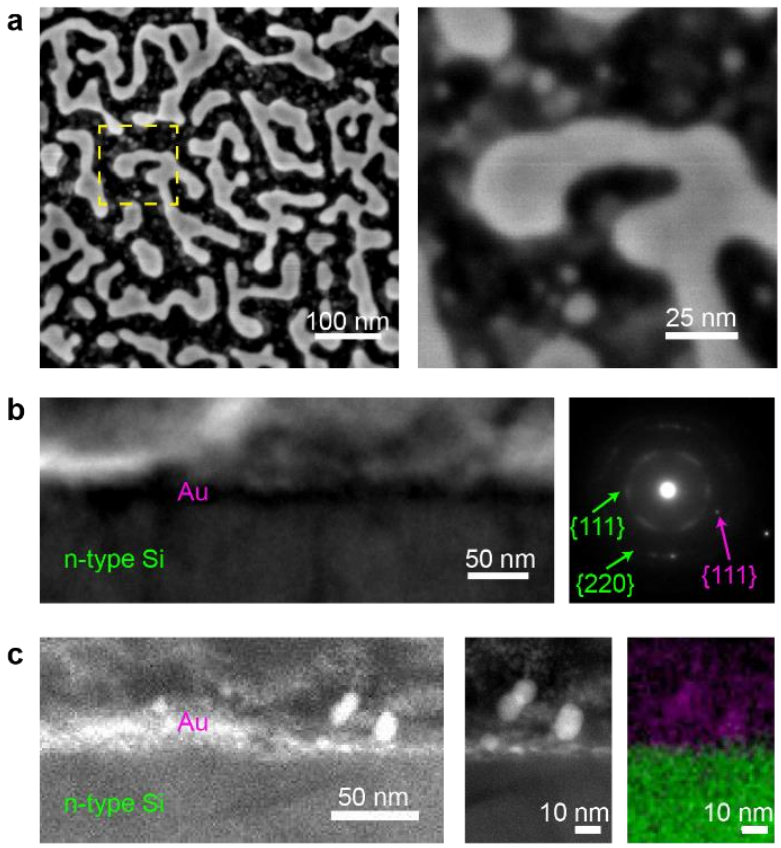

Figure 3-7. Structural characterizations of the gold-decorated *p-i-n* heterojunction. a, Top-view SEM images showing the interconnected meshes made of gold. The yellow box in the left image highlights the region for a zoom-in view (right), and shows the coexistence of small nanoparticles together with the large meshes. **b,** A cross-sectional bright field TEM image (left) taken at the Au-Si interface where Au appears to be dark. A SAED pattern (right) shows the diffraction features from both Si and Au. **c,** A high-angle annular dark field (HAADF) STEM image (left) taken at the Au-Si interface where Au has a higher contrast than Si. A zoom-in view (middle) and its corresponding XEDS map (right, purple, Au M series; green, Si K series) highlights the sharp interface. The existence of small Au nanoparticles right at the interface allows potential charge transfer pathways between Si and Au to promote the photoelectric responses.

To enable intracellular biointerfaces, we chose Si nanowires as recent studies showed that they can be internalized into mammalian cells through phagocytosis[25] and, when inside, form active interfaces with cytoskeletal systems[14]. Additionally, to promote light absorption from single nanowire structures[26], we deposited nanocrystalline Si shells over a thin, vapor-liquid-solid (VLS)

grown Si nanowire backbone (~ 50 nm in diameter) (**Fig. 3-8b**, left and upper right). Cross-sectional and side-view TEM images reveal that > 95% of the total volume is nanocrystalline (**Fig. 3-8b**, lower right).

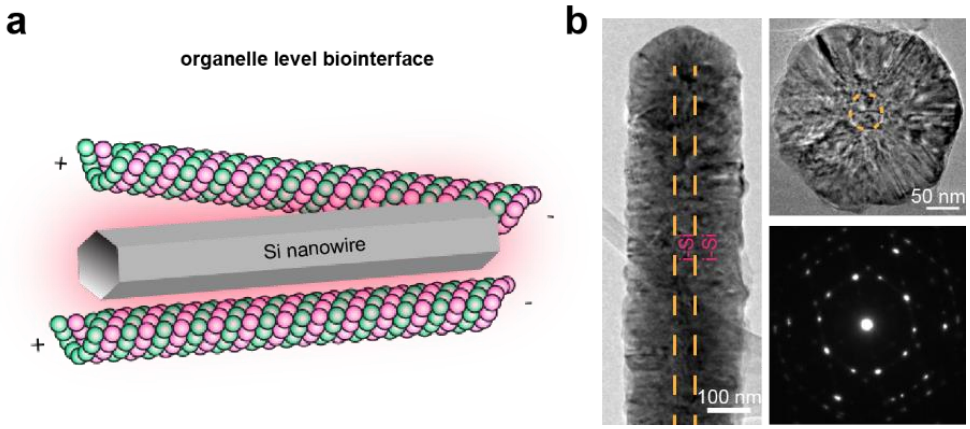

Figure 3-8. A Si nanowire for organelle-level biointerface. a, Coaxial Si nanowires are chosen after **Selection I** to form tight interfaces with organelles. **b,** An intrinsic-intrinsic coaxial Si nanowire is synthesized from the deposition of a thick shell over a thin VLS-grown nanowire backbone as shown in a side-view TEM image (left). A cross-sectional TEM image (upper right) shows diameters of ~ 50 nm and ~ 270 nm for the core and shell, respectively. A corresponding SAED pattern (lower right) confirms the nanocrystalline structure. Orange dashed lines highlight the core/shell boundaries.

3.2.3 Selection II for material functions

Given that cellular physiology can be altered with a ~ pA level ionic current, we next utilized a high-precision electrochemical tool, *i.e.*, a patch-clamp setup, to investigate the light-induced and biointerface-relevant physicochemical processes (**Fig. 3-1**, **Selection II**) that originated from the freestanding Si surfaces[27]. Briefly, we immersed different types of Si materials (*e.g.*, dopant-modulated, surface-treated and size-tuned nano-membranes, and nanocrystalline nanowires, as selected from the first step) into a phosphate-buffered saline solution, and positioned glass micropipette electrodes in close proximity to the Si surfaces (~ 2 μm) where ionic flows

across the pipette tips were measured in the voltage-clamp mode (**Fig. 3-9**, upper). Specifically, we delivered light pulses (530 nm light-emitting diode (LED) or 532 nm laser, 10 ms) through a microscope objective to illuminate Si and recorded the ionic current dynamics under different pipette holding potentials (**Fig. 3-9**, lower).

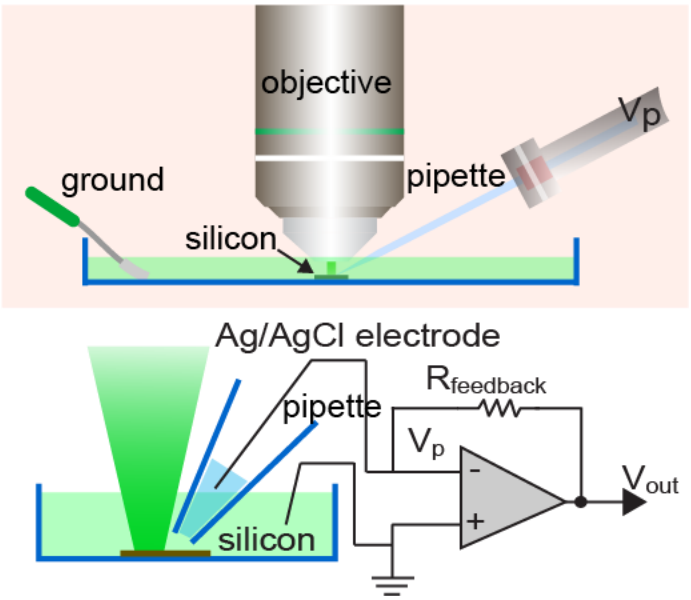

Figure 3-9. Schematic diagrams illustrating the experimental setup for the photo-response measurements from Si structures. Light pulses (530 nm LED or 532 nm laser) are delivered through a water-immersion objective to the Si submerged in a PBS solution. Light-induced currents are recorded at different pipette command potentials (V_p) using a voltage-clamp mode, from which capacitive, faradaic and thermal components can be either directly measured or derived by mathematic fitting.

Using pulsed light illuminations, we developed a universal analysis and unambiguously identified and mostly importantly, decoupled two explicit and one implicit element of the photo-responses.

3.2.4 Analysis of the photo-response measurements.

In a typical photo-response measurement, a glass micropipette, with the potential holding at a fixed level (V_p), was positioned near a Si material surface immersed in PBS, and a 10-ms long

light pulse was delivered to the material in the middle of the trial (**Fig. 3-10**). Therefore, the recorded current across the pipette tip can be divided into two parts, namely the baseline current I_0 at the dark stage and the time-dependent light-generated current $\Delta I_{light}(t)$ at the light stage. During the light illumination period, two parallel processes originated from the Si material can contribute to $\Delta I_{light}(t)$.

The first one is the photoelectric process where the light-generated excessive carriers will accumulate on the Si surface and change the local surface potential. Ions in the nearby medium will be attracted/repelled with respect to this photo-generated potential and create the ionic currents. Since the variation of the surface potential is only a function of the carrier dynamics on the Si surface, the photoelectrically-induced ionic current ($\Delta I_{electric}(t)$) is therefore independent of the holding current level I_0.

Another process is related to the photothermal effect of Si where the recombination of light-generated carriers converts part of the input photon energy into the vibrational energy of the Si lattice, which dissipates heat through both Si and the surrounding electrolyte. For the electrolyte with an elevated temperature, mobilities of the ions will increase, resulting in a reduced pipette tip resistance R. Even under a fixed holding potential V_p, the current during the light illumination period will change due to the decrease of the pipette resistance. Therefore, the thermally-induced current ($\Delta I_{thermal}(t)$), is strongly related to the holding potential V_p and the baseline current I_0 , where $V_p = I_0 \times R_0$, R_0 is the pipette resistance in dark.

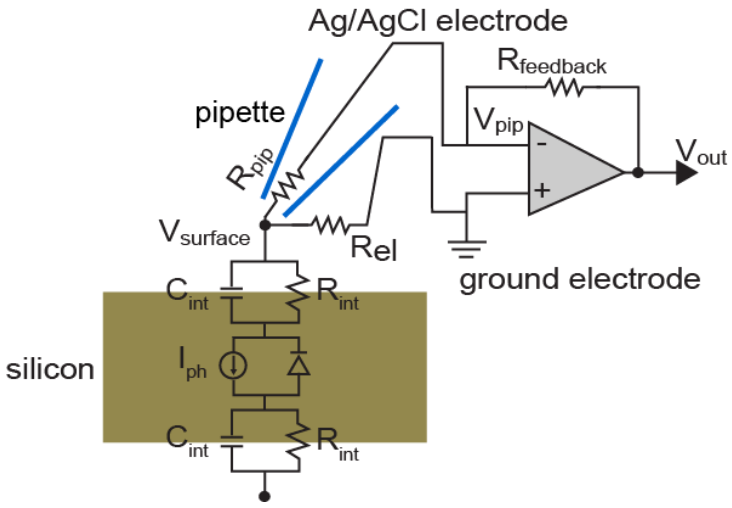

Figure 3-10. A schematic diagram illustrating the equivalent circuit for the photo-response measurements from Si structures.

Given the significantly different dependences on the holding current I_0 for the electrically-($\Delta I_{electric}(t)$) and thermally-induced currents ($\Delta I_{thermal}(t)$), the total light-generated currents ($\Delta I_{light}(t)$ = $\Delta I_{electric}(t)$ + $\Delta I_{thermal}(t)$) can be potentially decoupled by analyzing current traces recorded at different holding levels.

At a given time point t during the light illumination period, the recorded current, I_0+ $\Delta I_{light}(t)$, excluding the photoelectrically-induced current part $\Delta I_{electric}(t)$, and the pipette tip resistance $R(t)$ follow the Ohm's law as long as the holding potential V_p is fixed.

$$V_p = I_0 \times R_0 = \left(I_0 + \Delta I_{light}(t) - \Delta I_{electric}(t) \right) \times R(t) . \qquad (3\text{-}1)$$

Rearranging Eq. 3-1 gives the relationship between the light-induced current $\Delta I_{light}(t)$ and the holding current I_0 that

$$\Delta I_{light}(t) = \left(\frac{R_0}{R(t)} - 1 \right) \times I_0 + \Delta I_{electric}(t) . \qquad (3\text{-}2)$$

As shown in Eq. 3-2, the photoelectric effect is explicitly manifested as the intercept of the curve. A photocurrent plot can be generated by plotting the fitted intercept values over time as shown in **Fig. 3-11**. Two types of photoelectric responses, *i.e.*, capacitive and Faradaic, are further identified based on the dynamics and the amplitude of the currents. Two spiky features at the onset and offset of the light illumination are capacitive currents corresponding to the capacitive charging/discharging processes at the Si/electrolyte interface. A long-lasting current with a lower amplitude is the Faradaic current due to the surface redox reactions.

The photothermal effect, on the other hand, is implicitly embedded in the fitted slope as the pipette resistance is a function of temperature. To calculate the photothermally-induced temperature change of the surrounding medium, a calibration curve of the pipette resistance over temperature is needed, which typically follows an Arrhenius-type relationship[54] that

$$\ln R = a \times \frac{1}{T} + c\,, \tag{3-3}$$

where a and c represent the slope and intercept values.

In conjunction with the slope $k(t)$ from the $\Delta I_{light}(t)$ - I_0 plot that

$$R(t) = \frac{R_0}{k(t)+1}\,, \tag{3-4}$$

the final temperature of the surround medium heated from the photothermal effect is determined only by the slopes of the $\Delta I_{light}(t)$ - I_0 and the $\ln R$ - $1/T$ curves that

$$T(t) = \frac{1}{\frac{1}{T_0} - \frac{1}{a}\ln(k(t)+1)}\,. \tag{3-5}$$

Notably, since the photothermal effect is a function of the illumination duration, the slope of the $\Delta I_{light}(t)$ - I_0 plot is also time dependent. The maximal temperature is reached after 10 ms of illumination so $\Delta I_{light,10\ ms}$ - I_0 plots were used to assess the photothermal responses of various Si materials. A temperature over time curve can also be generated using the fitted slope values from each time point as shown in **Fig. 3-11**.

In summary, the $\Delta I_{light,10\ ms}$ - I_0 plot method can be applied to virtually all kinds of materials other than just Si to assess their photo-responses, which will fall into the following four categories.

1) In one extreme case where the material has only the photothermal effect without any photoelectric effect, *i.e.,* $\Delta I_{electric} = 0$ at all time, Eq. 3-2 will be reduced to

$$\Delta I_{light,10\ ms} = \left(\frac{R_0}{R_{10\ ms}} - 1 \right) \times I_0 . \qquad (3\text{-}6)$$

The $\Delta I_{light,10\ ms}$ - I_0 plot will be a slanted line with a zero intercept.

2) In another extreme scenario where the material has only the photoelectric effect without any photothermal effect, *i.e.,* $R_0 = R_{10\ ms}$, Eq. 3-2 can be written as

$$\Delta I_{light,10\ ms} = \Delta I_{electric,10\ ms} . \qquad (3\text{-}7)$$

The $\Delta I_{light,10\ ms}$ - I_0 plot will be a horizontal line with a non-zero intercept.

3) If a material does not have any photo-responses, Eq. 3-2 will be

$$\Delta I_{light,10\ ms} = 0 . \qquad (3\text{-}8)$$

The $\Delta I_{light,10\ ms}$ - I_0 plot will be a horizontal line with a zero intercept.

4) In any intermediate situations where both the photoelectric and the photothermal effects coexist, the original form of Eq. 3-2 applies that

$$\Delta I_{\text{light,10 ms}} = \left(\frac{R_0}{R_{\text{10 ms}}} - 1 \right) \times I_0 + \Delta I_{\text{electric,10 ms}} . \quad (3\text{-}9)$$

The $\Delta I_{\text{light,10 ms}}$ - I_0 plot will be a slanted line with a non-zero intercept.

In a representative trial from an Au nanomesh-decorated *p*-*i*-*n* Si membrane (**Fig. 3-11**, upper), we first noticed two 'spiky' features under a LED light pulse (~ 12.05 mW, ~ 500 μm spot size) with a power density of ~ 6 W/cm^2. The upward (~ 86 nA, with a transient peak current density at the pipette tip of ~ 2700 mA/cm^2) and downward (~ -34 nA, transient current density of ~ 1100 mA/cm^2) components correspond to capacitive charging/discharging processes at the Si/electrolyte interface. The second photo-response element is manifested as a long-lasting current with a lower amplitude (*e.g.*, ~ 2 nA for the same Au-decorated Si membrane) (**Fig. 3-11**, upper inset), which is indicative of a Faradaic current leading to redox reactions. Metal-free *p*-*i*-*n* Si membranes only display symmetrical capacitive current spikes, with negligible Faradaic components detected from the local patch-clamp electrode. The last photo-response element is implicit and it corresponds to the local temperature elevation of the solution due to the photothermal effect from Si. In this scenario, the recombination of carriers converts part of the input photon energy into the vibrational energy of the Si lattice, which dissipates heat through both Si and the surrounding electrolyte. Because the glass micropipette resistance is temperature-dependent, we determined the thermal dynamics by fitting the recorded patch-clamp currents at various holding potentials. For example, we recorded a ~ 5.4 K peak temperature rise from a nanocrystalline Si nanowire upon laser illumination (~ 47.1 mW, ~ 5 μm spot size) at ~ 240 kW/cm^2 for 10 ms (**Fig. 3-11**, lower).

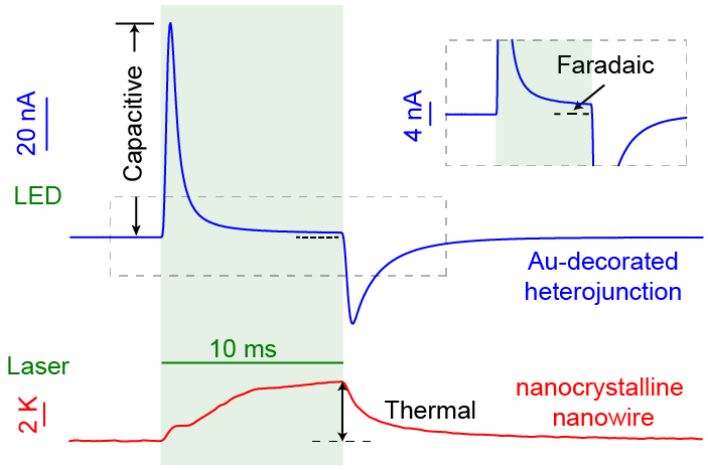

Figure 3-11. Representative Si photo-responses. Recorded data from an Au-decorated *p-i-n* Si heterojunction (top, from 1 mM $HAuCl_4$, LED illumination, ~ 12.05 mW, ~ 500 μm spot size, ~ 6 W/cm^2) and an *i-i* nanocrystalline nanowire (bottom, laser illumination, 47.1 mW, ~ 5 μm spot size, ~ 240 kW/cm^2) showing three major types of the responses, *i.e.,* capacitive (upper), Faradaic (upper inset), and thermal (lower). LED-induced capacitive and Faradaic currents are pronounced in the Au-decorated heterojunction. The capacitive current is defined as the maximal current amplitude reached after the light onset while the Faradaic current is defined as the current amplitude at the time point of 8.5 ms since illumination starts. The nanocrystalline nanowire generate significant heating of the surrounding PBS via its photothermal effect under laser illumination. Green shaded areas highlight the light illumination periods. The grey dashed box marks the region for the inset. Measurements from control surfaces without Si materials showed no photo-responses.

To build quantitative matrices for these three photo-response elements, we screened a library of Si-based materials to evaluate the impact of doping, surface chemistry and size (**Table 3-1)**. We extracted the capacitive, Faradaic, and thermal components from the patch-clamp recordings of 16 representative Si samples (**Table 3-1**), and projected them onto three axes to decouple any individual contributions (**Fig. 3-12**).

Light source	Si material	Capacitive (pA)	Faradaic (pA)	Thermal (K)
LED	p-type	49.8	14.6	0.0
	p-i-n	7388.4	6.5	0.0
	0.01mM $HAuCl_4$	9525.4	45.2	0.1
	0.1mM $HAuCl_4$	43305.0	1038.7	0.0
	1mM $HAuCl_4$	85774.5	2114.4	0.0
	0.01mM K_2PtCl_4	6193.1	89.5	0.0
	0.1mM K_2PtCl_4	11784.0	242.9	0.0
	1mM K_2PtCl_4	10935.0	93.1	0.0
	0.01mM $AgNO_3$	6887.7	30.3	0.1
	0.1mM $AgNO_3$	10531.9	193.4	0.0
	1mM $AgNO_3$	6505.4	81.7	0.0
Laser	p-i-n bulk	4376.4	26.0	0.0
	p-i-n 500 μm	484.8	0.7	0.6
	p-i-n 100 μm	65.5	2.6	1.1
	p-i-n 20 μm	30.0	6.9	2.8
	i-i nanowire	14.3	1.9	5.4

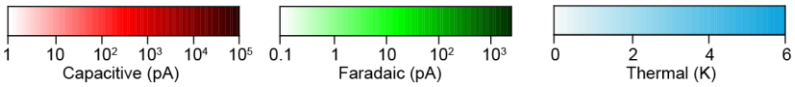

Table 3-1. A summary of individual photo-responses from 16 selected Si structures. A *p-i-n* heterojunction promotes the capacitive current (Red) over a uniformly doped *p*-type Si. Metal decorations on the heterojunction further enhance the capacitive current (Red), and more importantly, increase the proportion of Faradaic component (Green). Laser illumination on Si materials with smaller dimensions yields stronger photothermal responses (Blue). The LED illumination condition: ~ 12.05 mW, ~ 500 μm spot size, ~ 6 W/cm^2; the laser illumination condition: ~ 47.1 mW, ~ 5 μm spot size, ~ 240 kW/cm^2. Pipette-Si distance ~ 2 μm.

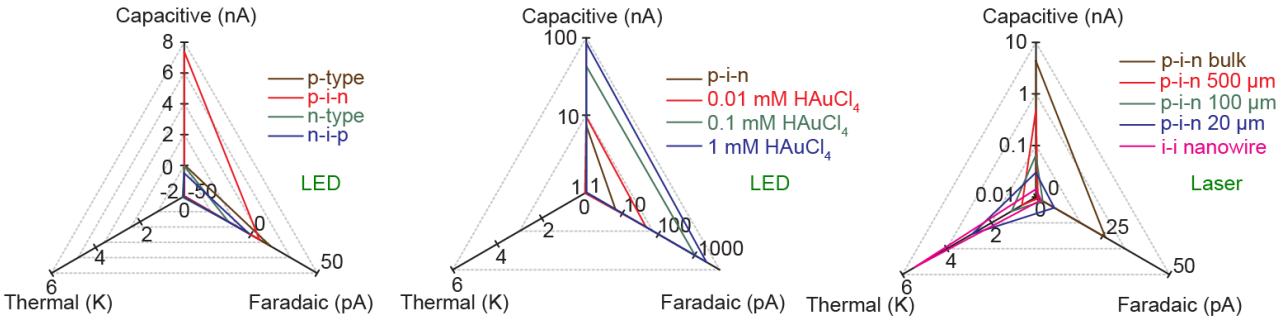

Figure 3-12. Quantitative matrices of the three photo-responses. The impact of important materials parameters, *e.g.*, doping (left), surface chemistry (middle), and size (right) were evaluated. Heterojunctions (left, *p-i-n* and *n-i-p*) show significantly enhanced capacitive currents versus uniformly doped SOI substrates (*p*-type and *n*-type). Au-decorated *p-i-n* heterojunctions (middle) promote both capacitive and Faradaic currents. Si structures with smaller dimensions (right) show stronger photothermal responses.

We first considered the simplest single-crystalline *p*-type Si SOI substrate (device layer thickness: ~ 2 μm). A typical experiment (LED illumination, ~ 12.05 mW, ~ 500 μm spot size, ~ 6 W/cm^2) shows a small capacitive current of ~ 50 pA, and a transient peak current density of ~ 1.6 mA/cm^2 at the pipette tip. However, upon deposition of the intrinsic and *n*-type layers (*i.e.*, forming a *p*-*i*-*n* heterojunction), the recorded capacitive current and transient peak current density were boosted to ~ 7400 pA and ~ 235 mA/cm^2, respectively (**Fig. 3-13**). This significant enhancement in the capacitive component is likely due to the enhanced light absorption from the nanocrystalline layers and more efficient charge separation by the built-in electric fields across the *p*-*i*-*n* diode junction. The polarity of the capacitive currents (*i.e.*, upward at the onset of light illumination; downward at offset) in both cases stays cathodic, although the dopant types of the electrolyte-interfacing layers are different (*p*- in *p*-type SOI device layer, and *n*- in *p*-*i*-*n* multilayers). This suggests that the primary light-generated carriers accumulated on the Si surfaces are electrons, which are the minority carriers in *p*-type SOI and the majority carriers in the *p*-*i*-*n* samples, respectively. With a reversed doping sequence, both *n*-type SOI substrate (~ - 48 pA) and the corresponding *n*-*i*-*p* (~ - 510 pA) heterojunction display the opposite capacitive current polarity, as expected. In these metal-free samples, the Faradaic and thermal components are negligible *e.g.*, ~ 7 pA and ~ 0 K as peak values for *p*-*i*-*n* multilayered sample (under ~ 6 W/cm^2 LED illumination). Overall, the dominant photo-response element in metal-free Si membranes is the capacitive current.

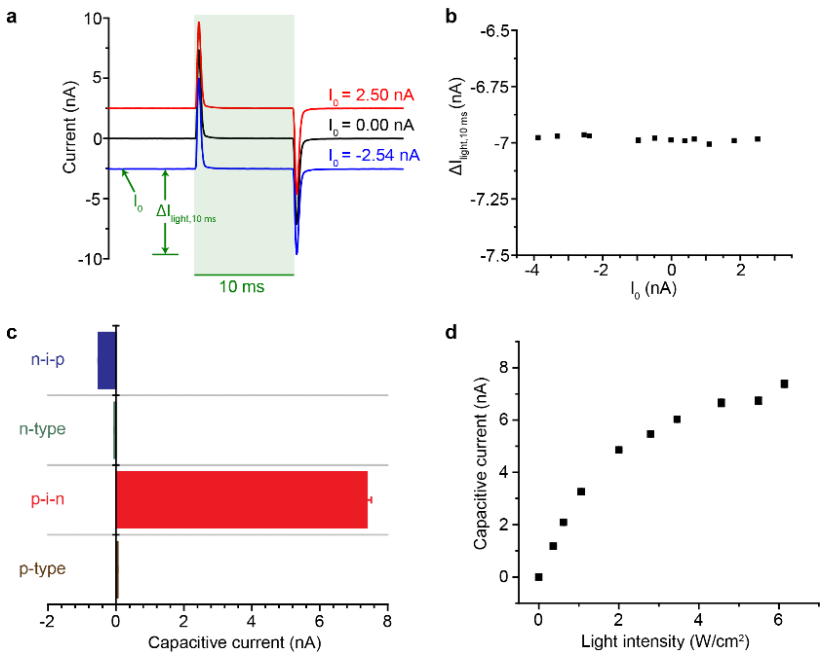

Figure 3-13. Photo-responses of dopant modulated Si structures. a, Representative current traces recorded from a *p*-*i*-*n* heterojunction under LED pulses (530 nm, 10 ms, ~ 12.05 mW, ~ 500 μm spot size, ~ 6 W/cm^2), showing strong capacitive currents and minimal Faradaic currents. I_0 is defined as the baseline holding level before the light illumination. $\Delta I_{\text{light,10 ms}}$ is defined as the maximal relative current amplitude after 10 ms of light illumination with respect to I_0. The light green shaded area marks the light illumination period. **b,** The $\Delta I_{\text{light,10 ms}}$ - I_0 plot shows a negligible slope and a prominent intercept indicating strong photoelectric and weak photothermal responses. **c,** Statistical analyses of capacitive currents from different types of Si structures highlight the importance of dopant modulations. Both *p*-*i*-*n* and *n*-*i*-*p* heterojunctions show significantly enhanced capacitive currents comparing to uniformly doped *p*-type and *n*-type Si. The polarities of the capacitive currents are opposite for Si with reversed doping profiles. Error bars denote standard deviations. **d,** The amplitude for the capacitive current of a *p*-*i*-*n* heterojunction can be monotonically tuned by the light intensity. Error bars denote standard deviations.

As shown in the Au nanomesh-decorated *p*-*i*-*n* Si membrane, the Faradaic current can reach ~ 2 nA (**Fig. 3-11**, upper inset), suggesting a means of charge injection into the solution. We next explored multiple metals (*e.g.*, Au, Ag, and Pt) by electroless deposition of nanoparticles/nanomeshes onto *p*-*i*-*n* Si surfaces (**Fig. 3-14**). In all experiments, the introduction of metal species promoted both the capacitive and the Faradaic elements (**Figs. 3-15, 3-16**), with

high stabilities over 1000 repetitive illuminations (**Fig. 3-17**), likely due to the fact that certain metals can more efficiently collect and solution-inject the photo-generated carriers (as opposed to carrier recombination in bulk Si). Thicker layers of metal, however, block light absorption by the buried Si layers, leading to reduced capacitive and Faradaic output (**Fig. 3-16**). Among all the conditions tested, Au nanomesh prepared by immersion of the *p-i-n* multilayered membrane in a 1 mM $HAuCl_4$ solution yielded the highest capacitive (~ 86 nA) and Faradaic (~ 2 nA) currents. The thermal components under ~ 6 W/cm^2 LED illumination were negligible in all metal-decorated Si membranes.

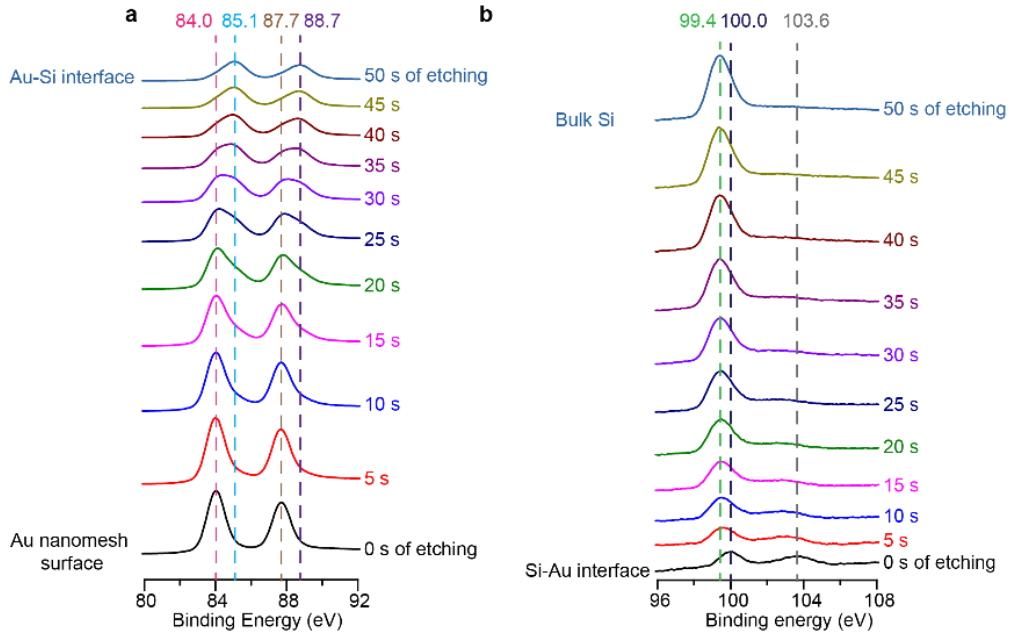

Figure 3-14. XPS depth profiles suggest the formation of Au-Si bonds at the interface. a, XPS spectra of Au taken at different depths from the surface of Au nanomeshes to the interface between Au and Si. Controlled Ar plasma etchings were employed to provide the depth profiles. The shift of binding energy peaks from metallic Au (84.0 eV of 4*f* 7/2 and 87.7 eV of 4*f* 5/2) to intermetallic Au (85.1 eV of 4*f* 7/2 and 88.7 eV of 4*f* 5/2) indicates the existence of Au-Si compound at the interface. **b,** XPS spectra of Si taken at different depths from the interface between Au and Si to the bulk Si. The facts that the Si^{4+} 2*p* peak at 103.6 eV diminishes and the Si^0 2*p* peak shifts from 100 eV to 99.4 eV as Si is being etched both suggest the existence of oxidized form of Si at the Au-Si interface.

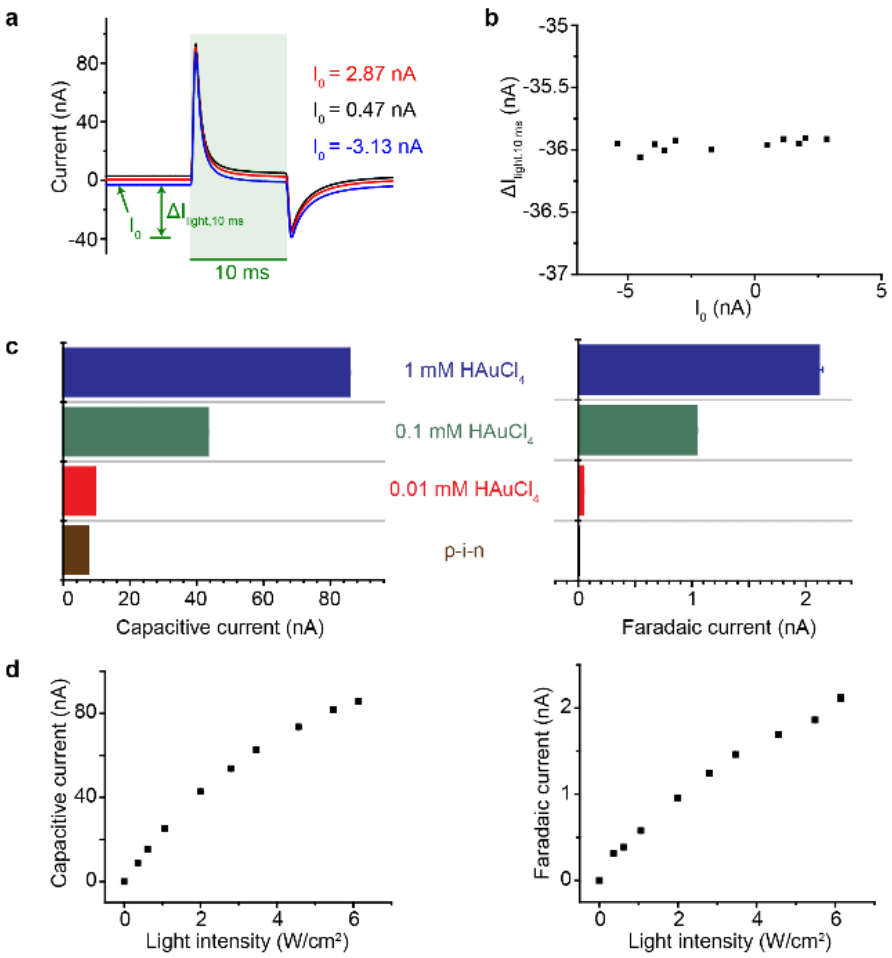

Figure 3-15. Photo-responses of Au-decorated Si structures. a, Representative current traces recorded from an Au-decorated *p-i-n* heterojunction (from 1 mM $HAuCl_4$) under LED pulsed illuminations (530 nm, 10 ms, ~ 12.05 mW, ~ 500 μm spot size, ~ 6 W/cm^2) show strong capacitive and Faradaic currents. I_0 is defined as the baseline holding level before the light illumination. $\Delta I_{\text{light,10 ms}}$ is defined as the maximal relative current amplitude after 10 ms of light illumination with respect to I_0. The light green shaded area marks the light illumination period. **b,** The $\Delta I_{\text{light,10 ms}}$ - I_0 plot shows a negligible slope and a prominent intercept indicating strong photoelectric and weak photothermal responses, similar to that from a pristine *p-i-n* heterojunction. **c,** Statistical analyses of capacitive (left) and Faradaic currents (right) from *p-i-n* Si heterojunctions with surface Au decorations show that the maximum values of both currents are achieved with Au deposited from 1 mM $HAuCl_4$. Error bars denote standard deviations. **d,** The amplitudes for both the capacitive (left) and Faradaic currents (right) of an Au-decorated *p-i-n* heterojunction can be monotonically tuned by the light intensity. Error bars denote standard deviations.

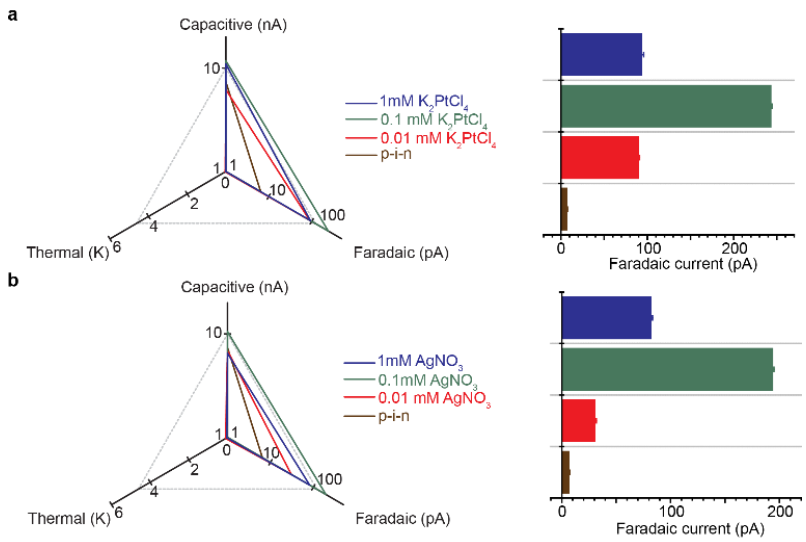

Figure 3-16. Metal-enabled promotions of photocurrents in *p-i-n* heterojunctions are general. Both Pt (**a**) and Ag (**b**) can be deposited to enhance the photoelectric responses of the *p-i-n* heterojunction. Maximal Faradaic currents are reached using 0.1 mM of K_2PtCl_4 or $AgNO_3$ although the enhancements enabled by Pt and Ag are not as pronounced comparing to Au. 1 mM of metal-containing solutions lead to thicker metal coatings and retard the photocurrents by blocking the light being absorbed by the buried Si. Error bars denote standard deviations.

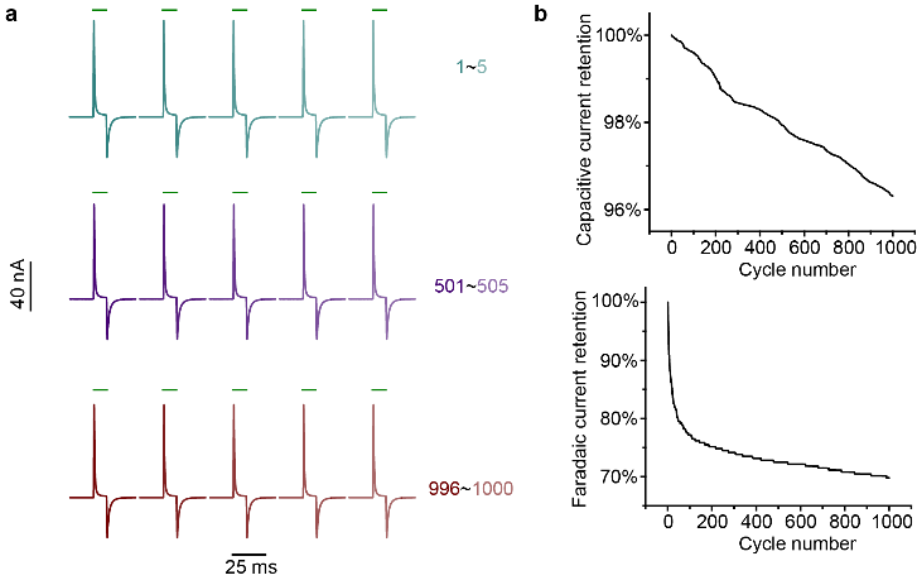

Figure 3-17. Photoelectric responses of Au-decorated heterojunctions possess high stabilities. a, A cyclability test of the same Au-decorated heterojunction from 1 mM $HAuCl_4$ with 1000 times of repetitive illuminations (530 nm, 10 ms, ~ 12.05 mW, ~ 500 μm spot size, ~ 6 W/cm^2) at a frequency of 2 Hz. Current traces between cycle number 1

Figure 3-17, continued. and 5 (green), 501 and 505 (purple), and 996-1000 (brown) are plotted. Green bars denote the 10-ms light illumination periods. **b,** Both the capacitive and Faradaic currents show high retentions after 1000 cycles. Notably, the capacitive current has an even higher cyclability (~ 96% retention) versus the Faradaic current (~ 70% retention), likely benefited from the reversible capacitive charging/discharging processes as oppose to the irreversible surface electrochemical reactions.

Since single cell or subcellular studies require highly localized interrogation, we measured the laser-induced (~ 47.1 mW, ~ 5 μm spot size, ~ 240 kW/cm^2) photo-responses of Si materials with variable lateral dimensions. We observed decreased electrical/enhanced thermal elements with reduced sizes of *p-i-n* Si membranes (**Fig. 3-18**). In the case of intrinsic nanocrystalline Si nanowire, the nano-confinement effect led to the highest photothermal response (~ 5.4 K peak temperature change) with negligible capacitive and Faradaic components.

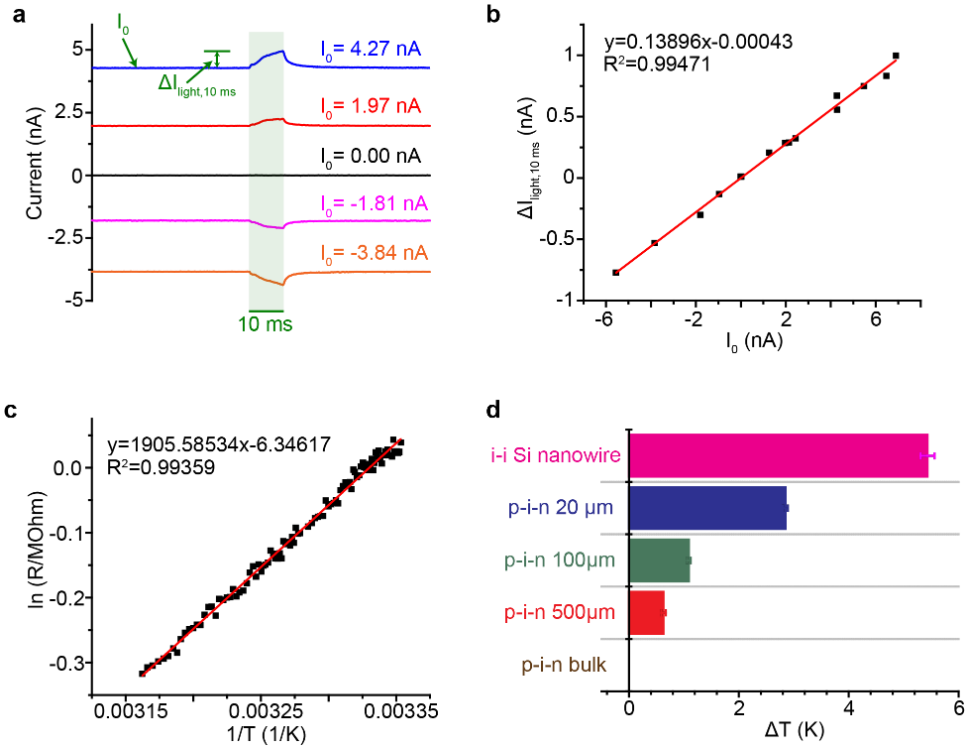

Figure 3-18. Photo-responses of Si structures with different sizes. a, Representative current traces recorded from an *i-i* nanocrystalline Si nanowire under laser pulses (532 nm, 10 ms, ~ 47.1 mW, ~ 5 μm spot size, ~ 240 kW/cm^2)

Figure 3-18, continued. exhibit a strong dependence on the baseline holding level I_0. $\Delta I_{\text{light,10 ms}}$ is defined as the maximal relative current amplitude after 10 ms of light illumination with respect to I_0. The light green shaded area marks the light illumination period. **b,** The $\Delta I_{\text{light,10 ms}}$ - I_0 plot shows a significant slope and a negligible intercept indicating strong photothermal and weak photoelectric responses. **c,** The pipette resistance over temperature curve calibrated from the same micropipette used for the photo-response measurements. The temperature increase of the PBS solution caused by the photothermal effect are calculated using both the $\Delta I_{\text{light,10 ms}}$ - I_0 plot and the *T*-*R* calibration curve. Briefly, the resistance of the pipette will decrease after 10 ms of illumination on the Si material due to the photothermal heating of the local PBS solution. The current amplitude during the light illumination will change accordingly following the Ohm's law. The relationship between the pipette resistances after 0 ms (R_0) and 10 ms ($R_{10\ \text{ms}}$) of illumination can then be linked by $R_{10\ \text{ms}}=R_0/(1+k)$, where k is the fitted slope value of the $\Delta I_{\text{light,10 ms}}$ - I_0. The temperature increase of the solution can then be inferred using the *T*-*R* calibration curve. **d,** Statistical analyses of the thermal responses of Si structures with different sizes show that the photothermal effect becomes more pronounced with the reduction of the Si dimension. *p*-*i*-*n* heterojunctions with different sizes were created by a combination of e-beam lithography and reactive ion etching processes. Error bars denote standard deviations.

3.2.5 Recommended materials and devices for multi-scale biointerfaces

Taken together, our physicochemical measurements highlight *p*-*i*-*n* heterojunction-enhanced capacitive currents, metal-enhanced capacitive and Faradaic currents, and nano-confinement-enabled thermal responses, all in freestanding configurations. For the present biointerface studies, most Si materials such as a simple *p-type* Si membrane or *p*-*i*-*n* Si multilayers with small lateral dimensions (< 500 μm), will not be considered given that their photo-response components are small (**Table 3-1**, with lower color intensity; **Fig. 3-1**, excluded materials from **Selection II**). We focused on the intrinsic nanocrystalline Si nanowires for intracellular and the related intercellular probing, and only used the photothermal effect. For single cell or small tissue level inter- and extracellular studies, we primarily explored a light-induced capacitive effect, *i.e.*, we used a *p*-*i*-*n* Si multilayered membrane where the biological invasiveness from capacitive

electrochemical currents are usually minimal[28]. Finally, given that the biological organization at the organ level is very complex, we used the Au nanomesh-coated Si heterojunctions for *in vivo* studies (**Fig. 3-19**, right). Therefore, the modulation therein would benefit most from an efficient combination of capacitate and Faradaic currents, a situation similar to where standard metal electrodes are used for the stimulation of brains or other body parts[28].

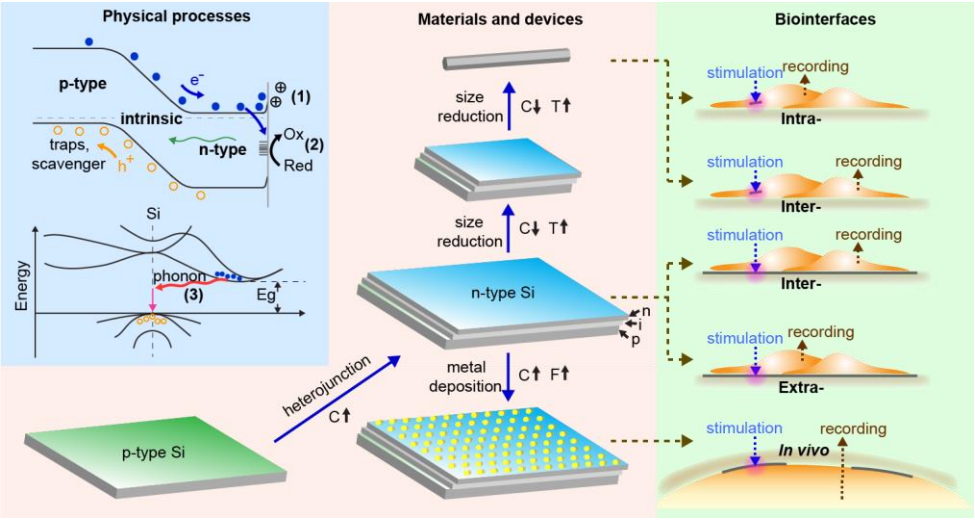

Figure 3-19. A principle for the construction of biointerface. The physical origins (light blue block), the material developing pathways (light orange block), and the projected biointerfaces (light green block) are highlighted. Fundamental processes include the accumulation of ions to balance light-generated excessive carriers near Si surface (**1**, capacitive, **C**), the metal-mediated redox reactions (**2**, Faradaic, **F**), and the thermalization through phonon emission (**3**, thermal, **T**). Considering the size and mechanics match at the biointerfaces, these Si structures can be utilized to form optically-controlled intra- (Si nanowires), inter- (Si nanowires and *p*-*i*-*n* heterojunctions), and extra-cellular (pristine and metal-decorated *p*-*i*-*n* heterojunctions) biointerfaces.

3.2.6 Organelle level biointerfaces

We first considered Si nanowires for intracellular stimulation biointerfaces because it is an unexplored domain that is beyond the previously studied intracellular sensing or delivery. In a primary culture of neonatal rat dorsal root ganglia (DRG) and associated satellite glia, we noticed

a cell-type-specific overlapping of nanocrystalline Si nanowires after ~ 24 hours of coculturing (**Fig. 3-20a**) Statistical analysis of the nanowire-cell colocalization revealed that ~ 87% of total nanowires overlapped with glial cells, ~ 3% with neurons, and ~ 10% stayed in the extracellular space (**Fig. 3-20b**). Perinucleus clustering, rather than random intracellular distributions, of the colocalized nanowires suggests the internalization of these nanowires[14,25]. Additionally, the presence of bent nanowires following the contours of a few glial cell membranes implies strong mechanical interactions between cells and nanowires[14]. As suggested by a recent study that label-free nanowires can be internalized through a phagocytosis pathway[25], the fact that glial cells (versus neurons) do have phagocytic activities supports the observed selective glial internalization[29].

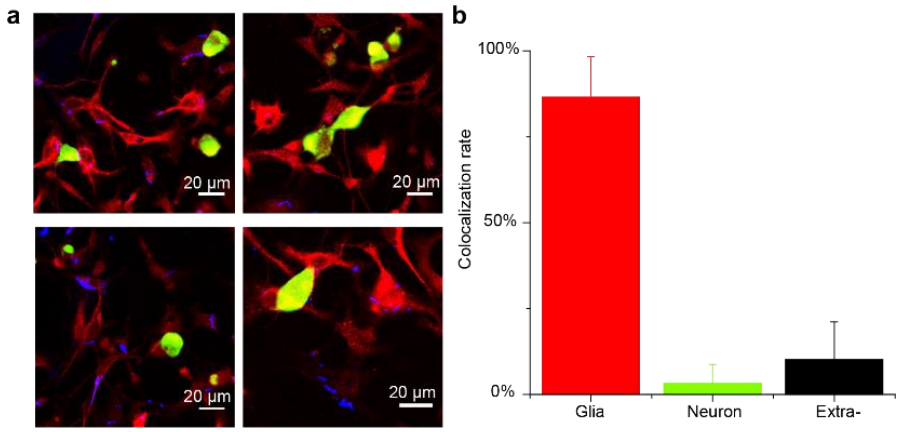

Figure 3-20. Nanocrystalline Si nanowires display cell-type specific overlapping with glial cells. a, Confocal microscope images of the DRG-glia system show that nanowires (blue) mostly overlap with glial cells (red) versus neurons (green). The fact that the overlapping nanowires exhibit alignment with cellular protrusions and perinucleus clustering rather than random intracellular distributions suggests that nanowires are internalized by the glial cells. **b**, Statistical analysis of the nanowire-cell colocalization rate reveals that ~ 87% of total nanowires overlap with glial cells, ~ 3% with neurons, and ~ 10% stay in the extracellular space. Error bars denote standard deviations.

As a result, we studied the control of glial activities with internalized nanocrystalline nanowires as the remotely-controlled stimulators. To this end, we illuminated an intracellularly-

bounded nanowire with a laser pulse (592 nm, ~ 14.4 mW, ~ 237 nm spot size, 1 ms) in the middle of a time-lapse calcium imaging series (**Fig. 3-21**). Upon light illumination, the glial cell of interest, with the nanowire inside, experiences a fast calcium concentration increase followed by a slow decay. Since the cell is being stimulated intracellularly, the observed calcium dynamics are likely related to the release of calcium from internal storage organelles, *e.g*., endoplasmic reticulum (ER) and mitochondria, rather than the calcium influx through ion channels at the plasma membrane, and therefore may be extended to other non-excitable cells (**Fig. 3-22**). As evidenced by the patch-clamp measurement, nanocrystalline nanowire exhibits a pronounced photothermal effect which results in a transient and localized temperature increase of surrounding cytosol and organelles following the laser pulse. This heating effect can either generate reactive oxygen species (ROS)[30] or transiently depolarize/perforate ER and mitochondrial membranes[31], all of which can trigger the release of calcium from its reservoir to the cytosol. Nevertheless, the same glial cell calcium dynamics can still be modulated repetitively (**Fig. 3-23**), indicating the minimal invasiveness of the intracellular stimulation method. Moreover, we not only observed the induced intracellular calcium flux from the glia under direct stimulation, but also the intercellular calcium wave propagation to both neighboring glia and DRG cells (**Fig. 3-21**). The selective uptake of nanowires by glia and the existence of glia-glia/glia-neuron communication suggest possible remote cellular modulations through naturally-occurring intercellular junctions.

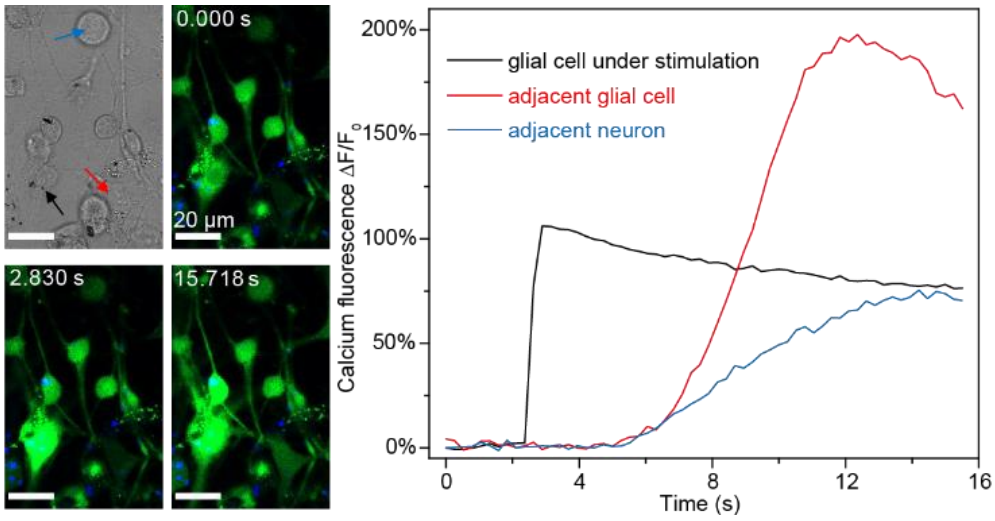

Figure 3-21. Si nanowire enables the intracellular stimulation of glial cells. Confocal microscope time series images (upper middle, lower left, and lower middle; green, calcium; blue, Si nanowires) show that a glial cell with an internalized nanowire can be optically stimulated to trigger intracellular calcium elevation and subsequent intercellular calcium wave propagations to both glial cells and neurons. A differential interference contrast (DIC) image (upper left) highlights the nanowire under stimulation (black arrow) and the morphologies of a neighboring glial cell (red arrow) and a neuron (blue arrow). The laser illumination (592 nm, ~ 14.4 mW) was on for 1 ms right before the time point of 2.830 s. Quantitative analysis of the fluorescence intensities over time (right) from three regions of interest show calcium dynamics in all cells (black, the glial cell being stimulated; red, a nearby glial cell; blue, a neighboring neuron).

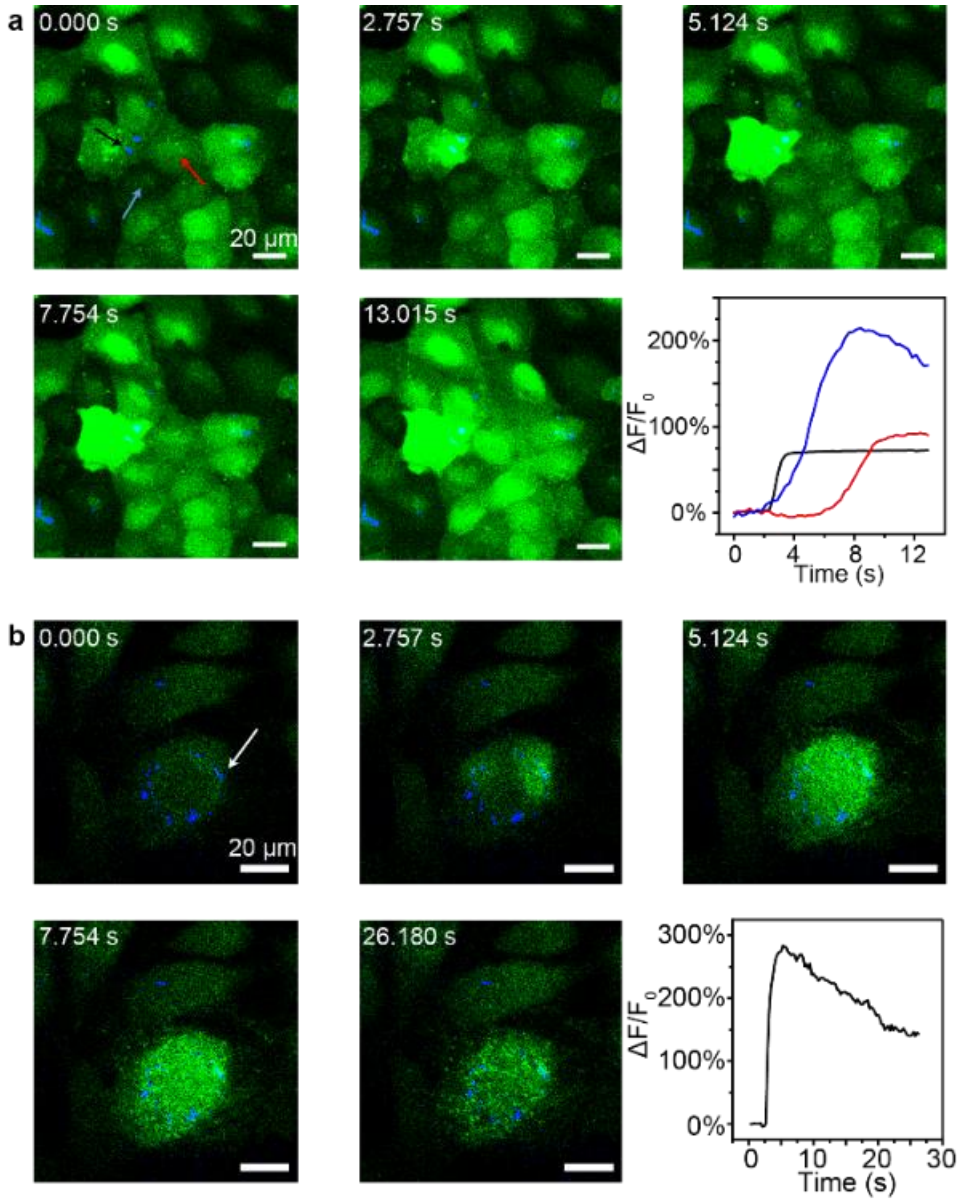

Figure 3-22. Intracellular stimulation can be extended to multiple cell lines. A cancer cell line, U2OS (**a**), and an endothelial cell line, HUVEC (**b**), can both be stimulated intracellularly to elicit the calcium dynamics. Since the intracellular stimulation of calcium largely utilizes the internal calcium storage organelles rather than ion channels on the plasma membranes, this modulation method is general to a broad range of mammalian cells. The stimulation laser (592 nm, ~ 14.4 mW, ~ 237 nm spot size) was on for 1 ms right before the time point of 2.757 s. Green, calcium; blue, Si nanowires. The black arrow marks the nanowire under stimulation, the blue and red arrows mark two adjacent cells of interest in **a**. The white arrow marks the nanowire under stimulation in **b**.

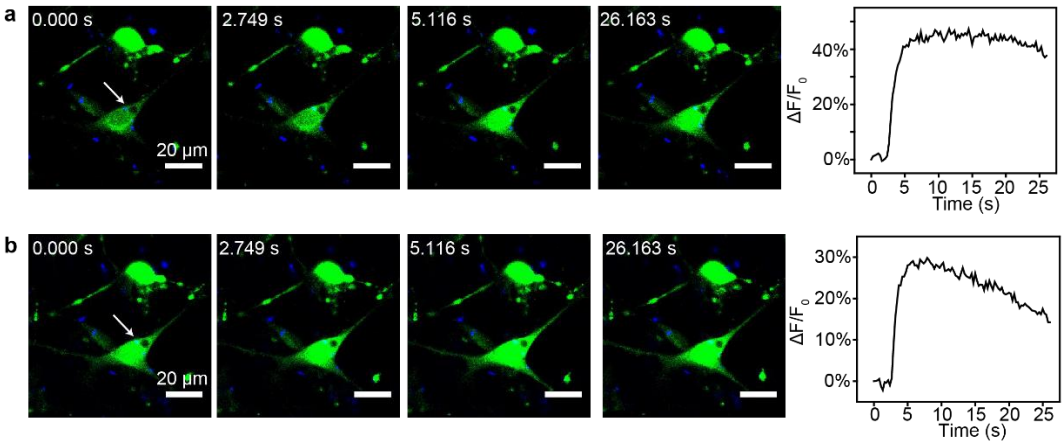

Figure 3-23. Intracellular stimulation of calcium is minimal invasive to cells. a and **b,** The same glial cell with internalized Si nanowires (green, calcium; blue, Si nanowires) is stimulated repetitively without being damaged. In the second time of stimulation (**b**), the intracellular calcium conentration can still increase even it is not at its base level. The stimulation laser (592 nm, ~ 14.4 mW, ~ 237 nm spot size) was on for 1 ms right before the time point of 2.749 s. White arrows mark the same nanowire under stimulation.

Since Si nanowires can also display active transport along microtubules[25], we next explored the possibility of using nanocrystalline Si nanowires as a dual-role intracellular biophysical tool, *i.e.*, a calcium modulator and a marker for motor protein-microtubule interactions. We simultaneously tracked the location of a single nanowire (*i.e.*, a transport marker) in a glial protrusion and monitored the nearby calcium dynamics, following a remote laser illumination of a different nanowire (*i.e.*, a calcium modulator) to initiate a calcium flux within a network (**Fig. 3-24**, first from left). The dynamics of local calcium concentration and the transverse distance of the nanowire, as well as the overlaid time series for both the calcium wave front and the nanowire center (**Fig. 3-24**, first from right), together suggest a calcium-triggered directional transport of intracellular cargo. Additionally, mean-squared displacement analysis reveals correlated nanowire transport modes with the local calcium dynamics, *i.e.*, from random or restricted diffusions (diffusivity coefficient $\alpha \leq 1$) without elevated intracellular calcium, to an active transport ($\alpha \sim 2$)

after the calcium wave front reached the original nanowire location (**Fig. 3-24**, first from right; **Fig. 3-25**). The nanowire transport along the glia protrusion is anterograde, *i.e.*, kinesin-based. The motor protein kinetics are typically enhanced by increased adenosine triphosphate (ATP) activities[32], which can be triggered by the elevation of intracellular calcium concentration[33,34]. Our results therefore support a mechanism where a cascade of calcium and ATP dynamics is involved for intracellular transport.

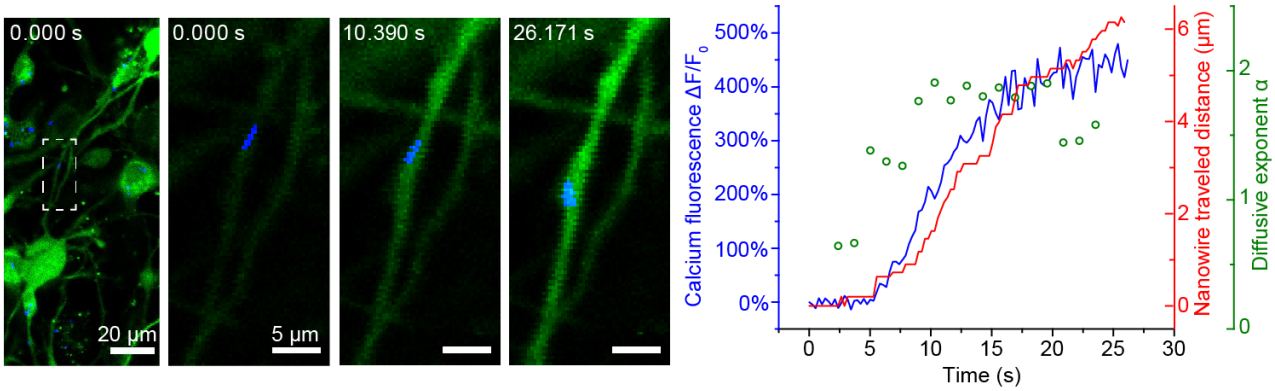

Figure 3-24. Si nanowires can serve as a dual-role intracellular biophysical tool. Both calcium modulator and marker for motor protein-microtubule interactions can be implemented by Si nanowires. The location of a nanowire (*i.e.*, a transport marker) in a glial protrusion is tracked while the nearby calcium dynamics is monitored simultaneously, following a remote laser illumination of a different nanowire (*i.e.*, a calcium modulator) to initiate a calcium flux within the network (green, calcium; blue, Si nanowires; first one from left). The white dashed box marks the region of interest for the transport study. Time series images (second one from left, middle one, second one from right) show a calcium-correlated motion of the Si nanowire. MSD analysis further reveals a mode shift of the nanowire motion from random or restricted diffusions (diffusivity coefficient $\alpha \leq 1$) to an active transport ($\alpha \sim 2$).

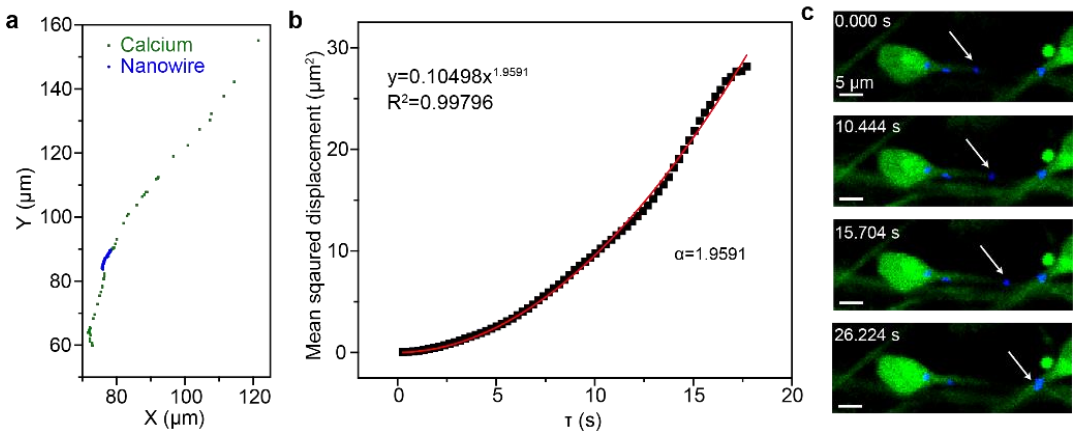

Figure 3-25. Correlated motions of calcium wave propagation and nanowire transport. a, Trajectories of the nanowire movement and the calcium wave-front propagation are overlaid, indicating that the nanowire is transported inside the cell protrusion. **b,** Mean-squared displacement analysis of the nanowire motion after the calcium wave-front reaches its original location shows a diffusivity coefficient $\alpha \sim 2$, suggesting the active transport motion of the nanowire being triggered by the calcium wave. **c,** An additional image series (green, calcium; blue, Si nanowires) from a different example, showing the calcium-triggered nanowire transport phenomena. White arrows indicate the nanowire of interest serving as a transport marker.

Besides serving as an intracellular calcium modulator and a transport marker, the photothermal properties of nanocrystalline Si nanowires may be explored to induce a photoacoustic effect for biomechanical manipulation at the subcellular level. To assess this, we chose human umbilical vein endothelial cells (HUVEC), which are active in the phagocytosis of silicon nanowires and have well-studied microtubule networks. Nanocrystalline Si nanowires are trapped in the microtubule meshes after coculturing with HUVEC for ~ 24 hours. When a laser pulse (592 nm, 1 ms, ~ 2.09 mW, ~ 211 nm spot size) was introduced to the nanowire, the surrounding microtubules were rapidly repelled and formed a void space near the nanowire (**Figs. 3-26a**, **3-27**), suggesting a shock-wave generation through a photoacoustic effect[35]. Besides intracellular microtubule networks, Si nanowires can also interface with intercellular conduits, where microtubules form compact bundles. Upon laser illumination of the entangled single

nanowire (592 nm, 1 ms, ~ 2.55 mW, ~ 211 nm spot size), the bundled microtubules are broken up immediately (**Fig. 3-26b**), possibly through a shock-wave-mediated, mechanically-induced microtubule depolymerization[36]. The optically-triggered, and nanowire-enabled mechanical manipulation of cytoskeletal structures may serve as a new tool for the study of intra- and intercellular dynamics where a remote structural manipulation of subcellular structures is desired.

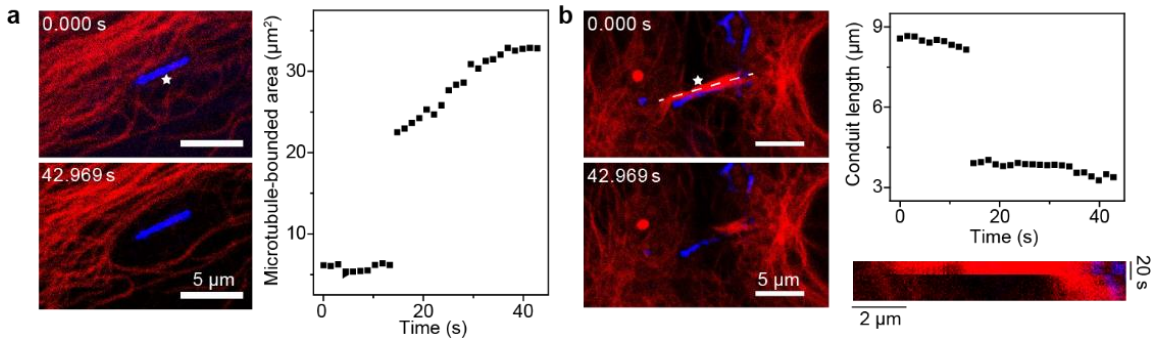

Figure 3-26. Si nanowires allows intracellular mechanical stimulations. a, Microtubule networks can be mechanically manipulated by laser illumination (592 nm, 1 ms, ~ 2.09 mW) of intracellular Si nanowires. Red, microtubules; blue, Si nanowires. The white star marks the illumination site. **b,** Intercellular conduits can also be manipulated (592 nm, 1 ms, ~ 2.55 mW). Red, microtubules; blue, Si nanowires. A kymograph (lower right) taken along the white dashed line (upper left) shows the evolution of the conduit length. The white star marks the illumination site.

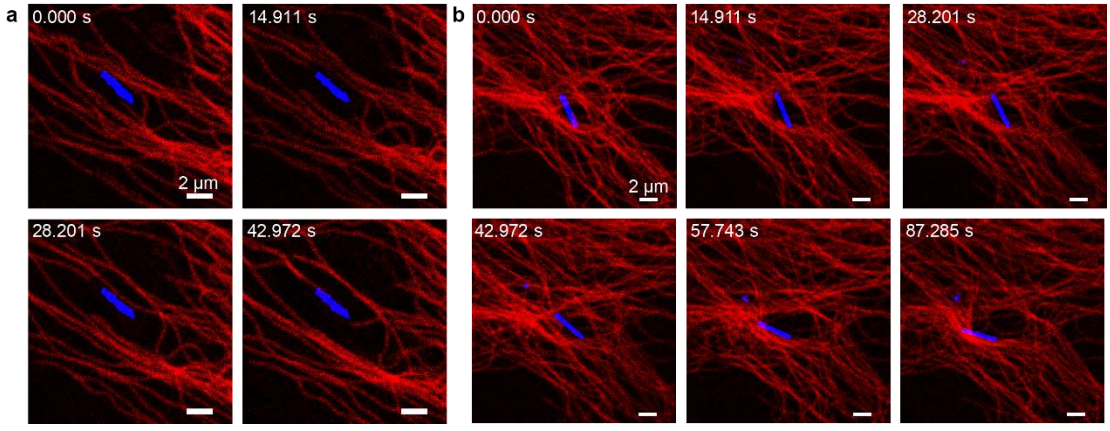

Figure 3-27. Microtubule networks can be remotely manipulated by intracellular stimulation of Si nanowires. **a** and **b**, Two live cell imaging series (red, microtubules; blue, Si nanowires) showing the repellant of microtubule

Figure 3-27, continued. networks by the laser illuminations (592 nm, ~ 2.09 mW, ~ 211 nm spot size) of internalized Si nanowires. The laser pulses were 1 ms long before the time point of 14.911 s. The facts that the nanowires can be moved and get entangled with other microtubules suggest that the cells are alive after the mechanical stimulations.

Control experiments without nanowires did not yield any of these intra- or intercellular observations. Moreover, the importance of using silicon nanowires instead of other nanostructures (*e.g.*, Au nanoparticles or nanorods) is due to the following: (1) silicon nanowires can be at least partially exposed in cytosol upon phagocytic cellular entrance[25], (2) silicon has only a moderate photothermal effect (compared to, *e.g.*, that of Au) such that the confocal imaging light source itself will not cause heating from the nanostructures, and (3) the high aspect ratio of silicon nanowires enables their axial alignment with respect to the cytoskeletal filaments.

3.2.7 Single cell and small tissue level biointerfaces

In addition to the nanowire-enabled intracellular biointerfaces, we also explored the possibility of implementing extracellular modulations with larger Si structures to match the sizes of cultured cellular assemblies and even small tissues. We first tested *p-i-n* Si heterojunctions because their significantly larger light-induced photocurrents (**Fig. 3-13**; **Table 3-1**) may be readily sensed by cells that are attached directly[37-39]. Patch clamp and calcium imaging studies show that DRGs cultured on Si heterojunctions can be stimulated with focused light pulses (**Fig. 3-28**) individually or sequentially in a cellular assembly, with a high spatiotemporal resolution (**Figs. 3-29**, **3-30**).

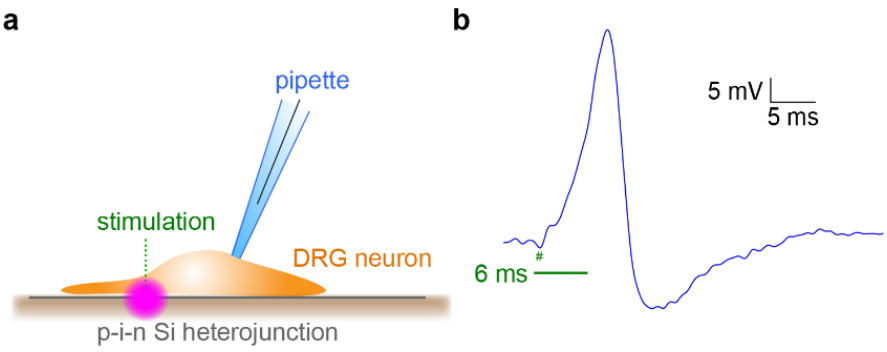

Figure 3-28. DRG neurons cultured on a *p-i-n* Si heterojunction can be optically stimulated. a, A schematic illustration of photostimulation of DRG neurons cultured on a Si heterojunction substrate. **b,** A 6 ms-long laser pulse (532 nm, ~ 47.1 mW, ~ 5 μm spot size) can elicit an action potential of the patched neuron. # marks the photoelectric artifact coinciding with the light onset[55,56].

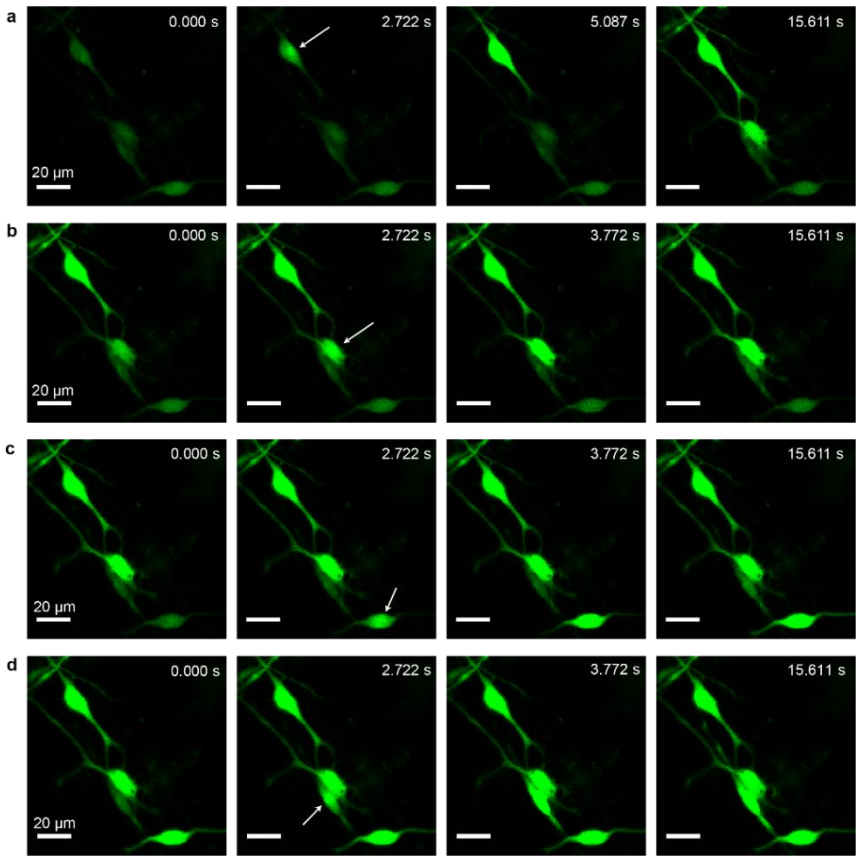

Figure 3-29. *p-i-n* Si heterojunctions enable high spatiotemporal-resolution extracellular stimulations of calcium dynamics. a-d, Laser illuminations (592 nm, ~ 14.4 mW) of different cells in a DRG culture (green: calcium) on a *p-i-n* Si heterojunction, showing stepwise cellular modulation. The illuminations induce localized and fast

Figure 3-29, continued. calcium elevations near the stimulation sites and subsequent calcium wave propagations both intra- and inter-cellularly. Laser stimulations were 1 ms long before the time point of 2.722 s. White arrows mark the laser stimulation sites.

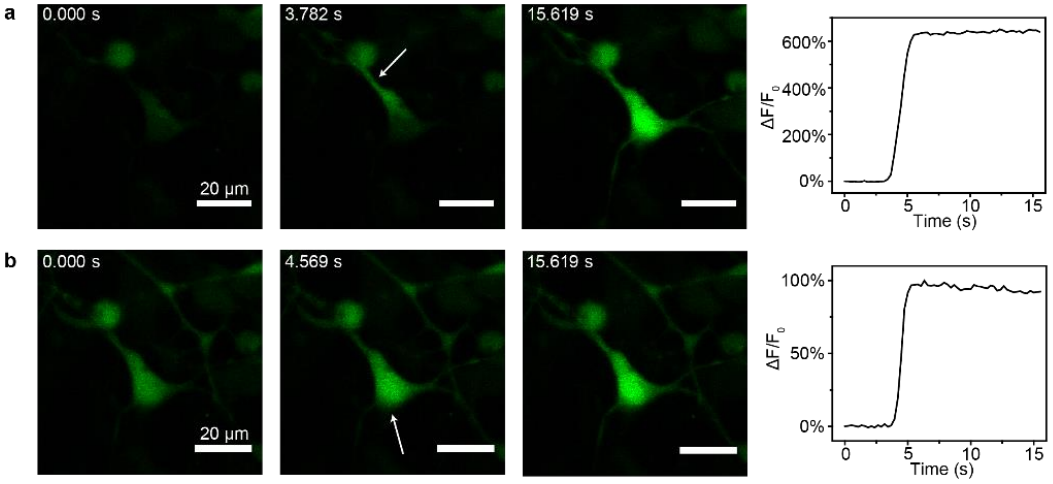

Figure 3-30. Extracellular stimulation of calcium is minimal invasive to cells. a and **b,** The same glial cell cultured on a *p-i-n* Si heterojunction (green, calcium) is stimulated extracellularly in two consecutive series without being damaged. As shown in the first time of stimulation (**a**), not only the cell body but also the protrusion can be stimulated to induce the cellular calcium dynamics. The stimulation laser (592 nm, ~ 14.4 mW) was on for 1 ms right before the time point of 3.782 s in each case. White arrows mark the laser stimulation sites.

We next explored an *in vitro* test on a mouse cortical brain slice interfacing with a distributed *p-i-n* Si mesh to evaluate the feasibility of the optically-controlled neuromodulation of a small tissue (**Fig. 3-31a**, left). A whole-cell recording in voltage-clamp mode was made in a cortical pyramidal neuron located in the middle of the 300-μm thick slice while the Si mesh was in contact with the bottom face of the slice (**Fig. 3-31a**, lower right). Immediately after the laser illumination on the Si mesh (473 nm, 1 ms, ~ 2 mW, ~ 57 μm spot size) (**Fig. 3-31a**, upper right), there were two fast electrical artifacts with opposite polarities (**Fig. 3-31b**, marked by #), likely due to the capacitive charging and discharging of the Si/electrolyte/cell interfaces. Excitatory postsynaptic currents (EPSCs) (**Fig. 3-31b**, marked by stars) were then recorded arriving with

short latency and low jitter after the photoelectric artifacts. Additionally, these recordings indicate that laser illumination of the Si mesh evoked spikes not in the patched neuron but in at least one presynaptic neuron in the slice, that provides the excitatory synaptic input to the recorded postsynaptic neuron. That the patched cell is not triggered to spike may be due to a combined reason that the cell is far away from the Si under illumination (difference in depth of ~ 150 μm) and only the immediately neighboring cells may be substantially activated by the localized laser stimulation. The ability to photo-activate presynaptic neurons and detect synaptic inputs with little or no direct activation of the recorded postsynaptic neuron is advantageous for photostimulation mapping of neuronal circuits[40,41]. The Si mesh in conjunction with focused laser scans thus suggests the potential of this new methodology for *ex vivo* analysis of brain circuit organization.

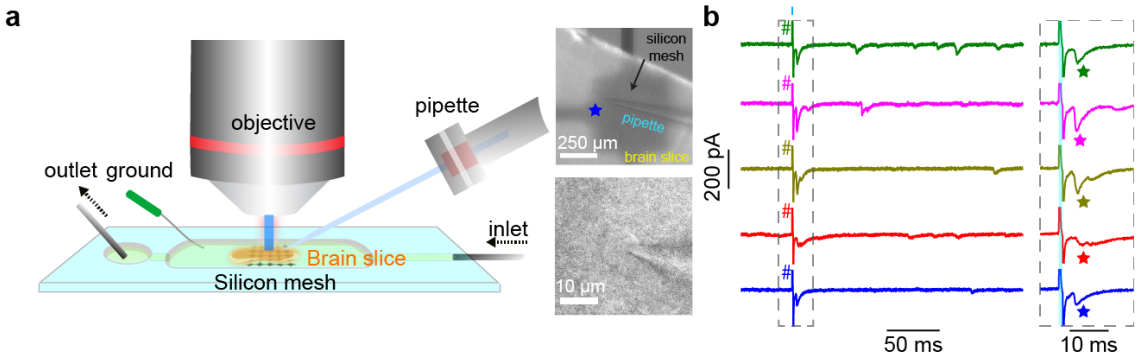

Figure 3-31. Photostimulation by Si meshes can elicit neurotransmitter release in brain slices. a, A schematic diagram of a photostimulation of a brain slice performed in a perfusion chamber (left). A pyramidal neuron in a cortex slice was held at -70 mV in the whole-cell voltage-clamp mode (lower right) while a distributed Si mesh was placed underneath the slice (upper right). Short laser pulses (473 nm, 1 ms, ~ 2 mW, ~ 57 μm spot size) were delivered to a spot on the Si mesh (marked by a blue star) to activate the nearby cells. **b,** Example traces from voltage clamp recordings of the patched pyramidal neuron over 5 trials (left) with 1-ms long laser stimulations (cyan bar). The grey dashed box marks the time frame for zoom-in views on the right. EPSCs are marked by stars following the illuminations of the Si mesh (right). The cyan shaded area marks the illumination period in each trial. # denotes the photoelectric artifact.

3.2.8 Organ level biointerfaces

Finally, we interfaced an Au-decorated and Si mesh-based flexible membrane with a mouse brain to control the brain activities, *e.g.*, the ability to sense, interpret, and act upon the environment. The bilayer device layout, consisting of the Au-decorated Si mesh and the holey PDMS membrane, allows the device's conformal attachment to the brain cortex (**Fig. 3-32**) with sufficient adhesion (**Fig. 3-33**).

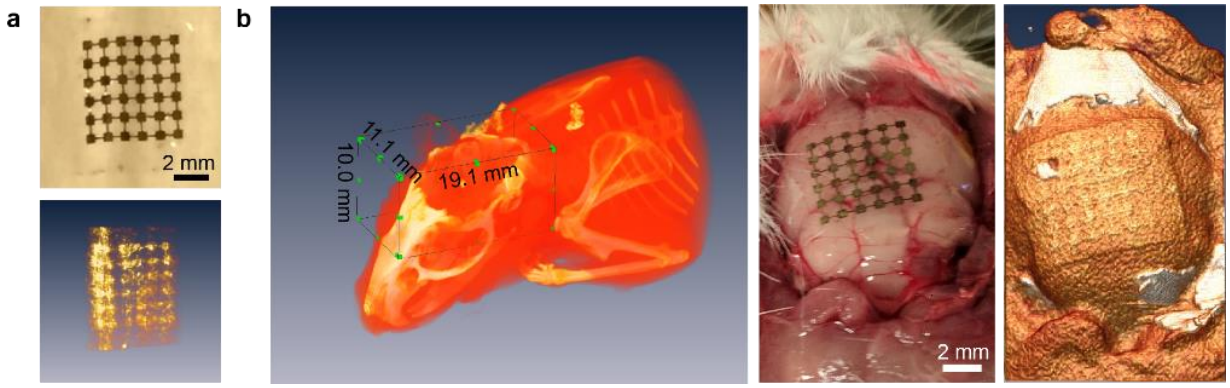

Figure 3-32. Distributed Si mesh form conformal interfaces with the brain cortex. a, A photograph (upper) and its corresponding micro-CT image (lower) of a flexible device made of a Si mesh a PDMS layer. The surface decoration with Au also provides additional contrast under x-ray scans. **b**, The device can conformally coat on the mouse brain cortex as shown both by the photograph (middle) and the CT image (right).

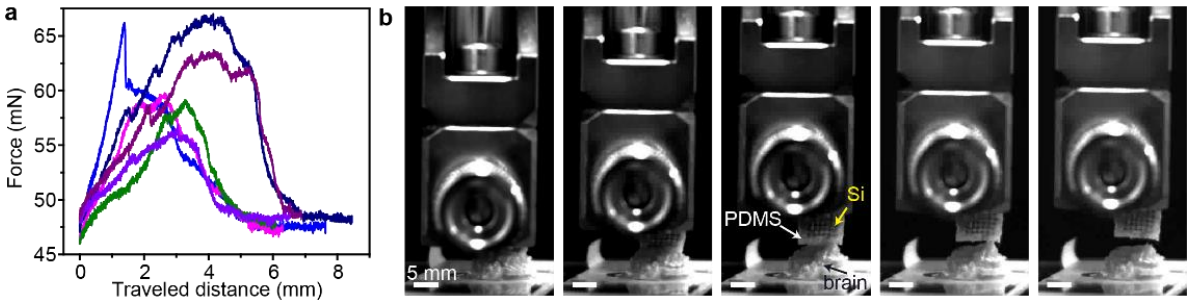

Figure 3-33. The flexible device made of Si and PDMS is adhesive to the brain tissue. a, Representative force-extension curves recorded during the peelings of the device from the brain cortex yielding an average adhesion energy

Figure 3-33, continued. of 1.34 ± 0.63 J/m^2. **b,** Snapshots of a typical peeling test showing the adhesion between the device and the brain when detaching.

We chose an Au decorated surface due to its large capacitive and faradic current components. We performed the *in vivo* photostimulation experiment using an extracellular linear array to record neural activities following laser illuminations (473 nm, ~ 5 mW, 100 ms, ~ 216 μm spot size) of the silicon mesh attached to the somatosensory cortex of an intact mouse brain (**Figs. 3-34a**, **3-35**). In individual trials of the test, enhanced neural activities were evident during the illumination period—with significant photoelectric artifacts at the light onsets and offsets (**Fig. 3-34b**). The detected spike-like events using criteria of a high pass filter of 800 Hz and a threshold of 5 times the noise level standard deviation (SD) exhibit waveforms typical of natural extracellular electrophysiological recordings (**Fig. 3-34c**)[42-44]. Peristimulus time histograms (PSTH) from 16 channels (**Fig. 3-34d**) (with the depths between 200 μm and 900 μm below the pia) clearly show the illumination-triggered neural responses, which are in the layers 2/3, 4, and 5A of the somatosensory cortex[45]. Statistical analyses further revealed that the evoked responses have a significantly higher rate than the spontaneous ones (**Fig. 3-35**). In addition, stronger short-latency activity was observed in more superficial neurons, which were closer to the silicon mesh and thus may be more easily activated. Over time, activity spreads to deeper layers (**Fig. 3-34d**), consistent with the propagation of signals through the local and long-range cortical circuits, similar to patterns observed with optogenetic photostimulation[46]. Moreover, parametric stimulations show a colligative behavior in that the activated neural response rate is correlated with the stimulation power (**Figs. 3-34e**, **3-36**), which is essential to the predictive control of the Si mesh as a precise neuromodulator.

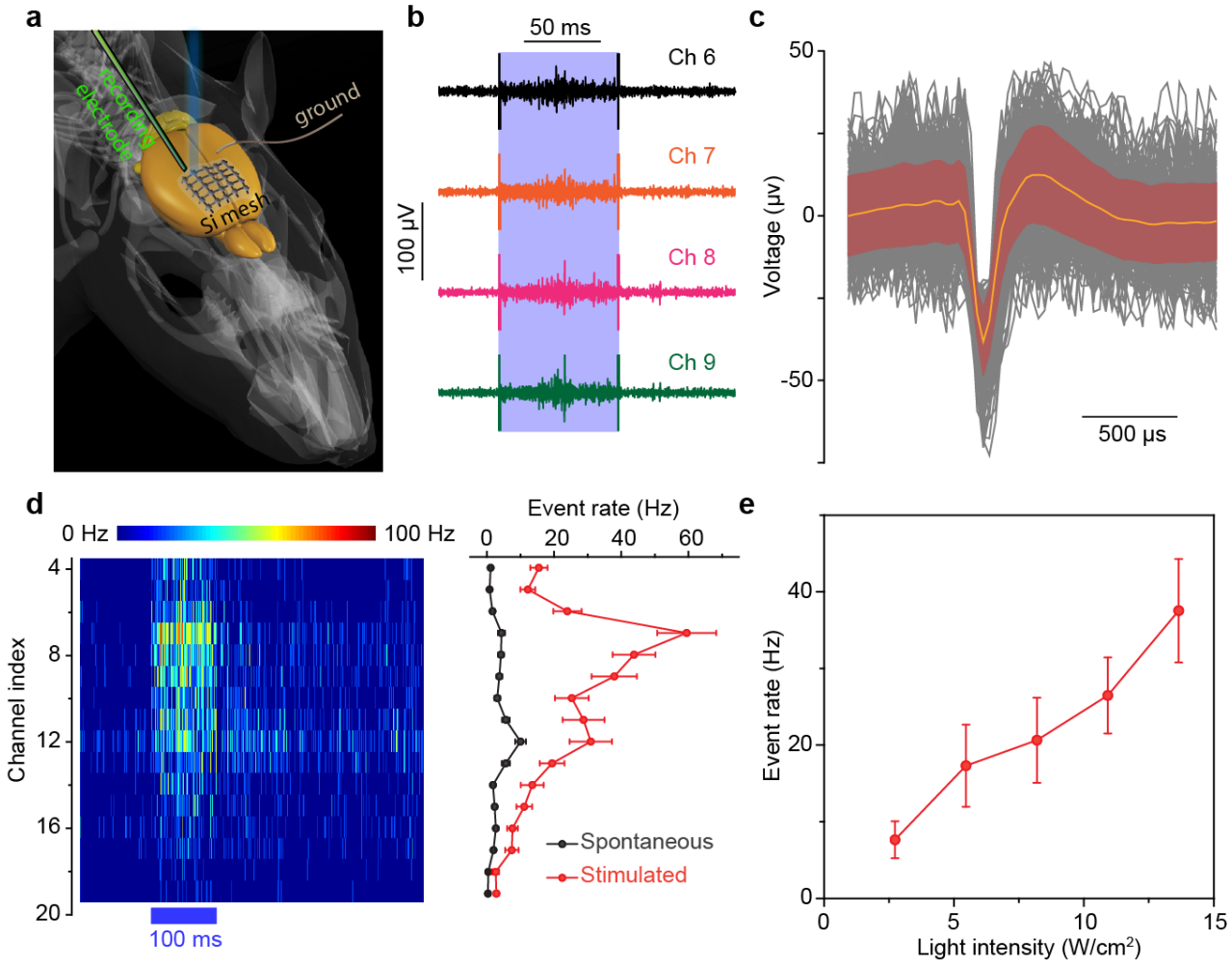

Figure 3-34. Flexible and distributed silicon mesh for optically-controlled extracellular neuromodulation. a, A schematic diagram illustrating the *in vivo* photostimulation test. A linear probe with 32 recording sites is guided into a head-fixed anesthetized mouse brain to sample the evoked neural activities by the illumination of an adjacent silicon mesh. **b,** Example traces of raw neural response data from four adjacent channels (Ch 6 to Ch 9) in a single trial of stimulation (473 nm, 100 ms, ~ 5 mW, ~216 µm spot size) marked by a light blue band. **c,** A mean neuron-firing waveform (orange) superposed on individual waveforms (black) of both spontaneous and stimulation-evoked activities. The maroon shaded area denotes SD. *n*=300 with 153 from stimulated and 147 from spontaneous. **d,** A heat map of PSTH for channels between 4 and 19 (left). The blue bar underneath indicates the period of laser stimulation. The mean spontaneous and evoked neural response rates across all trials for the same channels in the PSTH heat map. **e,** The evoked neural response rate is positively correlated with the stimulation laser intensity. Error bars represent the s.e.m from 50 trials in channel 9.

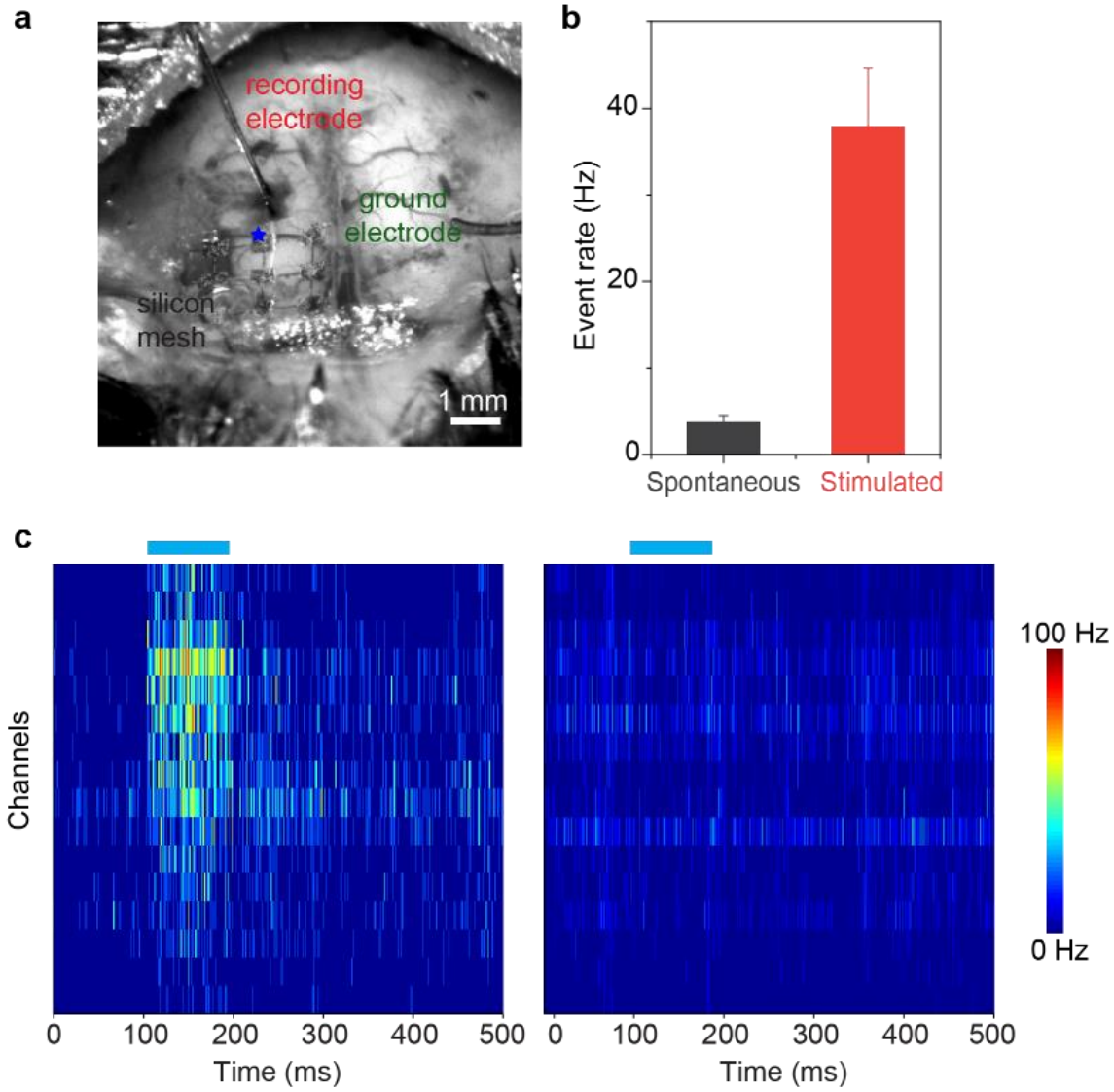

Figure 3-35. The recorded brain responses under illumination is due to the Si mesh. a, The experimental paradigm of an *in vivo* photostimulation test. A linear probe is inserted into the somatosensory cortex with an attached silicon mesh in the close proximity. The laser illumination site (473 nm, ~ 216 μm spot size) is marked by a blue star. **b**, The mean spontaneous response rate (~ 3.7 Hz) is significantly different from the evoked one (~ 37.9 Hz). Error bars represent the s.e.m from 50 trials. Wilcoxon rank sum test, $p=5.5\times10^{-8}$; paired *t*-test, $p=4\times10^{-6}$. Event rates were calculated from channel 9 with the 5-mW and 100-ms stimulation condition. **c**, Recordings from a control experiment without the Si mesh (right) did not yield significant signals under illumination. Cyan bars mark the illumination periods.

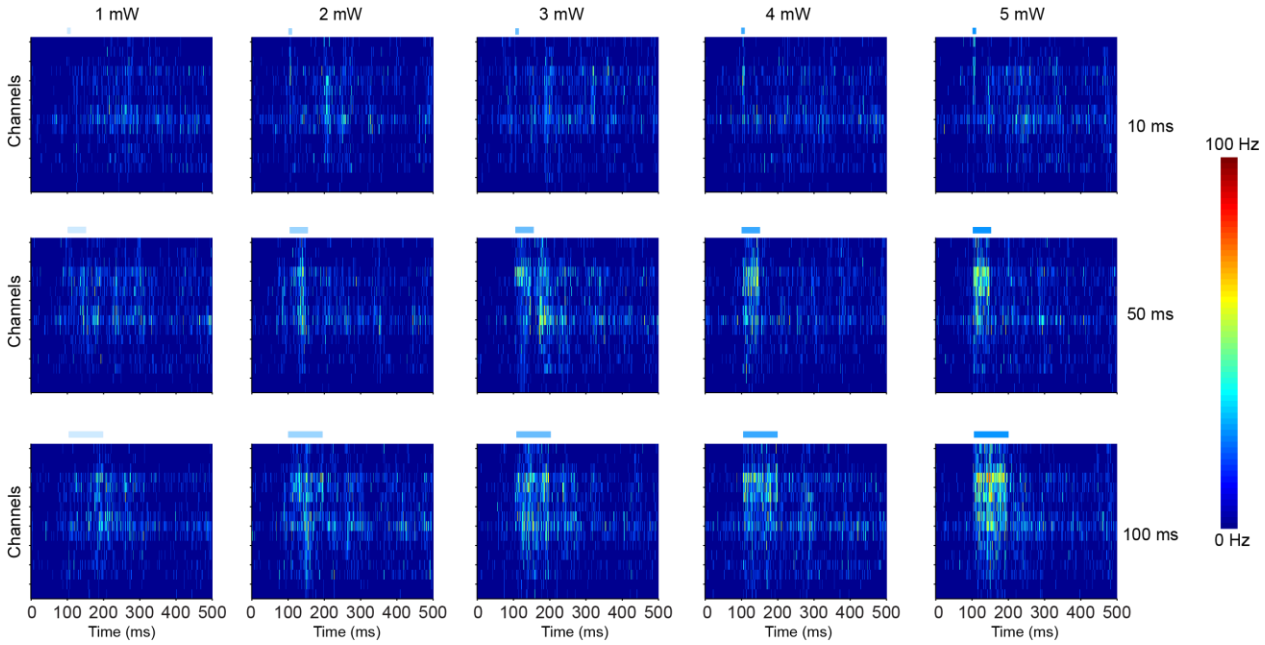

Figure 3-36. The stimulated neural response is controllable. Parametric stimulations with varied laser powers and durations (1~5 mW, 10 ms, 50 ms, 100 ms) show a positive correlation between the evoked event rate and the stimulation power, which is essential to the predictive control of the Si mesh as a precise neuromodulator. Cyan bars with different transparencies indicate illumination periods with different laser powers.

Finally, based on the electrophysiology studies, we tested if the Si mesh-enabled photostimulations of the brain cortex can trigger movements of anesthetized mice. When we illuminated a Si mesh attached to the right side of the forelimb primary motor cortex, the contralateral left forelimb of the mouse showed a large, rapid up-and-down (flexion-extension) movement shortly after the stimulation (**Figs. 3-37**, **3-38**). Conversely, photostimulation of the left forelimb motor cortex evoked movements of the contralateral right forelimb (**Fig. 3-39**). In some cases, small ipsilateral forelimb movements were also evoked (**Fig. 3-37**), possibly reflecting activation of uncrossed (ipsilateral) corticospinal projections. Overall, our observations of cortically evoked movements are consistent with the functional organization of the forelimb motor control system[47].

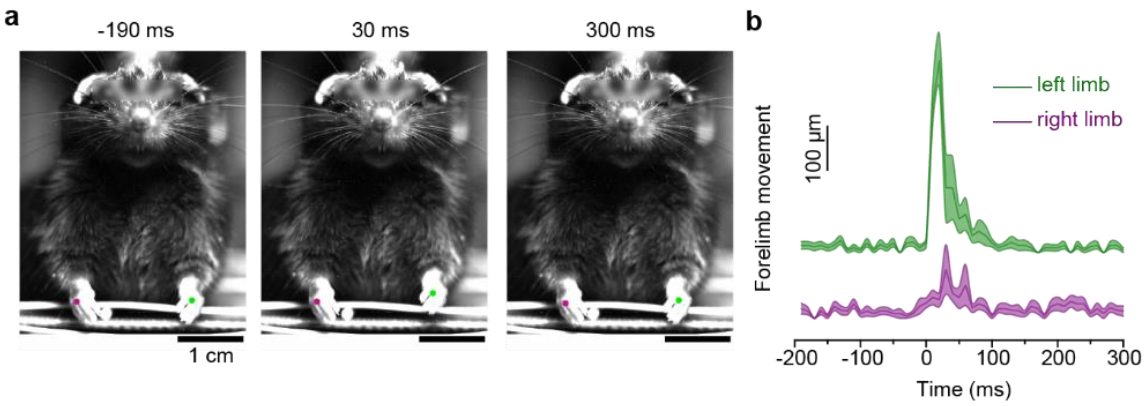

Figure 3-37. Photostimulaiton of Si meshes can evoke forelimb movements. a, Snapshots of a forelimb movement study following photostimulations. The left limb (the limb on the right side of the photos) moves up and down following the laser illumination (473 nm, 50 ms, ~ 4 mW, ~ 216 µm spot size) on a Si mesh attached to the right side of the forelimb primary motor cortex. **b,** Time-dependent limb movements show a preferred motion of the left forelimb after the stimulation. The 0 ms time point represents the start of the light pulse. Shaded areas denote s.e.m of the data. *n*=15.

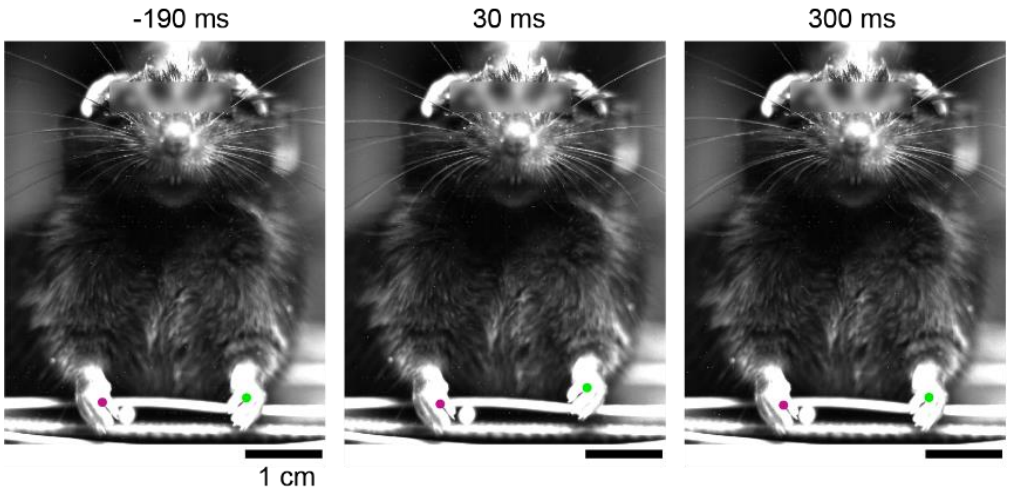

Figure 3-38. Photostimulation of the Si mesh can trigger mouse forelimb movements. Another example showing the preferred left forelimb movement following the laser illumination (473 nm, 50 ms, ~ 4 mW, ~ 216 µm spot size) of a Si mesh attached to the right side of the forelimb primary motor cortex. The 0 ms time point denotes the light onset.

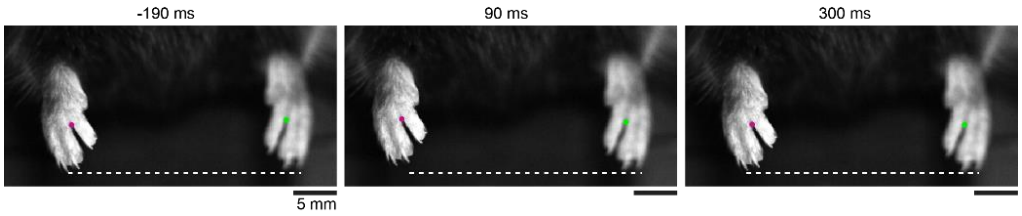

Figure 3-39. Photostimulation of the forelimb motor cortex triggers the contra side forelimb preferred movement. The right forelimb movement can be triggered by the laser illumination (473 nm, 100 ms, ~ 5 mW, ~ 216 μm spot size) of a Si mesh attached to the left side of the forelimb primary motor cortex. The 0 ms time point denotes the light onset.

Collectively, Si heterojunction-based materials are demonstrated as optically-controlled freestanding devices that can modulate brain activities and simple animal behaviors. Compared to traditional electrode-based neuromodulation, the current freestanding device configuration may have a higher flexibility to implement multiplexed and patterned stimulations on a large scale. Additionally, as an alternative to optogenetics, the non-genetic approach offers a unique opportunity to modulate brain activities in nonhuman primates or even human where genetic engineering on these subjects are currently challenging[48-50].

3.3 Experimental

Synthesis of silicon-based materials. Silicon (Si) materials (*p*-type/intrinsic/*n*-type heterojunctions and intrinsic-intrinsic coaxial nanowires) were prepared using a chemical vapor deposition (CVD) method. In a typical synthesis of a *p*-*i*-*n* heterojunction, a silicon-on-insulator (SOI) wafer (Ultrasil, USA, device layer, *p*-type, (100), 0.001-0.005 Ω·cm, 2 μm; buried oxide layer, 1 μm; handle layer, *p*-type, (100), 1-20 Ω·cm, 650 μm) was used as the substrate for subsequent deposition of intrinsic and *n*-type layers. The native oxide on the SOI wafer was removed with hydrofluoric acid (HF, 49%, Sigma-Aldrich, USA) right before placing the substrate inside a quartz tube for evacuation. Each of the intrinsic and *n*-type Si layers was deposited under

650 ^{o}C and a chamber pressure of 15 Torr for 20 min. During the intrinsic layer deposition, the flow rates of hydrogen (H_2) and silane (SiH_4) were set as 60 and 0.3 standard cubic centimeters per minute (sccm), respectively. The *n*-type layer was deposited with the same flow rates of H_2 and SiH_4 during the intrinsic layer growth plus a 1.5 sccm flow rate of the dopant gas, phosphine (PH_3, 1000 ppm in H_2).

The nanocrystalline Si nanowire (intrinsic core/intrinsic shell) was synthesized from a two-step process involving an initial growth of a thin intrinsic backbone and a subsequent deposition of a thick intrinsic shell. The core was grown with a gold (Au) nanocluster-catalyzed CVD process where Au colloidal nanoparticles (Ted Pella Inc., USA, 50 nm in diameter) were deposited onto a Si (100) substrate (Nova Electronic Materials, *n*-type, 0.001-0.005 Ω·cm) as the catalyst. The growth was maintained at 470 ^{o}C and 40 Torr for 20 min. The flow rates of H_2 and SiH_4 were controlled as 60 and 2 sccm, respectively. After the intrinsic nanowire core growth, the SiH_4 flow was switched off and the chamber was kept under a H_2 atmosphere (60 sccm, 15 Torr) until the temperature ramped up to 600 ^{o}C for the subsequent shell deposition. The H_2 atmosphere was used to minimize Au diffusion. The intrinsic shell was deposited with flow rates of H_2 and SiH_4 at 0.3 and 60, respectively, and a chamber pressure of 15 Torr for 40 min.

The metal-decorated Si heterojunctions were prepared with an electroless deposition method. In general, the as-synthesized *p*-*i*-*n* heterojunctions were dipped into a mixture of metal-containing solutions (chloroauric acid ($HAuCl_4$), potassium tetrachloroplatinate(II) (K_2PtCl_4), silver nitrate ($AgNO_3$); 0.01 mM, 0.1 mM, 1 mM) and 1% HF for 3 min at room temperature.

Fabrication of Si-based flexible devices for *in vivo* experiments. The device fabrication process was divided into two parallel steps including the preparations of both distributed Si meshes and porous polydimethylsiloxane (PDMS, Corning, USA) membranes. The fabrication of distributed

Si meshes were performed with a combination of photolithography and etching techniques. In brief, a bilayer of undercut (MicroChem, USA, LOR-3A) and photoresist (MicroChem, USA, SU-8 2005) was spin-coated on the as-synthesized *p-i-n* heterojunction SOI wafer. A mesh structure of SU-8 was patterned with a standard photolithography process consisting of ultraviolet (UV) light exposure (200 mJ/cm^2) and developing (MicroChem, USA, SU-8 developer). The as-patterned SU-8 mesh served as an etch mask for the subsequent reactive ion etching (RIE) of Si. The unprotected *p-i-n* Si layers (~ 2.3 μm) were removed after 10 min of etching (radiofrequency (RF) power, 100W; inductive-coupled plasma (ICP) power, 400 W) with a gaseous mixture of tetrafluoromethane (CF_4, 45 sccm) and argon (Ar, 5 sccm). The SU-8 protection layer was lift-off by dissolving the undercut LOR-3A layer in Remover-PG (MicroChem, USA). A final wet etching of the oxide layer with 49% HF was performed to release the as-patterned Si heterojunction.

The PDMS membrane was prepared using a soft-lithography technique. In general, a SU-8 pillar array (~ 120 μm in height) was patterned on a Si substrate with the standard photolithography process and served as the soft-lithography mold. A layer of PDMS (precursor: curing agent ratio = 10:1) was then spin-coated onto the SU-8 mold and cured at 80 ^{o}C overnight. The as-cased PDMS layer was finally released in hexane (Fisher Scientific, USA) to get the holey structure. The distributed Si mesh was then transferred onto the holey PDMS membrane to form the entire device.

Finite element analysis (FEA) of stress distribution. The FEA was performed using COMSOL Multiphysics 5.3 (COMSOL Inc. USA). A 2D plate model in the structural mechanics module was set for the simulation. The von Mises stress distribution was calculated after a point displacement of 500 μm in the *z* direction at the device center while fixing four edge points.

Electron microscopy. A transmission electron microscope (TEM, JEOL, Japan, JEM-3010) and an aberration-corrected scanning transmission electron microscope (STEM, JEOL, Japan, JEM-ARM200F) were used to image the cross-sectional structures of both the pristine *p*-*i*-*n* Si heterojunction and the gold-decorated one. X-ray energy dispersive spectroscopy (XEDS) maps were using the JEM-ARM200F, which was equipped with an Oxford X-Max^N 100TLE windowless SDD X-ray detector (Oxford Instruments, UK). Selected area electron diffraction (SAED) patterns were taken using the JEM-3010. TEM cross-sectional specimen preparations were carried out by controlled tripod polishing[51,52] followed by liquid-nitrogen-cooled Ar ion millings using a Fischione 1050 TEM mill (Fischione Instruments, USA). A 4-kV ion milling was used to further thin the specimen and a final 0.5 kV milling was performed to remove surface damages. A scanning electron microscope (SEM, Carl Zeiss, Germany, Merlin) was used to image the top view of the gold-decorated Si heterojunction, the cross-sectional view of the heterojunction, and the flexible device made of the distributed Si mesh and the holey PDMS membrane. Nanocrystalline Si nanowires were sonicated in isopropanol (Sigma-Aldrich, USA) and then dispersed over copper grids (Ted Pella Inc., USA, Lacey Formvar/Carbon, 200 mesh) for side-view imaging using a TEM (JEOL, Japan, JEM-3010). The cross-sections of the nanowires were prepared by ultramicrotomy. In general, Si nanowires were embedded in epoxy resins which were then solidified at 60 °C for 24 h. Thin epoxy sections of ~100 nm were cut using a ultramicrotome (Ultracut E, Reichert-Jung, USA), collected on lacey carbon grids (Ted Pella Inc., USA), and imaged using the same TEM.

X-ray photoelectron spectroscopy (XPS). XPS data were collected using ESCALAB 250 Xi (Thermo Scientific, USA) with a monochromatic Al Kα ($h\nu$ = 1486.6 eV) excitation. The diameter of the X-ray beam was 500 μm. The survey scans were performed with a pass energy of 160 and

a step size of 1 eV whereas the high-resolution scans were done with a pass energy of 50 and step size of 0.1 eV. The correction of the XPS spectra for charge accumulation was performed using the Si 2*p* peak (binding energy = 99.4 eV). The Si 2*p* peaks were fitted using a Shirley background with G/L 30% for Si^0 and pure Gaussian for Si^{4+}. Peak fitting for the Au 4*f* signal was determined with a linear background G/L 30%, asymmetric 0.9, and a height factor of 0.75. With these parameters the FWHM range for the gold was from 0.8 eV to 1.25 eV.

Si photo-response measurements. For the photo-response measurements, a standard patch-clamp setup was employed. In particular, an upright microscope (Olympus, Japan, BX61WI) with a 20×/0.5 NA water immersion objective was used to deliver light pulses from a light emitting diode (LED, M530L3, Thorlabs, USA, 530 nm, ~ 500 μm spot size) or a laser (Laserglow, Canada, 532 nm, diode-pumped solid-state laser, ~ 5 μm spot size). The light pulses were controlled by transistor-transistor logic (TTL) signals (10 ms) delivered from a digitizer (Molecular Devices, USA, Digidata 1550). Voltage-clamp protocols were done by an Axopatch 200B amplifier (Molecular Devices, USA), controlled by pClamp software (Molecular Devices, USA). Glass pipettes were pulled in a flaming/brown type micropipette puller (Sutter Instrument, USA, P-97) for a final resistance of ~1 M□ when filled with 1× phosphate buffered saline (PBS, Fisher Scientific, USA) solution. In a typical measurement, a Si material was immersed in the same PBS solution where the pipette tip was positioned in close proximity to the Si surface (~ 2 μm). The ionic currents across the pipette tip were recorded in the voltage-clamp mode where the holding levels of the pipette were adjusted using the pipette offset knob. The individual quantities of each photo-response, *i.e.*, capacitive, Faradaic, and thermal, were calculated by fitting the plot of the light-induced current amplitude (ΔI_{light}) over the holding level (I_0). At a given time point, the slope of the ΔI_{light}-I_0 plot represents the photothermal response whereas the intercept of the plot is

contributed by the photoelectric responses. Within the photoelectric responses, the capacitive current is defined as the maximal current amplitude after the light onset while the Faradaic current is defined as the current amplitude at the time point of 8.5 ms since illumination starts. The amplitude of the photothermal-induced local temperature increase of the solution was calculated after the calibration of the pipette resistance. After the photo-response measurement, the same micropipette was placed into another dish of pre-heated PBS with an initial temperature of about 50 ^{o}C. A thermocouple was positioned close to the pipette tip during the temperature measurement. A calibration curve was created, based on the pipette resistance changes in the range between 50 ^{o}C and 20 ^{o}C, which was then used in conjunction with the ΔI_{light}-I_0 curve to estimate the local temperature increase.

Mammalian cell cultures.

All animal protocols used were in accordance to the policies of the University of Chicago and were approved by the Institutional Animal Care and Use Committees (IACUC).

a) Dorsal root ganglia (DRG) culture. DRGs were extracted from decapitated P1-P3 Sprague-Dawley rats (Charles River Laboratories, USA) and were placed immediately in ice-cold Dulbecco's modified eagle medium (DMEM/F12, Life Technologies, USA). The ganglia were then transferred to a 2.5 mg/mL trypsin solution (Worthington, USA) in Earle's balanced salt solution (EBSS, Life Technologies, USA) and digested for 20 min in a 37 ^{o}C shaker with a speed of 144 rpm. Afterwards, the cells were centrifuged and the supernatant was replaced with EBSS supplemented with 10% fetal bovine serum (FBS) (ATCC, USA). After the mechanical trituration with pipetting, the cell suspension was centrifuged again and the supernatant was replaced with DMEM/F12 containing 5% FBS. Next, cells were seeded onto poly-L-lysine (PLL, Sigma-Aldrich, USA) coated substrates, *e.g.,* glass-bottom Petri dishes, *p-i-n* heterojunction SOI wafers, and

allowed 30 min for cell adhesion. Finally, the dishes were filled with DMEM/F12 supplemented with 5% FBS, 100 U/ml penicillin (Sigma-Aldrich, USA), and 100 μg/ml streptomycin (Sigma-Aldrich, USA), and cultured in a 37 ^{o}C incubator with 5% carbon dioxide (CO_2) until used for experiments.

2) Other cell lines. Human umbilical vein endothelial cells (HUVEC, Life Technologies, USA) and U2OS cells (ATCC, USA) were cultured on glass-bottomed Petri dishes and passaged following standard procedures from the vendors.

3) Cellular internalization of Si nanowires. In all cell cultures, intrinsic nanocrystalline Si nanowires were introduced and allowed for coculturing for at least 24 hours. Specifically, nanowire suspensions in different cell culture media were prepared by extensively sonicating small pieces of nanowire growth substrates (~ 2 mm × 2 mm) in culture media for 2 min. The as-made nanowire suspensions were added to the cultures in a drug-like fashion (~ 10 μL of suspension per 1 mL of medium). Before all experiments, cells were washed three times with fresh media.

Immunofluorescence labeling of the DRG culture. DRG and nanowire cocultures were first fixed with 4% paraformaldehyde in PBS (Alfa Aesar, USA, with magnesium and ethylene glycol tetraacetic acid) for 10 min at room temperature. After rinsing in PBS, cells were then permeabilized with 0.1% Triton X-100 in PBS (Sigma Aldrich, USA) for another 10 min at room temperature. Following blocking with 1.5% bovine serum albumin (BSA, Sigma-Aldrich, USA) in PBS for 1 hour, the cells were incubated with primary antibodies (GFAP (GA5) Mouse mAb, 1:300 in 1.5% BSA-PBS for glia; NeuN (D4G40) XP Rabbit mAb, 1:50 in 1.5% BSA-PBS for neuron, Cell Signaling, USA) at room temperature for 1 hour. After washing, secondary antibodies (Goat anti-Mouse IgG (H+L) Superclonal Secondary Antibody, Alexa Fluor 647, 1:1500 in 1.5% BSA-PBS for glia; Goat anti-Rabbit IgG (H+L) Secondary Antibody, Alexa Fluor 488, 1:1500 in

1.5% BSA-PBS for neuron, Life Technologies, USA) were finally applied. After washing in PBS, the as-labelled cells were imaged using a confocal laser scanning microscope (Leica, Germany, SP5 II STED-CW) with Si nanowires being imaged simultaneously with the scattered light.

Calcium imaging. Cells, either cocultured with intrinsic nanowires or cultured on *p-i-n* heterojunctions, were stained with 2 μM of Fluo-4 AM (Life Technologies, USA) for 30 min at 37 ^{o}C and washed three times with dye-free culture media before imaging. The as-stained cells were imaged using the same Leica SP5 confocal microscope. In a typical experiment, a laser pulse (1 ms, 592 nm) was delivered to the nanowire of interest in the middle of a calcium imaging time series. The cellular fluorescence intensity over time was then analyzed using ImageJ software (National Institutes of Health, USA). For the intracellular transport study, a custom-written program in Python was run to automatically track the nanowire and calcium wave-front locations in all 100 frames. Rolling diffusivity coefficient α values were calculated for every 5 frames with a window size of 9.

Live cell microtubule dynamics. In a typical experiment, HUVEC cells with internalized Si nanowires were stained with 200 nM of SiR-tubulin (Cytoskeleton, USA) at 37 ^{o}C for 1 hour. 10 μM of verapamil (Cytoskeleton, USA) was also added to inhibit the efflux of the SiR-tubulin. Three times of washing with the dye-free medium was applied before imaging. Under the same Leica SP5 confocal microscope, the Si nanowire of interest was illuminated with a 592 nm laser pulse (1 ms) and the subsequent microtubule dynamics were recorded. The as-recorded videos were processed and analyzed using ImageJ including the analysis of microtubule bounded areas and intercellular conduit lengths over time, and the generation of kymographs.

Electrophysiology and photo-stimulation experiments.

All animal protocols used were in accordance to the policies of the University of Chicago and Northwestern University, approved by the Institutional Animal Care and Use Committees (IACUC), and followed the animal welfare guidelines of the Society for Neuroscience and National Institutes of Health.

1) DRG culture on Si heterojunctions. Before the experiment, FBS supplemented DMEM/F12 in the culture dish was rinsed three times with the extracellular recording solution (in mM: NaCl 132, KCl 4, $MgCl_2$ 1.2, $CaCl_2$ 1.8, HEPES 10, glucose 5.5; pH 7.4). Desired neurons were patched with a ~2 M□ pipette, filled with the intracellular pipette solution (in mM: NaCl 10, KCl 150, $MgCl_2$ 4.5, EGTA 9, HEPES 10; pH 7.3). Voltage recordings were made in current-clamp mode using the same setup for the photo-response measurements. Suprathreshold current injections were first delivered to the patched neuron to assess its excitability. Laser pulses (532 nm) with incremental durations were delivered subsequently to excite the cell.

2) Brain slice with Si heterojunctions.

Wild-type mice (C57BL/6, female and male; Jackson Laboratory, USA) were bred in-house. Mice were 6-9 weeks old at the time of the slice experiments.

a) Slice preparations. Mice were euthanized by anesthetic overdose and decapitation. Brain slices were made in a 4 ^oC cutting solution (in mM: 110 choline chloride, 11.6 sodium L-ascorbate, 3.1 pyruvic acid, 25 $NaHCO_3$, 25 D-glucose, 2.5 KCl, 7 $MgCl_2$, 0.5 $CaCl_2$, 1.25 NaH_2PO_4; aerated with 95% O_2/5% CO_2) using a vibratome (VT 1200S, Leica, Germany) to make 250 μm thick slices. The slices were transferred to an artificial cerebrospinal fluid (ACSF, composition in mM: 127 NaCl, 25 $NaHCO_3$, 25 D-glucose, 2.5 KCl, 1 $MgCl_2$, 2 $CaCl_2$, 1.25 NaH_2PO_4; aerated with 95% O_2/5% CO_2) and maintained at 34 ^oC for 30 min. The slices were then returned to room temperature for at least 1 hour prior to the recordings.

b) Electrophysiology. Distributed Si meshes were placed in a recording chamber under an upright microscope (BX51WI; Olympus, Japan), which is equipped with a video camera (Retiga 2000R; QImaging, Canada). Brain slices were then transferred on top of the Si meshes to form contacts. Slices were visualized by bright-field gradient contrast microscopy using an infrared LED (850 nm, M850L2, Thorlabs, USA) as the light source. A low-magnification objective lens (UPlanSApp 4×/ NA 0.16, Olympus, Japan) was used to visualize and position the slices. A high-magnification water immersion lens (LUMPlanFLN 60×/ NA 1.00, Olympus, Japan) was used to identify neurons for whole-cell recordings.

Borosilicate glass (inner diameter 0.86 mm, outer diameter 1.5 mm with filament, Warner Instruments, USA) was pulled using a P-97 micropipette puller (Sutter Instrument, USA) into patch pipettes with a tip resistance of 2~4 MΩ. Neurons targeted for whole-cell recordings were obtained using micromanipulators (MP-225, ROE-200, MPC-200, Sutter Instrument, USA) and a patch-clamp amplifier (Multiclamp 700B, Axon Instruments, USA). Pipettes containing potassium-based or cesium-based internal solutions were used for voltage-clamp recordings (composition of the internal solution, in mM: 128 potassium or cesium methanesulfonate, 10 HEPES, 10 phosphocreatine, 4 $MgCl_2$, 4 ATP, 0.4 GTP, 3 ascorbate, 1 EGTA, 1 QX-314, and 0.05 Alexa Flour hydrazide, with 4 mg/ml biocytin, at 7.25 pH and 290-295 mOsm). All recordings were made in 34°C ACSF with the temperature controlled by an in-line feedback-controlled heater (TC 324B, Warner Instruments, USA). Recordings with series resistance > 40 MΩ were excluded.

A command potential of -70 mV was applied to isolate excitatory (glutamatergic) post synaptic currents (EPSCs). To test for input to a neuron, blue-laser illuminations (1 ms long pulses, 473 nm, ~ 2 mW, ~ 57 μm spot size; MLL-FN473, CNI Laser, China) were delivered onto a nearby spot of the Si mesh.

Multiple trials were sampled at an interstimulus interval of at least 30 s. Recorded currents were amplified, filtered at 4 kHz, and sampled at 40 kHz. Data were acquired using Ephus software[53] and analyzed using routines written in MATLAB (MathWorks, USA).

3) *In vivo* experiments with distributed Si meshes.

Wild-type mice (C57BL/6, female and male; Jackson Laboratory, USA) were used, at an age of 6-9 weeks old at the time of the in vivo experiments.

a) Pre-stimulation surgeries. The mouse was deeply anesthetized with ketamine-xylazine (ketamine 80~100 mg/kg, xylazine 5~15 mg/kg, injected intraperitoneally) before the placement of the cranial mounting hardware. A small skin incision was first made over the cerebellum to expose the skull. A stainless-steel set screw (single-ended #8-32, SS8S050, Thorlabs, USA), crimped with a spade terminal (non-insulated, 69145K438, McMaster-Carr, USA) was then affixed with dental cement to the skull. This set screw was later screwed into a tapped hole located at the top of a 1/2" optical post for the head fixation.

After being head-fixed as described above, craniotomies were made over the motor and somatosensory cortices using a dental drill with large enough openings (~ 2.5 mm) to allow the attachment of a silicon mesh on the cortex and the passage of a linear probe. The dura was peeled for a full exposure of the cortex, which was important for a good signal transduction at the Si-brain interface. The mouse was then placed in the recording apparatus with the body temperature monitored with a rectal probe and maintained at ~ 37.0 °C via a feedback-controlled heating pad (FHC, Bowdoin, USA). During the subsequent recordings, ACSF was frequently applied to the exposed brain area to prevent the damage from dehydration. The level of anesthesia was continuously monitored based on whisker movements and paw-pinching/eye-blinking reflexes. Additional anesthetics with 50% of the induction dosage were given when required.

b) Photostimulation apparatus. A customized laser scanning apparatus with a blue laser source (LY473III-100, wavelength 473 nm, maximum power ~ 100 mW, beam diameter ~2 mm) mounted on a 3D linear stage was positioned above the mouse head. In the apparatus, the laser beam from the light source goes through an acousto-optic modulator (AOM) and an iris before being deflected by a pair of galvanometer scanners and focused to the Si mesh by a plano-convex spherical lens.

The output laser power was controlled using a customized AOM driver modulated by signal waveforms delivered via a commercial multifunction (analog and digital) interface board (NI USB 6229, National Instruments, USA). A short pulse train was also sent to digitally encode the parameters of the light waveform such as the start point through the digital input port of the electrophysiology data acquisition (DAQ) board. Software tools (LabVIEW, National Instruments, USA) including a graphical user interface (GUI, GenWave) were developed to generate and transfer waveforms to the AOM driver. The system was calibrated using a power meter to determine the relationship between the driver input voltage and the laser scanner output power.

c) Electrophysiology apparatus. Silicon probes of 32-channel linear microelectrode arrays with ~1 MΩ impedances and 50-μm spacings (model A1 32-6mm-50-177, NeuroNexus, USA) were used for electrophysiological recordings. The probe was fixed to a motorized 4-axis micromanipulator, assembled by mounting a MTSA1 linear translator (Thorlabs, USA) onto a MP285 3-axis manipulator (Sutter Instrument, USA), and positioned under stereoscopic visualizations over a distributed silicon mesh which has been attached to the cortical surface (with the Si layer facing towards the tissue). The probe was tilted by ~ 30° off the vertical axis for a better collection of the neural signals under the silicon mesh. The probe was then slowly inserted into the cortex at a rate of 2 μm/s controlled by LabVIEW, until it reached a depth of 1600 μm from the pia, with the entry point adjacent to the edge of the silicon mesh. Laser pulses with various

powers (up to 5 mW, ~ 216 μm spot size) and durations (up to 100 ms) were delivered onto the Si mesh for the photostimulation of the brain.

Signals were amplified using a RHD2132 amplifier board based on a RHD2132 digital electrophysiology interface chip (Intan Technologies, USA). The filter was set to an analog bandpass of 0.1 ~ 7.5 kHz with a digital filter cutoff of 1 Hz. The single channel sample rate was set to 30K SPS.

For hardware control, we used a RHD2000 USB Interface Board (Intan Technologies, USA) for the communication with other digital devices and the streaming of all the neural-signal data from the RHD2000 amplifiers. The USB port of the module was linked with a USB cable to pipe the data stream in to and out of the computer. In this experiment, the digital ports included in the DAQ board were only used for the acquisition of the photostimulation parameters from the AOM controller.

C++/Qt based experimental interface software (Intan Technologies, USA) was used for the amplifier configuration, online visualization, and data logging.

d) Forelimb movement study apparatus. A Chameleon3 USB3 CMOS Mono camera (CM3-U3-13Y3M-CS, FLIR Systems, USA) configured at 640 × 512 pixels (2 × 2 binning) was used to record the body movements following the laser stimulations. The video recording was triggered and synchronized by the laser scanning control board with the frame rate of 100 Hz. 50 frames were collected before the start of the stimulation and a total of 100 frames were recorded for a full trial. A fixed focal length lens (35 mm EFL, *f*/2.0, Navitar, USA) was mounted on the camera for the focusing. The centroids of the mouse claws were tracked in each frame to investigate the forelimb movements following the laser stimulations. The trajectories of the centroids were quantified to illustrate the movements in each trial.

e) Data analyses. The recorded data were stored as raw signals from the amplifiers and filtered by a 60 Hz notch filter. To reduce the contaminations of the probe recording signals due to the strong photovoltaic effect of the Si mesh, we used a digital high-pass filter (800 Hz cut-off, 2nd-order Butterworth), to shrink the photovoltaic artifact to the first 3 ms post-stimulus window.

The following routines were performed to further analyze the data. First of all, a threshold detector was applied, with the threshold set to the 5 times of the standard deviation (5 SD) to detect the spikes. To mask the photovoltaic effect, spike counts of the first 3 ms window were then replaced by null values. Finally, neural response time stamps were determined for each detected spike and the response waveforms were plotted from -0.67 ms to 1.33 ms with respect to the detected spike time stamp, *i.e.*, 20 points before and 40 points after the spike time stamp with a sampling rate of 30 kHz. The detected waveforms were sorted according to the similarity of the shapes, *i.e.*, peak to valley amplitudes of the responses. All the analysis codes were written in Matlab (Mathworks, USA).

The time stamps of all the spikes from each channel were used to generate the peristimulus time histogram and the heat maps, which represent the instantaneous firing rate, with 1-ms binning. Responses were averaged across all trials in each channel to yield a mean histogram.

Micro computed tomography (microCT) of the Si/brain interface. MicroCT images of gold-decorated Si meshes attached to dead mouse brains were performed on the XCUBE (Molecubes NV., Belgium) by the Integrated Small Animal Imaging Research Resource (iSAIRR) at the University of Chicago. Images were acquired with an x-ray source of 50 kVp and 200 μA in a single frame of 960 projections. Volumetric CT images were reconstructed in a 400 × 400 × 400 format with voxel dimensions of 100 μm^3. Images were analyzed using AMIRA 5.6 (Thermo Fisher Scientific, USA).

Device-brain peeling adhesion test. Adult C57BL/6 mice (Jackson Laboratory, USA) were sacrificed shortly before the mechanical test. Mouse brains were harvested from dead animals and placed inside PBS solutions prior to the adhesion tests by a tensile test machine (Zwick-Roell, Germany, zwickiLine Z0.5). Briefly, the brain was fixed on a glass slide using a tissue adhesive (Ted Pella, USA, Pelco Pro CA44) and the device was held tightly by a grip. After forming a conformal contact between the device and the brain cortex with an area of ~ 8 mm × 4 mm, a unidirectional tension was applied to peel the device off the brain while the force and the extension were recorded simultaneously. The loading rate was kept constant at 3 mm/min. The adhesion energy per area was calculated by the integration of the force-extension curves divided by the contact areas.

3.4 Bibliography

1 Viventi, J., Kim, D. H., Vigeland, L., Frechette, E. S., Blanco, J. A., Kim, Y. S., Avrin, A. E., Tiruvadi, V. R., Hwang, S. W., Vanleer, A. C., Wulsin, D. F., Davis, K., Gelber, C. E., Palmer, L., Van der Spiegel, J., Wu, J., Xiao, J., Huang, Y., Contreras, D., Rogers, J. A. & Litt, B. Flexible, foldable, actively multiplexed, high-density electrode array for mapping brain activity in vivo. *Nature Neuroscience* **14**, 1599-1605, doi:10.1038/nn.2973 (2011).

2 Tian, B., Cohen-Karni, T., Qing, Q., Duan, X., Xie, P. & Lieber, C. M. Three-dimensional, flexible nanoscale field-effect transistors as localized bioprobes. *Science* **329**, 830-834, doi:10.1126/science.1192033 (2010).

3 Liu, J., Fu, T. M., Cheng, Z., Hong, G., Zhou, T., Jin, L., Duvvuri, M., Jiang, Z., Kruskal, P., Xie, C., Suo, Z., Fang, Y. & Lieber, C. M. Syringe-injectable electronics. *Nature Nanotechnology* **10**, 629-636, doi:10.1038/nnano.2015.115 (2015).

4 Chiappini, C., De Rosa, E., Martinez, J. O., Liu, X., Steele, J., Stevens, M. M. & Tasciotti, E. Biodegradable silicon nanoneedles delivering nucleic acids intracellularly induce localized in vivo neovascularization. *Nature Materials* **14**, 532-539, doi:10.1038/nmat4249 (2015).

5 Tian, B., Liu, J., Dvir, T., Jin, L., Tsui, J. H., Qing, Q., Suo, Z., Langer, R., Kohane, D. S. & Lieber, C. M. Macroporous nanowire nanoelectronic scaffolds for synthetic tissues. *Nature Materials* **11**, 986-994, doi:10.1038/nmat3404 (2012).

6 Fang, H., Yu, K. J., Gloschat, C., Yang, Z., Chiang, C. H., Zhao, J., Won, S. M., Xu, S., Trumpis, M., Zhong, Y., Song, E., Han, S. W., Xue, Y., Xu, D., Cauwenberghs, G., Kay, M., Huang, Y., Viventi, J., Efimov, I. R. & Rogers, J. A. Capacitively coupled arrays of multiplexed

flexible silicon transistors for long-term cardiac electrophysiology. *Nature Biomedical Engineering* **1**, 0038, doi:10.1038/s41551-017-0038 (2017).

7 Colicos, M. A., Collins, B. E., Sailor, M. J. & Goda, Y. Remodeling of synaptic actin induced by photoconductive stimulation. *Cell* **107**, 605-616 (2001).

8 Tee, B. C., Chortos, A., Berndt, A., Nguyen, A. K., Tom, A., McGuire, A., Lin, Z. C., Tien, K., Bae, W. G., Wang, H., Mei, P., Chou, H. H., Cui, B., Deisseroth, K., Ng, T. N. & Bao, Z. A skin-inspired organic digital mechanoreceptor. *Science* **350**, 313-316, doi:10.1126/science.aaa9306 (2015).

9 Khodagholy, D., Gelinas, J. N., Thesen, T., Doyle, W., Devinsky, O., Malliaras, G. G. & Buzsaki, G. NeuroGrid: recording action potentials from the surface of the brain. *Nature Neuroscience* **18**, 310-315, doi:10.1038/nn.3905 (2015).

10 Fu, T. M., Hong, G., Zhou, T., Schuhmann, T. G., Viveros, R. D. & Lieber, C. M. Stable long-term chronic brain mapping at the single-neuron level. *Nature Methods* **13**, 875-882, doi:10.1038/nmeth.3969 (2016).

11 Chortos, A., Liu, J. & Bao, Z. Pursuing prosthetic electronic skin. *Nature Materials* **15**, 937-950, doi:10.1038/nmat4671 (2016).

12 Someya, T., Bao, Z. & Malliaras, G. G. The rise of plastic bioelectronics. *Nature* **540**, 379-385, doi:10.1038/nature21004 (2016).

13 Chiappini, C., Martinez, J. O., De Rosa, E., Almeida, C. S., Tasciotti, E. & Stevens, M. M. Biodegradable nanoneedles for localized delivery of nanoparticles in vivo: exploring the biointerface. *ACS Nano* **9**, 5500-5509, doi:10.1021/acsnano.5b01490 (2015).

14 Zimmerman, J. F., Murray, G. F., Wang, Y., Jumper, J. M., Austin, J. R., II & Tian, B. Free-standing kinked silicon nanowires for probing inter- and intracellular force dynamics. *Nano Letters* **15**, 5492-5498, doi:10.1021/acs.nanolett.5b01963 (2015).

15 Chu, B., Burnett, W., Chung, J. W. & Bao, Z. Bring on the bodyNET. *Nature* **549**, 328-330, doi:10.1038/549328a (2017).

16 Sakimoto, K. K., Wong, A. B. & Yang, P. Self-photosensitization of nonphotosynthetic bacteria for solar-to-chemical production. *Science* **351**, 74-77, doi:10.1126/science.aad3317 (2016).

17 Liu, C., Colon, B. C., Ziesack, M., Silver, P. A. & Nocera, D. G. Water splitting-biosynthetic system with CO(2) reduction efficiencies exceeding photosynthesis. *Science* **352**, 1210-1213, doi:10.1126/science.aaf5039 (2016).

18 Chen, R., Romero, G., Christiansen, M. G., Mohr, A. & Anikeeva, P. Wireless magnetothermal deep brain stimulation. *Science* **347**, 1477-1480, doi:10.1126/science.1261821 (2015).

19 Seo, D., Neely, R. M., Shen, K., Singhal, U., Alon, E., Rabaey, J. M., Carmena, J. M. & Maharbiz, M. M. Wireless recording in the peripheral nervous system with ultrasonic neural dust. *Neuron* **91**, 529-539, doi:10.1016/j.neuron.2016.06.034 (2016).

20 Nadeau, P., El-Damak, D., Glettig, D., Kong, Y. L., Mo, S., Cleveland, C., Booth, L., Roxhed, N., Langer, R., Chandrakasan, A. P. & Traverso, G. Prolonged energy harvesting for ingestible devices. *Nature Biomedical Engineering* **1**, 0022, doi:10.1038/s41551-016-0022 (2017).

21 Jiang, Y., Carvalho-de-Souza, J. L., Wong, R. C., Luo, Z., Isheim, D., Zuo, X., Nicholls, A. W., Jung, I. W., Yue, J., Liu, D. J., Wang, Y., De Andrade, V., Xiao, X., Navrazhnykh, L., Weiss, D. E., Wu, X., Seidman, D. N., Bezanilla, F. & Tian, B. Heterogeneous silicon mesostructures for lipid-supported bioelectric interfaces. *Nature Materials* **15**, 1023-1030, doi:10.1038/nmat4673 (2016).

22 Grossman, N., Bono, D., Dedic, N., Kodandaramaiah, S. B., Rudenko, A., Suk, H. J., Cassara, A. M., Neufeld, E., Kuster, N., Tsai, L. H., Pascual-Leone, A. & Boyden, E. S. Noninvasive deep brain stimulation via temporally interfering electric fields. *Cell* **169**, 1029-1041 doi:10.1016/j.cell.2017.05.024 (2017).

23 Dagdeviren, C., Javid, F., Joe, P., von Erlach, T., Bensel, T., Wei, Z., Saxton, S., Cleveland, C., Booth, L., McDonnell, S., Collins, J., Hayward, A., Langer, R. & Traverso, G. Flexible piezoelectric devices for gastrointestinal motility sensing. *Nature Biomedical Engineering* **1**, 807-817, doi:10.1038/s41551-017-0140-7 (2017).

24 Dalby, M. J., Gadegaard, N. & Oreffo, R. O. Harnessing nanotopography and integrin-matrix interactions to influence stem cell fate. *Nature Materials* **13**, 558-569, doi:10.1038/nmat3980 (2014).

25 Zimmerman, J. F., Parameswaran, R., Murray, G., Wang, Y., Burke, M. & Tian, B. Cellular uptake and dynamics of unlabeled freestanding silicon nanowires. *Science Advances* **2**, e1601039, doi:10.1126/sciadv.1601039 (2016).

26 Tian, B., Zheng, X., Kempa, T. J., Fang, Y., Yu, N., Yu, G., Huang, J. & Lieber, C. M. Coaxial silicon nanowires as solar cells and nanoelectronic power sources. *Nature* **449**, 885-889, doi:10.1038/nature06181 (2007).

27 Ghezzi, D., Antognazza, M. R., Maccarone, R., Bellani, S., Lanzarini, E., Martino, N., Mete, M., Pertile, G., Bisti, S., Lanzani, G. & Benfenati, F. A polymer optoelectronic interface restores light sensitivity in blind rat retinas. *Nature Photonics* **7**, 400-406, doi:10.1038/nphoton.2013.34 (2013).

28 Merrill, D. R., Bikson, M. & Jefferys, J. G. Electrical stimulation of excitable tissue: design of efficacious and safe protocols. *Journal of Neuroscience Methods* **141**, 171-198, doi:10.1016/j.jneumeth.2004.10.020 (2005).

29 Ziegenfuss, J. S., Biswas, R., Avery, M. A., Hong, K., Sheehan, A. E., Yeung, Y. G., Stanley, E. R. & Freeman, M. R. Draper-dependent glial phagocytic activity is mediated by Src and Syk family kinase signalling. *Nature* **453**, 935-939, doi:10.1038/nature06901 (2008).

30 Yoon, J., Park, J., Choi, M., Choi, W. J. & Choi, C. Application of femtosecond-pulsed lasers for direct optical manipulation of biological functions. *Annalen Der Physik* **525**, 205-214, doi:10.1002/andp.201200099 (2013).

31 White, J. A., Blackmore, P. F., Schoenbach, K. H. & Beebe, S. J. Stimulation of capacitative calcium entry in HL-60 cells by nanosecond pulsed electric fields. *Journal of Biological Chemistry* **279**, 22964-22972, doi:10.1074/jbc.M311135200 (2004).

32 Hua, W., Young, E. C., Fleming, M. L. & Gelles, J. Coupling of kinesin steps to ATP hydrolysis. *Nature* **388**, 390-393, doi:10.1038/41118 (1997).

33 Stout, C. E., Costantin, J. L., Naus, C. C. & Charles, A. C. Intercellular calcium signaling in astrocytes via ATP release through connexin hemichannels. *Journal of Biological Chemistry* **277**, 10482-10488, doi:10.1074/jbc.M109902200 (2002).

34 Guthrie, P. B., Knappenberger, J., Segal, M., Bennett, M. V., Charles, A. C. & Kater, S. B. ATP released from astrocytes mediates glial calcium waves. *Journal of Neuroscience* **19**, 520-528 (1999).

35 Chen, H. X. & Diebold, G. Chemical generation of acoustic waves: A giant photoacoustic effect. *Science* **270**, 963-966, doi:DOI 10.1126/science.270.5238.963 (1995).

36 Tang-Schomer, M. D., Patel, A. R., Baas, P. W. & Smith, D. H. Mechanical breaking of microtubules in axons during dynamic stretch injury underlies delayed elasticity, microtubule disassembly, and axon degeneration. *FASEB Journal* **24**, 1401-1410, doi:10.1096/fj.09-142844 (2010).

37 Maya-Vetencourt, J. F., Ghezzi, D., Antognazza, M. R., Colombo, E., Mete, M., Feyen, P., Desii, A., Buschiazzo, A., Di Paolo, M., Di Marco, S., Ticconi, F., Emionite, L., Shmal, D., Marini, C., Donelli, I., Freddi, G., Maccarone, R., Bisti, S., Sambuceti, G., Pertile, G., Lanzani, G. & Benfenati, F. A fully organic retinal prosthesis restores vision in a rat model of degenerative blindness. *Nature Materials* **16**, 681-689, doi:10.1038/nmat4874 (2017).

38 Ghezzi, D., Antognazza, M. R., Dal Maschio, M., Lanzarini, E., Benfenati, F. & Lanzani, G. A hybrid bioorganic interface for neuronal photoactivation. *Nature Communications* **2**, 166, doi:10.1038/ncomms1164 (2011).

39 Lorach, H., Goetz, G., Smith, R., Lei, X., Mandel, Y., Kamins, T., Mathieson, K., Huie, P., Harris, J., Sher, A. & Palanker, D. Photovoltaic restoration of sight with high visual acuity. *Nature Medicine* **21**, 476-482, doi:10.1038/nm.3851 (2015).

40 Katz, L. C. & Dalva, M. B. Scanning laser photostimulation: a new approach for analyzing brain circuits. *Journal of Neuroscience Methods* **54**, 205-218 (1994).

41 Yamawaki, N., Suter, B. A., Wickersham, I. R. & Shepherd, G. M. Combining optogenetics and electrophysiology to analyze projection neuron circuits. *Cold Spring Harbor Protocols* **2016**, doi:10.1101/pdb.prot090084, doi:10.1101/pdb.prot090084 (2016).

42 Paralikar, K. J., Rao, C. R. & Clement, R. S. New approaches to eliminating common-noise artifacts in recordings from intracortical microelectrode arrays: inter-electrode correlation and virtual referencing. *Journal of Neuroscience Methods* **181**, 27-35, doi:10.1016/j.jneumeth.2009.04.014 (2009).

43 Veerabhadrappa, R., Lim, C. P., Nguyen, T. T., Berk, M., Tye, S. J., Monaghan, P., Nahavandi, S. & Bhatti, A. Unified selective sorting approach to analyse multi-electrode extracellular data. *Scientific Reports* **6**, 28533, doi:10.1038/srep28533 (2016).

44 Rossant, C., Kadir, S. N., Goodman, D. F. M., Schulman, J., Hunter, M. L. D., Saleem, A. B., Grosmark, A., Belluscio, M., Denfield, G. H., Ecker, A. S., Tolias, A. S., Solomon, S., Buzsaki, G., Carandini, M. & Harris, K. D. Spike sorting for large, dense electrode arrays. *Nature Neuroscience* **19**, 634-641, doi:10.1038/nn.4268 (2016).

45 Yamawaki, N., Borges, K., Suter, B. A., Harris, K. D. & Shepherd, G. M. A genuine layer 4 in motor cortex with prototypical synaptic circuit connectivity. *Elife* **3**, e05422, doi:10.7554/eLife.05422 (2014).

46 Li, X., Yamawaki, N., Barrett, J. M., Kording, K. P. & Shepherd, G. M. G. Corticocortical signaling drives activity in a downstream area rapidly and scalably. *bioRxiv*, doi: 10.1101/154914 (2017).

47 Tennant, K. A., Adkins, D. L., Donlan, N. A., Asay, A. L., Thomas, N., Kleim, J. A. & Jones, T. A. The organization of the forelimb representation of the C57BL/6 mouse motor cortex as defined by intracortical microstimulation and cytoarchitecture. *Cerebral Cortex* **21**, 865-876, doi:10.1093/cercor/bhq159 (2011).

48 Boyden, E. S., Zhang, F., Bamberg, E., Nagel, G. & Deisseroth, K. Millisecond-timescale, genetically targeted optical control of neural activity. *Nature Neuroscience* **8**, 1263-1268, doi:10.1038/nn1525 (2005).

49 Dai, J., Brooks, D. I. & Sheinberg, D. L. Optogenetic and electrical microstimulation systematically bias visuospatial choice in primates. *Current Biology* **24**, 63-69, doi:10.1016/j.cub.2013.11.011 (2014).

50 Stauffer, W. R., Lak, A., Yang, A., Borel, M., Paulsen, O., Boyden, E. S. & Schultz, W. Dopamine neuron-specific optogenetic stimulation in Rhesus Macaques. *Cell* **166**, 1564-1571 doi:10.1016/j.cell.2016.08.024 (2016).

Chapter 4

Atomic gold-enabled three-dimensional lithography for silicon mesostructures

4.1 Introduction

Semiconductors with three-dimensional (3-D) mesoscale features[1-5] are an emerging class of materials, with promising applications from stretchable bioelectronics[3] to alternative plasmonics and metamaterials[6]. However, progress in this area has been impeded by challenges in chemical synthesis[5] and limitations in 3-D fabrication methods[1,2,4,7]. As a result, this area would benefit from new synthetic concepts or new components in lithography. One place to look for such inspiration is from biomaterial-based processes, which routinely assemble mesostructured materials. In the growth of natural hard biomaterials, trace amount of interfacial organic species represent a unique component[8], yielding unusual 3-D biomaterial shapes and properties. The application of trace organic molecules as components (*e.g.*, an etching resist) in semiconductor-based lithography is hard to achieve, given semiconductor processing typically involves either high temperature gas-phase or harsh solution-phase preparations. However, inorganic species are much more stable and can be introduced as trace component into various semiconductors, as either impurities in the bulk volume[9-11] or as diffused species near the surface[12-16], with the latter holding great potential in 3-D semiconductor lithography given surface diffusion is versatile and more controllable. In this chapter, I will exploit the phenomena for 3-D mesoscale lithography, by showing one example where iterated deposition-diffusion-incorporation of gold over silicon nanowires forms etchant-resistant patterns. I will also show that this process is facet selective and

can produce mesostructured silicon spicules with skeleton-like morphology, three-dimensional tectonic motifs, and reduced symmetries. Atom-probe tomography, coupled with other quantitative measurements, indicates the existence and the role of individual gold atoms in forming 3-D lithographic resists. Finally, compared to other more uniform silicon structures, the anisotropic spicule requires greater force for detachment from collagen hydrogels, suggesting enhanced interfacial interactions at the mesoscale.

4.2 Results and Discussion

4.2.1 Graded, anisotropic, three-dimensional spicules

Three-dimensional (3-D) mesostructured semiconductors show promising properties and applications, however to date few methods exist to synthesize or fabricate such materials. Metal can diffuse along semiconductor surfaces, and even trace amount can change the surface behavior. Here, we focus on 3-D mesoscale lithography of Si nanowires with diffused gold (Au)[13,14,17], where Au originates from the nanoparticle catalyst used for nanowire nucleation and elongation[18] (**Fig. 4-1**). Because Au diffusion over Si surfaces is pressure-dependent[16], we first adopted periodic pressure-modulation during an Au-catalyzed Si nanowire synthesis to develop Au diffusion-induced patterns along nanowire sidewalls (**Fig. 4-2**), where silane (SiH_4) and diborane (B_2H_6) were used as a Si precursor and a *p*-type dopant, respectively.

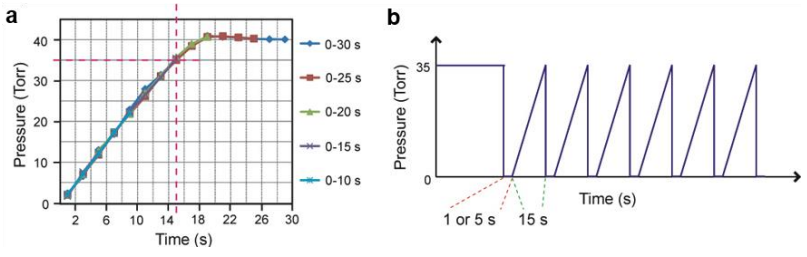

Figure 4-1. Chemical synthesis of Si spicules requires pressure modulation. a, Real total pressure changes during chemical growth. The color-coded traces represent pressure changes in five independent tests with 10, 15, 20, 25 or

Figure 4-1, continued. 30 s growth durations. The target pressure setting in MKS Model 250 Pressure Controller is 40 Torr. Most experiments reported in this article used 15 s ramp duration (vertical dashed magenta line), which reached a final pressure of ~ 35 Torr (horizontal dashed magenta line) in a quasi-linear manner. **b**, Schematic pressure variation during synthesis of modulated silicon. The evacuation duration is typically 1 or 5 s, while the pressure ramp duration is 15 s.

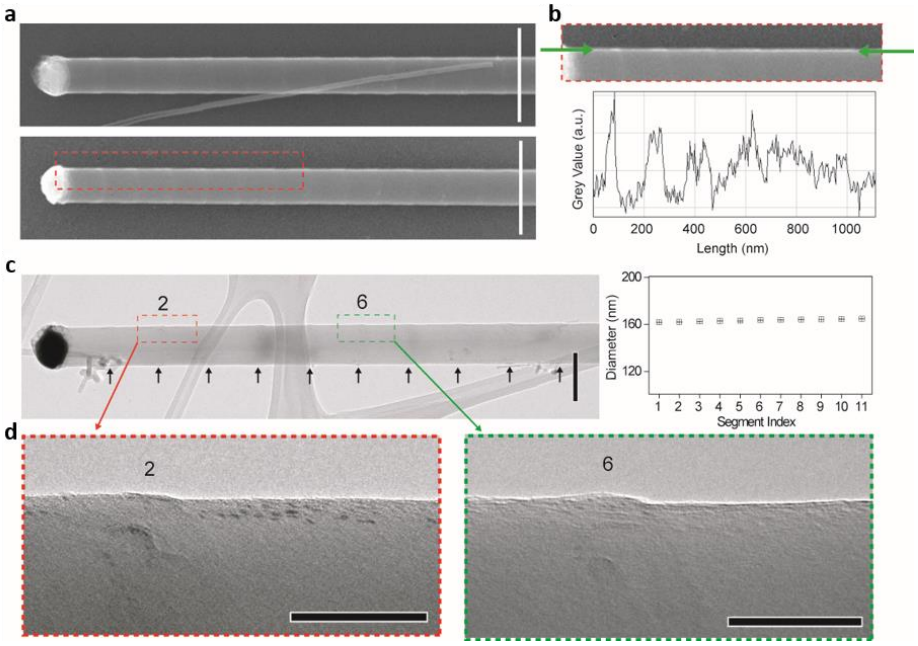

Figure 4-2. Structures of as-grown *p*-type Si nanowires. a, SEM images of two typical nanowires. The *p*-type Si nanowires were grown at 470 ºC, and evacuated for 1 s in each pressure modulations. Scale bars: 500 nm. **b**, 'Grey value' profile along a straight line defined by the two green arrows. The region is selected from the lower SEM image (dashed red box) in **a**. The profile qualitatively suggests a step-wise diffusion of gold along Si nanowire sidewalls. **c**, TEM image (left) of an as-grown *p*-type Si nanowire, with pressure drop positions marked with arrows. Scale bar, 200 nm. The diameter profile (right) suggests minimum tapering. The segment diameters are the widths measured at the middle of adjacent pressure drop points (marked with arrows). Error bars indicate ± 1 SD from the mean. **d**, Zoom-in views of the regions marked in **c**, showing nanowire surfaces near #2 and #6 pressure drop locations. Scale bars, 50 nm.

Next, we revealed the Au-based patterns with anisotropic wet chemical etching in KOH solutions (**Fig. 4-3**). The as-grown Si structures have rather uniform diameters except periodic

swells at the evacuation locations (**Fig. 4-2**). After etching, we identified two Si mesostructures from the same growth batch, Type I spicule with plate-like nodes and Type II spicule with triangle shaped nodes (**Fig. 4-4a**, **4-4b**). Portions of nanowire surfaces remained after etching, suggesting the diffused Au acted as an etching resist. Both spicule structures show gradient, curved and anisotropic surface textures. These formations are reminiscent of other complex nanowire morphologies[19-24], but are also similar to some naturally occurring hard materials, such as skeleton[8].

Transmission electron microscopy (TEM) images of *p*-type Si spicules (**Fig. 4-4**) show that Type I and Type II structures grow along the <111> and <112> directions, respectively. While Type I is a single crystal, Type II spicule has a {111} twin plane [11] which separates subunits α and β (**Fig. 4-4f**, TB marks the twin boundary), as determined by the two sets of diffraction spots (**Fig. 4-4f**, magenta/white and blue/white dashed circles) in the selected area electron diffraction (SAED) pattern.

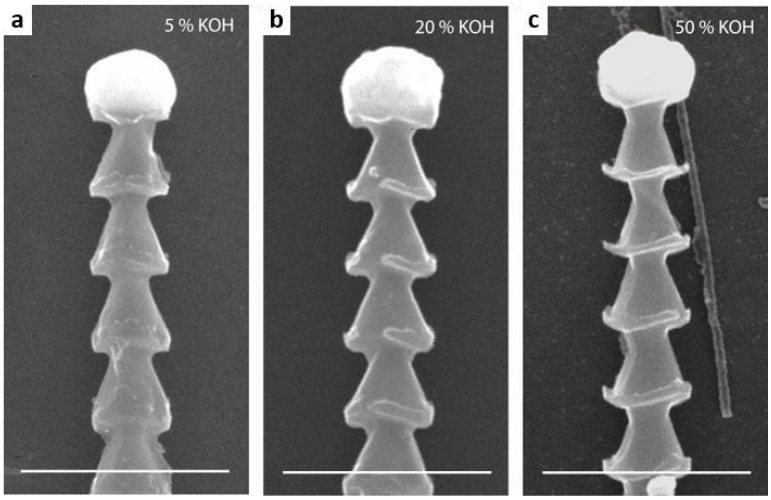

Figure 4-3. SEM images of spicule structures prepared at different KOH concentrations. We tested etching in 5 % (weight by volume, w/v) (**a)** 20 % (w/v) (**b**) and 50 % (w/v) (**c**) KOH solutions. The duration was 5 s and temperature was 60 ^{o}C. We chose a moderate concentration (20 %) in most part of our work. Scale bars, 500 nm.

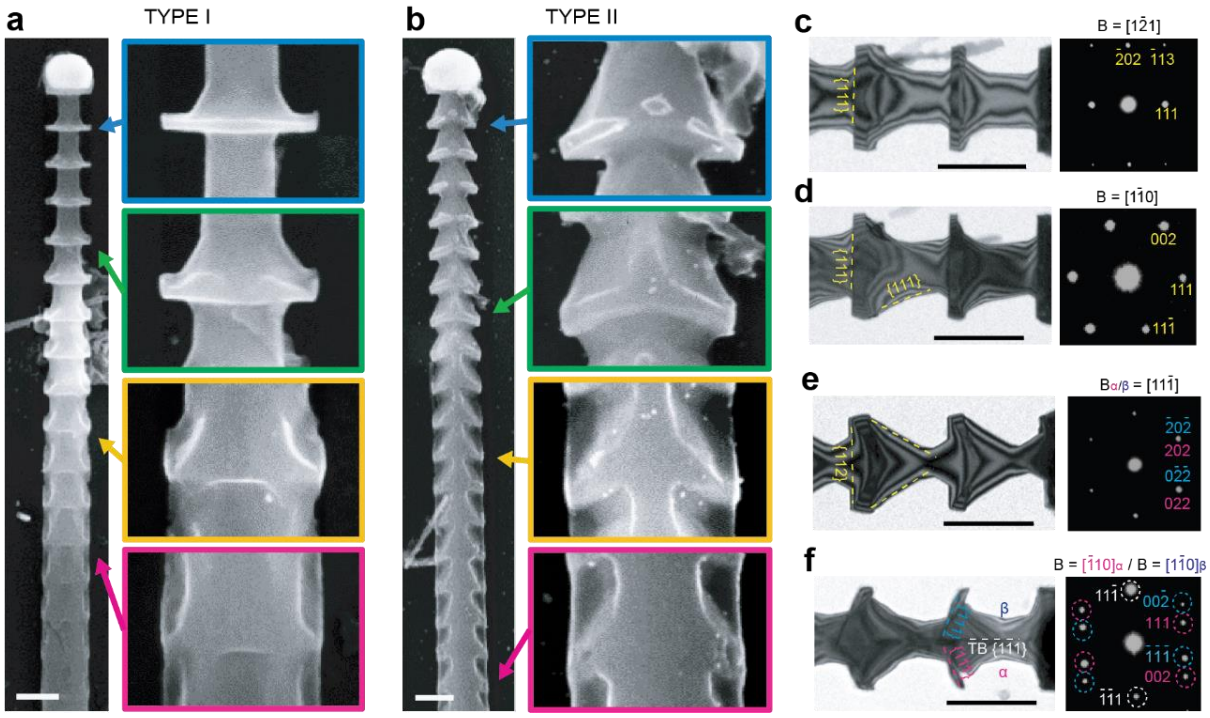

Figure 4-4. Electron microscope images of Type I (a, c, d) and Type II (b, e, f) skeleton-like silicon spicules. **a** and **b**, SEM images. The right columns are zoomed-in views of individual segments shown in the left columns. **c-f**, TEM and SAED patterns of Type I and Type II structures, viewed from $[1\bar{2}1]$ (**c**), $[1\bar{1}0]$ (**d**), $[11\bar{1}]$ (**e**) and $[\bar{1}10]_{\alpha}/[1\bar{1}0]_{\beta}$ (**f**) zone axes. The numbers in SAED patterns are diffraction spots, which reveal [111] and $[112]_{\alpha}/[\bar{1}\bar{1}\bar{2}]_{\beta}$ growth orientations for Type I and II structures. Red and blue colors in **e** and **f** highlight information from twinning subunit α and β, respectively. Scale bars, 200 nm.

We used scanning transmission electron microscopy (STEM) for tomograms of mesostructured Si spicules[18] (**Fig. 4-5**). In addition to the expected structural gradient and anisotropy, we reveal convex and concave components in both types of spicules. Combined with the faceted edges observed in TEM, we constructed curved anisotropic shells (magenta lines) and {111} facets-based polyhedron cores (Type I: octahedron; Type II: trigonal bipyramid, blue and green lines) as the coupled two principal 'tectonic' motifs for individual nodes (**Fig. 4-6**).

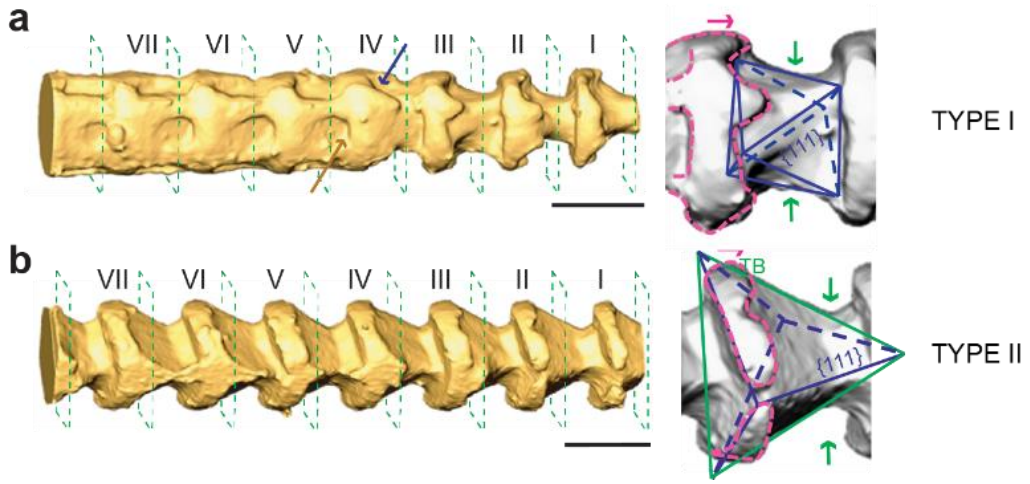

Figure 4-5. Mesostructured silicon spicules show defined motifs. a and **b**, STEM tomography of Type I (**a**) and II (**b**) spicules, with polyhedron-curved shell models shown on the right. The blue and brown arrows in the STEM tomography mark two different concave features. The magenta and green arrows in the models suggest 'morphogenesis' orientations for the two 'tectonic' motifs. Scale bars, 200 nm.

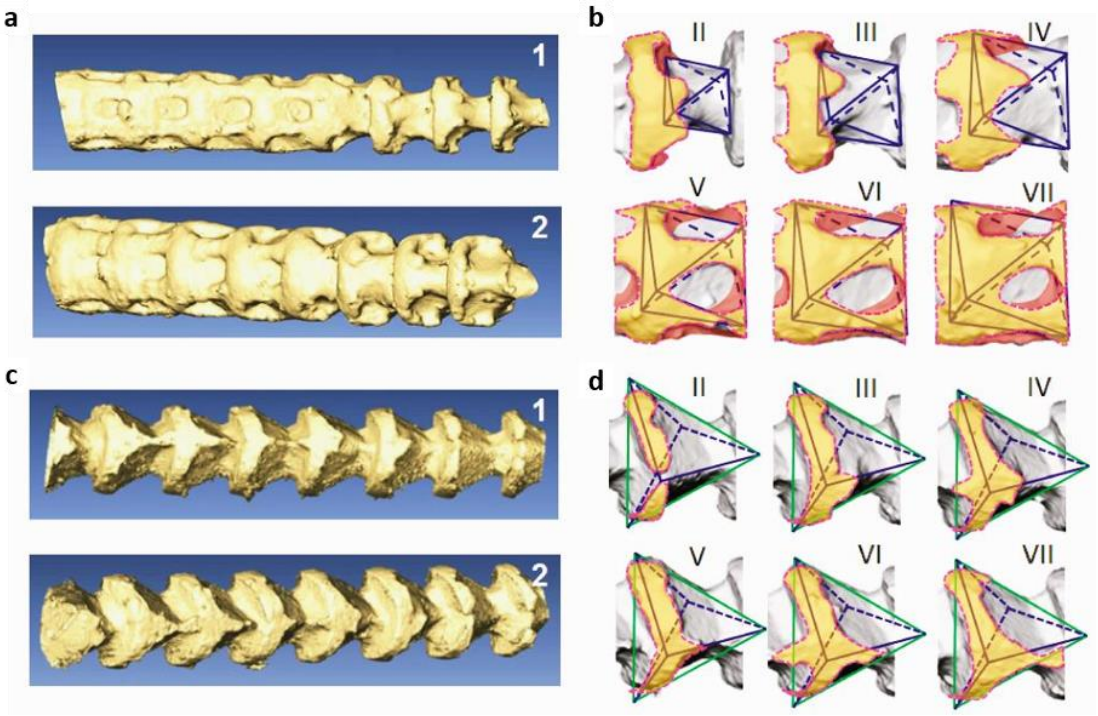

Figure 4-6. Two structural motifs (polyhedron and curved shell) can recover the complex features in mesostructured Si spicules. a, STEM tomography of a <111> Si spicule, viewed from different perspectives from those shown in **Fig. 4-5**. **b**, Polyhedron-curved shell models for segment II-VII of the sample shown in **a**. The

Figure 4-6, continued. octahedra evolve radially, while curved shells change axially. **c**, STEM tomography of a <112> Si spicule, viewed from different perspectives from those displayed in **Fig. 4-5**. **d**, Polyhedron-curved shell models for segment II-VII of the sample shown in **c**. The trigonal bipyramids do not change significantly for those segments, while curved shells evolve axially. The midplane of the bipyramids is a twin plane (marked with green lines).

We analyzed the surfaces[18] and mean curvatures (*i.e.* the average of the two principal curvatures) of individual segments (**Fig. 4-7**). We confirmed two groups of concave and highly curved patches in a Type I spicule segment (Segment IV, **Fig. 4-7a**, left) -- lower (brown arrows) and higher (blue arrows) sets -- consistent with the octahedron model (**Fig. 4-8**). They are arranged with a three-fold symmetry and were formed from selective etching of the left (**Fig. 4-5a**, brown arrow) and right (**Fig. 4-5a**, blue arrow) domains about the central plate, respectively (**Fig. 4-8**). In contrast, a Type II spicule segment (Segment VI, **Fig. 4-7b**, left) is capped with {111} planes, and only one {110} mirror plane is observed. 3-D mean curvature maps (**Figs. 4-7a** and **4-7b**, right) confirm the concave (blue) and convex (red) surfaces, and show that large mean-curvatures concentrate at the coupling regions between lateral shells and polyhedron cores.

The individual segment volumes and specific surface areas (*i.e.*, surface area/volume) generally increase and decrease, respectively, from Segment I to VII in both structures (**Figs. 4-7c** and **4-7d**, left). These facts suggest that etching of Si and the corresponding porosity, are more significant near the Au catalyst. The segment cross-sectional areas (**Figs. 4-7c** and **4-7d**, right; **Fig. 4-9**), {112} and {110} planes in Type I spicule and {110} and {111} planes in Type II spicule, all generally increase from Segment I to VII, suggesting a gradient in the pattern of etching resistance. Interestingly, the ratios of the two cross-sectional areas also change in different segments (**Figs. 4-7c** and **4-7d**, right), indicating non-uniform radial evolution of segment geometry.

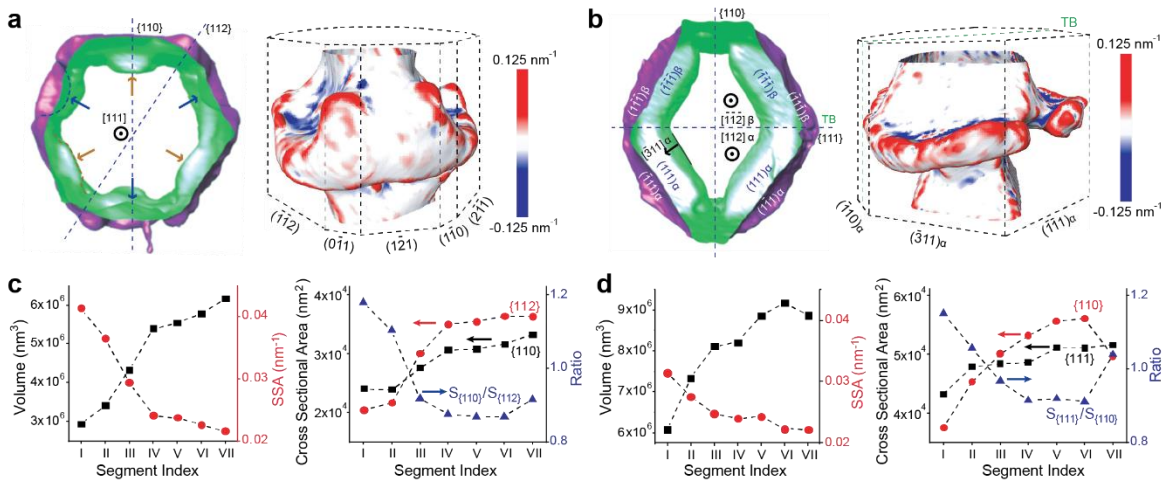

Figure 4-7. Mesostructured silicon spicules show pronounced curvature, anisotropy, and gradient. a-d, Iso-surfaces (**a** and **b**, left), 3-D curvature maps (**a** and **b**, right) and quantitative analysis of gradient (**c** and **d**) in Type I (**a**, **c**) and II (**b**, **d**) spicules. The numerical values in each segment are obtained using Amira 5.5 (FEI Visualization Sciences Group). Green and magenta colors in **a** mark the inside and outside surfaces, respectively. SSA stands for specific surface area. Scale bars in **a** and **b** represent 200 nm.

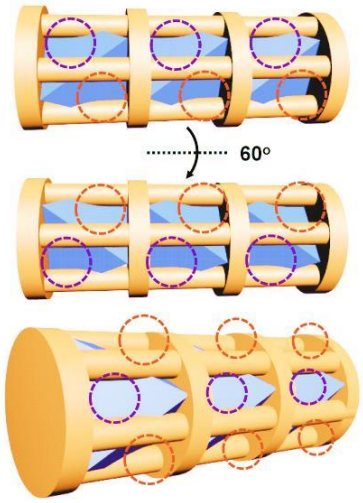

Figure 4-8. A model displaying two concave regions in <111> Si spicules. For simplicity, curved shells are replaced by regular struts (orange). Each octahedron (blue) has two of their {111} facets attached to adjacent strut discs. Dashed circles with different colors mark the two sets of concave regions. The three images display the same model viewed from different perspectives. It is noted that this simplified model does not recover the gradient in Si spicules.

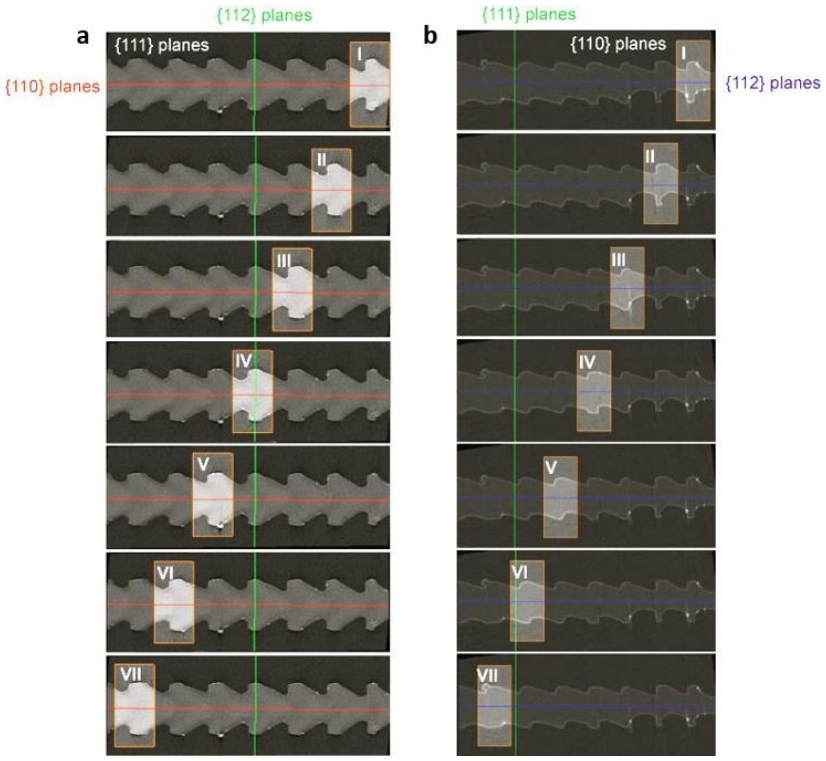

Figure 4-9. Complete-tilt STEM tomograms utilized for surface area analysis. a, A series of tomograms of <112> Si spicules sectioned at {111} planes. The highlighted regions are individual segments I-VII, where {111} cross-sectional areas in **Fig. 4-7c** were calculated. **b**, A series of tomograms of <111> Si spicules sectioned at {110} planes. The highlighted regions are individual segments I-VII, where {110} cross-sectional areas in **Fig. 4-7d** were calculated. Other cross-sectional areas were similarly analyzed. The tomograms were constructed and visualized using Amira 5.5 (FEI Visualization Sciences Group). The bright spots are Au nanoparticles, which are used as fiducial markers.

4.2.2 Atomic gold-based etch resist

To understand the pattern formation mechanism, we used X-ray photoelectron spectroscopy (XPS) to characterize Si surfaces prior to wet chemical etching (**Fig. 4-10**). Deconvolution of Au *4f* lines indicates the presence of two principle Au components in the detectable regime (< 10 nm), metallic Au and intermetallic silicide-like Au (**Fig. 4-10**, upper panel). For example, an Au 4*f* 7/2 peak at 84.0 eV with a full-width at half-maximum (FWHM) of 1.9 eV indicates metallic Au, while the one at 85.3 eV with a FWHM of 2.1 eV suggests the

intermetallic Au species [25]. The fact that intermetallic Au yields a notable XPS signal (area ratio: intermetallic/metallic ~ 1.068) suggests significant Au diffusion and subsequent incorporation into Si sub-surface regions. To decouple the role of metallic Au from the intermetallic one in establishing the sculpted structure, we removed metallic Au with a standard gold etchant, as confirmed from XPS (**Fig. 4-10**, lower panel). Notably, the primary sculpted structures can still be achieved even after prior removal of metallic gold (**Fig. 4-11**), suggesting that intermetallic Au in Si sub-surface play a major role as an etching resist.

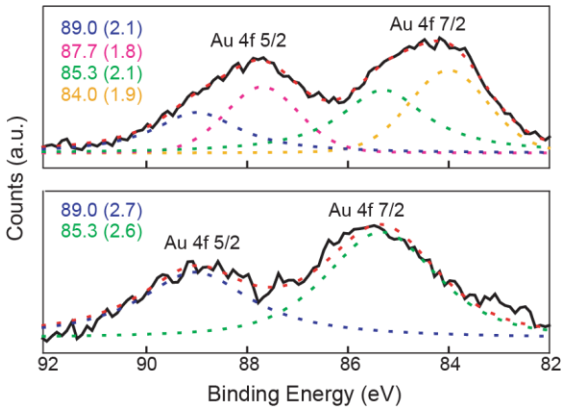

Figure 4-10. Intermetallic gold exists on Si surfaces. XPS spectra of modulated structures prior to silicon etching. Upper panel: without metallic gold removal. Lower panel: with metallic gold removal. Insets show the binding energy and FWHM (in parenthesis) of deconvoluted peaks.

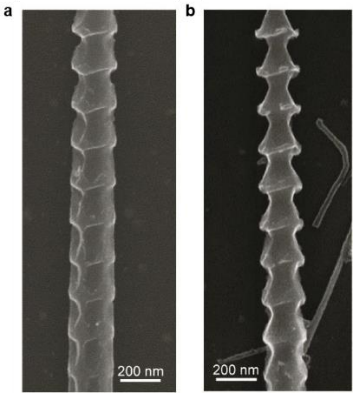

Figure 4-11. SEM images of <112> Si spicules suggest that metallic gold is not critical as the etching resist. SEM images of two Si spicules without (**a**) and with (**b**) metallic Au removal prior to Si etching displaying similar structures.

Figure 4-11, continued. This fact suggests that Au atoms that are incorporated into Si surface serve as the key resist component, while metallic Au is primarily the Au reservoir.

Utilizing a laser-assisted local-electrode atom-probe tomography (APT), we studied Au together with other elements with sub-nanometer spatial resolution. Proximity histogram (**Fig. 4-12a**)[18,26], plotted along the spicule radial direction and collected from an etching-resistive portion, indicates a gold enriched region localized at the Si/silica interface (*i.e.*, Si sidewall). The width of this region is ~ 7 nm. Surprisingly, the Au peak concentration is ~ 370 atomic ppm, which is less than that of boron (B) (~ 1370 atomic ppm in Si) but is substantially greater than the equilibrium Au concentration in bulk Si[27] and Si nanowires[17]. The enhanced concentration of Au in Si sub-surface may be due to the kinetic trapping[9] of Au by radially deposited Si upon SiH_4 decomposition. Significantly, a 3-D, atom-by-atom chemical reconstruction from a 30 nm × 30 nm × 20 nm region (**Fig. 4-12b**) reveals that Au exists mostly as isolated atoms, instead of continuous Au films, which are routinely used as etch masks for Si. The incorporation of Au atoms in a Si matrix also explains the intermetallic Au feature in XPS.

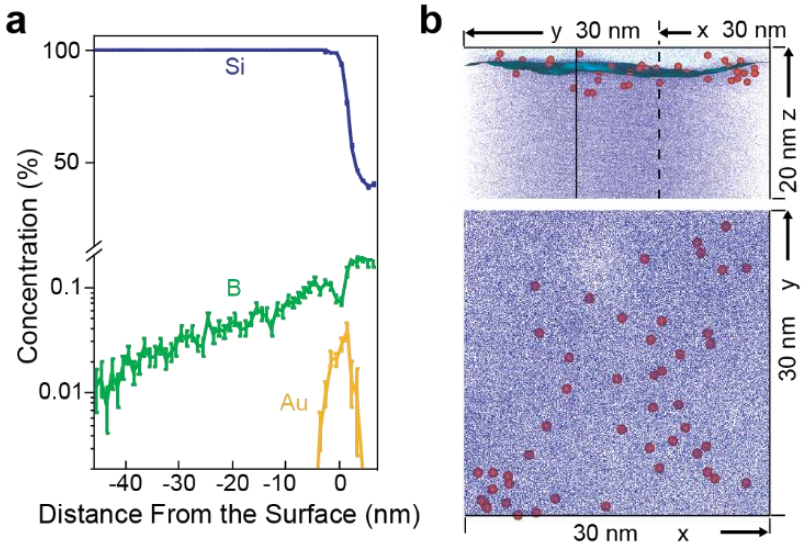

Figure 4-12. Atom-probe tomography analysis. a, Radial Si, B and Au concentration profiles. **b**, 3-D chemical reconstruction viewed from parallel (upper panel) and perpendicular (lower panel) directions to the sample axis,

Figure 4-12, continued. showing Si/SiO_2 interface (5% of O iso-surface, blue/cyan), Si (blue dots, 50%), Au (red dots, 100%) and O atoms (cyan dots, 50%).

Si wet chemical etching involves electron transfer at solid/liquid interface[28]. To answer how Au atoms induce an etch resist effect, we performed three-electrode electrochemical measurements (**Fig. 4-13**) using pressure modulated (black) and conventional non-modulated (red) *p*-type Si nanowires as the working electrodes (**Fig. 4-13**, inset), where bulk metallic Au (*i.e.*, Au that is not incorporated in Si) was removed with a gold etchant. Representative current versus voltage scans recorded in 5 (w/v) % KOH at room temperature (**Fig. 4-13**) demonstrate that the open circuit potential (*i.e.*, the potential difference between working and reference electrodes at open-circuit state, V_{ocp}) shifts anodically (from -1.199 to -1.081 V) when pressure-induced Au diffusion was applied, suggesting more difficult etching. A passivation potential, ~ -0.595V, appears in both pressure modulated and non-modulated samples and can be attributed to a blocking oxide layer formation[29]. However, in the conventional Si nanowire sample (red), we identified a shoulder peak centered around -0.785 V, which is not apparent in Au incorporated Si sample (black) and can be ascribed to an etching process at Au-free Si nanowire surfaces. Since Au atoms are known to form recombination centers in Si, the random Au-based carrier traps effectively retard adjacent electron-based reactions[28,29] over the Au incorporated nanowire shell region. This etching resist effect involves a shallow chemical reaction through individual atoms, and is different from that in traditional silicon nitride (Si_xN_y) or Au film based etching masks, where physical blockage by chemically inert materials plays a key role.

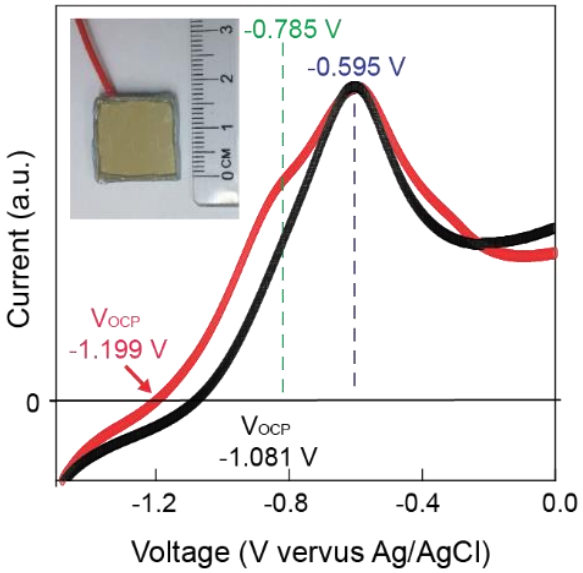

Figure 4-13. Electrochemical characterizations. Current-Voltage curves collected using pressure modulated (black) and pressure non-modulated (red) silicon structures as working electrodes. Metallic gold was removed with a gold etchant. Inset shows the device image, where the edge and back side of silicon wafer were passivated with epoxy. Two curves are normalized using the peak at -0.595 V.

We studied the effect of a *p*-type dopant, diborane (B_2H_6), on the spicule morphologies. Results collected in <112> Si spicules (**Fig. 4-14**) demonstrate that as B_2H_6 feeding increases from 1:4000 to 1:1000 (B:Si), the areas of Au-atom-decorated shells (enclosed in dashed yellow lines, **Fig. 4-14**) and the widths along the midline on the remaining {111} facets (dashed red lines, **Fig. 4-14**, inset) increase. Additionally, the midline width versus segment plot (**Fig. 4-14**) exhibits typically zero values in the segments closer to Au catalysts (phase I), followed by a linear increase (phase II, see linear fittings, **Fig. 4-14**) and finally a plateau regime (phase III). The initial absence of Au protected {111} facets suggests that in <112> Si spicules, {113} facets are the major Au deposition zones, while {111} facets are primarily used for Au diffusion and incorporation which initiates at a later stage (**Fig. 4-15**). The linear advance of the interface (*i.e.*, $L \propto t$ or $L \propto n$, where *n* is the segment index) in phase II suggests that the patterned resist formation is a Au/Si reaction

limited process [18], as a diffusive one is usually described by nonlinear power laws ($L \propto t^{\alpha}$, $\alpha \leq 0.5$) [12]. The plateau indicates the merging of Au incorporated patterns from adjacent segments, after which interconnection is achieved. The higher feeding ratio of B:Si, 1:1000 vs.1:4000, yields a larger slope (*i.e.*, 37.6 nm/segment vs. 28.7 nm/segment) and an earlier onset (*i.e.*, segment 5 vs. 9) for the linear regions, suggesting that B_2H_6 can promote Au deposition, diffusion and incorporation. A similar behavior was observed in <111> silicon spicules, and we note that $\{11\bar{2}\}$ facets are primary Au deposition zones (**Fig. 4-16**).

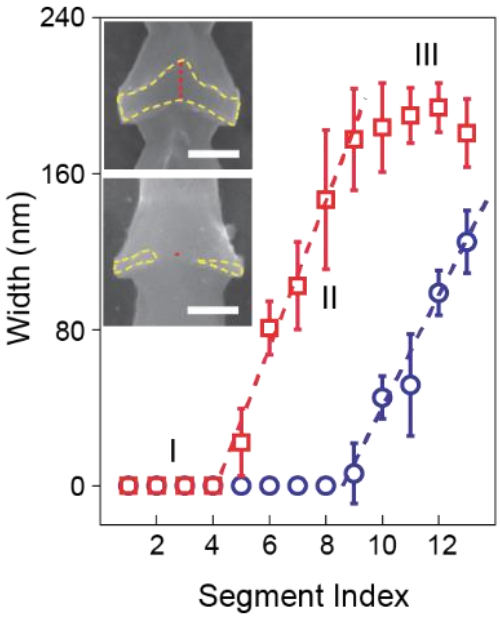

Figure 4-14. The effect of diborane on spicule morphogenesis and Au diffusion profiles. Insets show SEM images of the 6th segment with 1:1000 (upper panel) and 1:4000 (lower panel) B:Si feeding ratios. Scale bars, 100 nm.

4.2.3 Theoretical analysis of gold diffusion process

The diffusion equation in cylindrical coordinates, *r*, θ, and *z*, is

$$\frac{\partial C}{\partial t} = \frac{1}{r}\left\{\frac{\partial}{\partial r}\left(rD\frac{\partial C}{\partial r}\right) + \frac{\partial}{\partial \theta}\left(\frac{D}{r}\frac{\partial C}{\partial \theta}\right) + \frac{\partial}{\partial z}\left(rD\frac{\partial C}{\partial z}\right)\right\}. \qquad (4\text{-}1)$$

For simplicity, we consider planar diffusion of Au on one facet of Si nanowires under the steady-state condition[12, 34],

$$\frac{d}{dL}\left(L\frac{dC}{dL}\right)=0, \tag{4-2}$$

where C is the atomic concentration of Au and L is the diffusion length.

The following boundary conditions were employed: (i) the concentration of Au is C_0 at the diffusion source (initial length L_0); and (ii) C_{Lt} is the concentration at the length L_t, at time t.

The solution to (2) is therefore:

$$C_L=\frac{\left(C_{L_t}-C_0\right)\ln(L)+C_0\ln\left(L_t\right)-C_{L_t}\ln(L_0)}{\ln\left(L_t/L_0\right)} \tag{4-3}$$

The steady-state diffusion flux of Au atoms is given by Fick's first law:

$$J_{\text{diff}}=-D_{\text{Au}}\frac{dC}{dL}, \tag{4-4}$$

where D_{Au} is the diffusivity of Au atoms. The diffusion flux can also be expressed in terms of chemical potentials according to:

$$C_L=\exp\left(\frac{\mu(L)-\mu^{\theta}}{k_BT}\right), \tag{4-5}$$

where $\mu(L)$ is the chemical potential of Au in a Au_ySi_{1-y} liquid alloy, μ^{Θ} is the chemical potential of Au in the standard state, k_B is Boltzmann's constant, and T is the thermodynamic temperature.

Then Au diffusion flux at the reaction front is given by:

$$J_{\text{diff}}\left(L_t\right)=-D_{\text{Au}}\left.\frac{dC}{dL}\right|_{L=L_t}=-\frac{D_{\text{Au}}}{L_t\ln\left(L_t/L_0\right)}\left[\exp\left(\frac{\mu_{L_t}-\mu^{\theta}}{k_BT}\right)-\exp\left(\frac{\mu_0-\mu^{\theta}}{k_BT}\right)\right], \tag{4-6}$$

where μ_0 and μ_{L_t} are the chemical potentials of Au near the diffusion source and reaction front, respectively.

The consumed Au flux for Au_xSi_{1-x} formation at reaction front is:

$$J_{\text{incorp}}(L_t) = M\left(\mu_{L_t} - \mu_{eq}\right), \tag{4-7}$$

where μ_{eq} is the equilibrium chemical potential of Au in solid Au_xSi_{1-x}, and M is a constant determined by how fast Au adatoms are incorporated into the Au_xSi_{1-x}/Si interface.

Equating J_{diff} and J_{incorp} at the reaction front yields:

$$\frac{D_{\text{Au}}}{L_t \ln\left(L_t/L_0\right)}\left[\exp\left(\frac{\mu_0 - \mu^{\theta}}{k_B T}\right) - \exp\left(\frac{\mu_{L_t} - \mu^{\theta}}{k_B T}\right)\right] = M\left(\mu_{L_t} - \mu_{eq}\right). \tag{4-8}$$

Taylor expanding the exponentials to first order yields:

$$\mu_{L_t} = \frac{D_{\text{Au}}\mu_0 + Mk_B T L_t \ln\left(L_t/L_0\right)\mu_{eq}}{D_{\text{Au}} + Mk_B T L_t \ln\left(L_t/L_0\right)}. \tag{4-9}$$

Substituting μ_{L_t} into Eq. 4-7, the diffusion speed of the reaction front averaged over one cycle of pressure modulation is estimated to be:

$$\overline{dL_t/dt} = \overline{J_{\text{incorp}}(L_t)} = \overline{M\left(\mu_0 - \mu_{eq}\right)\Big/\left\{1 + [Mk_B T L_t \ln\left(L_t/L_0\right)]/D_{\text{Au}}\right\}}.$$

Herein, M and D_{Au} are dependent on temperature, and partial pressures for silane and dopant gases.

If $D_{\text{Au}}/M >> k_B T L_t \ln\left(L_t/L_0\right)$ the process is reaction-limited[12, 34] and $\overline{dL_t/dt}$ becomes a constant, $\overline{M\left(\mu_0 - \mu_{eq}\right)}$. This leads to the observed linear dependence of L on segment index in phase II (**Fig. 4-14**). However, we note that the real synthesis involves much more complicated

processes, *e.g.*, radial incorporation of Si, and more boundary conditions due to crystal faceting, which are not considered in this estimation.

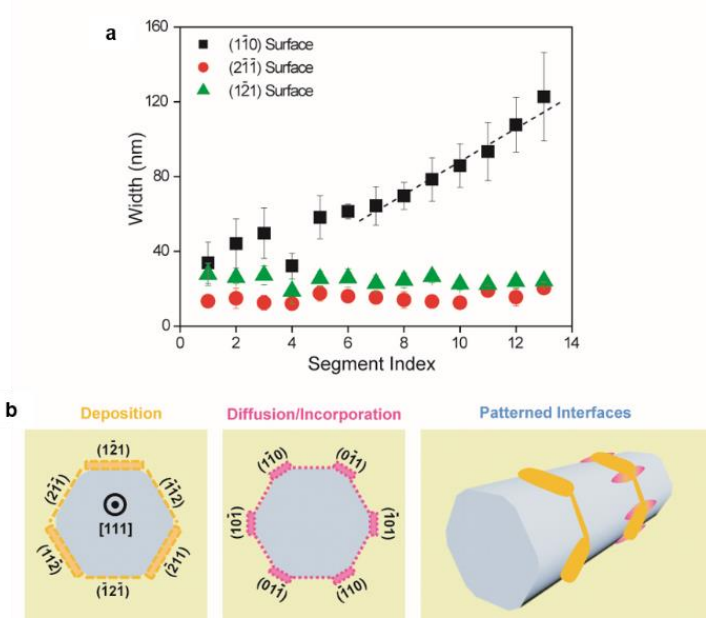

Figure 4-15. A study of the protected surfaces in <112> Si spicules reveal distinct facets for Au deposition, diffusion and incorporation. **a**, A plot showing midline widths (L) of the remaining surfaces in different segments. A linear evolution can be identified in part of both (111) and (1$\bar{1}$0) surface profiles, suggesting a reaction-limited Au diffusion/incorporation process. Additionally, the slopes are 37.6 nm/segment and 28.7 nm/segment for the width profiles on the (111) and (1$\bar{1}$0) surfaces, respectively, suggesting a larger Au diffusion/incorporation mobility over {111} facets. A very slow variation of widths on the (3$\bar{1}$1) surface suggests that {113} facets are primarily used for Au deposition, consistent with prior studies[35]. **b**, Schematic diagrams show that Au deposition and diffusion/incorporation take place on different facets, yielding patterned interfaces. This proposal is based on the results shown in **a**.

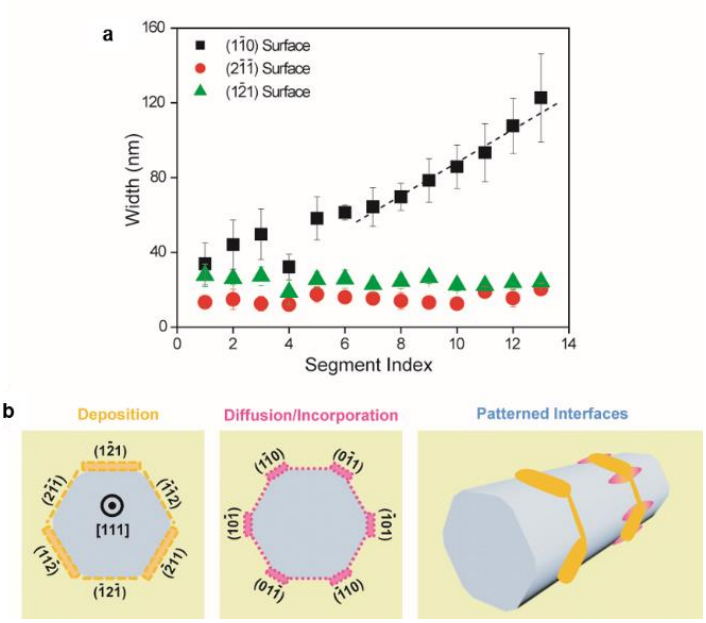

Figure 4-16. A study of the protected surfaces in <111> Si Spicules reveals distinct facets for Au deposition, diffusion and incorporation. **a**, A plot showing midline widths (*L*) of the remaining surfaces in different segments. A linear evolution can be identified in part of ($1\bar{1}0$) surface profile, suggesting a reaction-limited Au diffusion/incorporation process. Very slow variations of widths for both the ($2\bar{1}\bar{1}$) and ($1\bar{2}1$) surfaces suggest that {112} facets are primarily used for Au deposition. Additionally, ($1\bar{2}1$) surface displays generally larger midline widths than does the ($2\bar{1}\bar{1}$) surface, suggesting that $\{11\bar{2}\}$ facets are better in receiving Au deposition than the $\{\bar{1}\bar{1}2\}$ facets, consistent with prior studies[35]. This property also contributes to the observed anisotropy. **b**, Schematic diagrams show that Au deposition and diffusion/incorporation take place at different locations, and explain the pattern formation. This mechanism is based on the results displayed in **a**. It should be noted that {110} facets are less defined given curved morphology in <111> spicules.

We tested the effect of an *n*-type dopant, phosphine (PH_3). STEM tomography (**Fig. 4-17**) displayed a mesostructure with less gradient. To achieve optimal growth, we identified an ~ 15 ^oC higher growth temperature than when B_2H_6 is used, consistent with the fact that PH_3 and B_2H_6 can inhibit and enhance SiH_4 decomposition[30], respectively. Additionally, we needed to use an ~ 5 times longer evacuation time to promote Au coverage, suggesting that PH_3 is less effective than B_2H_6 in enabling the spreading of Au on silicon surfaces (**Figs. 4-17**, **4-18**), and such spreading is

critical for both efficient Au deposition and diffusion. Finally, if neither B_2H_6 nor PH_3 was added, *i.e.* intrinsic Si, we observed a larger number of isolated Au nanoparticles on the Si sidewalls (**Fig. 4-18d**), which yielded less defined mesostructures upon etching (**Figs. 4-19**, **4-20**).

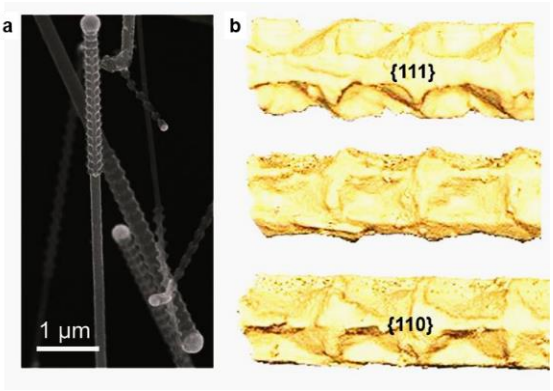

Figure 4-17. *n*-type Si spicules exhibit similar structures. a, SEM image of *n*-type Si spicules collected from their growth substrate, indicating a high yield. All spicules exhibit tilted views. **b**, STEM tomography of one *n*-type spicule viewed from different perspectives.

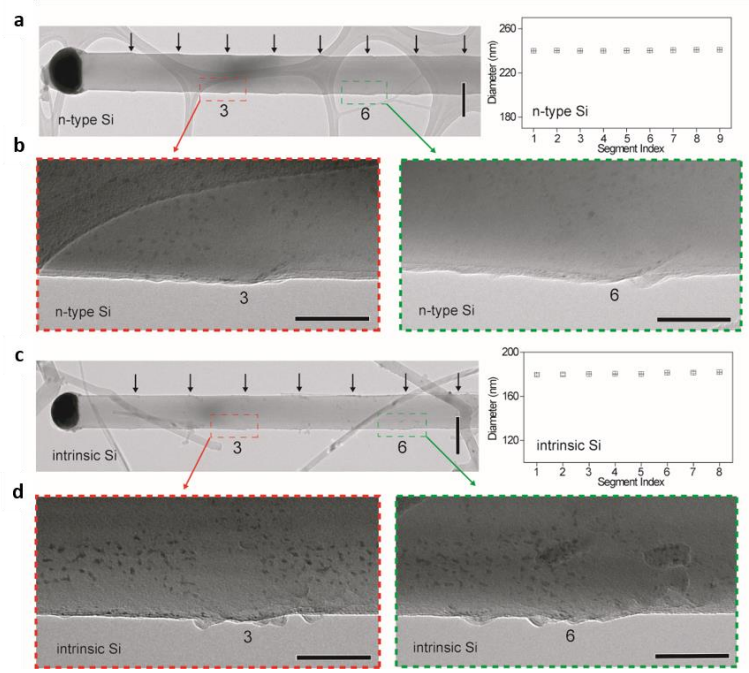

Figure 4-18. Structures of as-grown *n*-type (a, b) and intrinsic (c, d) Si nanowires. a, TEM image (left) of an as-grown *n*-type Si nanowire, with pressure drop positions marked with arrows. The *n*-type Si nanowires were grown at

Figure 4-18, continued. 485 ºC, and evacuated for 5 s in each pressure modulations. Scale bar, 200 nm. The diameter profile (right) suggests minimum tapering. The segment diameters are the widths measured at the middle of adjacent pressure drop points (marked with arrows). Error bars indicate ± 1 SD from the mean. **b**, Zoom-in views of the regions marked in **a**, showing nanowire surfaces near the #3 and #6 pressure drop locations. Scale bars, 50 nm. **c**, TEM image (left) of an as-grown intrinsic Si nanowire, with pressure drop positions marked with arrows. The intrinsic Si nanowires were grown at 485 ºC, and evacuated for 5 s in each pressure modulations. Scale bar, 200 nm. Likewise, the diameter profile (right) suggests minimum tapering. **d**, Zoom-in views of the regions marked in **c**, showing nanowire surfaces near the #3 and #6 pressure drop locations. Scale bars, 50 nm.

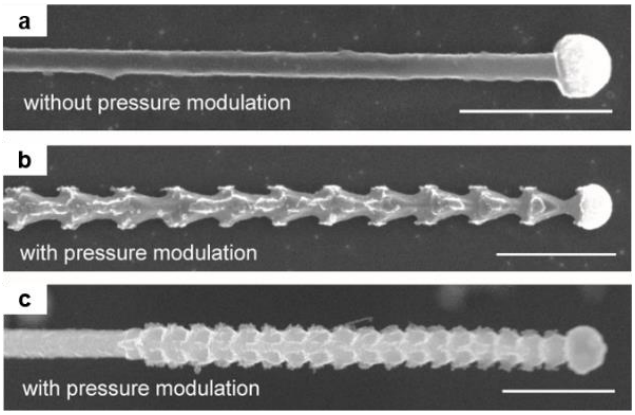

Figure 4-19. Intrinsic Si nanowires grown with pressure modulations yield rough etching structures. a, SEM image of an etched intrinsic <112> Si nanowire grown without pressure modulations, showing uniform etching around sidewalls. **b** and **c**, SEM images of KOH-etched, modulated, intrinsic <112> Si nanowires, recorded on a flat substrate **b** and a growth substrate **c**. The modulated intrinsic Si nanowires were grown at 485 ºC, and evacuated for 5 s in each pressure modulations. Results showed that although diffused Au over intrinsic Si can protect some of the Si surfaces, the etched structures have rough edges. Scale bars, 500 nm.

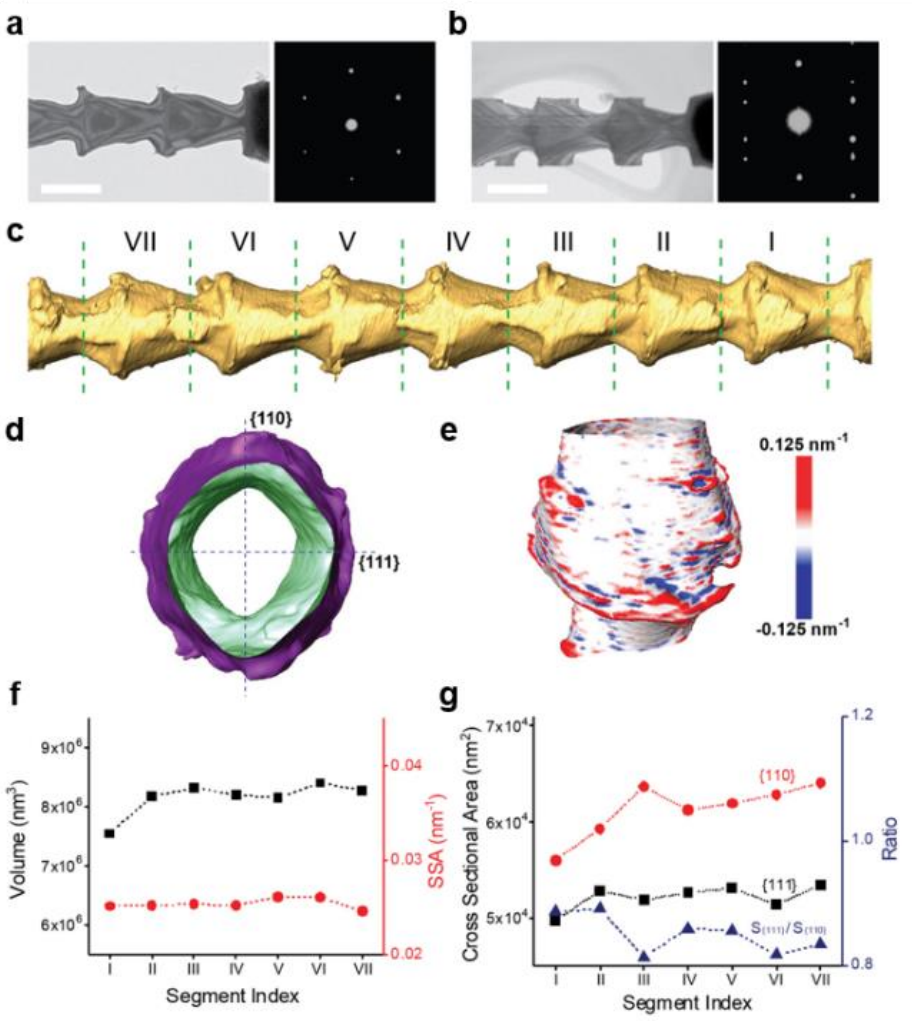

Figure 4-20. Intrinsic Si spicules show less defined 3D structures. a and **b**, TEM and SAED pattern, viewed from <111> (**a**) and <110> (**b**) zone axes. **c**-**g**, STEM tomography and quantitative analysis of an intrinsic Si spicule, with seven segments marked (**c**). Iso-surface map (segment I, **d**), 3D curvature map (segment I, **e**), and gradient analysis (**f**, **g**) of intrinsic Si spicule suggest less-defined structures, consistent with the SEM results in **Fig. 4-19**. The numerical values in each segment are obtained using Amira 5.5 (FEI Visualization Sciences Group). Green and magenta colors in **d** mark the inside and outside surfaces, respectively. SSA stands for specific surface area. Scale bars in **a** and **b** represent 200 nm.

4.2.4 Gold deposition-diffusion-incorporation mechanism

We propose a modular deposition-diffusion-incorporation mechanism for patterned-interface formation. Initially, the Si structure follows vapor-liquid-solid axial growth (**Fig. 4-21,**

1). Upon evacuation, the growth stops (**Fig. 4-21, 2**), and catalyst instability at a low pressure (~ 0.2 Torr) initiates Au deposition (**Fig. 4-21**, **III**, graded orange color band) and subsequent diffusion (**Fig. 4-21**, **II**, graded pink color band). During SiH_4 pressure recovery in the ramp period, the Au deposition and diffusion ceases [13], while the Si growth rate increases (**Fig. 4-21**, **I**, graded blue color band) to form a new segment (**Fig. 4-21, 3**). Decomposition of SiH_4 on the Si sidewalls assists robust incorporation of Au atoms into Si sub-surface. Iteration of this process (**Fig. 4-21, 4-6**) generates the anisotropic and graded Au/Si interfaces.

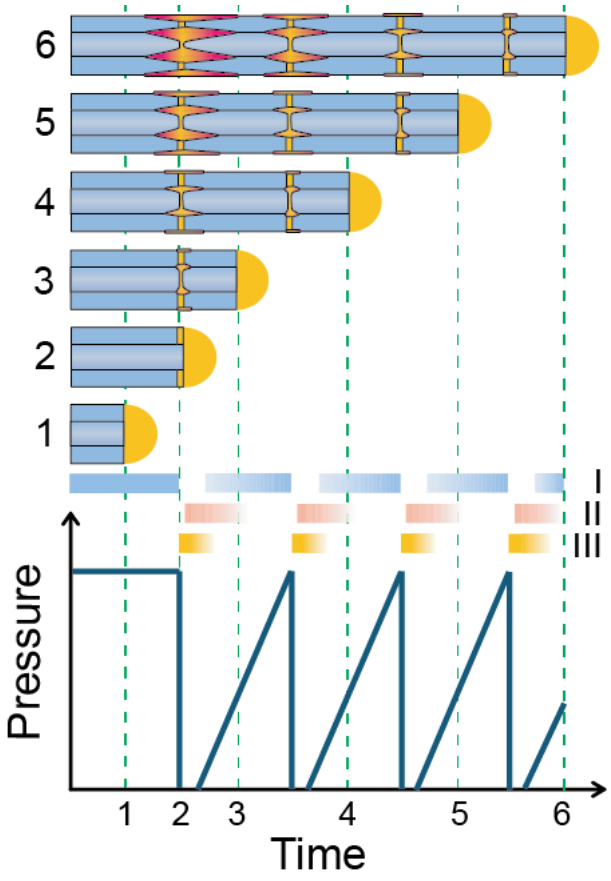

Figure 4-21. A schematic diagram illustrating the patterned interface formation. Graded color-bands denote Si axial elongation (**I**, blue), Au deposition (**III**, orange) and diffusion (**II**, pink). The numbers indicate different stages during a typical growth, and dashed lines mark the catalyst/Si interfaces at each stage.

This proposed mechanism is further corroborated by the fact that (1) B-doped nanowires grown without pressure modulation only yielded uniform etching structures (**Fig. 4-22**)[19], (2) intentional gold diffusion only at the end of *p*-type nanowire synthesis also yield etch resist (**Fig. 4-23**), (3) diffused Au did not recruit B which is known to affect Si etching, and (4) possible B incorporation directly from the gas phase is along the spicule radial direction, which is orthogonal to the direction for resist formation. Overall, we show dopant incorporation or nanowire initial morphology itself cannot yield the observed complex structures. The curvatures of the final spicules are defined by the shapes of patterned resists, curved catalyst-silicon interfaces, crystallographic orientations, and etching conditions. The initial, isolated Au nanoparticles play multiple roles, *i.e.*, catalyzing silicon growth, defining edge curvature and supplying diffused gold atoms and clusters. Finally, we note that since metal diffusion along semiconductor surfaces is general, *e.g.*, in GaP-Au[15], GaAs-Au[13,15], and Si-In/Sn[10] systems, similar patterning and lithography approach may be applied in other semiconductors.

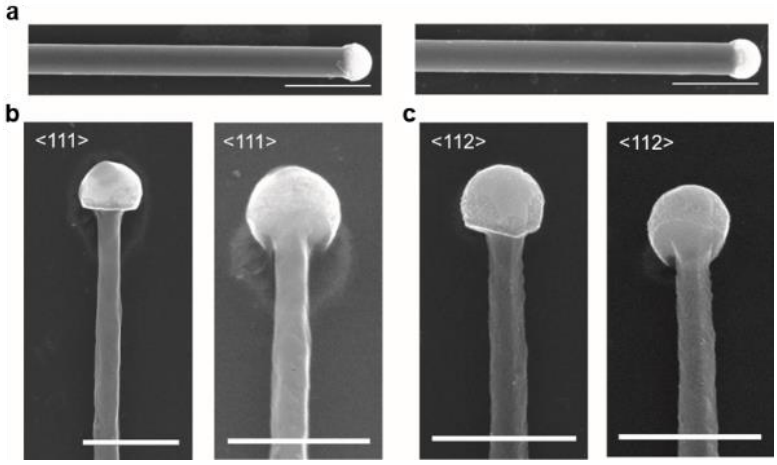

Figure 4-22. KOH etching of *p*-Si nanowires grown without pressure modulation is not sensitive to starting facets. a, SEM images of two typical as-grown *p*-Si nanowires. No pressure modulation was used during the synthesis. **b**, SEM images of an etched <111> *p*-Si nanowire. The right panel shows a tilted view and suggests uniform etching from sidewalls. **c**, SEM images of an etched <112> *p*-Si nanowire. The right panel shows a tilted view and suggests

Figure 4-22, continued. KOH etching is not sensitive to its starting facets (two {111}, four {113} and two {110} in an ideal model). The etching insensitivity to starting facets can be explained by assuming that etchant can attack Si from many possible orientations, avoiding slow-etching facets (*e.g.*, {111}). Scale bars: 500 nm.

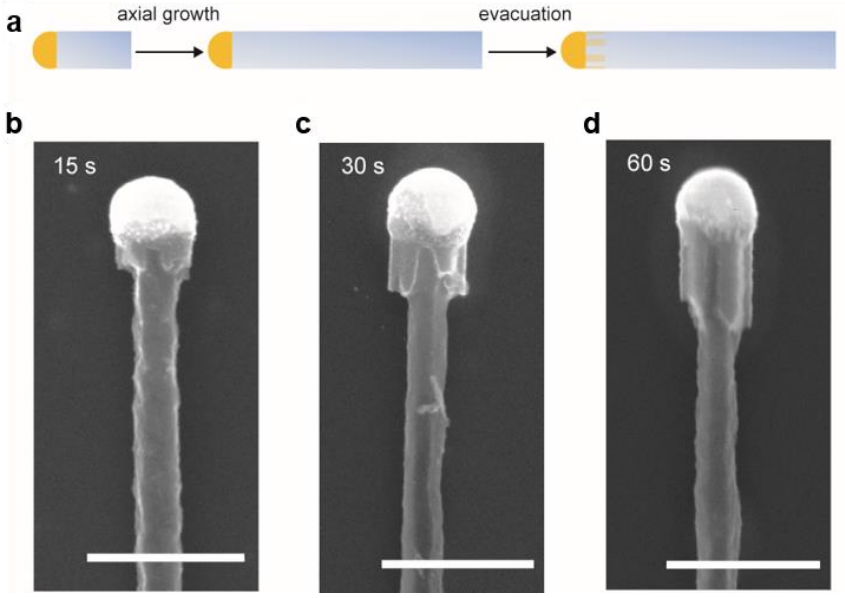

Figure 4-23. One-step diffused gold can serve as etch resist for Si nanowire etching. In this experiment, we first grew *p*-type Si nanowires using the same flow rates (60 sccm of H_2, 2 sccm of SiH_4 and 10 sccm of B_2H_6 (100 ppm in H_2) as adopted in Si spicule synthesis. After the synthesis was complete, we kept the nanowires at base pressure (~ 1.5 mTorr) and the growth temperature (465 ^oC) for 15 s, 30 s and 60 s. Then we quickly lowered the temperature and took out samples. Nanowires were etched in 20 % (w/v) KOH at 60 ^oC for 5 s. Upon etching, the nanowire tips have been partially protected. The edges are patterned and curved, and the axial lengths of the protected regions are evacuation-time dependent. Although these experiments used very different gold diffusion conditions, they eliminate the effects of gaseous dopants, and independently confirm the etch resist effect from diffused gold. Scale bars: 300 nm.

4.2.5 Interfacial interactions with extracellular matrices

The anisotropic mesoscale texture of Si spicules suggests that they may have different interactions with surrounding matrices such as hydrogels or biological tissues, as compared to other more isotropic Si structures such as diameter-modulated nanowires[18,19]. To test this

possibility, we first mounted single mesostructured Si spicules (<112>-oriented, *p*-type) onto atomic force microscopy cantilever tips with a focused ion-beam system (**Fig. 4-24a**, inset). Next, by approaching/retracting the spicules to/from collagen Type-I hydrogel (**Fig. 4-24b**), we were able to monitor the force and work of the spicule-matrix interactions in both the forward and reverse directions. For each recording, we chose a fresh location over the hydrogel surface. To study the effects of probe geometry and surface, we performed control measurements (**Fig. 4-25**) with an un-etched silicon nanowire, a uniform diameter-modulated silicon nanowire[18,19], and a nanoporous silicon nanowire[18]. A representative force-distance (*F-D*) curve recorded from the Si spicule probe exhibits a detachment force of ~ 3.9 nN, and a detachment work of ~ 15.6 fJ (**Fig. 4-24a**). Statistical analyses of *F-D* measurements with the single Si spicule and different Si nanowire probes (**Fig. 4-26**, N=50) demonstrates that the unique anisotropic mesostructure, rather than surface area or nanoscale roughness, yield a major enhancement in detachment force and detachment work. The observation that anisotropic spicule requires the largest detachment force from collagen, is reminiscent of natural systems, such as a 'bee's stinger' which can become rooted in skin. This suggests the potential of adopting mesostructured Si spicules for building tight junctions with other soft materials, such as in tissue-interfacing adhesives or bioelectronics.

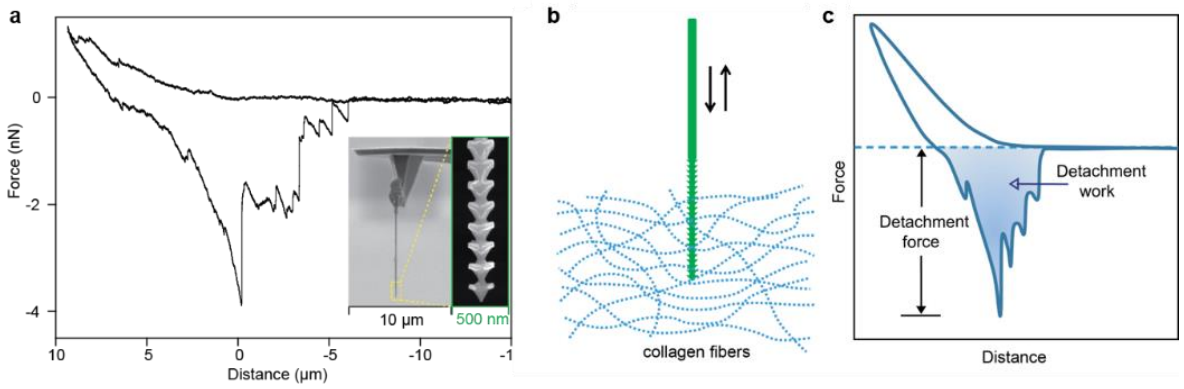

Figure 4-24. Mechanical interactions between Si spicules and collagen hydrogel. a, Representative force-distance (*F-D*) curves collected using individual silicon spicule as a probe. Insets displace the spicule-based AFM probe at

Figure 4-24, continued. different magnifications. **b**, A schematic diagram of the experiment, highlighting the interfaces between the Si spicule and individual collagen fibers. **c**, A schematic diagram illustrating detachment force and detachment work.

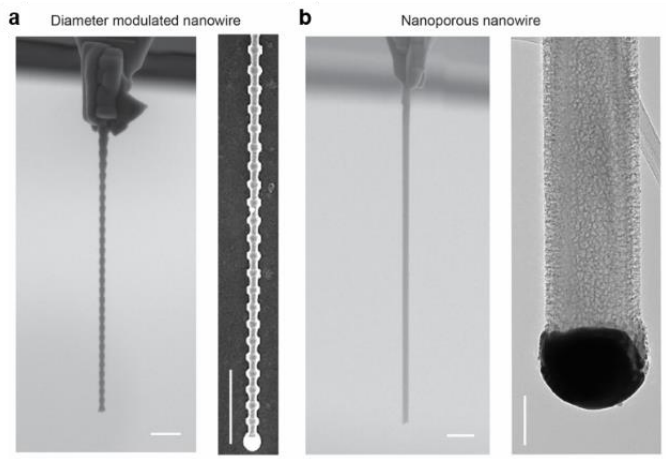

Figure 4-25. Diameter-modulated (a) and nanoporous (b) Si nanowire probes. The left panels in **a** and **b** show SEM images of diameter-modulated (**a**) and nanoporous (**b**) Si nanowires, which are assembled onto the tips of AFM cantilevers with a micromanipulator and fixed with a dual-beam FIB system. The right panels in **a** and **b** show details of the as-made nanowire structures, *i.e.*, SEM image of a diameter-modulated Si nanowire (**a**) and TEM image of a nanoporous Si nanowire (**b**). The pore size over nanoporous Si nanowire surface is 8.5 ± 4.4 nm (mean ± 1 SD, N=60). Metallic Au was removed with a standard Au etchant prior to mounting process. Scale bars: 1 μm in **a** and the left panel in **b**, 100 nm in the right panel of **b**.

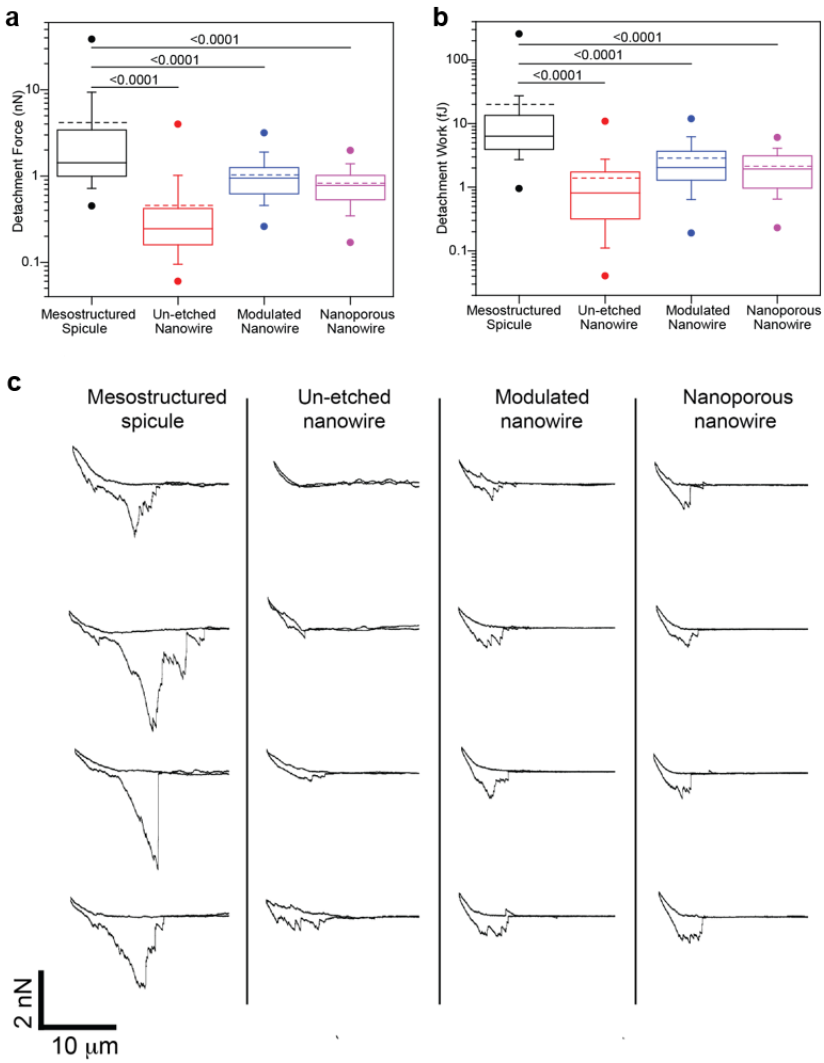

Figure 4-26. Si spicules show enhanced interactions with collagen fibers. a and **b**, Box-and-whisker plots of forces (**a**) and work (**b**) required to detach silicon spicules (black), un-etched silicon nanowires (red), diameter-modulated silicon nanowires (blue), and nanoporous silicon nanowires (purple). Half of the data points are within the box and 80% are within the whiskers. Solid and dashed lines mark median and mean, respectively. The dots represent maximum and minimum values. The means of detachment force are: 4.16 nN (mesostructured spicule), 0.455 nN (un-etched nanowire), 1.03 nN (modulated nanowire), and 0.827 nN (nanoporous nanowire). The means of detachment work are: 20.0 fJ (mesostructured spicule), 1.39 fJ (un-etched nanowire), 2.86 fJ (modulated nanowire), and 2.15 fJ (nanoporous nanowire). N=50, and numbers above bars indicate the P-value of the Mann-Whitney test. **c**, Representative recording traces from mesostructured Si spicule, un-etched Si nanowire, uniform diameter-modulated Si nanowire and nanoporous Si nanowire.

4.3 Experiment

Synthesis of silicon spicule. Silicon spicules were synthesized using a two-step, combined gas- and solution-phase process. The gas-phase growth utilized a nanocluster-catalyzed chemical vapor deposition (CVD) method. The citrate-stabilized gold (Au) colloidal nanoparticles (Ted Pella Inc., 100, 150 or 200 nm diameter) were deposited onto Si (100) substrates (Nova Electronic Materials, *p*-type, 0.001 Ω cm) and used as catalysts. Prior to catalyst deposition, the native oxide on the Si substrates was removed with buffered hydrofluoric acid (BHF) (Alfa Aesar) to yield a hydrogen-terminated surface. The gas phase synthesis part was performed at 465-485 ^{o}C using silane (SiH_4) as the silicon reactant source, hydrogen (H_2) as the carrier gas, and phosphine (PH_3, 1000 ppm in H_2) and diborane (B_2H_6, 100 ppm in H_2) as the *n*- and *p*-type dopants. In a typical preparation for *p*-type Si spicules with a doping ratio of 1000:1, the flow rates of H_2, SiH_4 and B_2H_6 were 60, 2 and 10 standard cubic centimeters per minute (sccm) in CVD synthesis, respectively. Periodic switches between 1 second of evacuation and 15 seconds of linear pressure ramp were used to generate patterned 3D interfaces over Si, following a growth of a base segment at constant pressure of 30-40 Torr for 7 min. The pressure dropped to ~0.2 Torr in the evacuation cycle and linearly increased to above ~35 Torr in 15 s during a growth cycle. Prior to the alkaline etching of modulated Si, the as-grown substrates were dipped into BHF to remove native oxide. After rinsing with deionized (DI) water, anisotropic etching was performed in 20% (w/v) potassium hydroxide (KOH) aqueous solution at 60 ^{o}C for 5-10 s. The etched samples were rinsed with DI water, isopropanol alcohol (IPA) and dried in air.

Synthesis of un-etched, pressure modulated Si nanowires. The procedure was the same as that used for the gas phase preparation of Si spicules. No KOH-based etching was used. In a typical CVD synthesis of Si nanowires with a doping ratio of 1000:1, the flow rates of H_2, SiH_4 and B_2H_6

were 60, 2 and 10 sccm, respectively. Periodic switches between 1 second of evacuation and 15 seconds of linear pressure ramp were used, following a growth of a base segment at constant pressure of 30-40 Torr for 7 min. These nanowires were used for XPS, APT, electrochemistry and AFM experiments in the main text.

Synthesis of conventional Si nanowires without pressure modulation. In a typical CVD synthesis of Si nanowires with a doping ratio of 1000:1, the flow rates of H_2, SiH_4 and B_2H_6 were 60, 2 and 10 sccm, respectively. Growth took place at a constant pressure of 30-40 Torr and at 465 ^oC, for 20 min. No intentional gold diffusion was applied during the synthesis, and these nanowires were used for electrochemistry experiments in the main text.

Synthesis of uniform, diameter-modulated Si nanowires. They were prepared by alkaline etching of Si nanowires with alternate *n*-type and undoped axial segments. The CVD synthesis was performed at 460 °C and a total pressure of 30-40 Torr, with alternate growths of *n*-type (PH_3/SiH_4 feeding ratio of 1:500) and undoped segments (10 s for each segment). Subsequent alkaline etching of the Si nanowires was conducted in a KOH/IPA solution (5 % (w/v) KOH in water; 1:1 v/v) for 2 min at 30 °C. The etched samples were rinsed with DI water, IPA, and dried in air. These nanowires were used for AFM experiments in the main text.

Synthesis of nanoporous Si nanowires. They were prepared by metal-assisted chemical etching of *n*-type Si nanowires synthesized at 480 °C with PH_3/SiH_4 feeding ratio of 1:500. Silver (Ag) nanoparticles were electrolessly deposited on the nanowires in an aqueous solution of 0.04 mM $AgNO_3$ and 0.4 % (v/v) HF for 10 s at room temperature. The Ag-assisted chemical etching was performed in a mixture of 1.5 % (v/v) H_2O_2 and 2 % (v/v) HF for 10 s at room temperature. The etched samples were rinsed with DI water, IPA, and dried in air. These nanowires were used for AFM experiments in the main text.

Electron microscopy and tomography. Si spicules were gently sonicated in IPA and dispersed onto silicon substrates (Nova Electronic Materials, *p*-type, 0.001 Ω cm) or lacey carbon grids (Ted Pella Inc.) for electron microscopy characterization. Scanning electron microscopy (SEM) (FEI Nova NanoSEM 200) and transmission electron microscopy (TEM) (FEI Tecnai F30 and Hitachi H-8100 TEM) were used to characterize the morphology and crystallography of Si spicules. For scanning transmission electron microscopy (STEM) tomography analyses, Si spicules from Si substrates were picked up and transferred with a micro-manipulator and attached to copper (Cu) tips with electron-beam-induced platinum (Pt)/carbon (C) deposition using a focused ion-beam (FIB) system (FEI Helios Nanolab 600 DualBeam FIB/SEM). The Cu tips were mounted on a Hitachi rotation holder, which permits rotary motion from 0 to 360°. The high-angle annular dark field (HAADF) STEM images of the samples were collected using a STEM (Hitachi HD-2300A) at tilt intervals of 2° from 0° up to 240°. The tilt series were aligned and reconstructed using a back-projection algorithm, in IMOD 4.5 (University of Colorado, Boulder) with 10 nm Au nanoparticles as fiducial marker. The tomograms and 3D iso-intensity surfaces were constructed and visualized using Amira 5.5 (FEI Visualization Sciences Group). Segmentation of the tomograms was carried out manually. The optimal threshold values in constructing 3D iso-intensity surfaces are 1320 and 1540 for Type I and Type II spicules, respectively.

X-ray photoelectron spectroscopy (XPS). The Si structures were gently sonicated in IPA and dispersed onto silicon substrates with a 100 nm thick titanium coating. XPS data were collected using ESCALAB 250 Xi (Thermo VG Scientific) with monochromatic Al Kα ($h\nu$ = 1486.6 eV) excitation. The diameter of the X-ray beam was 900 μm and the scan step was 0.1 eV. The correction of the XPS spectra for charge accumulation was performed using the C 1s peak (binding

energy = 285.0 eV) of hydrocarbons. The XPS peaks were fitted using a Gaussian/Lorentzian peak shape after correcting background with the Shirley method.

Atom-probe tomography (APT). The un-etched Si structures were transferred and mounted onto silicon microposts with a micromanipulator, pre-coated with nickel (Ni), post-coated and filled-in with platinum (Pt)/carbon (C) composites, and milled into needle-like microtip specimens using an FIB system (FEI Helios Nanolab 600 DualBeam FIB/SEM). The APT was performed using a ultraviolet (UV) laser-assisted local-electrode atom-probe (LEAP 4000XSi, Cameca, Madison). Laser-assisted evaporation of the surface atoms from a microtip was achieved using an applied voltage of 1∼6 kV direct current (dc) and 30 pJ UV (wavelength λ = 355 nm) laser at a pulse rate of 250 kHz. The mass-to-charge-state (m/z) ratios of individual evaporated ions, in addition to their (x, y, z) coordinates in direct space, were recorded employing a position sensitive detector. During APT analyses, the samples were held at 30 K at an ambient pressure of 2×10^{-11} Torr. The 3D reconstructions and data interpretations were performed utilizing Cameca's IVAS3.4 code.

For 3D rendering, data were created in Cameca Integrated Visualization and Analysis Software (IVAS, www.cameca.com/support/ivas.aspx). The delocalization parameters were 3 nm × 3 nm × 3 nm. Finally, proximity histograms were created with respect to 5% oxygen iso-concentration surface. The displacement in oxide layer was assigned positive sign.

Electrochemical measurements. The voltammograms were recorded using a potentiostat (Autolab, Eco Chemie BV) with a three-electrode system in 5% (w/v) KOH aqueous solution at room temperature (23 ^{o}C). Si structures with their growth substrates, Pt wire, and a Ag/AgCl electrode were used as the working electrode, counter electrode, and reference electrode, respectively. The electrical back contacts to the working electrodes were isolated from the solution

using an epoxy (Devcon) coating. The potential was scanned from -1.5 Vdc to 0 Vdc at a rate of 5 mV/s.

Atomic force microscopy (AFM) measurements. Si structures were micro-manipulated and mounted onto AFM cantilevers (ScanAsyst-Air, Bruker, nominal spring constant 0.4 $N \cdot m^{-1}$) with an FIB system (FEI Helios Nanolab 600 DualBeam FIB/SEM). The integrated probes were used to measure the force-distance (*F-D*) curves from collagen fibril networks. Collagen (Corning, Collagen I, Rat Tail, 4.04 mg/mL), phosphate buffered saline (PBS 10x), 1M NaOH, and DI water were mixed and adjusted to a pH of 7.4, and applied onto Petri dishes placed on ice. The collagen gels formed after subsequent incubation at 37 ^{o}C for 1 hour. The *F-D* curves were collected on the collagen gels immersed in 1x PBS solutions at room temperature (23 °C) using a MFP-3D-BIO AFM (Asylum Research), with an approaching and retracting speed of 1 $\mu m \cdot s^{-1}$ and a trigger force of 1 nN. Prior to the measurement, each AFM cantilever mounted with a Si spicule or nanowire was calibrated to determine the cantilever's deflection sensitivity ($nm \cdot V^{-1}$) and then the spring constant ($N \cdot m^{-1}$) using the thermal tuning method. 50 force-distance curves were recorded from different points on the samples for statistical analyses of the detachment force and detachment work (integration of the adhesive forces over the distance traveled by the cantilever). The data sets were plotted using box-and-whisker diagrams in which the boxes and the whiskers contain 50% and 80% of the data points, respectively. The maximum, minimum, median and mean were also marked in the diagrams. In these experiments, the surfaces of silicon structures were not modified with biomolecules given chemical modification itself can significantly affect bio-interfaces.

4.4 Bibliography

1 Tawfick, S., De Volder, M., Copic, D., Park, S. J., Oliver, C. R., Polsen, E. S., Roberts, M. J. & Hart, A. J. Engineering of Micro- and Nanostructured Surfaces with Anisotropic Geometries and Properties. *Advanced Materials* **24**, 1628-1674, doi:10.1002/adma.201103796 (2012).

2 Xu, S., Yan, Z., Jang, K. I., Huang, W., Fu, H. R., Kim, J., Wei, Z., Flavin, M., McCracken, J., Wang, R., Badea, A., Liu, Y., Xiao, D. Q., Zhou, G. Y., Lee, J., Chung, H. U., Cheng, H. Y., Ren, W., Banks, A., Li, X. L., Paik, U., Nuzzo, R. G., Huang, Y. G., Zhang, Y. H. & Rogers, J. A. Assembly of micro/nanomaterials into complex, three-dimensional architectures by compressive buckling. *Science* **347**, 154-159, doi:10.1126/science.1260960 (2015).

3 Rogers, J. A., Someya, T. & Huang, Y. G. Materials and Mechanics for Stretchable Electronics. *Science* **327**, 1603-1607, doi:10.1126/science.1182383 (2010).

4 Shenoy, V. B. & Gracias, D. H. Self-folding thin-film materials: From nanopolyhedra to graphene origami. *Mrs Bulletin* **37**, 847-854, doi:10.1557/mrs.2012.184 (2012).

5 Mann, S. & Ozin, G. A. Synthesis of inorganic materials with complex form. *Nature* **382**, 313-318, doi:10.1038/382313a0 (1996).

6 Naik, G. V., Shalaev, V. M. & Boltasseva, A. Alternative Plasmonic Materials: Beyond Gold and Silver. *Advanced Materials* **25**, 3264-3294, doi:10.1002/adma.201205076 (2013).

7 Ozel, T., Bourret, G. R. & Mirkin, C. A. Coaxial lithography. *Nature Nanotechnology* **10**, 319-324 (2015).

8 Cusack, M. & Freer, A. Biomineralization: Elemental and Organic Influence in Carbonate Systems. *Chemical Reviews* **108**, 4433-4454, doi:10.1021/cr078270o (2008).

9 Moutanabbir, O., Isheim, D., Blumtritt, H., Senz, S., Pippel, E. & Seidman, D. N. Colossal injection of catalyst atoms into silicon nanowires. *Nature* **496**, 78-82, doi:10.1038/nature11999 (2013).

10 Chen, W. H., Yu, L. W., Misra, S., Fan, Z., Pareige, P., Patriarche, G., Bouchoule, S. & Cabarrocas, P. R. I. Incorporation and redistribution of impurities into silicon nanowires during metal-particle-assisted growth. *Nature Communications* **5**, doi:10.1038/ncomms5134 (2014).

11 Hemesath, E. R., Schreiber, D. K., Gulsoy, E. B., Kisielowski, C. F., Petford-Long, A. K., Voorhees, P. W. & Lauhon, L. J. Catalyst Incorporation at Defects during Nanowire Growth. *Nano Letters* **12**, 167-171, doi:10.1021/nl203259f (2012).

12 Ferralis, N., El Gabaly, F., Schmid, A. K., Maboudian, R. & Carraro, C. Real-Time Observation of Reactive Spreading of Gold on Silicon. *Physical Review Letters* **103**, doi:25610210.1103/PhysRevLett.103.256102 (2009).

13 Madras, P., Dailey, E. & Drucker, J. Spreading of Liquid AuSi on Vapor-Liquid Solid-Grown Si Nanowires. *Nano Letters* **10**, 1759-1763, doi:10.1021/nl100249j (2010).

14 Hannon, J. B., Kodambaka, S., Ross, F. M. & Tromp, R. M. The influence of the surface migration of gold on the growth of silicon nanowires. *Nature* **440**, 69-71, doi:10.1038/nature04574 (2006).

15 Dick, K. A., Deppert, K., Samuelson, L., Wallenberg, L. R. & Ross, F. M. Control of GaP and GaAs Nanowire Morphology through Particle and Substrate Chemical Modification. *Nano Letters* **8**, 4087-4091, doi:10.1021/nl8027153 (2008).

16 den Hertog, M. I., Rouviere, J. L., Dhalluin, F., Desre, P. J., Gentile, P., Ferret, P., Oehler, F. & Baron, T. Control of gold surface diffusion on Si nanowires. *Nano Letters* **8**, 1544-1550, doi:10.1021/nl073356i (2008).

17 Allen, J. E., Hemesath, E. R., Perea, D. E., Lensch-Falk, J. L., Li, Z. Y., Yin, F., Gass, M. H., Wang, P., Bleloch, A. L., Palmer, R. E. & Lauhon, L. J. High-resolution detection of Au catalyst atoms in Si nanowires. *Nature Nanotechnology* **3**, 168-173, doi:10.1038/nnano.2008.5 (2008).

18 Voyles, P. M., Muller, D. A., Grazul, J. L., Citrin, P. H. & Gossmann, H. J. Atomic-scale imaging of individual dopant atoms and clusters in highly n-type bulk Si. *Nature* **416**, 826-829, doi:10.1038/416826a (2002).

19 Christesen, J. D., Pinion, C. W., Grumstrup, E. M., Papanikolas, J. M. & Cahoon, J. F. Synthetically Encoding 10 nm Morphology in Silicon Nanowires. *Nano Letters* **13**, 6281-6286, doi:10.1021/nl403909r (2013).

20 Lim, S. K., Crawford, S., Haberfehlner, G. & Gradecak, S. Controlled Modulation of Diameter and Composition along Individual III-V Nitride Nanowires. *Nano Letters* **13**, 331-336, doi:10.1021/nl300121p (2013).

21 Musin, I. R., Boyuk, D. S. & Filler, M. A. Surface chemistry controlled diameter-modulated semiconductor nanowire superstructures. *Journal of Vacuum Science & Technology B* **31**, doi:02060310.1116/1.4792660 (2013).

22 Ross, F. M., Tersoff, J. & Reuter, M. C. Sawtooth faceting in silicon nanowires. *Physical Review Letters* **95**, 146104, doi:14610410.1103/PhysRevLett.95.146104 (2005).

23 Algra, R. E., Verheijen, M. A., Borgstrom, M. T., Feiner, L. F., Immink, G., van Enckevort, W. J. P., Vlieg, E. & Bakkers, E. Twinning superlattices in indium phosphide nanowires. *Nature* **456**, 369-372, doi:10.1038/nature07570 (2008).

24 Day, R. W., Mankin, M. N., Gao, R., No, Y.-S., Kim, S.-K., Bell, D. C., Park, H.-G. & Lieber, C. M. Plateau-rayleigh crystal growth of periodic shells on one-dimensional substrates. *Nature Nanotechnology* **10**, 345-352 (2015).

25 Zhao, L. Y., Siu, A. C. L., Petrus, J. A., He, Z. H. & Leung, K. T. Interfacial bonding of gold nanoparticles on a H-terminated Si(100) substrate obtained by electro- and electroless deposition. *Journal of the American Chemical Society* **129**, 5730-5734, doi:10.1021/ja070441j (2007).

26 Hellman, O. C., Vandenbroucke, J. A., Rusing, J., Isheim, D. & Seidman, D. N. Analysis of three-dimensional atom-probe data by the proximity histogram. *Microscopy and Microanalysis* **6**, 437-444 (2000).

27 Stolwijk, N. A., Schuster, B., Holzl, J., Mehrer, H. & Frank, W. Diffusion and solubility of gold in silicon. *Physica B & C* **116**, 335-342, doi:10.1016/0378-4363(83)90271-1 (1983).

28 Seidel, H., Csepregi, L., Heuberger, A. & Baumgartel, H. Anisotropic etching of crystalline silicon in alkaline-solutions. 1. Orientation dependence and behavior of passivation layers. *Journal of the Electrochemical Society* **137**, 3612-3626, doi:10.1149/1.2086277 (1990).

29 Chen, L. C., Chen, M. J., Lien, C. H. & Wan, C. C. The band model and the etching mechanism of silicon in aqueous KOH. *Journal of the Electrochemical Society* **142**, 170-176, doi:10.1149/1.2043860 (1995).

30 Mehta, B. & Tao, M. A kinetic model for boron and phosphorus doping in silicon epitaxy by CVD. *Journal of the Electrochemical Society* **152**, G309-G315, doi:10.1149/1.1864452 (2005).

Chapter 5

Alloy-assisted deposition of three-dimensional arrays of atomic gold catalyst for crystal growth studies

5.1 Introduction

Large-scale assembly of individual atoms over smooth surfaces is difficult to achieve. A configuration of an atom reservoir, in which individual atoms can be readily extracted, may successfully address this challenge. In this chapter, I will demonstrate that a liquid gold-silicon alloy established in classical vapor-liquid-solid growth can deposit ordered and three-dimensional rings of isolated gold atoms over silicon nanowire sidewalls. I will show that *ab initio* molecular dynamics simulation unveils a surprising single atomic gold-catalyzed chemical etching of silicon. Additionally, I will show the experimental verification of the catalytic process in silicon nanowires and yield dopant-dependent, massive and ordered 3D grooves with spacing down to ~ 5 nm. Finally, we can use these grooves as self-labelled and ex situ markers and resolved several complex silicon growths, including the formation of nodes, kinks, scale-like interfaces, and curved backbones.

Atom-by-atom manipulation by scanning probe microscope (SPM) is an effective method of assembling functional structures and devices on a solid substrate[1-3], and has enabled numerous fundamental studies of chemical and physical processes (**Fig. 5-1a**). Despite its high precision, this technique suffers from low throughput due to its serial operation. Periodic assembly of individual atoms (*e.g.*, aluminum and gallium) over step edges of a crystalline substrate is

possible[4,5], especially when the bonding of adatoms at the step edges of the substrate is energetically more stable than that on the crystal terraces. However, the nanoscale features obtained this way are limited by the crystal lattice of the underlying substrates.

High throughput, sequential and tunable printing of individual atoms over a large area has not been achieved, but if successful, it could impact fields other than quantum science[2], surface chemistry[4,5], or single molecule studies[3]. A configuration of an atom reservoir, in which individual atoms can be readily extracted, may successfully address this challenge.

The liquid alloy established in classical vapor-liquid-solid (VLS) growth could be an option for the reservoir. Indeed, in VLS growth of silicon (Si) nanowires[6-9], many metal species such as gold (Au)[10-17], alunimum[5,18], indium[19], tin[19], are able to incorporate over or into Si nanowires during the growth. Moreover, in a VLS process, alloy droplet instability or oscillatory motions can occur even under classical growth conditions[20-24], and they have yielded periodic changes of crystal structure and morphology.

Here we discover a new oscillatory motion of Au/Si alloy droplet, which enables a three-dimensional (3D) patterning of atomic Au over Si nanowire sidewalls. The Au atoms catalyze an etching of Si nanowires, which subsequently forms massive grooves that are used for probing many crystal growth behaviors.

5.2 Results and Discussion

5.2.1 New concept for the parallel atom manipulation

We hypothesize that a liquid silicon-metal alloy, a reservoir of mobile and dispersed atomic species, could be explored for the parallel printing of individual atoms (**Fig. 5-1b**). We test this possibility in Au catalyzed VLS growth of Si nanowires, because the catalysts during growth are

liquid alloy droplets and they can deposit both metal nanoparticles and atoms over Si sidewalls. Besides having an atom reservoir, another key factor in controllable atom patterning is the realization of a switch that allows atom deposition only during certain time points of a sequential process. These oscillations in Au-catalyzed VLS growth can potentially be utilized for such a switch in atom printing, especially given the classical coffee-ring effect[25] that provides information on droplet instability-induced sequential patterning of a range of nano- and micro-particles.

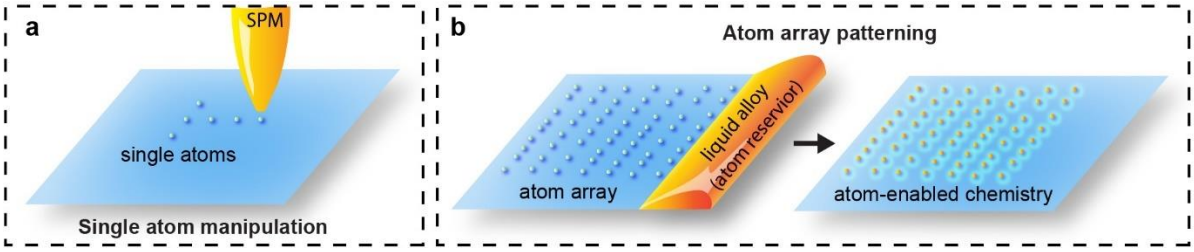

Figure 5-1. Liquid may be used for atom manipulation. Schematic illustrations of (**a**) single atom manipulation by SPM and (**b**) large scale and sequential manipulation of atom arrays with liquid alloy.

5.2.2 Discovery of atomic Au-based line patterns

Given that alloy droplet instability can occur under typical VLS conditions[20-24], we extensively surveyed the surfaces of classical Si nanowires for the potential occurrence of atomic Au patterns over their sidewalls. We chose to focus our studies on nanowires with a diameter range of 100 nm ~ 1 μm, as this is a critical length scale that bridges traditional nanomaterials and micron-level objects but has surprisingly received very little attention. Additionally, it is known that larger diameter in Si nanowires favors Au deposition[14,15]. To enable high-resolution imaging of individual atoms from these relatively thick nanowires and to preserve the sample surface information, we microtomed samples for aberration-corrected scanning transmission electron microscope (STEM) imaging (thickness, ~ 70 nm), and used horizontally placed samples made by a focused ion beam system for laser-assisted local-electrode atom-probe tomography (APT).

Significantly, for Si nanowires synthesized with high phosphine doping (*i.e.*, heavy *n*-type), we consistently found ordered line patterns over Si surface with a minimum line spacing of ~ 5 nm (**Figs. 5-2a, 5-3a**). High-resolution STEM images and energy dispersive X-ray spectrum (EDS) indicated that the lines consisted of isolated gold atoms (**Figs. 5-2c**, **5-3b**, and **5-3c**). The fact that these gold atom lines do not align with planar defects (**Fig. 5-3c**) rules out the possibility of gold trapping by a superlattice[10,23,24,26]. Atomic force microscope (AFM) imaging of the Si nanowire showed smooth surfaces with a roughness less than 2 nm (**Fig. 5-4**), ruling out another gold trapping situation at the diameter-modulated sidewalls[22,27,28].

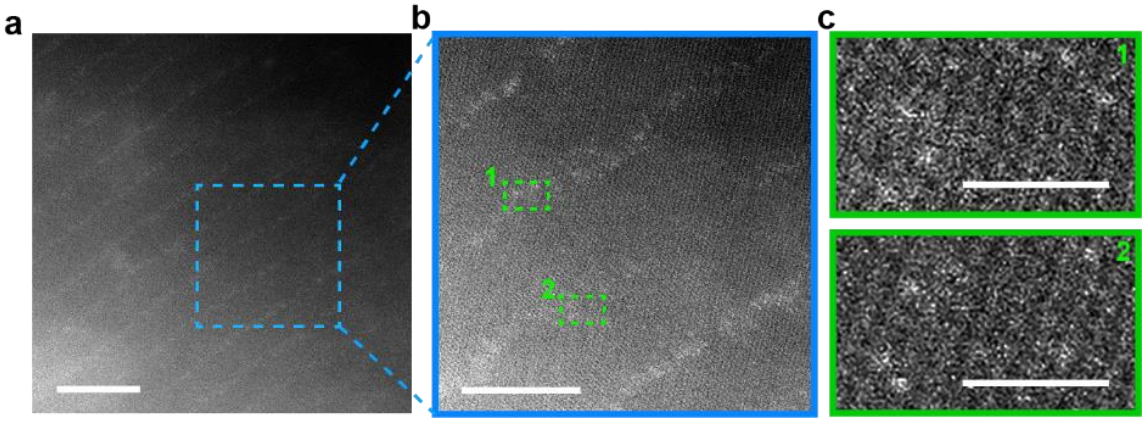

Figure 5-2. Order lined patterns are found on Si nanowire sidewalls. a, Aberration-corrected STEM image of ordered line patterns over Si surfaces. Scale bar, 10 nm. **b**, High-resolution STEM image for a zoom-in view from **b** (region labeled with blue dashed box). Scale bar, 5 nm. **c**, Isolated gold atoms images highlighted in the lines regions from **c** (marked by two green dashed boxes). Scale bars, 1 nm.

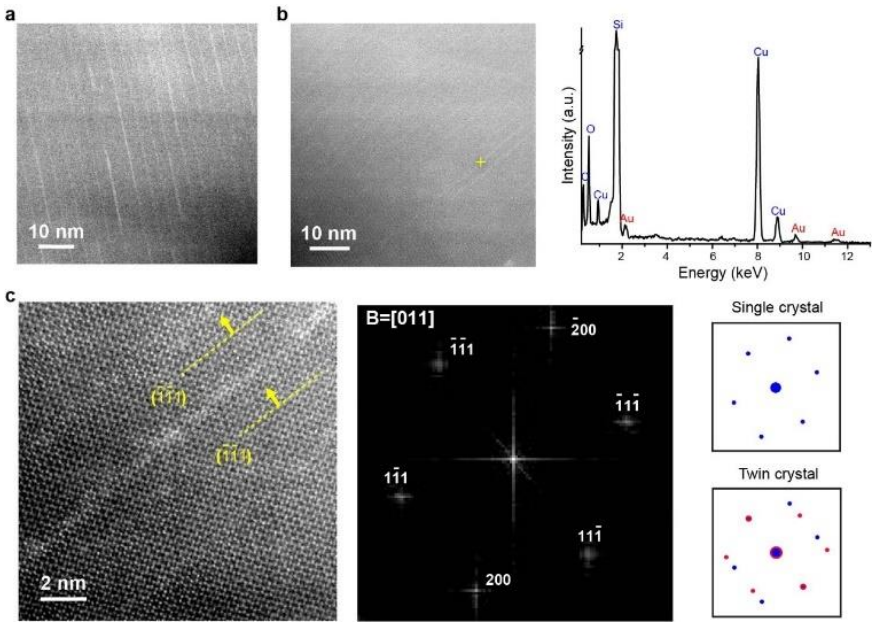

Figure 5-3. STEM and EDX studies of ordered line patterns on Si nanowire surfaces. a, Ordered line patterns recorded from a different Si nanowire sample. **b,** A STEM image and an EDX spectrum taken from the same Si nanowire used for **Fig. 5-2**. Characteristic x-ray peaks of Au were identified. The yellow cross on the STEM image (left) marks the spot where the EDX spectrum was collected. **c,** A high-resolution HAADF-STEM image (left) and its corresponding fast Fourier transform (FFT) diffractogram (middle) show a single crystalline characteristic when viewed from [011] zone. The fact that Au lines are not aligned with any {111} twin boundaries excludes the possibility that the line patterns are formed by trapped Au atoms in a twinning superlattice structure. A simulated FFT from a twinning superlattice (lower right panel) should show two sets of diffraction spots (red and blue), which are not identified in our case (middle and upper right panels).

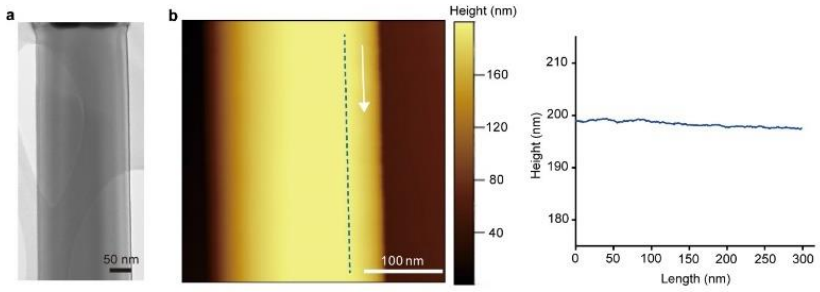

Figure 5-4. As-grown Si nanowires have smooth surfaces. TEM (**a**) and AFM (**b**) images show that the surfaces of *n*-type Si nanowires are smooth, without sawtooth sidewall faceting. A height profile taken along the nanowire axial direction (**b**, right) quantifies the observed surface smoothness.

A 3-D, atom-by-atom chemical reconstruction from a nanowire surface region (**Fig. 5-5a**, green, Ni; cyan, O; blue, Si) revealed the presence of mostly isolated Au atoms (**Fig. 5-5b**, orange spheres; **Fig. 5-6**), with a local peak volume concentration of 0.01 ~ 0.03 atoms nm^{-3}, determined at a concentration sampling grid voxel size of 0.6 nm x 0.6 nm x 1.5 nm. Compared to STEM imaging, the APT chemical reconstruction showed less clear chain-like arrangement (dashed arrow, **Fig. 5-5b**), likely due to the limited spatial resolution and the destructive sample preparation in APT. A proximity histogram concentration profile with a direction normal to the Si/Ni interface revealed a gold enriched region (thickness, ~ 2 nm) localized at the Si sidewall surface (**Fig. 5-5c**), with an Au concentration as high as ~ 1120 atomic ppm. These results highlight the possibility of atom array patterning during a VLS process (**Fig. 5-1**).

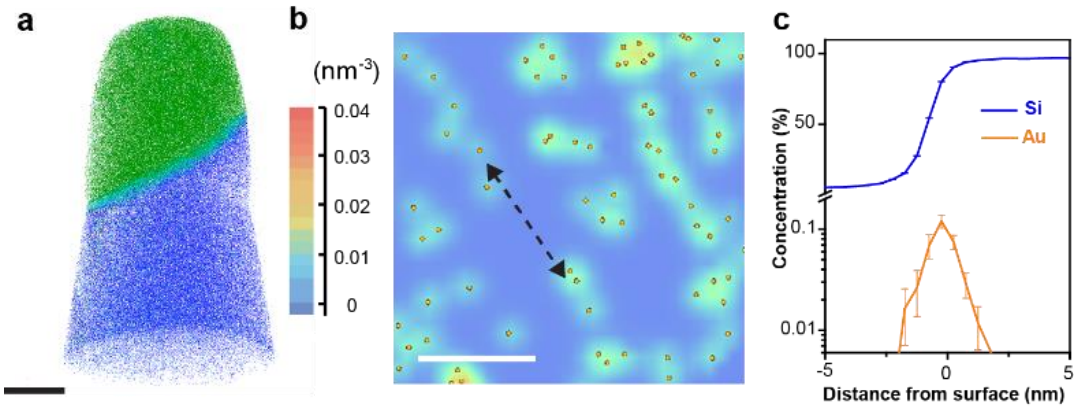

Figure 5-5. APT analysis. a, A 3-D atom-by-atom chemical reconstruction of a nanowire surface region. Atomic positions are represented by blue (Si, 2.5% shown), cyan (O, 100% shown), and green (Ni, 10% shown) dots. Scale bar, 20 nm. **b**, A 2-D color-coded map of gold atomic density exhibits a chain-like arrangement, indicated by a black dashed arrow (right panel). Orange spheres represent gold atoms. Scale bar, 10 nm. **c**, Proximity histogram concentration profile of Si and Au in the direction normal to the Si surface.

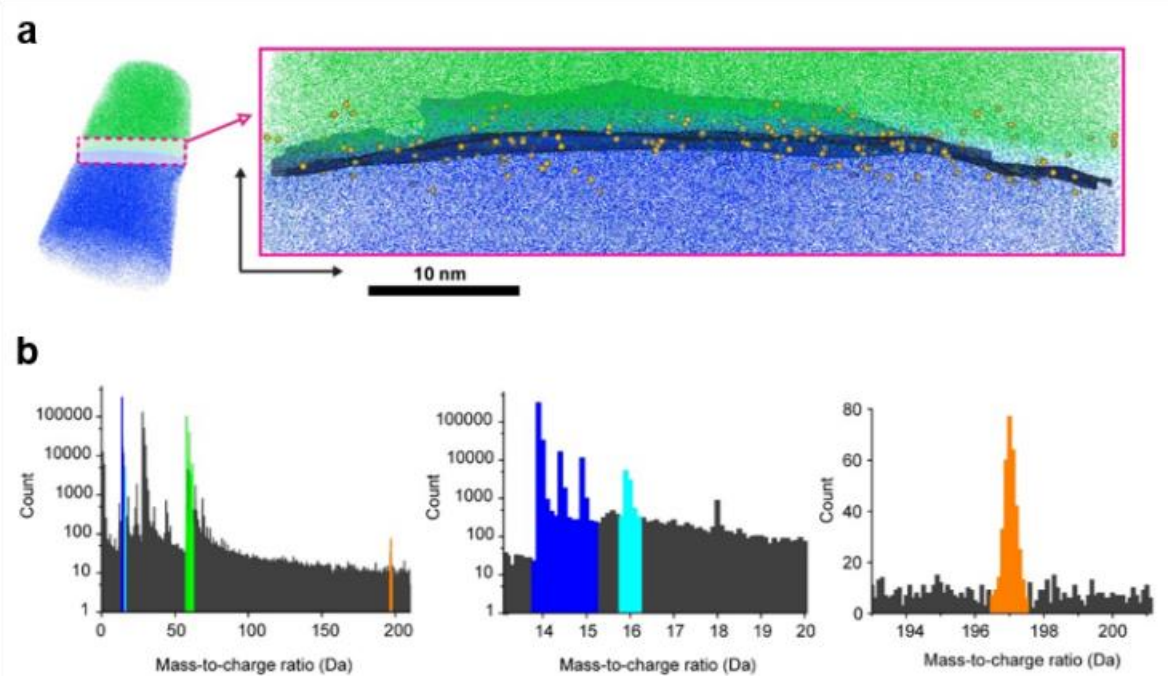

Figure 5-6. Gold atoms sit on the Si surface. a, An atom-by-atom 3-D reconstructed data set of the Si nanowire specimen (Si, blue dots, 4% shown) with the SiO_2 (O, cyan dots, 75%) native surface oxide and the Ni (Ni, green dots, 7.5%) capping layer (left). The pink dashed box marks the region for the enlarged cross-sectional view of the Si/SiO_2/Ni interfaces (right). An 80 at% Si isoconcentration surface (blue) delineates the Si/SiO_2 interface. 20% of total Si (blue dots), 100% of O (cyan dots), 75% of Ni (green dots), and 100% of Au (yellow spheres) atoms are displayed to highlight the enrichment of Au at the Si nanowire surface. **b**, Mass spectra of the interfacial region shows a distinct peak for the ^{197}Au isotope, corroborating the EDX results that suggest the presence of Au atoms on the nanowire surface.

5.2.3 *Ab initio* molecular dynamics simulations

The parallel and ordered atom manipulation implies new opportunities in chemistry and applications for atomic metal-based interfaces. To explore this, we performed long-time *ab initio* molecular dynamics (AIMD) simulations of a model Si(111) surface with and without an isolated surface Au atom. Specifically, we wanted to assess the etching propensity of Si in an environment of hydrofluoric acid (HF), hydrogen peroxide (H_2O_2) and water (H_2O) species. This chemical

process was chosen because it was relevant to the metal-assisted chemical etching (MACE) for porous Si[29-32]. These AIMD simulations were used to observe the dynamics of reactant molecules as well as the structural evolution of Si in the vicinity of the Au atom (**Fig. 5-7**). In general, the Si(111) surface without an Au atom maintained structural integrity (**Fig. 5-8b**), whereas the presence of a single Au atom showed pronounced disorder in the vicinity of the Au atom within the limited time scales accessible to AIMD (~50 ps) (**Fig. 5-8a**).

To understand the role played by a single Au atom in driving the Si etching, we sampled several different configurations (**Figs. 5-7a**, **5-7c**) from the long-time scale AIMD run and analyzed the evolving electronic structure of the Si substrate (in the vicinal regions as well as those beyond the influence of Au atoms). Au being more electronegative than Si, it draws electrons from the Si atoms with which it bonds, thereby rendering the Si atoms slightly electron-deficient (**Fig. 5-7a**). A corresponding increase in the charge of Si bonded to Au was also seen in the distribution of Bader charges of Si atoms (**Fig. 5-7b**), where Si bonded to Au (bars in blue) had the highest positive charges in the system. In two representative configurations (**Fig. 5-7a**, **Fig. 5-7c**), the Au atom received a charge of ~0.97 e, with the relative amounts of charge depletion on the neighboring Si atoms varying with time depending on the instantaneous structure. These positively charged Si atoms serve as active etching sites for the chemical species in solution, preferentially attracting electron-rich oxidizing agents such as hydrogen fluoride (HF) and hydroxyl group (OH). Such charge transfer does not occur in a Si(111) substrate without Au (**Fig. 5-8c**). We note that the ease of etching Si in the presence of Au is also energetically favorable given that the Au-Si bond dissociation energy is 15 kJ/mol lower compared to that for Si-Si[33]. Square displacement (SD) of the Au atom (**Fig. 5-7d**) suggested its significant mobility with an average diffusivity of ~ 5×10^{-10} m^2s^{-1}, which was significantly higher than that for passive Au diffusion in bulk Si (< ~ 10^{-20} m^2s^{-}

[1])[34]. Additionally, height analysis of the Au atom (**Fig. 5-7d**) revealed its transport into the sub-surface (**Figs. 5-7c**, **5-8a**) layers. This would enable continuation of the etching process after the removal of the surface Si atoms (beyond the timescales accessible to AIMD).

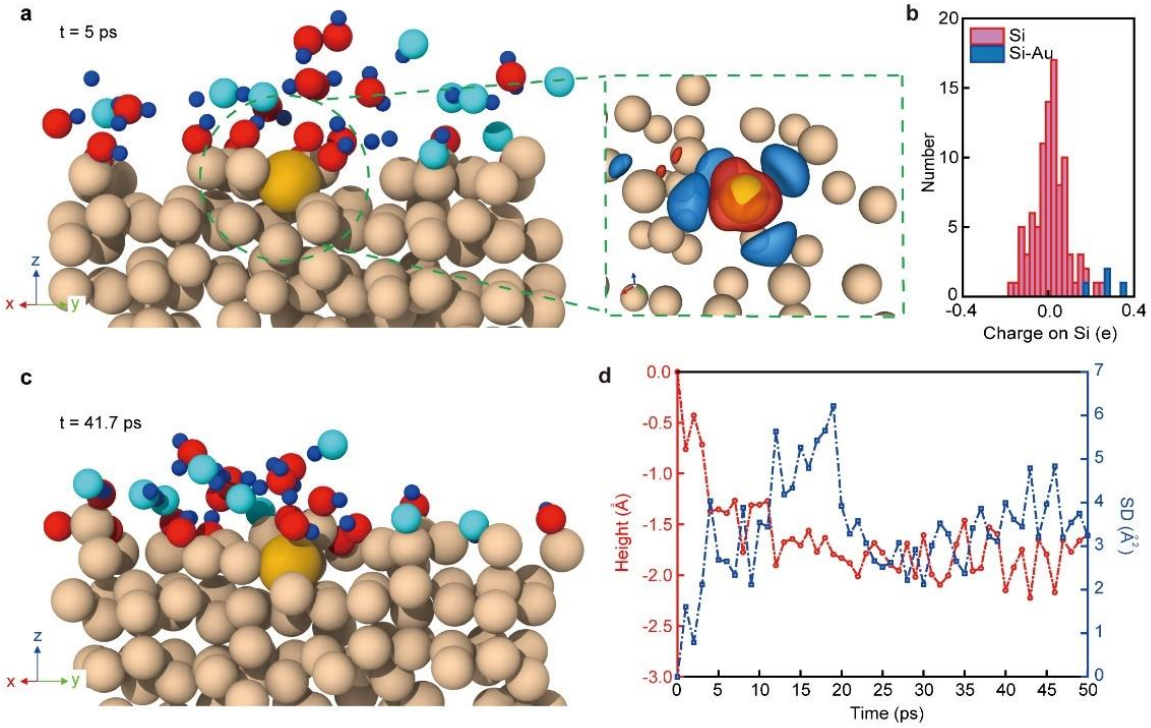

Figure 5-7. *Ab initio* molecular dynamics simulation of the catalytic effect of atomic Au. a, A representative AIMD snapshot (left) and corresponding charge transfer between Au and Si atoms (right) at t = 5 ps. Atoms are represented as almond (Si), yellow (Au), red (O), cyan (F), and blue (H) spheres. Isosurfaces represent volumes where electron density decreases (blue) and increases (red) due to the influence of the Au atom. **b**, A histogram showing the distribution of charges on Si atoms bonded to Au (blue) and far-away bulk Si (red) atoms. Si atoms bonded to Au have the highest positive charges. **c**, An AIMD snapshot sampled at a later time point, *i.e.* t = 41.7 ps. In both sampled configurations, the first nearest neighbor Si atoms lose electrons to the more electronegative Au atom. This increase in electropositivity of adjacent Si atoms translates to higher reactivity in the presence of electron rich species such as OH and HF. **d**, Relative height and square displacement (SD) of the Au atom over the course of the simulation. Within the first 10 ps, the surface Au atom moved to the sub-surface. An enhanced in-plane mobility was observed in the subsequent 15 ps.

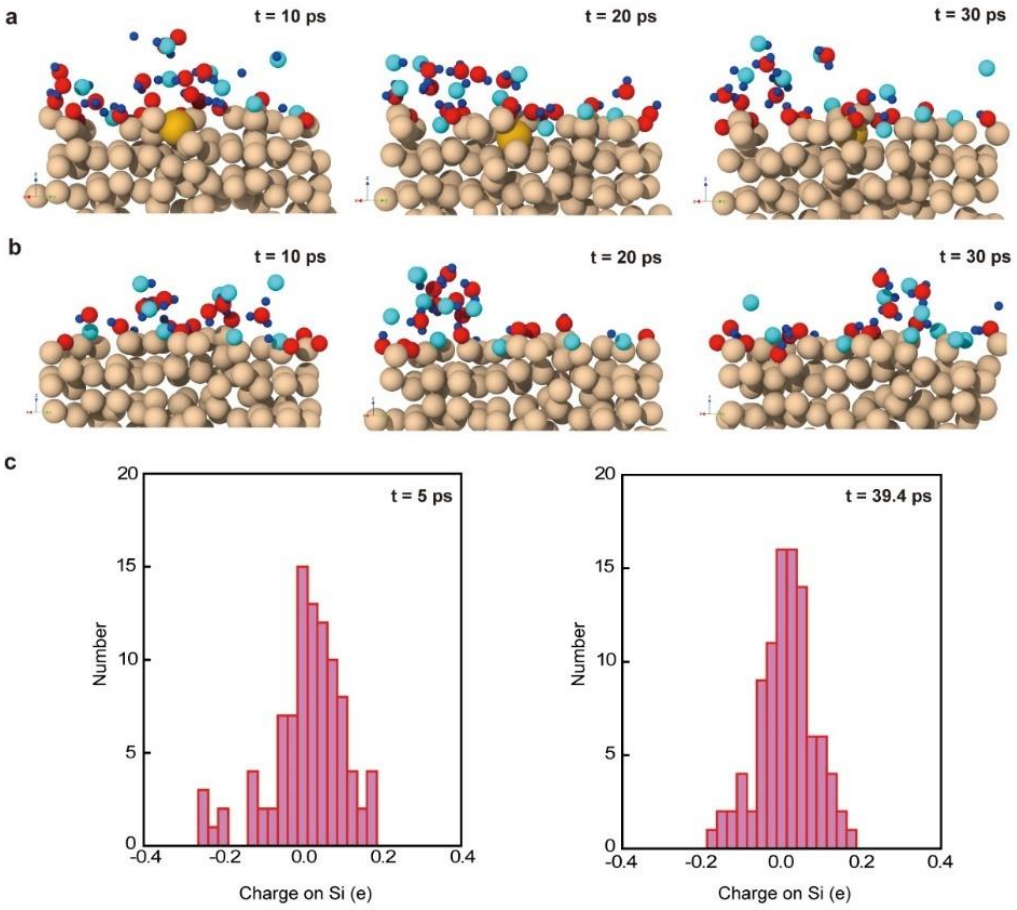

Figure 5-8. AIMD snapshots (10, 20 and 30 ps) in Si(111) with atomic gold and distribution of Si charges in pure Si(111) system. a, Single Au atom caused local disorder and showed significant mobility in Si. Atoms are represented as almond (Si), yellow (Au), red (O), cyan (F), and blue (H) spheres. **b**, The Si(111) surface without Au atom maintains its structural integrity. **c**, Charge histograms for Si atoms in the Si(111) substrate without Au atom, at 5 ps (left panel) and 39.4 ps (right panel), respectively. Compared with Si atoms bonded to Au, Si atoms with large positive charges are not observed during the course of the AIMD simulations.

5.2.4 Si nanowires with porous grooves

The results from AIMD simulations suggest an atom-catalyzed etching to yield porous Si surfaces, an atomic version of classical MACE. We verified this process in wafer-scale and atomic Au-decorated Si nanowires for sub-10 nm[27] and atom array-based catalytic lithography (*i.e.* atom deposition and catalytic etching). Transmission electron microscope (TEM) and scanning electron

microscope (SEM) images recorded from etched *n*-type Si nanowires revealed massive, ordered, 3D and porous grooves over all of the nanowire surfaces (**Fig. 5-9**), reminiscent of ordered mesoporous materials[35,36]. Additionally, given only atomic scale Au was deposited, we did not observe obvious tapering of nanowires in our synthesis (**Fig. 5-10**). Upon etching, the yield of original atomic Au lines over *n*-type Si nanowires could be easily determined; they are ca. ~ 90 % and ~ 30 % for <112> and <111> growth orientations (growth condition: at ~ 470 ^{o}C, with an Si to P feeding ratio of ~ 500, and a diameter range of 120 ~ 480 nm) (**Fig. 5-10)**. Given that <112> orientation takes ~ 80 % of the total nanowire population, the overall yield of Si nanowires that contained ordered atomic Au lines is ~ 78 %. Due to their high growth percentage and etching yield, <112> nanowires will be the focus of our subsequent discussion.

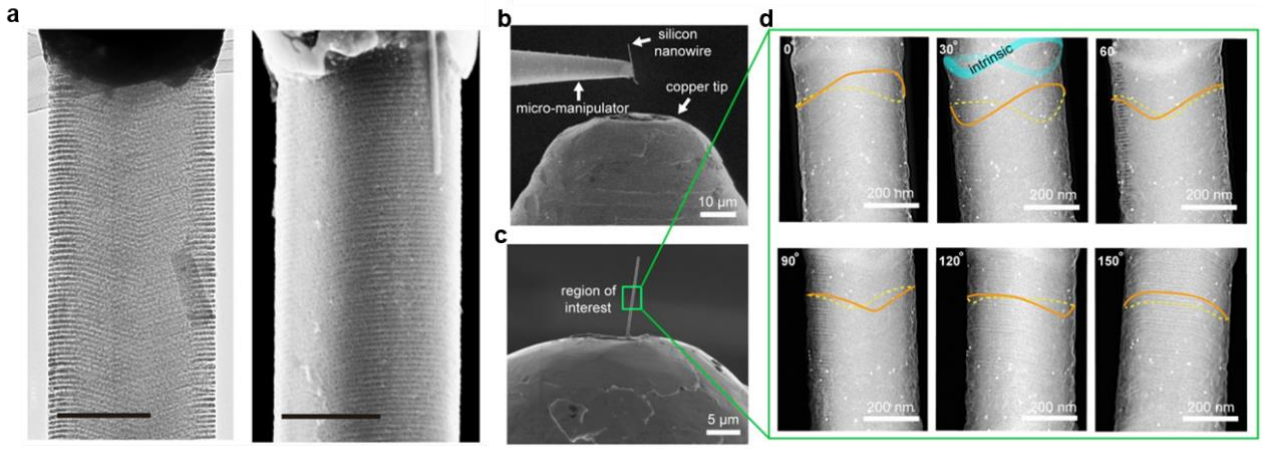

Figure 5-9. Atomic Au-catalyzed etching on Si nanowires. a, TEM and SEM images showing ordered and 3D grooves over the entire *n*-type nanowire surfaces. Scale bars, 200 nm. **b**, An SEM image showing a Si nanowire picked up by a micromanipulator. **c**, The nanowire was mounted on a Cu tip. The green box marks the region of interest for the STEM tilting image series. **d**, HAADF-STEM images of the same nanowire imaged from six different perspectives. Relative tilting angles are marked in individual panels. Orange (top surface) and dashed yellow (bottom surface) lines mark the orientations of the etched grooves. The cyan ribbon highlights the shape of an intrinsic segment.

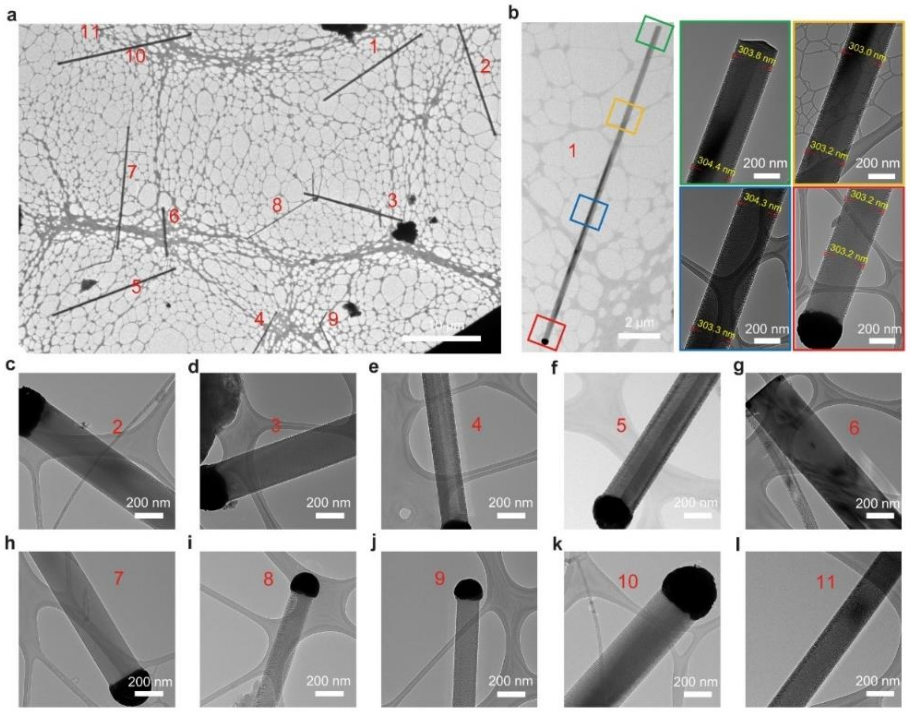

Figure 5-10. Si nanowires with ordered grooves display high yield and minimal tapering. a, A TEM overview of etched *n*-type Si nanowires. Numbers correspond to individual nanowires with zoom-in views. **b**, An etched Si nanowire with TEM images taken at multiple locations along its axial direction. Ordered grooves were observed on the entire nanowire with marginal differences. Minimal nanowire tapering was observed. **c-l**, TEM images of individual nanowires showing a high yield of ordered grooves. Among 11 nanowires, only #6 and #7 did not show ordered grooves.

TEM images and selected area electron diffraction (SAED) patterns recorded at different zone axes of <112> nanowires define a secondary building unit (SBU) and highlighted several key structural features (**Fig. 5-11**). First, we observed that all the original atomic Au lines ran along <110> directions over the sidewalls (yellow dotted lines, **Fig. 5-11a**). Second, the etched porous grooves were placed on {110} facets if etching was initiated from the {113} sidewall, while the grooves sat on {112} facets if starting from the {111} sidewall (**Fig. 5-11a**). Third, the atomic Au lines and corresponding grooves from {111} sidewalls were perpendicular to the nanowire growth axis, while those from {113} the sidewalls were not (**Fig. 5-11a**).

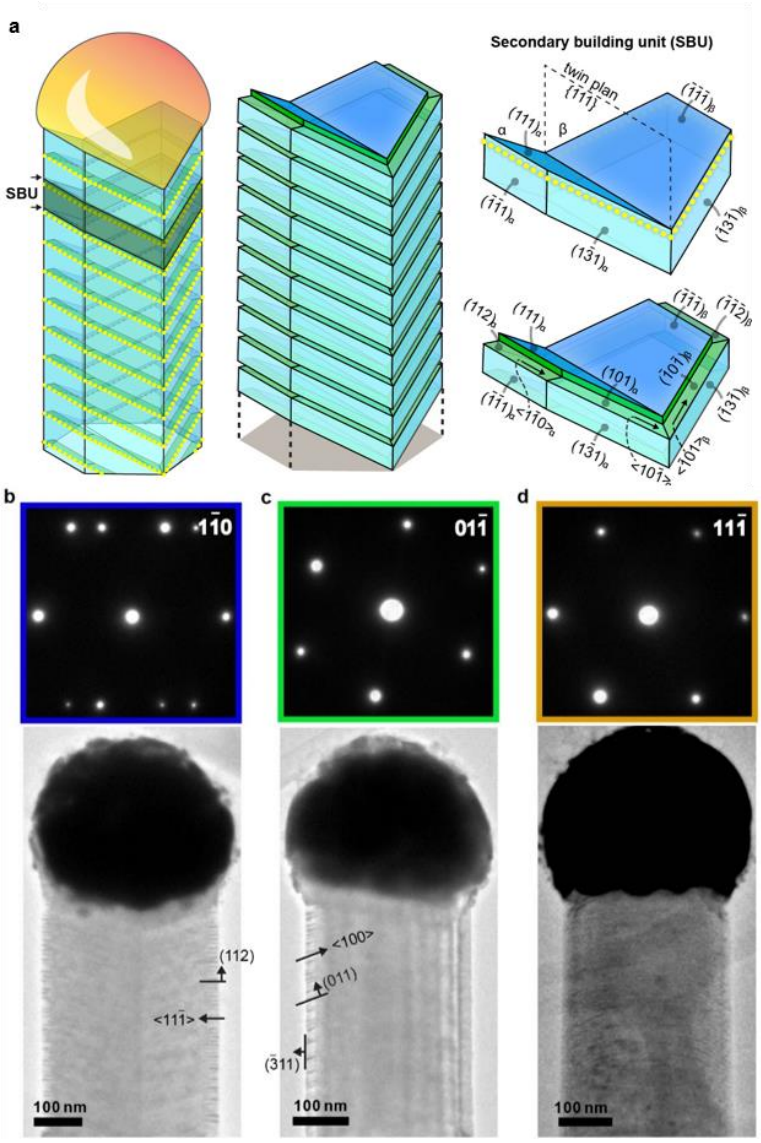

Figure 5-11. Structures of etched grooves on <112> grown Si nanowires. a, Schematics of the structure model of gold line patterns and corresponding etched grooves on Si nanowire sidewall facets. Secondary building units before and after etching are highlighted. A twin plane is usually observed for <112> grown Si nanowires. **b-d**, TEM images and corresponding SAED patterns collected from the same color-coded viewing orientations as shown in **a** ($1\bar{1}0$, left; $01\bar{1}$, middle; $11\bar{1}$, right). Groove orientations and nanowire sidewall facets are labelled in individual panels.

Statistical imaging analysis with users' script (**Fig. 5-12**) indicated that larger nanowire diameter (*e.g.*, > 120 nm), moderate temperature (*e.g.*, 460 ~ 480 ^{o}C), and a high phosphine concentration (*e.g.*, Si/P feeding ratio < 1000) enabled high yield line and groove formation (**Fig.**

5-13). While nanowire diameter and growth temperature (**Fig. 5-13**) did not significantly affect the average groove spacing, the distribution became narrower under certain conditions (*i.e.*, 360 ~ 480 nm diameter and 470 ^{o}C). Phosphine concentration (**Fig. 5-12**), however, had a significant effect, with a Si/P feeding ratio > 2000 yielding no grooves or atomic Au lines, and an increased groove spacing and wider distribution when the Si/P feeding ratio varied from 500 to 250 (**Fig. 5-13**).

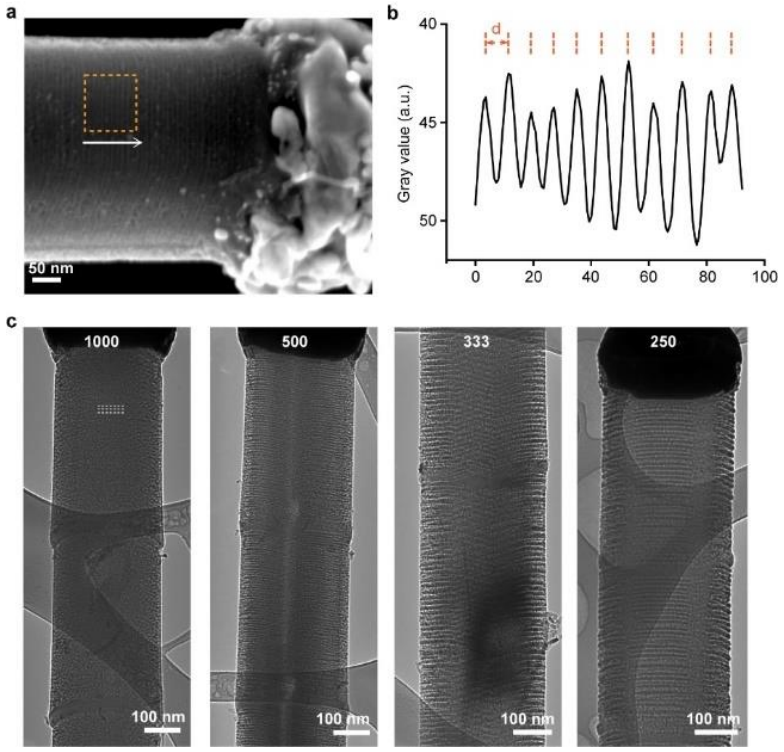

Figure 5-12. Spacing of grooves on Si nanowires. a and **b**, Statistical analysis of the groove spacing. **a**, A representative SEM image of an etched Si nanowire, showing prominent parallel grooves on its surface. The orange dashed box and the white arrow mark the region and the direction of analysis in **b**, respectively. **b**, A 1-D profile of the marked region highlights a periodic oscillation of the image grey value. Local minimal positions, marked by orange dashed lines, represent the centers of each groove. *d* represents the spacing value plotted in **Fig. 5-13**. **c**, TEM images of nanowires with different Si/P feeding ratios show the significant impact of doping levels on the groove formation. Intrinsic segments (smooth segments) were inserted in all cases to help visualize the interface shapes.

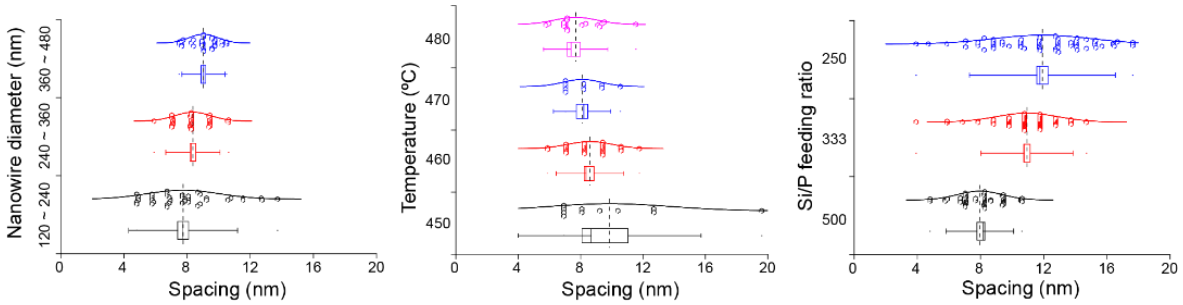

Figure 5-13. Statistical analyses of the groove spacing. The effects of the nanowire diameter (n = 36, 41, 43), growth temperature (n = 21, 11, 32, 11), and Si/P feeding ratio (n = 75, 92, 57) on the groove formation are examined. Boxes, error bars and dots represent standard errors, standard deviations, maximum and minimal values, respectively. Dashed and solid lines represent mean and median values, respectively.

Different from *n*-type Si nanowires, intrinsic and *p*-type nanowires do not yield ordered grooves upon etching (**Fig. 5-14**). When *n*-type/intrinsic dopant modulation was employed, we observed a <10 nm sharp transition (**Fig. 5-14**) from parallel grooves (*i.e.*, *n*-type Si) to smooth surface (*i.e.*, intrinsic Si). These facts suggest that the alloy droplet dynamics are highly sensitive to their immediate chemical environment near the triple-phase boundary (TPB), which can be switched reversibly and quickly between multiple states.

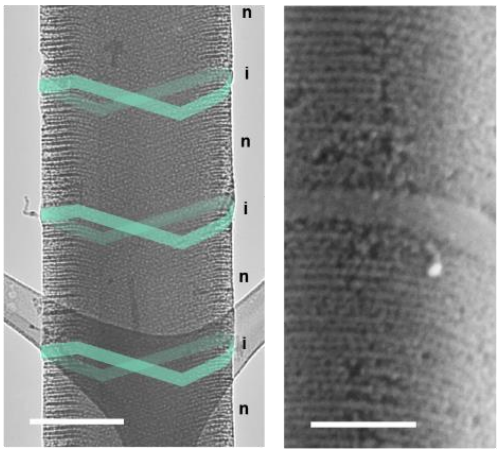

Figure 5-14. TEM and SEM images of etched dopant modulated nanowires. Only the *n*-type segments yielded the grooves upon etching while the intrinsic segments (cyan ribbons) remained smooth. Scale bars, 200 nm (**d**), 100 nm (**e**).

5.2.5 Mechanistic understanding

The easier imaging and enhanced clarity of etched grooves enable a mechanistic understanding of the underlying atomic Au pattern formation. Specifically, we sought to address the following questions. First, why do the <112>-oriented Si nanowires show much higher patterning yield than <111>-oriented ones, *i.e.*, ~ 90 % versus ~ 30 %? Second, why do dopants exert a significant impact? And specifically, why does only phosphine yield the observed line patterns? Last, what is the built-in "switching" mechanism to regulate the Au deposition during an *n*-type Si nanowire growth?

Regarding the orientation-dependent line pattern yield, we noted two structural differences between <112>- and <111>-oriented nanowires. In <112>-oriented nanowires, there are two exposed {111} facets and four exposed {113} that are known to promote wetting or accumulation of Au species[11,14,37-39]. Moreover, essentially all <112>-oriented Si nanowires display at least one {111} twin plane that runs parallel to the nanowire axis[11]; such a planar defect is known to accumulate gold species[40]. <111>-oriented nanowires, however, do not have {111} sidewall facets (unless it has a sawtooth geometry[22,39] which was not the case under our growth condition) and only occasionally contain inclined {111} faults that occupy a small portion of nanowires[37,38]. These two factors together suggest that the sidewalls of <112>-oriented nanowires (that contain {111} and {113} facets and exposed twin plan edges) are more sticky to Au/Si alloy droplets and promote the droplet contact to the sidewall[41] and subsequent atomic Au line patterning. <111>-oriented nanowires do not have significant sticky features, giving lower yield or incoherent line patterns, or line patterns that are accumulated primarily around the inclined {111} faults (**Fig. 5-15**).

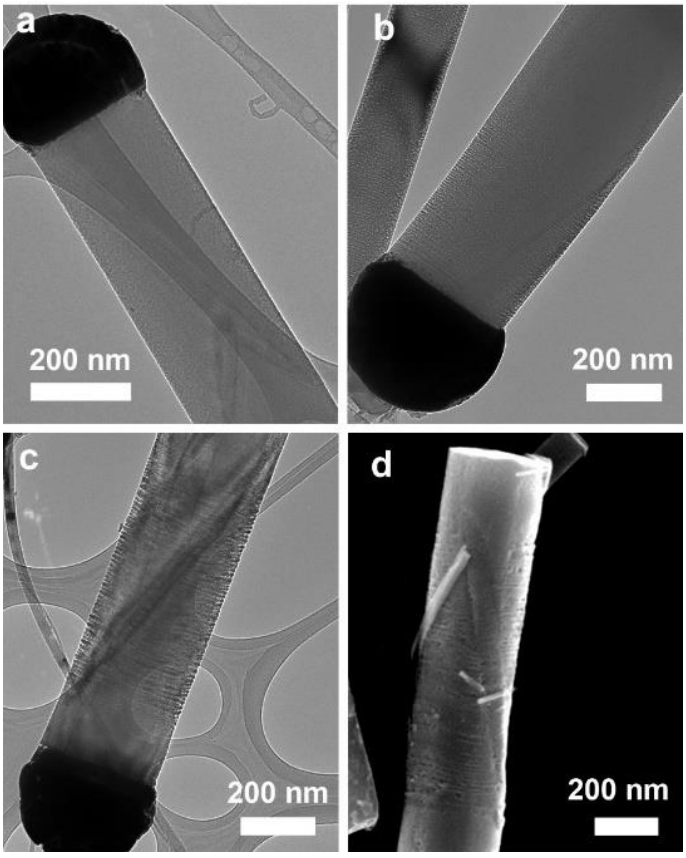

Figure 5-15. TEM and SEM images of etched Si nanowires with <111> growth orientation. a, The <111>-oriented nanowires do not show a high yield of parallel grooves after etching. **b-d**, The <111>-oriented nanowires show incoherent line patterns, and these lines are usually accumulated around the inclined {111} faults.

Next, we only observed ordered Au lines in phosphorus-doped (*i.e.*, n-type) Si nanowires, but not in boron-doped (*i.e.*, p-type) or intrinsic Si nanowires. This can be understood by considering two criteria that must be satisfied simultaneously: (I) the as-deposited Au should be patterned, and (II) the as-deposited Au should be immobilized/stabilized so that the patterns won't randomize during the later stage of synthesis.

Without *in situ* imaging tools, we cannot rule out the possibility that the as-deposited atomic Au in intrinsic, boron-doped, and phosphorus-doped Si nanowires would all be ordered, *i.e.* criteria I may be satisfied for intrinsic and doped nanowires. However, for criteria II, different

surface chemistry can have drastic effects on the stability of as-deposited Au. The boron (*i.e.*, a p-type dopant) precursor was shown to promote Au diffusion along Si nanowire sidewalls[11], which produced silicon spicules with graded gold coverage. This fact suggests that boron cannot immobilize atomic Au. For intrinsic Si nanowires, the sidewall was passivated with atomic hydrogen, which typically inhibited Au deposition. Even if Au atoms were deposited over the sidewall during the synthesis, they tended to quickly de-wet and form nanoparticle aggregates[11]. Finally, phosphorus, as decomposed from phosphine (PH_3, an *n*-type dopant precursor), is known to interact strongly with both Si and Au[16,33,42] and preferentially accumulate around the nanowire surfaces in n-type Si nanowires[43]. Indeed, previous results on n-type silicon spicules indicate minimum gold-based gradient along Si nanowire sidewalls[11], confirming the immobilization role of phosphorus over Au. Overall, only phosphorus-doped Si nanowires can satisfy criteria II, *i.e.*, stabilizing the as-deposited ordered atomic Au lines.

Phosphorus exists in multiple phases of the nanowire system. The key question is, "Which part of phosphorus is critical?" The sharp pattern transition between phosphorus-doped and undoped segments (**Fig. 5-14**) suggests that the dopant reservoir effect[44], which usually covers a characteristic length of ~ the nanowire diameter, would not impact the line patterning. Therefore, the phosphorus inside the liquid alloy droplet (to be used for doping) and the solid Si nanowire (already used for bulk or sub-surface doping) is not critical for the observed Au patterns. Instead, only phosphorus in the gas phase and over the silicon surfaces regulate the pattern formation.

Finally, regarding the built-in switching mechanism for atom printing, it requires that the VLS growth system allow both the alloy-based nozzle positioning and atomic Au-based ink delivery. As shown below, we propose that a stick-slip motion and a chemical potential variation enable the positioning and the delivery (**Fig. 5-16**), respectively.

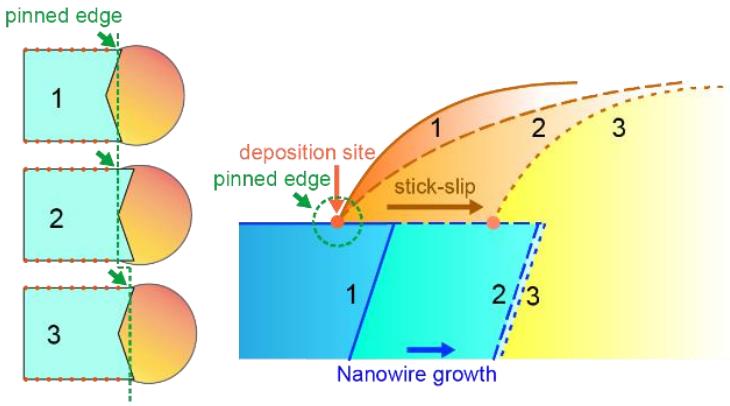

Figure 5-16. Schematic diagrams illustrating the mechanism for atomic Au line pattern formation. A model is proposed, combining a stick-slip motion and an Au deposition process.

As stated earlier, phosphorus binds strongly with Au and Si nanowires[16,33,42]. Such a robust interaction would cause pinning of the alloy droplet at the Si sidewall with a pinning potential barrier (U), as well as the immobilization of as-deposited atomic Au so as to maintain the patterns. During nanowire growth, the alloy droplet contact angle (θ) decreases initially because the TPB is pinned at the sidewall (*i.e.*, 'Stick'). When the θ reaches its minimum (θ_{min}), the potential barrier U can subsequently be overcome by the gain in Gibbs free energy (ΔG) upon snapping to the next equilibrium/quasi-equilibrium position with a contact angle θ_0 (*i.e.*, 'Slip')[45]. This droplet motion can position the droplet edge (the "nozzle").

Because Si supersaturation near the TPB is proportional to contact angle θ[21,46], a reduction of θ upon nanowire elongation caused a local drop of supersaturation, and correspondingly, a transfer of Au atoms (*i.e.* "ink") from the liquid alloy to the solid Si surfaces near the TPB. This angle-dependent atom deposition is reminiscent of the coffee-ring effect[25]. However, unlike the traditional coffee-ring process where evaporation of the droplet causes θ reduction and capillary flow, the driving force for the θ dynamics and atomic Au deposition in our case was the elongation

of the Si nanowire and the corresponding chemical potential changes at TPB. Iterations of this θ variation then yielded the observed parallel atomic Au line patterns on Si nanowire sidewalls.

5.2.6 Analysis of atomic gold deposition

The formation of the parallel line pattern on silicon (Si) nanowires can be explained by a combination of a stick-slip motion that positions the liquid alloy droplet edge and a chemical potential variation that delivers Au.

5.2.6.1 Stick-slip motion

During the growth of an *n*-type Si nanowire, the dopant gas phosphine (PH_3) decomposes into phosphorus (P) which bonds strongly to Si[57-59]. Additionally, P also interacts robustly with Au species[42], leading to pinning of the droplet and an energy barrier for unpinning (U). During the nanowire growth, the alloy droplet contact angle is constantly decreasing because the triple-phase boundary (TPB) contact line is pinned at the equilibrium or quasi-equilibrium position. During the nanowire growth, the alloy droplet contact angle (θ) is initially decreasing because the TPB is pinned at the sidewall (i.e., 'Stick'). When θ reaches its minimum (θ_{min}), the potential barrier U can subsequently be overcome by the gain in Gibbs free energy (ΔG) upon snapping the TPB to the next equilibrium/quasi-equilibrium position with a contact angle θ_0 (i.e., 'Slip'). Because the Si chemical potential near the TPB is proportional to the contact angle, a reduction of θ upon nanowire elongation causes a local drop of $\mu_{Si,l}$, and correspondingly a local elevation of Au concentration and Au atom deposition near the TPB. However, unlike traditional droplet stick-slip motions due to either evaporation-induced droplet shrinking or directional droplet movement by external manipulation, the driving force for the current TPB dynamics is the elongation of Si nanowire through a VLS mechanism.

Detailed analysis of the stick-slip motion[45] can be performed based on an interfacial energy consideration. In most of the existing literature on VLS surface energetics, alloy droplet wetting over semiconductor sidewalls were not considered. However, our work revealed that this situation could occur. Specifically, when the TPB randomly shifts leftward and touches the solid sidewall, the droplet may get pinned if there is a strong 'retention' due to the presence of chemical species (in our case, phosphorus, P) over the semiconductor sidewalls (Phase I, **Fig. 5-17a**).

At any given contact angle θ, the interfacial Gibbs free energy of the Au/Si alloy droplet can be described as

$$G = A_{lv}\gamma_{lv} + A_{sl}\gamma_{sl} - A_{sl}\gamma_{sv}, \qquad (5\text{-}1)$$

where A_{lv} and A_{sl} represent the contact areas of liquid/vapor and solid/liquid interfaces, γ_{lv}, γ_{sl} and γ_{sv} are the line tensions at liquid/vapor, solid/liquid and solid/vapor interfaces, respectively.

Under thermodynamic equilibrium, Young's contact angle equation gives

$$\gamma_{lv}\cos\theta_0 = \gamma_{sv} - \gamma_{sl}, \qquad (5\text{-}2)$$

where θ_0 is the equilibrium contact angle. Combining Eqs. 5-1 and 5-2, the Gibbs free energy could be rewritten as

$$G = A_{lv}\gamma_{lv} - A_{sl}\gamma_{lv}\cos\theta_0. \qquad (5\text{-}3)$$

During nanowire growth, the TPB contact line is assumed to become pinned at its equilibrium/quasi-equilibrium position starting from a certain time point. When the nanowire continues to elongate for an extra length of L, this newly grown segment would cause an increase of the solid/liquid interfacial area by $L \times d$, where d is a geometrical factor at the TPB. The corresponding contact angle of the alloy droplet decreases from θ_0 to θ (Phase II, **Fig. 5-17b**).

The excess Gibbs free energy under the non-equilibrium state is

$$\begin{aligned}\Delta G = G - G_0 &= (A_{\mathrm{lv}} - A_{\mathrm{lv}}^0)\gamma_{\mathrm{lv}} - (A_{\mathrm{sl}} - A_{\mathrm{sl}}^0)\gamma_{\mathrm{lv}}\cos\theta_0 \\ &= (A_{\mathrm{lv}} - A_{\mathrm{lv}}^0)\gamma_{\mathrm{lv}} - Ld\gamma_{\mathrm{lv}}\cos\theta_0\end{aligned}. \qquad (5\text{-}4)$$

Besides θ, A_{lv} is also a function of d from the geometrical analysis of the alloy droplet shape.

When the excess Gibbs free energy reaches its maximum.

$$\Delta G_{\max} = U, \qquad (5\text{-}5)$$

where U is the pinning energy due to the interaction between Au/Si liquid alloy and solid *n*-type Si nanowire sidewall, the droplet has enough driving force to overcome the pinning potential barrier so the TPB contact line can jump to its next equilibrium/quasi-equilibrium position (Phase III, **Fig. 5-17c**)[60]. In general, U should be highly dependent on the chemical environment during the VLS growth. In our case, the higher the PH_3 feeding concentration, the higher the amplitude of U as it is related to the interaction between P and Au/Si.

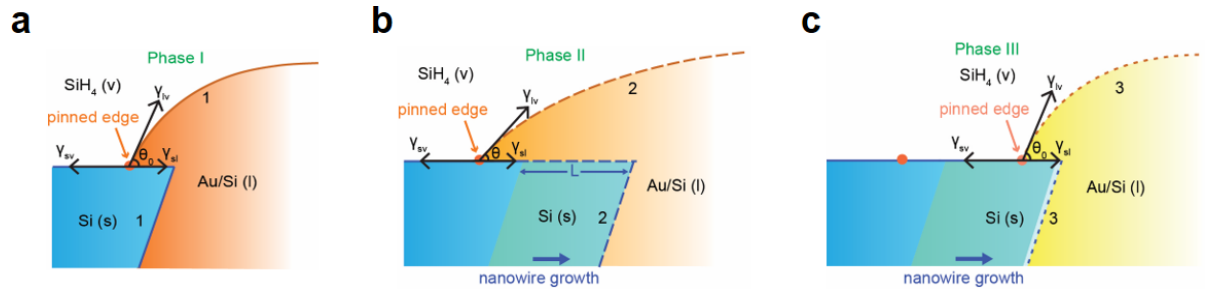

Figure 5-17. Three phases of SiNW growth (Phase I, II and III) during one cycle of stick-slip motion.

5.2.6.2 Chemical potential variation

During the above stick-slip motion, Au atoms would be deposited on the Si nanowire sidewall due to contact-angle-dependent Au delivery. This process can be understood by a chemical potential argument.

In a typical Si nanowire growth process, the Gibbs free energy change during the process of Si deposition at TPB can be described as[21]

$$\Delta G_{\mathrm{Si}} = G_{\mathrm{Si,s}} - G_{\mathrm{Si,l}} = (\mu_{\mathrm{Si,s}} - \mu_{\mathrm{Si,l}} + \delta \sin\theta) N_{\mathrm{Si}}, \qquad (5\text{-}6)$$

where $\mu_{\mathrm{Si,s}}$ and $\mu_{\mathrm{Si,l}}$ are the chemical potentials of Si in the solid nanowire and liquid alloy, respectively, δ is a positive constant that is relevant to the geometry and energy at TPB and displaces a property of a *δ-function*, θ is the alloy droplet contact angle, N_{Si} is the total number of Si under consideration. The contact angle dependence is introduced due to a force normal to the solid-liquid interface that induced a stress on the nanowire sidewall[21].

Since the nanowire has a uniform diameter, *i.e.*, there is no radial deposition of Si atoms, therefore ΔG_{Si}=0. Eq. 5-6 can be reorganized to[21]

$$\mu_{\mathrm{Si,l}} - \mu_{\mathrm{Si,s}} = \delta \sin\theta . \qquad (5\text{-}7)$$

Within a single oscillation cycle, the contact angle is constantly decreasing from the initial pinning time point, due to the stretching of the liquid alloy droplet by the newly elongated segment. From Eq. 5-7, the chemical potential difference of Si ($\mu_{\mathrm{Si,s}}$ - $\mu_{\mathrm{Si,l}}$) at TPB reaches its maximum at the minimum contact angle, which triggers Au deposition at the solid Si nanowire surface to counterbalance the change of ($\mu_{\mathrm{Si,s}}$ - $\mu_{\mathrm{Si,l}}$). The extraction of Au atoms from the alloy droplet and their deposition at the TPB may also be facilitated by the strong interaction between P and Au.

Finally, since such a chemical potential variation follows a *δ-function* around the TPB, we therefore only expect Au deposition in the form of lines, instead of patches.

5.2.7 *Ex situ* studies of complex crystal growths

Since the grooves faithfully delineated the 3D TPB geometry, tracing these features can imply complex material growth dynamics, which are typically studied by *in situ* techniques[20,21,47] in a constrained environment. For these studies, we intentionally introduced narrow intrinsic segments (cyan bands, **Figs. 5-18, 5-19**), as their smooth surfaces upon etching can either mark the locations of growth perturbations (**Fig. 5-18**) or help evaluate the stability of structural evolution (**Fig. 5-19**).

We first studied two complex building blocks, nodes and kinks[48] (**Fig. 5-18**). We found that during node growth (**Figs. 5-18a**, **5-18c**), the droplet edge first pinned heavily on one facet upon dopant switching (or growth perturbation) while the rest of the droplet continued to evolve (pink dashed lines). Subsequent unpinning (yellow dashed lines, **Fig. 5-18a**) recovered the original growth behavior, leaving a node behind (red dashed line in **Figs. 5-18a**, **5-18c**). However, for a kinked unit (**Figs. 5-18b**, **5-18c**), the pinned droplet edge remained attached to the Si sidewall (yellow arrow), while the growth orientation switched between two <112> (red arrows) by shrinking/enlarging the droplet/Si interfaces that are parallel to the original/new ones (*i.e.*, highlighted in pink and green dashed lines, respectively). These observations are consistent with previous models[37,48,49].

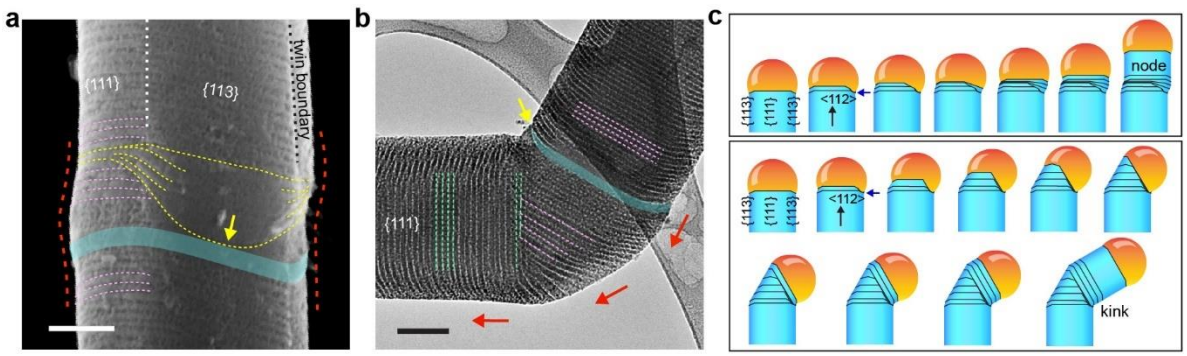

Figure 5-18. Atomic gold patterns enable the study of the growth dynamics of existing structures. **a**, A SEM image of a nanowire with a node. Yellow and pink dashed lines mark the evolution of the alloy droplet during node formation. The yellow arrow marks the pinning edge of the droplet on an intrinsic segment (cyan ribbon). Red dashed lines highlight the node evolution. Scale bar, 100 nm. **b**, A TEM image of a kinked nanowire. Red arrows indicate the switches of the nanowire growth orientations. The yellow arrow marks the pinning edge of the droplet on the sidewall at an intrinsic segment (cyan ribbon). Pink and green dashed lines highlight the grooves in the original and the new arms, respectively. Scale bar, 100 nm. **c**, Schematics of the growth dynamics. A node is formed when the droplet edge first gets pinned heavily on one facet (blue arrow) while the rest of the droplet continues to evolve. Subsequent unpinning recovers the original growth behavior, leaving a node behind. In the formation of a kinked unit, the pinned droplet edge remains attached to the Si sidewall (blue arrow), while the growth orientation switches between two <112> directions by shrinking/enlarging the Au/Si alloy droplet/Si nanowire interfaces that are perpendicular to the original/new arm orientations.

With this atom-enabled etching, we also discovered two new growth behaviors (**Fig. 5-19**). First, we found that a Si/Au alloy droplet crossing multiple twinning units (labelled as **1**, **2**, **3** and **4**) can gradually switch the growth orientation from <112> to <111> (**Fig. 5-19**), without involving a kinked unit. SAED from different portions (**Fig. 5-19b**) and dark field TEM images from selected SAED spots (**Fig. 5-19c**) showed the existence and size evolution for each unit. Zoom-in TEM images (**Figs. 5-19d**, **5-19e**) revealed sharp twin boundaries (**Fig. 5-19d**) and the hierarchical nanoscale and atomic scale ordering (**Fig. 5-19e**). The TPB showed zigzag shapes (**Fig. 5-19d**), and the projected lengths for each TPB segment and the nanowire angular orientation changed

smoothly during the <112> to <111> transition (**Fig. 5-19f**). This observation highlights an unusual curvature formation mechanism, *i.e.*, through the size evolution of multi-twinned units in crystalline materials (**Fig. 5-19i**, upper panel). Second, the scale-like TPB was observed when the phosphine concentration was high (100 < Si/P feeding ratio < 300), with a typical yield of < 15 %, together with a majority of parallel TPB patterns. The TPB oscillated between two wavy line shapes (red and blue lines in **Fig. 5-19g**, lower panel in **Fig. 5-19i**), and the spacing between adjacent TPB lines ($d_{(i+1)-i}$) fluctuated (versus being mostly constant for parallel TPB patterns) and were location-dependent (**Fig. 5-19h**, recorded along black, brown and green dashed lines in **Fig. 5-19g**). Finally, in both curvature-forming TPB (**Fig. 5-19a**) and scale-like TPB (**Fig. 5-19g**), the insertion of intrinsic segments (cyan bands) did not terminate the material growth behaviors.

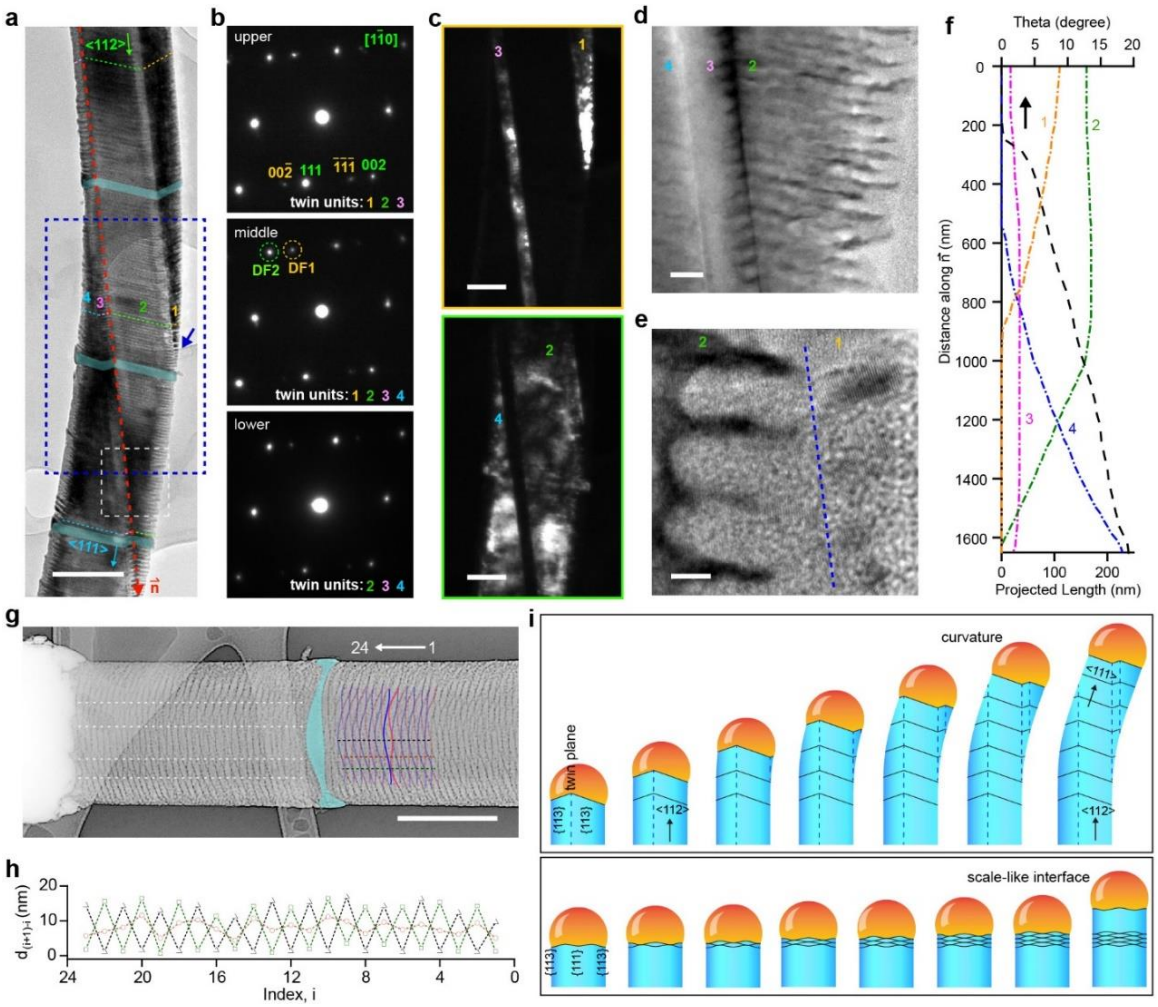

Figure 5-19. Atomic gold patterns enable the discovery of new crystal growth behaviours. a, A BF TEM image of the nanowire with multiple twin units labelled by numbers. The growth orientation is shifted gradually from <112> to <111>. Cyan ribbons highlight the intrinsic segments. Scale bar, 200 nm. **b**, SAED patterns taken at upper, middle and lower portions of the nanowire in **a**. **c**, DF TEM images formed by selecting diffraction spots marked by yellow (DF1) and green (DF2) dashed circles in **b**. Scale bars, 100 nm. **d** and **e**, HRTEM images from different regions in **a**, marked by a white dashed box (**d**) and a blue arrow (**e**). Scale bars, 20 nm (**d**), 5 nm (**e**). **f**, Growth behavior analysis shows a smooth transition of the nanowire orientation from a <112> (marked by $\vec{n}$ in **a**) to a <111> direction. Projected lengths of individual twin units and the nanowire angular orientation are plotted along $\vec{n}$. **g**, A TEM image (with color inversion) of a nanowire with a scale-like TPB. Scale bar, 200 nm. **h**, The growth behavior is analyzed by tracking spacing $d_{(i+1)-i}$ between adjacent wavy lines (blue and pink lines) at three different locations (black, brown and green dashed lines in **g**). The white arrow in **g** indicates the direction of analysis. **i**, Schematics of the growth dynamics. A

Figure 5-19, continued. curved nanowire can be formed when it gradually switches the growth orientation from <112> to <111> (black arrows), without involving a kink unit. During the transition, the droplet crosses multiple twin boundaries, marked by black dashed lines. A scale-like alloy/Si interface is formed when the TPB oscillates between two wavy line shapes. The cyan ribbon in **a** and **g** marks an intrinsic segment.

5.2.8 Outlook

In this work, we demonstrated a new approach for parallel patterning/printing of individual atoms over smooth substrates. We revealed an atomic version of MACE, where single Au atoms can catalyze the etching of Si to create < 5 nm features. We also discovered an alloy droplet instability during the classical VLS growth which would promote a stick-slip motion along the nanowire sidewalls. Finally, using new atom patterning and atom-catalyzed etching, we revealed several complex crystal growth dynamics that are hard to probe in the past.

In particular, the previous alloy droplet instabilities in VLS systems are all related to a configuration where the liquid is supported by the nanowire end facets[20-24]. In this work, the new droplet instability is relevant to droplet wetting over the nanowire sidewall[41]. This wetting configuration has received very little attention in the past, although theoretical analysis has predicted its existence[41].

There are several important experimental factors that contribute to a series of new observations in this work. First, the use of STEM imaging from thin nanowire sections (by microtoming) is important. Even under STEM, the atomic Au lines are only visible with a careful tilting of the sample. Traditional TEM cannot reveal such atomic Au lines unless chemical etching is used to amplify their original locations. Therefore, the phenomena revealed in this work may have existed for a very long time, but were overlooked due to non-ideal imaging techniques used before. Second, we only observed Au patterns in large diameter Si nanowires (>120 nm), which is

beyond the most studied diameter range of 5 ~ 100 nm. This fact is consistent with the prior studies that larger diameter Si nanowires tend to accumulate more Au[14,15]. Third, the nanowire orientation and doping type are both critical for the high yield deposition of Au lines, which are discussed in detail in the Results section. Most prior studies on Si nanowires have been focused on <111> orientation, instead of the <112> in the current work. Finally, the atomic scale MACE revealed in this work also facilitates the discovery and understanding of this new droplet instability. This atomic scale catalytic etching highlights the location of the original Au lines.

With regards to potential applications, the atom-based self-labelling may be used to reveal the growth mechanisms for many other complex nanowire structures, such as epitaxial lateral nanowires[50] and island-chain nanowires[51]. This labelling may be applied broadly to chemistry and materials science with a role analogous to the use of fluorescent molecules in probing biological dynamics. Additionally, the parallel atom deposition and etching over nanowire sidewalls may be extended to atom-based catalytic lithography over planar substrates.

5.3 Experimental

Synthesis of *n*-type silicon (Si) nanowires. Silicon nanowires were synthesized using a gold (Au) nanocluster-catalyzed chemical vapor deposition (CVD) method. The citrate-stabilized Au colloidal nanoparticles (Ted Pella, USA, 200 nm) were deposited onto Si (100) substrates (Nova Electronic Materials, USA, *n*-type, 0.001~0.005 Ω cm) as catalysts. Prior to the catalyst deposition, native oxide layers on the Si substrates were removed with hydrofluoric acid (HF) (Sigma-Aldrich, USA) to yield hydrogen-terminated surfaces. The growth of Si nanowires were effectuated at 450~490 ^{o}C using silane (SiH_4) as the silicon source, phosphine (PH_3, 1000 ppm in H_2) as the *n*-type dopant, and hydrogen (H_2) as the carrier gas. In a typical synthesis of *n*-type Si nanowires with a Si/P feeding ratio of 500:1, the flow rates of SiH_4, PH_3 and H_2 were 2, 4 and 60 standard

cubic centimeters per minute (sccm), respectively. The growth chamber pressure was maintained at 40 Torr throughout the synthesis. The Si/P feeding ratio was varied by changing the flow rate of PH_3 between 2 sccm and 8 sccm while fixing the SiH_4 flow rate as 2 sccm to reach Si/P feeding ratios from 1000:1 to 250:1.

Synthesis of doping and pressure modulated Si nanowires. In a typical growth, an *n*-type base segment was grown under 470 ^oC with a Si/P feeding ratio of 500:1 by setting the flow rates of SiH_4, PH_3 and H_2 as 2, 4 and 60 sccm, respectively. The base segment was grown under a constant pressure of 40 Torr for 1 minute. Later on, periodic switches between 7 s of evacuation and 23 s of pressure ramping were performed to modulate the growth chamber pressure during the nanowire growth. During the 23 s of pressure ramping periods, the PH_3 flow was turned off in the first 3 seconds to modulate the doping level of the nanowires. The pressure switching cycles were iterated for 10 minutes after the base segment growth to yield doping and pressure modulated Si nanowires.

***Ab initio* molecular dynamics simulations.** We performed *ab initio* molecular dynamics (AIMD) simulations within the generalized gradient approximation (GGA) using the projector-augmented wave formalism as implemented in the Vienna *Ab initio* Simulation Package (VASP) [52]. We used the empirical method of Grimme[53] to account for vdW interactions. The exchange correlation was described by the Perdew-Burke-Ernzerhof (PBE) functional[54], with the pseudopotentials supplied by VASP. The plane wave energy cut-off was set at 400 eV. The Brillouin zone was sampled at the Γ-point only. The computational supercell (96 atoms) consisted of diamond cubic Si oriented such that X (1-10), Y (11-2) and Z (111). An Au atom was placed on an Si site in the initial structure. Periodic boundary conditions were employed along all directions. A vacuum of 20 Å was introduced in the Z direction to model the (111) surface. HF and H_2O_2 (10 molecules of each) were placed randomly on the (111) surface of Si. Subsequently, we performed AIMD simulations

in the canonical (NVT) ensemble at 600 K via the ***Nosé***-Hoover thermostat[55] as implemented in VASP, using a time step of 0.5 fs to update the atom positions.

Etching of the Si nanowires. The parallel atomic gold-based line patterns on Si nanowires were revealed using an etching system consisting of HF and hydrogen peroxide (H_2O_2). In a typical etching experiment, the as-grown Si nanowire substrates were dipped into a 10.85 wt% H_2O_2 (Fisher Scientific, USA) and 10.37 wt% HF aqueous mixture solution at 10 °C for 8~45 s. The etched samples were rinsed with deionized (DI) water, isopropyl alcohol (IPA) and blown dry by nitrogen (N_2).

Microscopy analysis. Unetched Si nanowires were sectioned using an epoxy resin-based ultramicrotome technique for the study of Au distribution on nanowire surfaces by STEM. Nanowires embedded with epoxy resin precursors (low viscosity Spurr, Ted Pella, USA) were first solidified at 60 °C for 24 h. Resin sections of ~70 nm were cut by an ultramicrotome (Ultracut E, Reichert-Jung, USA) and collected by lacey carbon copper grids (Ted Pella, USA, Lacey Carbon, 200 mesh). The high-angle annular dark field (HAADF) STEM images of sectioned Si nanowires were taken on an aberration-corrected STEM operated at 200 keV (JEM-ARM200CF, JEOL, Japan). The electron-dispersive X-ray (EDX) spectra were obtained using an Oxford X-Max^N 100TLE windowless SDD X-ray detector (Oxford Instruments, UK) on the same JEOL STEM while imaging. For electron microscopy of etched Si nanowires, they were gently sonicated in IPA and dispersed onto silicon substrates (Nova Electronic Materials, USA, *n*-type, 0.001~0.005 Ω cm) or lacey carbon copper grids. A Carl Zeiss SEM (Merlin FE-SEM, Carl Zeiss, Germany) and an FEI TEM (Tecnai F30, FEI, USA) were used to characterize the morphology of etched Si nanowires. Crystallography of the Si nanowires was studied by analyzing bright-field (BF) and dark-field (DF) TEM images and selected area electron diffraction (SAED) patterns taken by a

JEOL TEM operated at 300 keV (JEM-3010, JEOL, Japan). DF TEM images in **Fig. 5-19c** were formed by tilting the electron beam to position the corresponding diffracted beams in **Fig. 5-19b**, marked by DF1 and DF2, into the objective aperture to highlight individual twin units. A Hitachi HD-2300A STEM (Hitachi, Japan) was used to study the etched morphology in three-dimensions (3D) by collecting tilting STEM series. Au nanoparticles of 10 nm were applied on to Si nanowires as fiducial markers. Etched Si nanowires on Si substrates were first picked up and transferred with a micro-manipulator and attached to copper (Cu) tips with electron-beam-induced platinum (Pt)/carbon (C) deposition using a focused ion-beam (FIB) system (FEI, USA, Helios Nanolab 600 DualBeam FIB/SEM). The HAADF-STEM images of the samples were collected at tilt intervals of 2° from 0° up to 210°. For atomic force microscopy (AFM), unetched Si nanowires were transferred to Si substrates (Nova Electronic Materials, USA, *n*-type, 0.001~0.005 Ω cm) and imaged using an Asylum Cypher AFM (Asylum Research, USA).

Atom-probe tomography (APT). Unetched *n*-type Si nanowire surfaces were first protected with a 50 nm Ni capping layer deposited by an electron beam evaporator (AJA International, USA). The nanowires were then transferred horizontally onto silicon microposts using a micromanipulator, mounted with Pt/C deposition, and milled into needle-like microtip specimens using a FEI Helios Nanolab 600 FIB (FEI, USA) system. APT was performed using an ultraviolet (UV) laser-assisted local-electrode atom-probe (Cameca, USA, LEAP 4000X Si). Surface atoms from the microtips were field-evaporated with an applied voltage of 1~7 kV direct current (dc) assisted with a UV (wavelength λ = 355 nm) laser pulsing at 250 kHz with a pulse energy of 20 pJ. The mass-to-charge (m/z) ratios of individual field-evaporated ions, in addition to their (x, y, z) coordinates in direct space, were recorded by a position sensitive time-of-flight detector. During the APT analyses, samples were held at a 30 K base temperature at an ambient pressure of ~$2\times10^{-}$

^{11} Torr. The 3D reconstructions of the data sets were performed utilizing Cameca's IVAS 3.6 code. In a typical analysis, a region-of-interest (ROI) selection tool was used to isolate a region that included the nickel (Ni) capping layer, the native surface silicon oxide layer (SiO_2), and a layer of the Si nanowires. A 2D concentration map of Au was created by analyzing the number of Au atoms per unit volume and projecting the density map on the Si/SiO_2/Ni interface plane. An 80 at% Si isoconcentration surface was created to delineate the region where the Si atomic concentration on one side was larger than 80 at%. A proximity histogram concentration profile[56] was created by analyzing concentrations of individual atoms per unit length, beginning in the Ni layer and moving along the normal direction to the Si isoconcentration surface into the Si nanowire.

X-ray photoelectron spectroscopy (XPS). Four planar Si substrates with different surface treatments were used for XPS analysis. A planar Si substrate (Nova Electronic Materials, USA, *n*-type, 0.001~0.005 Ω cm) with only HF treating for native oxide removal was used as a control sample. The second sample was HF treated before dipping in an Au etchant for 4 minutes and a 10.85 wt% H_2O_2 solution for another 15 s at 10 °C. On the third sample, 200 nm Au nanoparticles (Ted Pella, USA) were deposited on the HF-treated Si surface. The Au-deposited Si substrate was annealed in a CVD system under vacuum at 700 °C for 5 minutes. Finally, the fourth sample underwent the same processing condition with the third one for Au diffusion on Si. It was then dipped in an Au etchant for 4 minutes before transferred into a 10.85 wt% H_2O_2 solution for 15 s at 10 °C. A Kratos AXIS Nova system was used for XPS analysis (Kratos, UK) with a monochromatic Al Kα ($h\nu$ = 1486.6 eV) source. The Al anode, for all measurements, was at 10 mA and 15 kV. The analysis spot of the X-ray beam was 300 × 700 μm^2. Samples were calibrated via the Si 2p peaks located at 99.8 eV. The C 1s peak at 285.5 eV was also used to support this calibration. Pt metal was added to the surface of a number of samples so the Pt 4f signal at 71.0

eV could verify the calibration. Surveys were collected at 160 eV pass energy and a step size of 1 eV. The high-resolution spectra for Si 2p were collected at 20 eV pass energy, a step size of 0.1 eV, 120s sweeps, and with 3 and 20 sweeps respectively.

5.4 Bibliography

1 Custance, O., Perez, R. & Morita, S. Atomic force microscopy as a tool for atom manipulation. *Nature Nanotechnology* **4**, 803-810, doi:10.1038/nnano.2009.347 (2009).

2 Eigler, D. M. & Schweizer, E. K. Positioning single atoms with a scanning tunneling microscope. *Nature* **344**, 524-526, doi:10.1038/344524a0 (1990).

3 Hla, S. W. & Rieder, K. H. STM control of chemical reactions: Single-molecule synthesis. *Annual Review of Physical Chemistry* **54**, 307-330, doi:10.1146/annurev.physchem.54.011002.103852 (2003).

4 Jung, T. M., Prokes, S. M. & Kaplan, R. Growth and energetics of Ga and Al chains on Si (112). *Journal of Vacuum Science & Technology a-Vacuum Surfaces and Films* **12**, 1838-1842, doi:10.1116/1.579014 (1994).

5 Moutanabbir, O., Senz, S., Scholz, R., Alexe, M., Kim, Y., Pippel, E., Wang, Y. W., Wiethoff, C., Nabbefeld, T., Heringdorf, F. M. Z. & Horn-von Hoegen, M. Atomically Smooth p-Doped Silicon Nanowires Catalyzed by Aluminum at Low Temperature. *ACS Nano* **5**, 1313-1320, doi:10.1021/nn1030274 (2011).

6 Law, M., Goldberger, J. & Yang, P. D. Semiconductor nanowires and nanotubes. *Annual Review of Materials Research* **34**, 83-122, doi:10.1146/annurev.matsci.34.040203.112300 (2004).

7 Wagner, R. S. & Ellis, W. C. Vapor-liquid-solid mechanism of single crystal growth. *Applied Physics Letters* **4**, 89-&, doi:10.1063/1.1753975 (1964).

8 Morales, A. M. & Lieber, C. M. A laser ablation method for the synthesis of crystalline semiconductor nanowires. *Science* **279**, 208-211, doi:10.1126/science.279.5348.208 (1998).

9 Lu, W. & Lieber, C. M. Semiconductor nanowires. *Journal of Physics D-Applied Physics* **39**, R387-R406, doi:10.1088/0022-3727/39/21/r01 (2006).

10 Allen, J. E., Hemesath, E. R., Perea, D. E., Lensch-Falk, J. L., Li, Z. Y., Yin, F., Gass, M. H., Wang, P., Bleloch, A. L., Palmer, R. E. & Lauhon, L. J. High-resolution detection of Au catalyst atoms in Si nanowires. *Nature Nanotechnology* **3**, 168-173, doi:10.1038/nnano.2008.5 (2008).

11 Luo, Z. Q., Jiang, Y. W., Myers, B. D., Isheim, D., Wu, J. S., Zimmerman, J. F., Wang, Z. G., Li, Q. Q., Wang, Y. C., Chen, X. Q., Dravid, V. P., Seidman, D. N. & Tian, B. Z. Atomic gold-enabled three-dimensional lithography for silicon mesostructures. *Science* **348**, 1451-1455, doi:10.1126/science.1257278 (2015).

12 Kim, B. J., Tersoff, J., Kodambaka, S., Jang, J. S., Stach, E. A. & Ross, F. M. Au Transport in Catalyst Coarsening and Si Nanowire Formation. *Nano Letters* **14**, 4554-4559, doi:10.1021/nl501582q (2014).

13 Sivaram, S. V., Hui, H. Y., de la Mata, M., Arbiol, J. & Filler, M. A. Surface Hydrogen Enables Subeutectic Vapor-Liquid-Solid Semiconductor Nanowire Growth. *Nano Letters* **16**, 6717-6723, doi:10.1021/acs.nanolett.6b01640 (2016).

14 den Hertog, M. I., Rouviere, J. L., Dhalluin, F., Desre, P. J., Gentile, P., Ferret, P., Oehler, F. & Baron, T. Control of gold surface diffusion on Si nanowires. *Nano Letters* **8**, 1544-1550, doi:10.1021/nl073356i (2008).

15 Madras, P., Dailey, E. & Drucker, J. Spreading of Liquid AuSi on Vapor-Liquid Solid-Grown Si Nanowires. *Nano Letters* **10**, 1759-1763, doi:10.1021/nl100249j (2010).

16 Kim, S., Hill, D. J., Pinion, C. W., Christesen, J. D., McBride, J. R. & Cahoon, J. F. Designing Morphology in Epitaxial Silicon Nanowires: The Role of Gold, Surface Chemistry, and Phosphorus Doping. *ACS Nano* **11**, 4453-4462, doi:10.1021/acsnano.7b00457 (2017).

17 Shin, N., Chi, M. F. & Filler, M. A. Interplay between Defect Propagation and Surface Hydrogen in Silicon Nanowire Kinking Superstructures. *ACS Nano* **8**, 3829-3835, doi:10.1021/nn500598d (2014).

18 Moutanabbir, O., Isheim, D., Blumtritt, H., Senz, S., Pippel, E. & Seidman, D. N. Colossal injection of catalyst atoms into silicon nanowires. *Nature* **496**, 78-82, doi:10.1038/nature11999 (2013).

19 Chen, W. H., Yu, L. W., Misra, S., Fan, Z., Pareige, P., Patriarche, G., Bouchoule, S. & Cabarrocas, P. R. I. Incorporation and redistribution of impurities into silicon nanowires during metal-particle-assisted growth. *Nature Communications* **5**, doi:10.1038/ncomms5134 (2014).

20 Wen, C. Y., Tersoff, J., Hillerich, K., Reuter, M. C., Park, J. H., Kodambaka, S., Stach, E. A. & Ross, F. M. Periodically Changing Morphology of the Growth Interface in Si, Ge, and GaP Nanowires. *Physical Review Letters* **107**, doi:10.1103/PhysRevLett.107.025503 (2011).

21 Gamalski, A. D., Ducati, C. & Hofmann, S. Cyclic Supersaturation and Triple Phase Boundary Dynamics in Germanium Nanowire Growth. *Journal of Physical Chemistry C* **115**, 4413-4417, doi:10.1021/jp1095882 (2011).

22 Ross, F. M., Tersoff, J. & Reuter, M. C. Sawtooth faceting in silicon nanowires. *Physical Review Letters* **95**, doi:10.1103/PhysRevLett.95.146104 (2005).

23 Caroff, P., Dick, K. A., Johansson, J., Messing, M. E., Deppert, K. & Samuelson, L. Controlled polytypic and twin-plane superlattices in III-V nanowires. *Nature Nanotechnology* **4**, 50-55, doi:10.1038/nnano.2008.359 (2009).

24 Algra, R. E., Verheijen, M. A., Borgstrom, M. T., Feiner, L. F., Immink, G., van Enckevort, W. J. P., Vlieg, E. & Bakkers, E. Twinning superlattices in indium phosphide nanowires. *Nature* **456**, 369-372, doi:10.1038/nature07570 (2008).

25 Deegan, R. D., Bakajin, O., Dupont, T. F., Huber, G., Nagel, S. R. & Witten, T. A. Capillary flow as the cause of ring stains from dried liquid drops. *Nature* **389**, 827-829, doi:10.1038/39827 (1997).

26 Gao, P. X., Ding, Y., Mai, W. J., Hughes, W. L., Lao, C. S. & Wang, Z. L. Conversion of zinc oxide nanobelts into superlattice-structured nanohelices. *Science* **309**, 1700-1704, doi:10.1126/science.1116495 (2005).

27 Christesen, J. D., Pinion, C. W., Grumstrup, E. M., Papanikolas, J. M. & Cahoon, J. F. Synthetically Encoding 10 nm Morphology in Silicon Nanowires. *Nano Letters* **13**, 6281-6286, doi:10.1021/nl403909r (2013).

28 Day, R. W., Mankin, M. N., Gao, R. X., No, Y. S., Kim, S. K., Bell, D. C., Park, H. G. & Lieber, C. M. Plateau-Rayleigh crystal growth of periodic shells on one-dimensional substrates. *Nature Nanotechnology* **10**, 345-352, doi:10.1038/nnano.2015 (2015).

29 Li, X. & Bohn, P. W. Metal-assisted chemical etching in HF/H(2)O(2) produces porous silicon. *Applied Physics Letters* **77**, 2572-2574, doi:10.1063/1.1319191 (2000).

30 Huang, Z. P., Geyer, N., Werner, P., de Boor, J. & Gosele, U. Metal-Assisted Chemical Etching of Silicon: A Review. *Advanced Materials* **23**, 285-308, doi:10.1002/adma.201001784 (2011).

31 Hochbaum, A. I., Chen, R. K., Delgado, R. D., Liang, W. J., Garnett, E. C., Najarian, M., Majumdar, A. & Yang, P. D. Enhanced thermoelectric performance of rough silicon nanowires. *Nature* **451**, 163-U165, doi:10.1038/nature06381 (2008).

32 Qu, Y. Q., Liao, L., Li, Y. J., Zhang, H., Huang, Y. & Duan, X. F. Electrically Conductive and Optically Active Porous Silicon Nanowires. *Nano Letters* **9**, 4539-4543, doi:10.1021/nl903030h (2009).

33 Cottrell, T. L. *The strengths of chemical bonds*. second edn, (Butterworth, London, 1958).

34 Fisher, D. J. *Diffusion in silicon: 10 years of research*. (Trans Tech Pubn, 1998).

35 Li, W., Yue, Q., Deng, Y. H. & Zhao, D. Y. Ordered Mesoporous Materials Based on Interfacial Assembly and Engineering. *Advanced Materials* **25**, 5129-5152, doi:10.1002/adma.201302184 (2013).

36 Lu, A. H. & Schuth, F. Nanocasting: A versatile strategy for creating nanostructured porous materials. *Advanced Materials* **18**, 1793-1805, doi:10.1002/adma.200600148 (2006).

37 Hillerich, K., Dick, K. A., Wen, C. Y., Reuter, M. C., Kodambaka, S. & Ross, F. M. Strategies To Control Morphology in Hybrid Group III-V/Group IV Heterostructure Nanowires. *Nano Letters* **13**, 903-908, doi:10.1021/nl303660h (2013).

38 Shin, N., Chi, M. F., Howe, J. Y. & Filler, M. A. Rational Defect Introduction in Silicon Nanowires. *Nano Letters* **13**, 1928-1933, doi:10.1021/nl3042728 (2013).

39 Wiethoff, C., Ross, F. M., Copel, M., Hoegen, M. H. V. & Heringdorf, F. Au stabilization and coverage of sawtooth facets on Si nanowires grown by vapor-liquid-solid epitaxy. *Nano Letters* **8**, 3065-3068, doi:10.1021/nl801146q (2008).

40 Hemesath, E. R., Schreiber, D. K., Gulsoy, E. B., Kisielowski, C. F., Petford-Long, A. K., Voorhees, P. W. & Lauhon, L. J. Catalyst Incorporation at Defects during Nanowire Growth. *Nano Letters* **12**, 167-171, doi:10.1021/nl203259f (2012).

41 Roper, S. M., Anderson, A. M., Davis, S. H. & Voorhees, P. W. Radius selection and droplet unpinning in vapor-liquid-solid-grown nanowires. *Journal of Applied Physics* **107**, doi:10.1063/1.3434403 (2010).

42 Schmid, H., Bjork, M. T., Knoch, J., Karg, S., Riel, H. & Riess, W. Doping Limits of Grown in situ Doped Silicon Nanowires Using Phosphine. *Nano Letters* **9**, 173-177, doi:10.1021/nl802739v (2009).

43 Connell, J. G., Yoon, K., Perea, D. E., Schwalbach, E. J., Voorhees, P. W. & Lauhon, L. J. Identification of an Intrinsic Source of Doping Inhomogeneity in Vapor-Liquid-Solid-Grown Nanowires. *Nano Letters* **13**, 199-206, doi:10.1021/nl3038695 (2013).

44 Christesen, J. D., Pinion, C. W., Zhang, X., McBride, J. R. & Cahoon, J. F. Encoding Abrupt and Uniform Dopant Profiles in Vapor-Liquid-Solid Nanowires by Suppressing the Reservoir Effect of the Liquid Catalyst. *ACS Nano* **8**, 11790-11798, doi:10.1021/nn505404y (2014).

45 Shanahan, M. E. R. Simple theory of stick-slip wetting hysteresis. *Langmuir* **11**, 1041-1043, doi:10.1021/la00003a057 (1995).

46 Schwarz, K. W. & Tersoff, J. From Droplets to Nanowires: Dynamics of Vapor-Liquid-Solid Growth. *Physical Review Letters* **102**, doi:10.1103/PhysRevLett.102.206101 (2009).

47 Ross, F. M. Controlling nanowire structures through real time growth studies. *Reports on Progress in Physics* **73**, doi:10.1088/0034-4885/73/11/114501 (2010).

48 Tian, B. Z., Xie, P., Kempa, T. J., Bell, D. C. & Lieber, C. M. Single-crystalline kinked semiconductor nanowire superstructures. *Nature Nanotechnology* **4**, 824-829, doi:10.1038/nnano.2009.304 (2009).

49 Schwarz, K. W. & Tersoff, J. Elementary Processes in Nanowire Growth. *Nano Letters* **11**, 316-320, doi:10.1021/nl1027815 (2011).

50 Rathi, S. J., Smith, D. J. & Drucker, J. Guided VLS Growth of Epitaxial Lateral Si Nanowires. *Nano Letters* **13**, 3878-3883, doi:10.1021/nl401962q (2013).

51 Xue, Z. G., Xu, M. K., Zhao, Y. L., Wang, J., Jiang, X. F., Yu, L. W., Wang, J. Z., Xu, J., Shi, Y., Chen, K. J. & Cabarrocas, P. R. I. Engineering island-chain silicon nanowires via a droplet mediated Plateau-Rayleigh transformation. *Nature Communications* **7**, doi:10.1038/ncomms12836 (2016).

52 Kresse, G. & Furthmuller, J. Efficient iterative schemes for ab initio total-energy calculations using a plane-wave basis set. *Physical Review B* **54**, 11169-11186, doi:10.1103/PhysRevB.54.11169 (1996).

53 Grimme, S. Semiempirical GGA-type density functional constructed with a long-range dispersion correction. *Journal Of Computational Chemistry* **27**, 1787-1799, doi:10.1002/jcc.20495 (2006).

54 Perdew, J. P., Burke, K. & Ernzerhof, M. Generalized gradient approximation made simple. *Physical Review Letters* **78**, 1396-1396, doi:10.1103/PhysRevLett.78.1396 (1997).

55 Allen, M. P. *Computer simulation of liquids*. (Clarendon Press ; Oxford University Press, 2011).

56 Hellman, O. C., Vandenbroucke, J. A., Rusing, J., Isheim, D. & Seidman, D. N. Analysis of three-dimensional atom-probe data by the proximity histogram. *Microscopy and Microanalysis* **6**, 437-444 doi: 10.1017.S1431927600000635 (2000).

57 Perea, D. E., Hemesath, E. R., Schwalbach, E. J., Lensch-Falk, J. L., Voorhees, P. J., & Lauhon, L. J. Direct measurement of dopant distribution in an individual vapour-liquid-solid nanowire. *Nature. Nanotechnology* **4**, 315-319, doi:10.1038/nnano.2009.51 (2009).

58 Xie, P., Hu, Y. J., Fang, Y., Huang, J. L. & Lieber, C. M. Diameter-dependent dopant location in silicon and germanium nanowires. *Proceedings of the National Academy of Sciences* **106**, 15254-15258, doi: 10.1073/pnas.0906943106 (2009).

59 Yu, M. L., Vitkavage, D. J. & Meyerson, B. S. Doping reaction of PH_3 and B_2H_6 with Si(100). *Journal of Applied Physics* **59**, 4032-4037, doi: 10.1063/1.336708 (1986).

60 Oksuz, M. & Erbil, H. Y. Comments on the energy barrier calculations during "Stick-Slip" behavior of evaporating droplets containing nanoparticles. *Journal of Physical. Chemistry C* **118**, 9228-9238, doi: 10.1021/jp5010083 (2014).

Chapter 6

Conclusion and Outlook

In this thesis, I introduced the general phenomena of bioelectricity and summarized existing techniques for the interrogation of bioelectric activities. Besides traditional metal-based electrodes, Si-based materials and devices are emerging as a unique platform for bioelectric studies, mostly because Si is biocompatible, biodegradable and exhibits a spectrum of important physical properties, especially the semiconducting property (**Chapter 1**).

In my Ph.D. research, I mainly focused on the design of remotely-controlled Si-based biointerfaces, with targets spanning multiple length scales from nanoscopic organelles, microscopic single cells up to macroscopic tissues or organs. Additionally, I also made substantial efforts to study the fundamental aspects of Si material synthesis, aiming to elucidate the underlying physicochemical processes that shape the Si structures and properties.

When I started my Ph.D., advances in device designs and fabrications have enabled a wide range of new Si-based electronic systems, which display multi-functional modalities that could be exploited for interfacing with various biological organizations. Although these electrically registered device components have yielded impressive results, remotely-controlled and freestanding Si systems has yet been employed in biointerface studies before.

Moreover, at the time, most of the applications using Si as biomaterials have been focused on or originated from single crystalline structures or substrates due to the excellent electrical conductivities. We believe, however, new forms of Si that are unique in composition, structure, and property have the potential to introduce new functionalities to the biointerfaces. For example, we hypothesized that amorphous porous Si, which was previously ignored for bioelectronic applications, may display a superior photothermal efficacy due to its enhanced light absorptivity and reduced thermal conductivity comparing to its solid single crystalline counterpart and therefore be applied for a remotely-controlled biointerface. To this end, we prepared a Si mesostructure with multiscale structural and chemical heterogeneities, using ordered mesoporous silica as a template through a chemical-vapor-deposition process. It has an amorphous atomic

structure, an ordered nanowire-based framework, and random sub-micrometer voids. It also shows an average Young's modulus that is 2-3 orders of magnitude smaller than that of single crystalline Si, which is critical to minimal invasive biointerfaces. Finally, we proved that the heterogeneous Si mesostructure indeed showed a pronounced photothermal effect and permitted non-genetic optical modulation of the electrophysiology dynamics in single neurons, representing the first biodegradable platform for light-controlled neuromodulations (**Chapter 2**).

With all kinds of Si materials being invented in the group, we realized that our understanding of the fundamental physicochemical processes at the freestanding Si surfaces under physiological conditions were rather limited, which significantly impeded further biointerface innovations. Additionally, biology also sets some other constraints on the materials properties that we need to consider for their designs. In particular, biological systems are hierarchical, with vastly different dimensions and mechanics, such that efficient signal transductions across the interfaces cannot be achieved only if Si materials and biological targets have matched properties. Following these selection rules, we systematically screened ~ 30 Si materials, with different scales, geometries, and electronic profiles, and developed a set of matrices to quantify and differentiate the light-induced capacitive, Faradaic and thermal outputs of Si in saline. Guided by the design principles, we were able to identify several key materials with unique structures and properties for efficient optically-controlled biointerfaces. Specifically, we demonstrated, for the first time, the intracellular modulation of calcium dynamics and cytoskeletal transport using phagocytosed Si nanowires. We could even scale up the biointerface to tissue and organ level and realized the first non-genetic photostimulation of mouse brain activities using a flexible device made of Si heterojunctions (**Chapter 3**).

Semiconductors with three-dimensional (3-D) mesoscale feature are an emerging class of materials. However, progress in this area has been impeded by challenges in chemical synthesis and limitations in 3-D fabrication methods. As a result, this area would benefit from new synthetic concepts or new components in lithography.

Taking inspiration from the natural biomineralization process where trace amount of organic species can significantly alter the mineral structures and properties, we exploited a similar phenomenon for 3-D lithography of Si, by showing one example where iterated deposition-diffusion-incorporation of gold (Au) over Si nanowires forms etchant-resistant patterns. We also

showed that this process is facet selective and can produce mesostructured Si spicules with skeleton-like morphology and 3-D tectonic motifs. We further found that individual Au atoms played a crucial role in forming the lithographic resists by changing the local electrochemical potential. This chemical etch resist effect is fundamentally different from the traditional film-based etch mask in lithography, where a physical blockage is in the presence. Finally, we showed that the bee-stinger-like anisotropic spicule displayed enhanced interfacial interactions with extracellular matrices, promising future applications in bioelectronics where a tight junction is required at the biointerface (**Chapter 4**).

In light of the critical role of single Au atoms in the Si morphogenesis, we argued that large-scale assembly of individual Au atoms over Si surfaces may provide unprecedented control of the Si structures. Taking advantage of the dynamic instabilities of liquid Au-Si alloy droplets established in the classical vapor-liquid-solid growth of Si nanowires, we were able to deposit ordered and 3-D rings of isolated Au atoms over Si nanowire sidewalls. Molecular dynamics simulations and subsequent experiments unveiled a surprising new chemistry that single Au atoms, not necessarily nanoparticles, are active enough to catalyze the chemical etching of Si. The catalytic etching of Si nanowires yielded dopant-dependent, massive and ordered 3-D grooves with spacing down to ~ 5 nm. Finally, we used these grooves as self-labelled and *ex situ* markers and resolved several complex Si growths, including the formation of nodes, kinks, scale-like interfaces, and curved backbones (**Chapter 5**).

At this point, we have demonstrated some of our efforts on the precise synthesis of Si structures and potential applications using Si devices for non-genetic biomodulations. In particular, we explored the important role of Au atoms on the morphogenesis of 3-D Si mesostructures. Furthermore, we also demonstrated a number of examples showing the capability of Si-based devices for the modulation of neural activities on the single cell, tissue, and animal levels. Looking forward, there are a number of natural extensions of our current systems that we can pursue in the next stage. First of all, we can further explore the effects of dopants and/or impurities on the Si material properties, especially surface properties. If the impacts of these additives are well understood, interfacial chemical and electrochemical reactions occurring at the Si-biological interfaces may be better tuned for precise controls of more delicate biochemical activities, such as enzymatic metabolic pathways, redox balances and electron transport chains. Additionally, we can also extend our platform to more biological targets rather than just the nervous system. For

example, we can move on to the modulation of other excitable tissues such as the muscular system including cardiac and skeletal muscles. For non-excitable cells, our intracellular stimulation mechanism can still be applied to organelles, such as the endoplasmic reticulum, mitochondria and cytoskeletal filaments. Finally, we can go beyond anesthetized animals to work on freely-moving animals and demonstrate more delicate control of complex behaviors using physical stimuli. To this end, a number of current issues need to addressed, which can potentially bring up many new opportunities in materials synthesis, biophysics and biomedical applications. For example, we first need to design the right form of the device to be administered to the animal, such as using injectable nanomaterials or implantable multiplexed probes. One advantage of nanomaterials is that we may perform surface functionalization to realize cell-type specific targeting, which is critical to precise neuromodulations. For the implantable probes, they are easy to handle and register but the implantation method and long-term biocompatibility need to be considered. An ideal platform would be a transformable device which can switch from a rigid form upon implantable to a soft and flexible configuration over time. Secondly, we need to identify the right properties of the materials. In the past, we almost solely focused on the development of Si-based materials. A multi-functional system can be constructed by incorporating many other candidates with unique electrical, optical, mechanical, magnetic, and chemical properties. For example, we may be able to perform imaging-guided device registration with optically-active materials and multimodal device activations with various contact-less fields. Next, we need to find out a proper way to fabricate the device. A number of elements can be borrowed from other fields, including directed self-assembly, 3-D printing to enrich the format and function of the device and we may be able to precisely position individual building blocks to form an organized matrix. Finally, we need to demonstrate the feasibility of the device for precise controls of animal behaviors. In this regard, targeting of the nanomaterials to circuit-specific neurons at the deep brain region can be extremely important. Additionally, the delivery method of the physical stimuli also needs to be designed based on the specific materials used. Ultimately, a close-loop adaptable system may be built when combining the readout of functional neural network signals with the physical modulation mechanisms.